UNIVERSITY OF HELSINKI REPORT SERIES IN PHYSICS

HU-P-D133

STRAW PERFORMANCE STUDIES AND QUALITY ASSURANCE FOR THE ATLAS TRANSITION RADIATION TRACKER

Peter Cwetanski

Division of High Energy Physics
Department of Physical Sciences
Faculty of Science
University of Helsinki
Helsinki, Finland

ACADEMIC DISSERTATION

To be presented with the permission of the Faculty of Science of the University of Helsinki, for public criticism in the Small Auditorium (E204) of Physicum, Gustaf Hällströmin katu 2a, on Thursday, 22th of June 2006, at 12 o'clock.

Helsinki 2006

ISSN 0356-0961
ISBN 952-10-2121-7 (paperback)
ISBN 952-10-2122-5 (pdf)
http://ethesis.helsinki.fi
Yliopistopaino
Helsinki 2006

P. Cwetanski: Straw Performance Studies and Quality Assurance for the ATLAS Transition Radiation Tracker, University of Helsinki, 2006, xiv, 128 p + appendices, University of Helsinki, Report Series in Physics, HU-P-D133, ISSN 0356-0961, ISBN 952-10-2121-7 (paperback), ISBN 952-10-2122-5 (pdf), http://ethesis.helsinki.fi.

Classification (INSPEC): A06, A29, B74, C73, E16

Keywords: CERN, LHC, ATLAS, TRT, transition radiation, gaseous detector, straw tracker, simulations, Penning effect, ageing, wire tension, straw straightness, acceptance tests, quality assurance.

Abstract

The Transition Radiation Tracker (TRT) of the ATLAS experiment at the LHC is part of the Inner Detector. It is designed as a robust and powerful gaseous detector that provides tracking through individual drift-tubes (straws) as well as particle identification via transition radiation (TR) detection. The straw tubes are operated with Xe-CO_2-O_2 70/27/3, a gas that combines the advantages of efficient TR absorption, a short electron drift time and minimum ageing effects. The modules of the barrel part of the TRT were built in the United States while the end-cap wheels are assembled at two Russian institutes. Acceptance tests of barrel modules and end-cap wheels are performed at CERN before assembly and integration with the Semiconductor Tracker (SCT) and the Pixel Detector.

This thesis first describes simulations the TRT straw tube. The argon-based acceptance gas mixture as well as two xenon-based operating gases are examined for its properties. Drift velocities and Townsend coefficients are computed with the help of the program *Magboltz* and used to study electron drift and multiplication in the straw using the software *Garfield*. The inclusion of Penning transfers in the avalanche process leads to remarkable agreements with experimental data.

A high level of cleanliness in the TRT's acceptance test gas system is indispensable. To monitor gas purity, a small straw tube detector has been constructed and extensively used to study the ageing behaviour of the straw tube in Ar-CO_2. A variety of ageing tests are presented and discussed.

Acceptance tests for the TRT survey dimensions, wire tension, gas-tightness, high-voltage stability and gas gain uniformity along each individual straw. The thesis gives details on acceptance criteria and measurement methods in the case of the end-cap wheels. Special focus is put on wire tension and straw straightness. The effect of geometrically deformed straws on gas gain and energy resolution is examined in an experimental setup and compared to simulation studies. An overview of the most important results from the end-cap wheels tested up to this point is presented.

Tiivistelmä

CERNissä Geneven lähistöllä, Sveitsin ja Ranskan rajalla, tuhannet tutkijat ja insinöörit valmistautuvat kokeisiin, joilla etsitään vastauksia fysiikan peruskysymyksiin: mistä alkeishiukkasten massa tai antimaterian häviäminen aiheutuu.
Luonnon ymmärtämisen kannalta keskeisiin kysymyksiin toivotaan vastauksia CERNiin rakennettavan 27 km pitkän LHC-törmäyttimen avulla. LHC-kiihdyttimen kokeissa, satakunta metriä maan alla, lähes valon nopeudella rengasta kiertävät protoniryppäät kohtaavat toisensa ja aiheuttavat perushiukkasten, kvarkkien ja gluonien, välisiä "nokkakolareita", joissa energia tiivistyy äärimmilleen - simuloiden maailmankaikkeuden syntymähetkeä. Hiukkasfysiikan laboratorion mikroskooppiseen mittakaavaan luodut energiatihentymät purkautuvat energiana ja hiukkasryöppyinä törmäyskohtiin rakennettavien koeasemien mitattaviksi. Massiiviset LHC-törmäyttimen koeasemat rekonstruoivat energiapurkauksista syntyneet hiukkasjäljet ja -energiat, identifioivat erityyppisiä törmäystuotteita ja tallentavat ne maailmanlaajuisten tutkijakollaboraatioiden tutkittaviksi.
LHC-törmäyttimen viisi koeasemaa koostuvat suuresta määrästä erityyppisiä hiukkasilmaisimia, säteilyantureita, joilla on omat tarkoin määrätyt tehtävänsä laboratoriossa aiheutettujen "alkuräjähdysten" mittaamisessa. Osa tuhansia tonneja painavan koeaseman hiukkasantureista on asemoitava hiuksen paksuutta vastaavalla tarkkuudella ja niiden on toimittava kymmenen vuotta supertörmäysten aiheuttamassa säteily-ympäristössä. Koeasemien sisälle sijoitettuja antureita ei juuri päästä huoltamaan.
Koeasemien ilmaisimien tarkkuuden ja luotettavuuden varmistamiseksi anturit valmistetaan ja testataan ensiksi puhdastilassa. Tämän jälkeen anturit läpikäyvät monipuolisen testiohjelman, joka jatkuu asennusvaiheen loppuun saakka. Tuhansien erillisten antureiden kokonaisuus on lopulta osa LHC-törmäyttimen koeasemaa, jonka rakentamiseen osallistuu suuri joukko fysiikan ja tekniikan asiantuntijoita eri maista. Tämän väitöskirjan tekijä on keskeisesti osallistunut LHC-ATLAS -koeaseman ns. transitiosäteilyyn perustuvan ilmaisinjärjestelmän (Transition Radiation Tracker - TRT) toteuttamiseen ja erityisesti sen toimivuuden testaamiseen.
CERN tunnetaan internet-teknologian pioneerina, joka loi World Wide Webin. Nyt CERNissä keskitytään www:n seuraavaan vaiheeseen, GRID-hankkeeseen, jolla LHC-törmäyttimen tuottama valtava tietomäärä jaetaan kansainvälisten tutkijakollaboraatioiden analysoitavaksi.

Acknowledgments

Since its beginning, so many individuals have contributed to the completion of this work that it is impossible for me to express my appreciation to all of them.

I am indebted to Prof. Dr. Risto Orava and Dr. Fido Dittus, who made it possible to engage in, and sometimes endure the endeavour of making a dissertation.
I especially wish to express my gratitude to Mar Capeans, who introduced me to the laboratory work on the TRT and who accompanied me over long periods of research and testing. She also did not hesitate to be the first reviewer of the biggest part of this work.
I also want to thank Anatoli Romaniouk, who was already supervising me during my summer student experience with the TRT in 1999. Almost seven years later we are still sharing the same office. His detailed knowledge and long experience with the TRT have always been of great value for me.
Further I wish to thank Daniel Froidevaux for his support and help in times needed.
I would like to acknowledge the TRT acceptance team, especially the help from Sergei Mouraviev, Victor Maleev, Sergei Konovalov, Sergei Kovalenko and Sergei Katunin. Serguei Olechko and Nikolay Klopov have always provided excellent assistance in solving database matters.
To Neil Dixon, Francisco Perez Gomez and Jerome Bendotti from the TA1 mechanics team; whenever I came to them with a problem, they were ready to tackle it without hesitation. Xavier Pons on the other side occupied himself with my electronics issues.
On the Finnish side I have to thank Kari Kurvinen, Jouni Heino and Rauno Lauhakangas for their contributions in the gas-monitor development. Special thanks also to the very helpful as charming Helsinki secretariat at CERN, Marika Flygar and Tuija Karppinen.
There are few individuals who so unselfishly attended to my questions and problems, as Rob Veenhof and Steve Biagi. It always has been a great pleasure to work with them.
I am also grateful to Fabio Sauli and Leszek Ropelewski for their technical help and critical discussion of results.
I very much appreciated the contributions to proof-reading by Christoph Rembser, Paul Bell and Ole Rohne. Christoph also has become a close colleague and guide in my present project bringing the TRT towards completion, always with an open ear far beyond scientific matters.
Always important to me, at times neglected, are my friends in Germany, in and around CERN and all over the world. I feel privileged to know you.
And finally I want to express my deepest gratitude to my family and my wife Nadia for their love and support. Their importance to me could never be put into adequate words.

Dedicated to my father.

Geneva, June 2006

Peter Cwetanski

List of Abbreviations

ACCESS Advanced Cosmic-ray Composition Experiment for the Space Station

ADC Analog-to-digital converter

ALICE A Large Ion Collider Experiment

AMS Alpha Magnetic Spectrometer (*experiment on the Intern. Space Station*)

ASDBLR Amplifier-Shaper-Discriminator with BaseLine Restoration (*ATLAS TRT*)

ASIC Application-Specific Integrated Circuit

ATLAS A Toroidal LHC Apparatus

BX Bunch-crossing

CAMAC Computer-Automated Measurement And Control
(*international standard of modularised electronics*)

CCD Charge-coupled device

CERN Counseil Européen pour la Recherche Nucléaire
(*The Council created in 1951 was a provisional body, that decided in 1953 to build a laboratory officially called "Organisation européenne pour la recherche nucléaire" or "European Organization for Nuclear Research". However, the name of the Council stuck to the organization. It is a common mistake to think of the "C" of CERN as the first letter of "Centre".)*
Source: `http://user.web.cern.ch/User/CERNName/CERNName.html`

CMS Compact Muon Solenoid

CSC Cathode Strip Chamber

DAQ Data acquisition

DME Dimethyl ether

DTMROC Drift Time Measurement Read-Out Chip (*ATLAS TRT*)

ECAL/ECal Electromagnetic Calorimeter

EDX Energy Dispersive X-ray (*spectroscopy or analysis*)

$FW_{0.2}$ Full Width at 20 % peak height

FWHM Full Width at Half Maximum (of peak height)

HCAL/HCal Hadronic Calorimeter

HTML Hyper Text Markup Language

HV High-voltage

JINR Joint Institute for Nuclear Research (*in Dubna, Russia*)

LAr Liquid argon

LHC Large Hadron Collider

LHCb A dedicated LHC Beauty experiment for precision measurements of CP-violation

MDT Monitored Drift Tubes (*of the ATLAS experiment*)

MIP	Minimum ionizing particle
MSSM	Minimally Supersymmetric Standard Model
MWPC	Multiwire proportional counter
PAMELA	A Payload for Antimatter Exploration and Light-nuclei Astrophysics
PCB	Printed-circuit board
PHENIX	Pioneering High Energy Nuclear Interaction eXperiment
PNPI	Petersburg Nuclear Physics Institute (*in Gatchina, Russia*)
PPAC	Parallel-plate avalanche counter
QC/QA	Quality Control/Quality Assurance
RICH	Ring-Imaging CHerenkov counter
RPC	Resistive Plate Chamber
SCT	Semiconductor Tracker (*of the ATLAS experiment*)
SEM	Scanning Electron Microscope
SM	Standard Model
SPD	Scintillator Pad Detector
SQS	Self-quenched streamer
SUSY	Supersymmetry
SWPC	Single wire proportional chamber
TGC	Thin Gap Chamber
TOTEM	A TOTal and Elastic Measurement experiment
TR	Transition Radiation
TRD	Transition Radiation Detector
TRT	Transition Radiation Tracker (*of the ATLAS experiment*)
UX15	Underground eXperimental area 15 (ATLAS cavern)
VELO	Vertex Locator (*of the LHCb experiment*)
Vol/h	(Detection) volume exchanges per hour
WEB	Wheel End-cap Board (*ATLAS TRT*)
WTS	Wheel Test Station (*ATLAS TRT*)

Note on abbreviations and units

Gases are denoted in the style *Ar-CO_2 70/30*, indicating a mixture composed of argon and carbon dioxide in the fractions 70 % and 30 %.
Although the proper SI unit for pressure is *kilopascal* (kPa), the author decided to keep the commonly used unit *millibar* (mbar), whenever pressure values are taken from written specifications or related laboratory measurements.

"Experience is the name everyone gives to their mistakes."
Oscar Wilde (1854-1900)

Preface

Between Lake Geneva and the Jura mountains an extraordinary project is approaching its completion, yet not its end. In the world's biggest scientific endeavour, scientists and engineers have chosen to transcend national, ethnic and religious borders and merge efforts on the quest for the missing links in our understanding of what is and what holds together our universe. A theory called the *Standard Model* will be put to test with the Large Hadron Collider (LHC), the most powerful instrument ever built to probe deeply into matter and investigate its properties. In 2007, the accelerator will provide to its four major experiments the first proton-proton collisions as well as offer the possibility to collide heavy lead nuclei. By then, a world-wide scientific computing network, the *Grid*, will facilitate scientists to share the enormous amount of data produced by the experiments. Together they will try to shed light on the smallest constituents of matter to understand nothing less than the architecture of the universe.
Already now a first experiment has shown great success: the peaceful and fruitful collaboration of more than 6000 scientists and engineers of over 80 nationalities.
It is as much a pleasure as it is a challenge to act and contribute in this truly international environment. And it is not seldom as a result of mistakes made, that one grows and gains from it, on a scientific, but also on a social level. Thus they deserve to be called experience.

Reported in this thesis are the results of the work that was carried out during the acceptance testing of the ATLAS Transition Radiation Tracker end-cap wheels. Studies devoted to gaseous detector simulations, in particular straw performance, accompanied the laboratory work all along and constitutes an important part of the thesis. In many aspects the results of the simulations and experimental studies are valid not only for the end-cap wheels of the TRT (the author's work domain), but also for the TRT barrel, which for the most part shares the operating gas and parameters as well as the basic straw geometry.
The work on the acceptance tests *per se* involves a team at CERN with rotating contributions from collaborators from the production sites in Russia. The ageing tests and following analyses, as well as the straw simulations, could not have been performed without the valuable contributions of others. Since the reported matter is often the result of the direct and indirect input of many collaborators, I will try to make explicit here the work for which I have been responsible.

The thesis is organised in seven Chapters, followed by three appendices, which contain a list of relevant publications of the author and the collaboration, a series of technical drawings and a sample “acceptance passport”. While Chapters 1-3 are of introductory nature and aim at bringing the reader closer to the matter, the author’s fields of activity framing the thesis are elaborated in Chapters 4-6, then concluded in Chapter 7.

Chapter 1 gives an overview of the LHC project, namely the accelerator and its experiments. The ATLAS experiment is described in more detail in **Chapter 2** with a focus on the various detector technologies. **Chapter 3** is devoted to the Transition Radiation Tracker (TRT), its design, requirements and performance. In particular, the detecting element - the straw tube - is described along with the operating gas mixture. Gas system and electronics are briefly outlined.

Chapter 4 treats of the straw tube simulations that were performed prior to the laboratory work and recommenced in the course of change of operating gas. They focus on the level of the single straw performance in terms of electric field and gas gain behaviour, electron drift properties and mechanical deformations, driven by the TRT’s requirements. The main goal of the work was to make a contribution to a better understanding of the straw behaviour and operation as seen in many experimental studies. Furthermore it serves as an excellent benchmark of the software and its input parameters (gas cross-sections).

Chapter 5 emphasises the cleanliness requirements for the gas system of the acceptance test laboratory and elaborates on the various ageing tests that were performed in order to validate the purity level or test run conditions. For this purpose a series of five small straw tube counters (hereafter called the *gas-monitor*) was designed, manufactured, assembled and tested. Assembly and operation are illustrated in detail. Additionally, studies on the ageing susceptibility of straws operating with Ar-CO_2 70/30 in the given gas system are presented and their results discussed. In some ageing runs the gas-monitor was operated in combination with a ultra-clean stainless steel single wire proportional counter (SWPC).

Chapter 6 introduces the methods and purpose of the different acceptance tests together with the defined acceptance criteria.
Special attention is given to two aspects: wire tension and straw straightness.
Firstly, the hardware component of the tension measurement setup had to be optimised for increased reliability and speed. The risk of tension loss is discussed and the global quality assessed by analyzing wire tension data of the tested wheels.
In the course of change of acceptance test gas, the correlation of gas gain variations along a straw with wire offset had to be re-evaluated. An additional criterion was determined to increase the reliability of identifying bent straws, which, for safety reasons, have to be disconnected at a certain point. One gas-monitor was modified to hold straws of original length in order to perform studies on geometrical straw tube deformations. A general quality assessment is made by analyzing wire offset data of the large number of straws measured to-date. Statistics are presented on channels lost due to different cause.
An overview of the tests and the respective acceptance criteria was presented at the 2004 IEEE Nuclear Science Symposium and submitted for publication [1].

A brief summary of the main work and conclusions is given in **Chapter 7**.

TABLE OF CONTENTS

CHAPTER 1

"Discovery consists of seeing what everybody has seen and thinking what nobody has thought."

Albert Szent-Györgyi (1893-1986)

The LHC and its Experiments

1.1 The Accelerator

In December 1994, five years after the start of the LEP (Large Electron-Positron) collider, the CERN Council approved the construction of a proton-proton collider working with two counter-rotating beams of protons accelerated to energies of 7 TeV: the LHC (Large Hadron Collider) project (Figure 1-1). This venture will enable physicists from all over the world to explore the energy regime that resembles the universe 10^{-12} seconds after the Big Bang when its temperature was still the order of 10^{16} Kelvin.

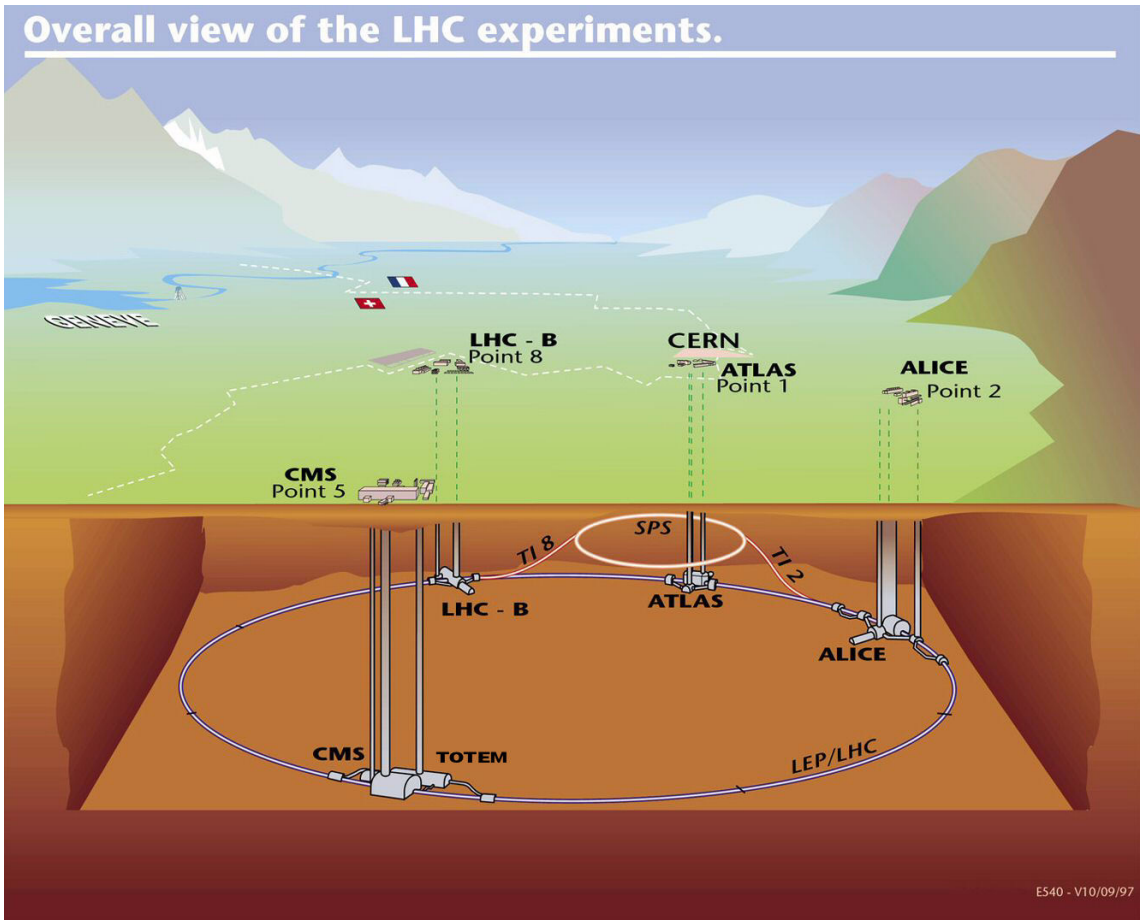

Figure 1-1 Overall view of the LHC tunnel and experiments under construction.

The new accelerator is currently being installed in the 27 km circular tunnel, that was built for LEP. To achieve the centre-of-mass energy of $\sqrt{s}$ = 14 TeV and the unprecedented luminosity of $\mathscr{L} = 10^{34}$ cm^{-2}s^{-1}, the LHC (which is unique among super-conducting synchrotrons) has to cool down 1232 dipole magnets to 1.9 Kelvin, the temperature at which helium becomes superfluid. Thus it is able to reach the nominal magnetic field of 8.4 Tesla. A novel two-in-one magnet construction allows both beam pipes to be housed in a single yoke and cryostat (see Figure 1-2), significantly saving space and costs. A total helium inventory of 96 000 kg is available to cool down the LHC total cold mass of 37 000 tons. This makes the LHC the world's biggest cryogenic system. One year after the start-up (foreseen in Spring 2007), the collider will also provide Pb-Pb head-on collisions mainly for its heavy-ion experiment ALICE. These ions will have a beam energy of 2.8 TeV/nucleon, yielding a total centre-of-mass energy of 1.15 PeV and a nominal luminosity of 10^{27} cm^{-2}s^{-1}. More details on design and operation can be found in Table 1-I and Ref. [2].

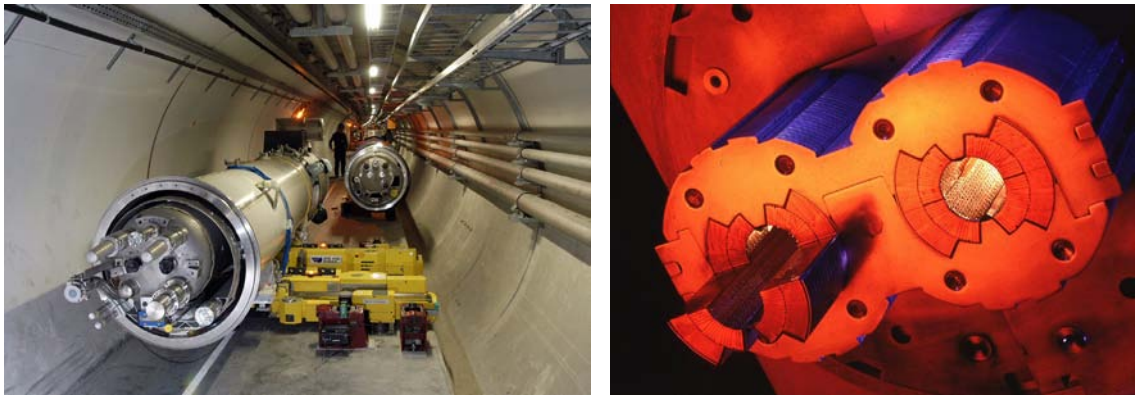

Figure 1-2 Cryomagnet in the LHC tunnel (left), superconducting dipole magnet (right).[a]

a. CERN Photos, CERN Document Server

TABLE 1-I A few selected machine and beam parameters[2].

Proton energy	7 TeV
Injection energy	450 GeV
Dipole field	8.4 T
Current at nominal field	11850 A
Luminosity	10^{34} cm^{-2}s^{-1}
Bunch spacing	25 ns
Particles per bunch	10^{11}
Number of bunches	2808
Bunch length (r.m.s.)	7.5 cm
Inelastic cross-section	60 mb
Total cross-section	100 mb
Events per bunch crossing	19
Stored beam energy	362 MJ (eq. to 80 kg of TNT)
Energy loss per turn	6.7 keV
Synchrotron radiation power per ring	3.6 kW

1.2 The Experiments at the LHC

LHC hosts four major experiments, namely two large multi-purpose detectors, ATLAS [3] and CMS [4], the heavy-ion experiment ALICE [5] and the B-Physics single-arm spectrometer LHCb [6]. Finally, an additional experiment for small angle scattering (TOTEM) [7] has been approved to be installed in the region of CMS. While ATLAS and CMS are designed to cover a wide range of physics of the *Standard Model* [8] and beyond, ALICE, LHCb and TOTEM have more specialised physics programmes.

1.2.1 On LHC physics

The physics potential of the LHC covers a wide range of precision measurements and searches for new physics phenomena. Therefore only a few highlights of particle searches are briefly outlined here.

Despite all the success of theoretical and experimental particle physics over the last few decades, numerous fundamental questions remain unanswered. One of the main issues in this context is the question of the violation of the electroweak symmetry. In other words, why the photon is massless, but W and Z gauge bosons very heavy. The answer to this question is closely related to the search for the *Higgs boson* - the last, important component of the Standard Model. To date, we have not been able to observe this particle directly, however measurements at recent accelerators have narrowed down the potential mass range of the Higgs boson. For example, from LEP data it was concluded that the mass cannot be less than 114.4 GeV [9] and based on precision measurements at LEP, SLD and the TEVATRON an upper limit of 280 GeV has been defined [10]. The strength of the LHC with centre-of-mass energies up to 14 TeV lies in the generation of particles with very high masses, thus it will be energetically possible to produce, observe and measure the Higgs boson - if it exists.

One of the most promising additions to the Standard Model is *Supersymmetry* [11], which unites the building blocks of matter with fundamental forces and entails numerous new particle species. Supersymmetry also requires the existence of several species of Higgs bosons. Although no supersymmetric particle has yet been observed, there are many indications that the LHC, with its ability to create heavy particles, may be able to answer the question whether Supersymmetry actually occurs in nature. The discovery of Supersymmetry and the proof of the existence of a lightest supersymmetric particle, the Neutralino, would give a promising candidate for dark matter, the large majority of the mass of our universe. At the LHC it will therefore be possible to create a natural and fascinating link between particle physics and cosmology.

1.2.2 ATLAS

A more detailed technical description of the ATLAS detector is given in Chapter 2.

1.2.3 CMS

As is the case for ATLAS, the physics programme of CMS (Compact Muon Solenoid, Figure 1-6) [4] features investigations of electroweak symmetry breaking (through the possible observation of one or more Higgs bosons), searches for phenomena beyond the Standard Model (such as Supersymmetry or extra dimensions), and detailed studies of Standard Model physics, CP violation and quark-gluon plasma (QGP) [12]. The CMS detector represents the other general-purpose experiment at the LHC. As the name suggests, it relies on a compact design with a large superconducting solenoid magnet generating a 4 T magnetic field. Although being "only" 15 m high and 22 m long, it weighs 12 500 tons, almost twice as much as ATLAS. Among others, the detector subsystems of CMS include:

- A full-silicon **inner tracker** (pixel and strips) [13][14] covering an active area of 210 m^2, sums up 44 million plus 9.3 million read-out channels for the pixel respectively the strip detector (Figure 1-3).
- An electromagnetic **calorimeter** (ECAL) [15] is placed around the tracker and is composed of 80 000 lead tungstate crystals (Figure 1-3). Read-out is carried out with avalanche photodiodes (APDs) and vacuum phototriodes (VPTs). A copper/steel/ brass/scintillating tiles hadronic calorimeter (HCAL) surrounds the ECAL.
- The **muon system** [16] is integrated in the gaps of the return yoke (Figure 1-3) layers. It combines Cathode Strip Chambers (CSCs), Resistive Plate Chambers (RPCs) and Drift Tubes (DTs), each technology optimised for it corresponding task (tracking, trigger etc.).

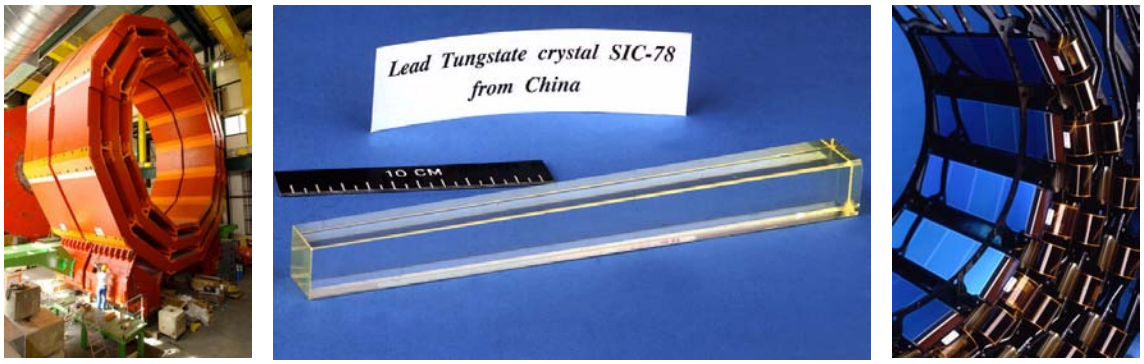

Figure 1-3 CMS: Barrel yoke ring (left), $PbWO_4$ crystal of the Electromagnetic Calorimeter (centre), Silicon Tracker (right).

TOTEM

The TOTEM experiment [7] will measure the total *pp* cross-section and study small angle elastic scattering and diffractive dissociation at the LHC. Two years after its proposal in 1997, CMS was identified as the optimal host experiment for TOTEM. Its main components are:

- Two **tracking telescopes**, that are proposed to be integrated directly at CMS, contributing charged particle tracking and trigger capabilities over a pseudo-rapidity interval of $3 < |\eta| < 6.8$.
- Silicon detectors in **Roman pots** (Figure 1-4), planned to be installed at 147 m, 180 m and 220 m distance from the interaction point down the beam line, operated to determine the total *pp* cross-section.

- **Microstations** (MS) are developed to detect leading 'beam-like' protons in the LHC environment. Integrated with the beam pipe, they will be placed at 18 m distance from the interaction point and approach the beam as close as 3 mm (ten times its r.m.s. size) during low luminosity runs. Their advantage is the independence of the precision mechanics from the vacuum chamber and the overall light and robust design in terms of vacuum leaks. Silicon-strip detectors present an attractive choice of technology.

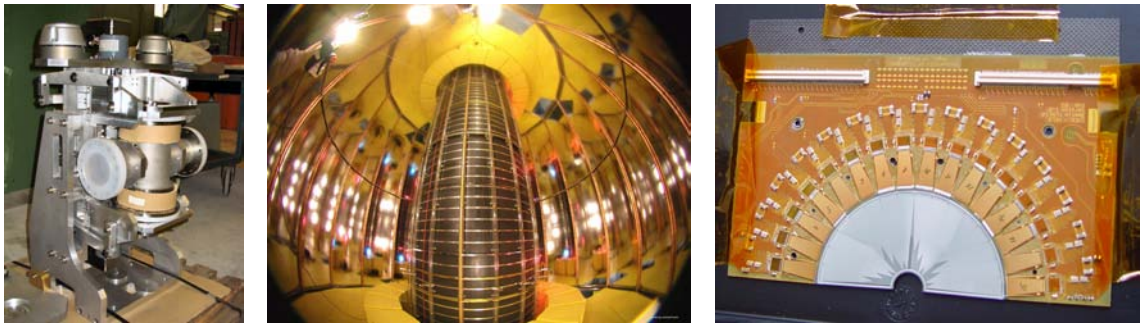

Figure 1-4 TOTEM roman pot (left), the ALICE TPC field cage (centre) and a LHCb VELO hybrid (right).

1.2.4 ALICE

CERN's heavy-ion experiment ALICE (A Large Ion Collider Experiment, Figure 1-8) [5] aims to study the physics of strongly interacting matter at extreme energy densities, where the formation of a new phase of matter, the quark-gluon plasma (QGP) [12], is expected. Apart from proton-proton collisions ALICE utilises lead-lead collisions of more than 1 PeV centre-of-mass energy. The main challenge of heavy-ion physics is recording the enormous number of particles which emerge from the collisions. At LHC energies, about 50'000 particles are produced in each collision. A large fraction of these must be tracked and identified. Only then can a clear picture emerge, and key signals be found pointing to different stages in the evolution from ordinary matter to QGP and back again. Without being exhaustive, the ALICE detector comprises the following detector technologies:

- The **Inner Tracking System** (ITS) employs silicon-pixel, -drift and -strip detectors for vertex reconstruction and dE/dx measurements.
- The main tracking detector of ALICE is its **Time Projection Chamber** (TPC) [17], with a gas volume of 88 m^3 the world's biggest (Figure 1-4). It operates with Ne-CO_2 90/10.
- A high-granularity (1.2 Mio. channels), large-area (126 m^2) **Transition Radiation Detector** (TRD) [18] provides pion rejection and fast trigger for high p_T electrons and jets. It utilises fibre/foam radiators and runs with Xe-CO_2 85/15.
- Multi-gap Resistive Plate Chambers (MRPCs) are used in the **Time-Of-Flight** (TOF) detector with a $C_2F_4H_2$-based gas mixture. Their time resolution is ~50 ps (250 µm gaps) exhibiting a rate capability of 1 kHz/cm^2.
- The photon and electron crystal **calorimeter** (PHOS) is built of ~20'000 $PbWO_4$ crystals.
- The **muon tracking system** operates Cathode Pad Chambers (CPCs) with Ar-CO_2 80/20.

The inherited **solenoid magnet** from the former L3 experiment is converted to provide a field uniformity inside the magnet of better than 2-4 mT.

1.2.5 LHCb

LHCb [6] is a single-arm spectrometer with a forward angular coverage from approximately 15 mrad to 300 (250) mrad in the bending (non-bending) plane. The choice of the detector geometry is motivated by the fact that at high energies both the b- and $b\bar{b}$-hadrons are predominantly produced in the same forward cone. The 19.7 m long LHCb detector's (Figure 1-7) characteristic components are the following:

- A high-resolution silicon-strip **vertex locator** (VELO, Figure 1-4) predominantly for identification of secondary vertices and accurate flight-time measurements.
- Two **Ring Imaging CHerenkov detectors** (RICH1 and RICH2) for particle identification ($\rightarrow$ K-π separation) capturing the image with pixelated Hybrid Photon Detectors (HPD).
- A four-stations **tracking system** providing charged particle track reconstruction and information to link hits in the calorimeters and muon chambers, which consists of a silicon micro-strip Inner Tracker (TT) and a straw tube based Outer Tracker (T1-T3).
- The **calorimeters** to identify photons, electrons and hadrons, with position and energy, utilizing a "shashlik" lead-scintillator ECAL, an HCAL with a structure of iron and scintillating tiles and a PreShower (PS) and Scintillator Pad Detector (SPD) for pion background reduction.
- The **muon detector**, which consists of five multiwire proportional chamber (MWPC) tracking stations (M1-M5) identifying muons and delivering high efficiency Level-0 trigger information.
- A warm **dipole magnet** of 1600 tons, placed directly after RICH, providing an integrated field of 4 Tm.

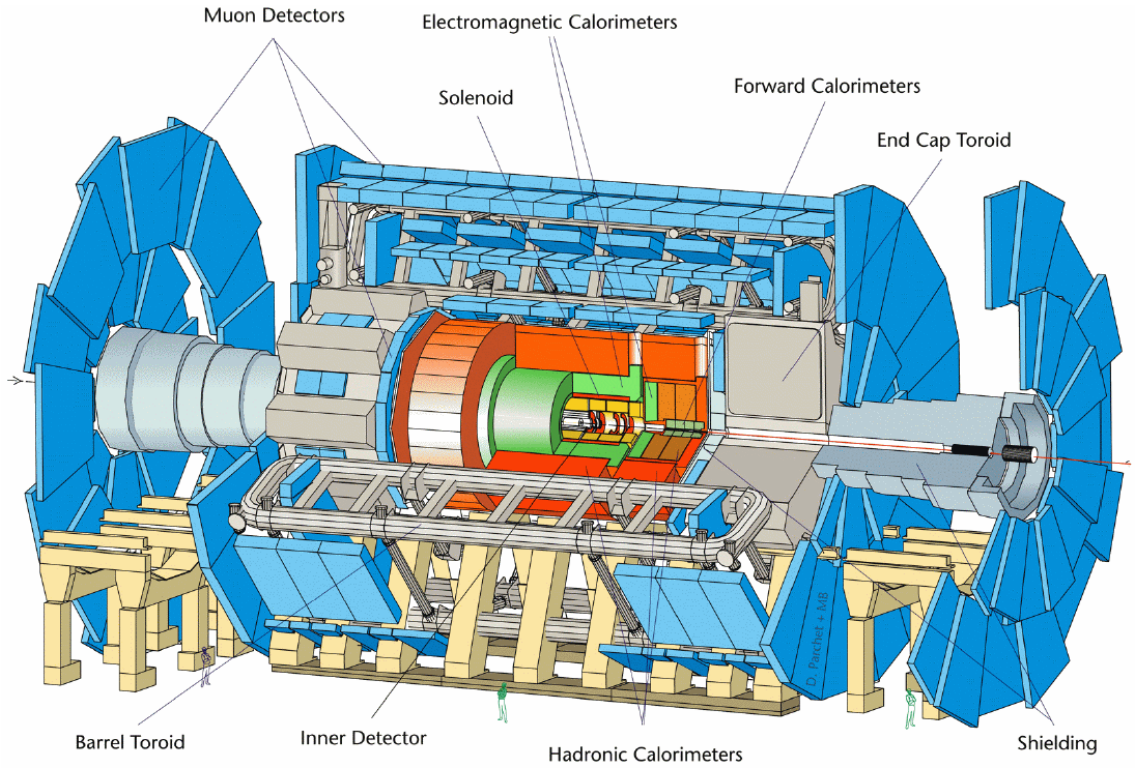

Figure 1-5 The ATLAS Detector with its subdetector systems (artist view).

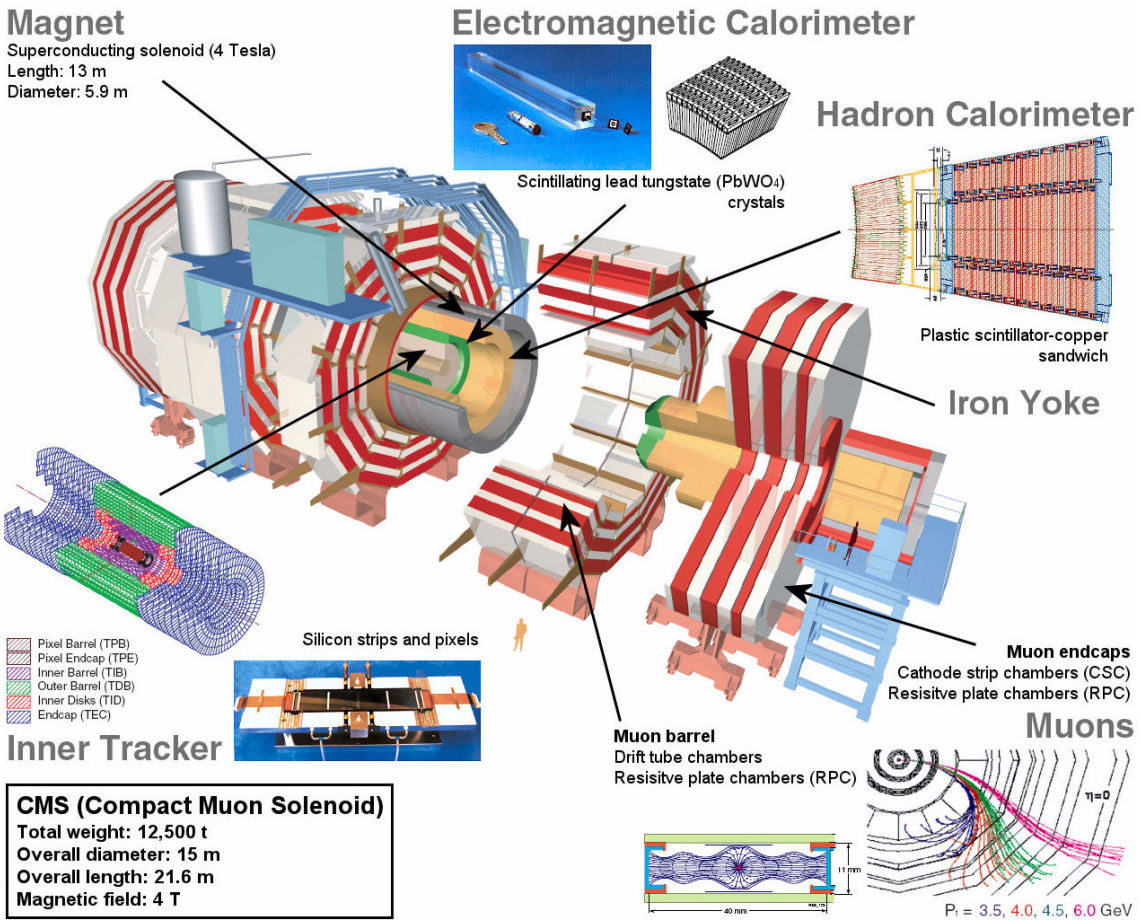

Figure 1-6 The CMS detector with its subdetector systems (artist view).

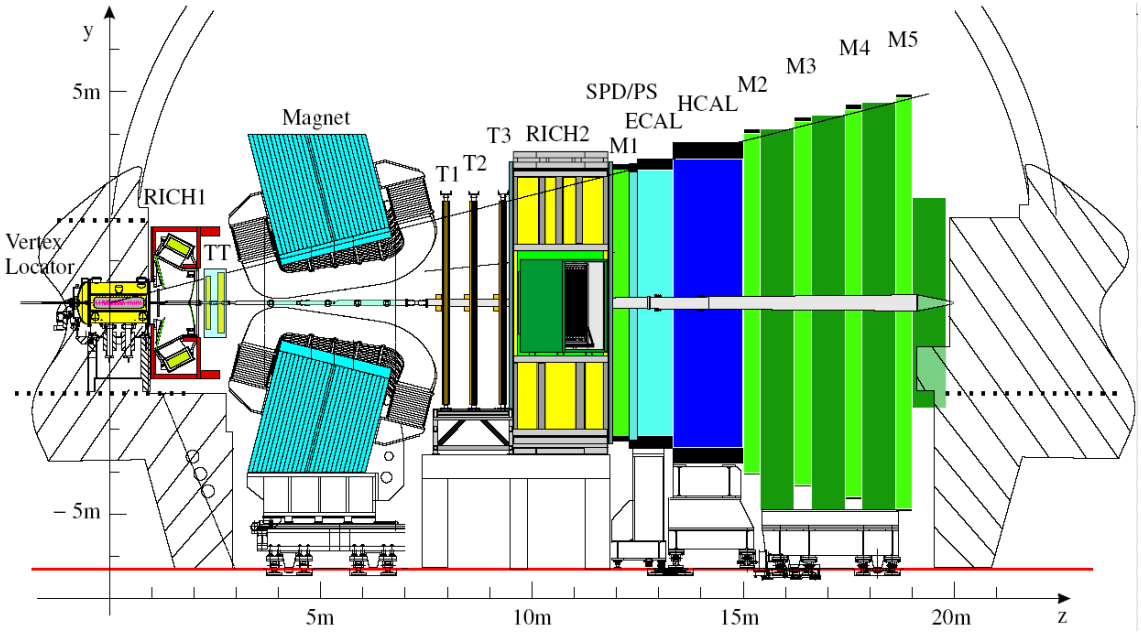

Figure 1-7 The LHCb detector in a cross-sectional schematic view (for explanations see 1.2.5).

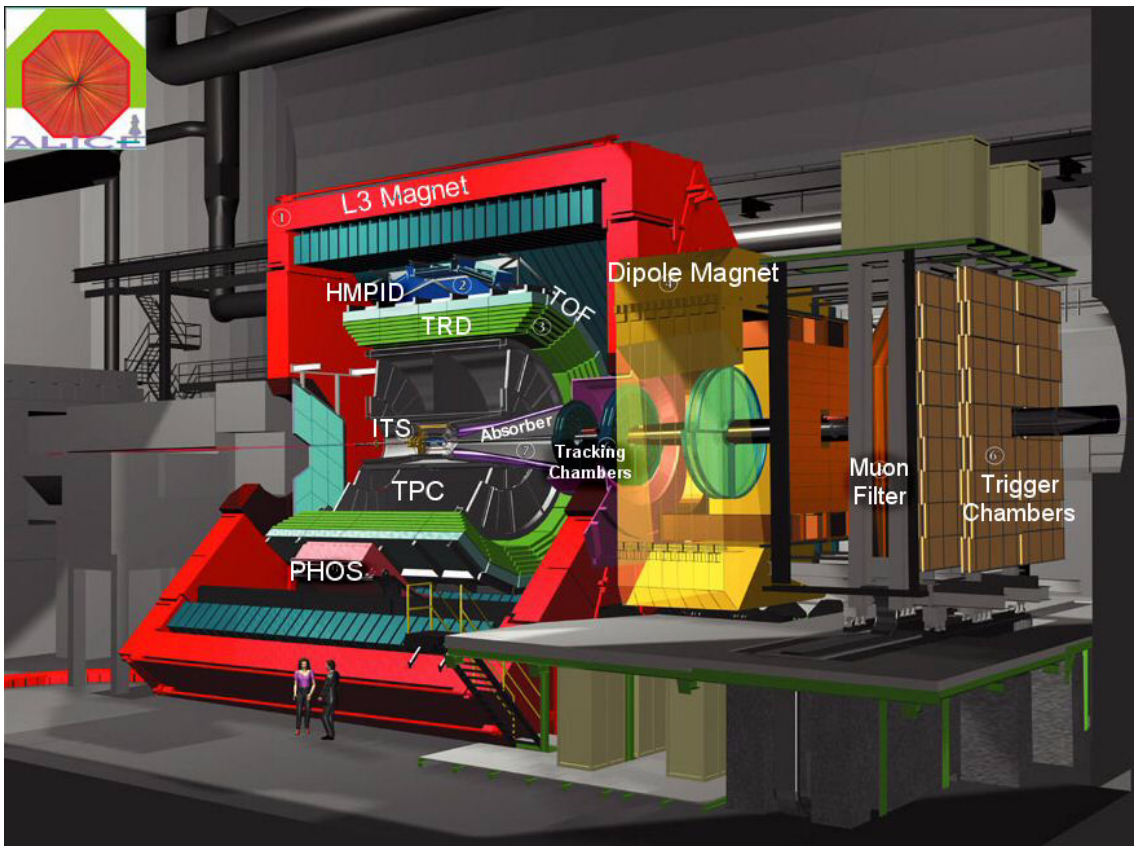

Figure 1-8 The ALICE detector.

CHAPTER 2

"And Atlas through hard constraint upholds the wide heaven with unwearying head and arms, standing at the borders of the earth..."

Hesiod (c.700 BC)

The ATLAS Experiment

2.1 Purpose

ATLAS (**A** **T**oroidal **L**HC **A**pparatu**S**) [3] is one of the four big particle physics experiments at the LHC to explore the fundamental nature of matter and the basic forces that shape our universe. It will search for new discoveries in the head-on collisions of protons accelerated to energies up to 7 TeV. The energy density in these high-energy collisions is similar to the particle collision energy in the early universe less than a billionth of a second after the Big Bang. ATLAS and CMS also are the largest collaborative efforts ever attempted in the physical sciences, each with around 2000 scientists and engineers participating from more than 150 universities and laboratories in 35 countries.

The ATLAS detector consists of **four major components**, that a described briefly later in this chapter. The **Inner Detector** [19] measures the paths of each charged particle and supports particle identification, while the **calorimeters** record the energies carried by the particles. Muons which are able to traverse both inner detector and calorimeters without being stopped are then identified in the Muon spectrometer. The **magnet system** consisting of a solenoid for the inner tracker and outer toroid coils, that create strong magnetic fields to bend charged particles and thereby achieve accurate momentum measurements. The interactions in the ATLAS detectors will create an enormous data flow. An elaborate **3-level trigger** and **data acquisition** system selects and stores about 100 interesting events out of 1 billion other interactions each second. Extensive **computing resources** are set up to analyse an expected one billion events recorded per year.

The ATLAS experiment offers a large physics potential with major focus on electroweak symmetry breaking, particularly the search for the **Higgs boson**, a hypothesised particle which, if it exists, would provide the mechanism by which particles acquire mass. The large cross-section for b-quark production allows for extensive **B-physics** studies, similarly the high $t\bar{t}$-pair production rate evokes relevant top quark studies. In ATLAS there are wide and open fields to search for **physics beyond the Standard Model** (SM), like supersymmetry (SUSY), Minimally Supersymmetric SM (MSSM) and Technicolor, to name only a few.

2.2 The ATLAS Detector

The 44 m long, 22 m high and 7000 tons heavy ATLAS detector (Figure 2-1) is installed in a cavern of 53 m length, 35 m width and 40 m height at 100 m below ground (floor level). In contrast to the size of the detector stands the required accuracy. The alignment of the detector's support (Figure 2-2) and components, also with respect to the LHC beam, will be constantly monitored to within several hundredths of a millimetre.

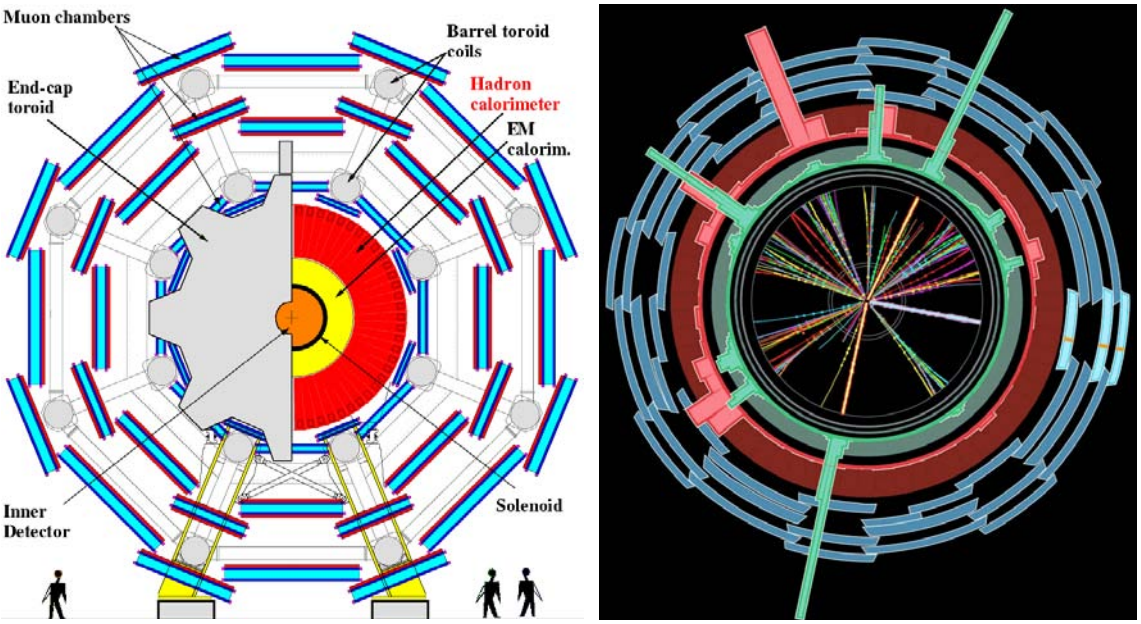

Figure 2-1 *Left*: A schematic cross-sectional view of the ATLAS detector in the XY-plane. *Right*: Simulated event in the ATLAS detector. Particle tracks and the energy deposits in the electromagnetic (green) and hadronic (red) calorimeters are shown as well as the response from the muon chambers (blue).

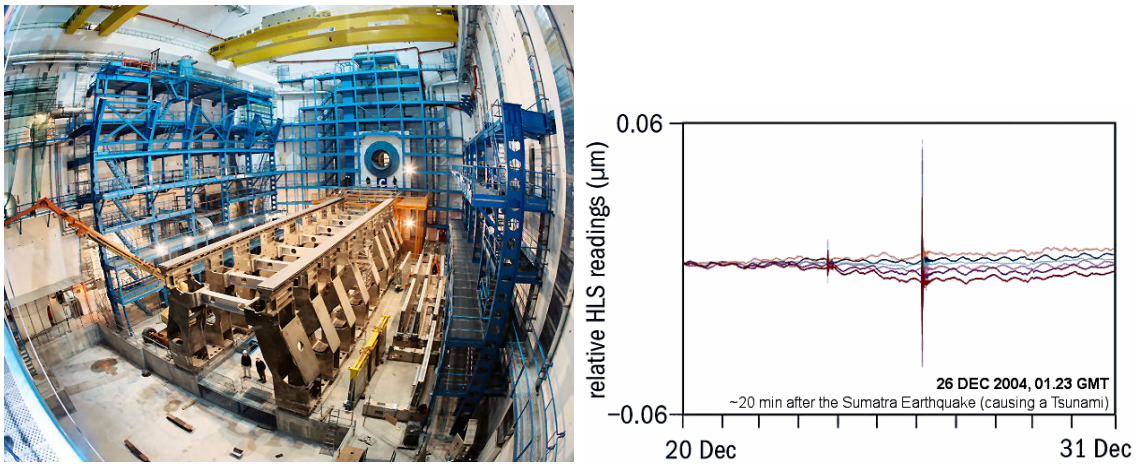

Figure 2-2 *Left*: View into the ATLAS cavern (UX15) during installation of the detector's support structure in February 2004.
Right: Perturbations registered by the hydrostatic level sensors (HLSs), which are installed under the ATLAS support feet to monitor deformations of the support structure at sub-micrometric resolution. The amplitudes were recorded on 26 December 2004 at 01.23 GMT and originate from the earthquake/tsunami that happened in front of the Sumatran coast at 00.59 GMT, almost 10 000 km away from CERN, in accordance with the travel speed of 6-8 km/s for P-waves.

2.2.1 Inner Detector

The Inner Detector [19], as seen in Figure 2-3, occupies the most central region of ATLAS with the main task of tracking charged particles from the interaction point to the calorimeter. It is 7 m long and extends to a radius of 1.15 m. A solenoid magnet envelopes the Inner Detector and provides a 2 T magnetic field to bend charged particles and allow for their charge sign and momentum measurement. It comprises three subdetector systems which are descibed briefly in the following paragraphs.

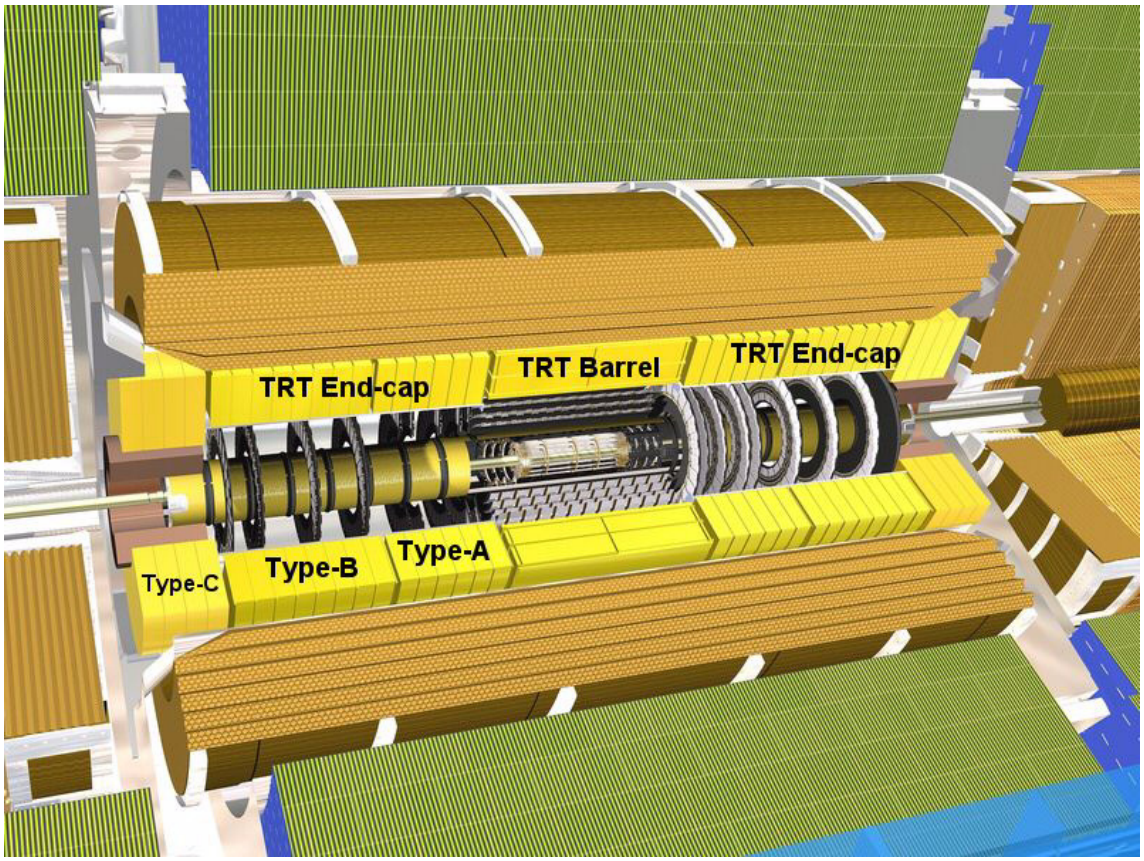

Figure 2-3 Artist view on the ATLAS Inner Detector.

The Pixel Detector

The sensors closest to the collision point forms the Pixel Detector (Figure 2-4) [20]. It has a very high granularity and provides high precision measurements (12 µm in r-ϕ and 110 µm in z) very close to the interaction point. The system contributes three precision measurements over the full acceptance, and largely determines the impact parameter resolution and the ability of the Inner Detector to find short lived particles such as B-hadrons. The detector comprises three barrels with three disks on each side. Each 6.4 cm × 2.1 cm pixel module contains 47268 pixel elements (of dimensions 50 µm × 400 µm and 50 µm × 600 µm), which are read out by 16 chips. The total of 80 million[1] pixels cover an area of 1.7 m^2. In ten years of operation the pixel detectors are expected to be exposed to ionizing radiation of 300 kGy and a neutron fluence of $5 \cdot 10^{14}$ 1 MeV n_{eq}/cm^2. The Pixel system can be installed independently of the other components of the Inner Detector.

[1] The system compares to an 80 Megapixel digital camera taking 40 million pictures per second!

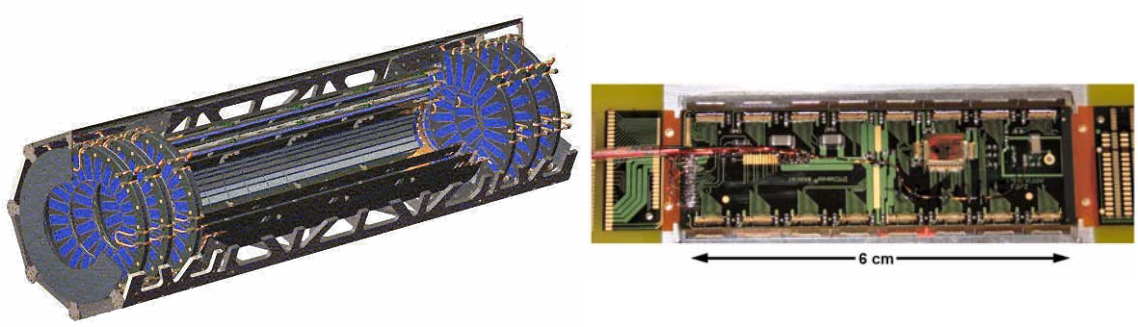

Figure 2-4 Artist view of the Pixel Detector (left). Each Pixel module contains 46080 channels (right).

The Semiconductor Tracker (SCT)

A little further from the collision point additional four position measurements per particle track (accuracy 16 µm in r-ϕ and 580 µm in z) are provided by the SCT (Figure 2-5) [21]. The SCT utilises layers of silicon, subdivided into narrow strips of about 80 µm width and several centimetres length. Each layer has two sets of strips, running at an angle of 2.3° relative to each other. On the four nested barrel layers, strips are oriented parallel to the beam axis, while on the nine end-cap disks on both sides, the sets run radially. With a total of 4088 modules, covering an active area of 61 m^2, the SCT is an order of magnitude larger than any such previous detector.

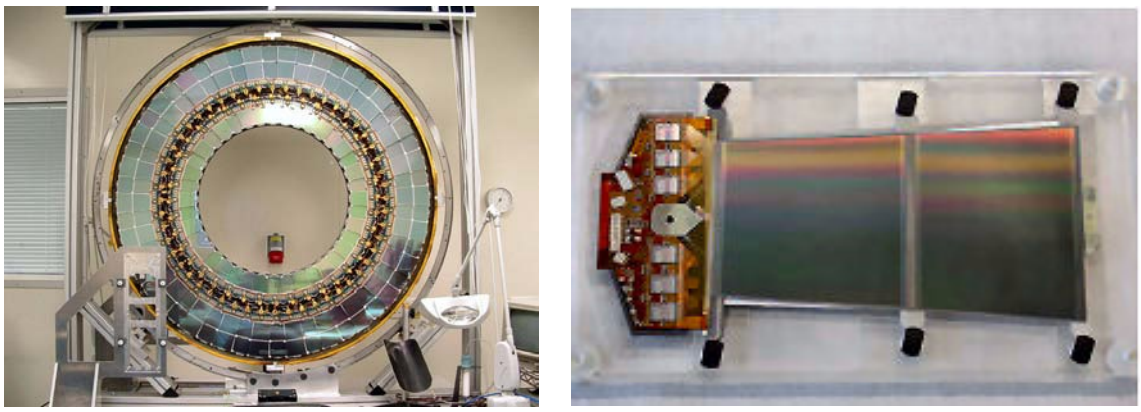

Figure 2-5 Equipped end-cap disk of the SCT (left) carrying the forward modules (right).

The Transition Radiation Tracker (TRT)

At larger radii, it becomes too expensive to cover the large areas required with silicon strip detectors, and a different set of devices is necessary. The TRT is made up of a total of 372 032 gaseous drift detectors, called “straw tubes” (or “straws”). The cylindrical tubes of 4 mm diameter are 40 - 150 cm long and hold a 30 µm thin gold-plated tungsten wire in their axes. The straw tubes are arranged axially in the central barrel and radially in the two end-caps (Figure 2-6). The TRT measures a further 36 points per track for the overall pattern recognition and provides particle identification information utilizing transition radiation from embedded radiator foils and fibres. The TRT is described in more detail in Chapter 3.

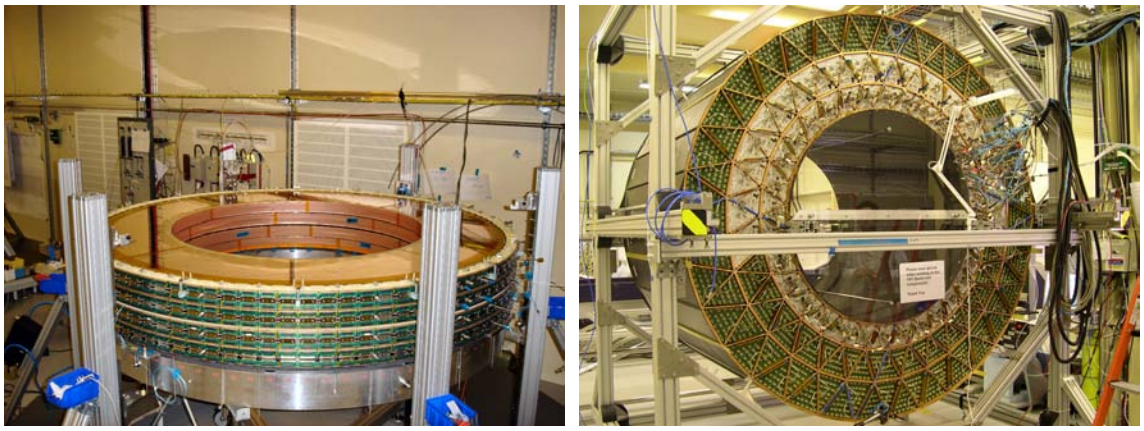

Figure 2-6 Four TRT 8-plane end-cap wheels of type A on the stacking table (left). Completed TRT barrel during electronics installation (right).

2.2.2 The Calorimeters

The ATLAS calorimetry (Figure 2-7) consists of an electromagnetic calorimeter (ECal) and a hadronic calorimeter (HCal).
The ECal records the energy of high-energy positrons, electrons and photons. ATLAS employs a Liquid Argon Calorimeter [22] using thin Pb absorbers immersed in a liquid argon (LAr) bath at 1 bar pressure and a temperature of 90 K. The incident particles interact in the metal plates and create cascades of secondary particles (Figure 2-7). Entering the liquid argon, they produce electron-ion pairs in ionizing collisions. The ionization products are collected on sensing electrodes to which they are guided through an appropriate electric field.

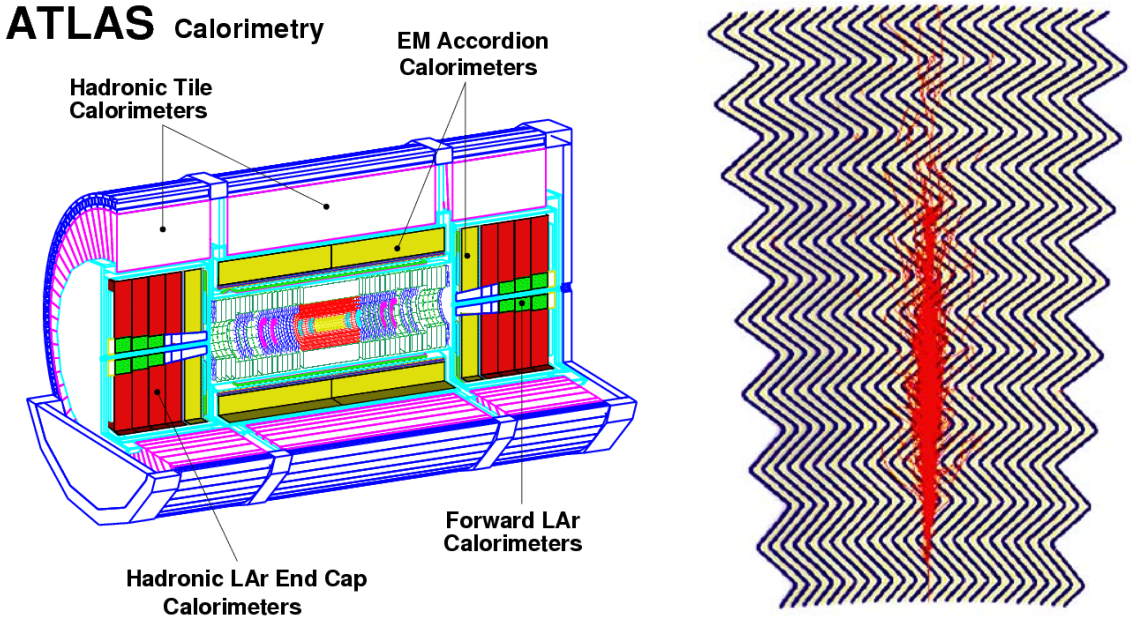

Figure 2-7 Schematic view of the ATLAS calorimetric system (left). Shower simulation in the Electromagnetic Accordion Calorimeter (left).

The HCal surrounds the ECal and converts heavier particles - mainly protons, neutrons, pions and kaons - into “hadronic showers”. It measures energies and direction of “jets” - asymptotic forms of partons (quarks and gluons) - and also attempts to infer the presence of particles that are not directly measurable (like neutrinos) through missing momentum

searches. In order to measure the direction in which the energy is deposited, the calorimeters are segmented.
The HCal is divided into three different units each best suited for the different requirements and radiation conditions in the respective region. The Tile Calorimeter [23] is composed of steel plates and scintillating tiles, that emit light proportional to the deposited energy. The LAr End-cap Calorimeters (Figure 2-8) use copper plates surrounded by LAr. The Forward Calorimeter, which forms a part of the ECal, covers the pseudorapidity region $3.2 < |\eta| < 4.9$, and is assembled of copper and tungsten rods filled with liquid argon. The calorimeter has about 180 000 electronic channels in total.

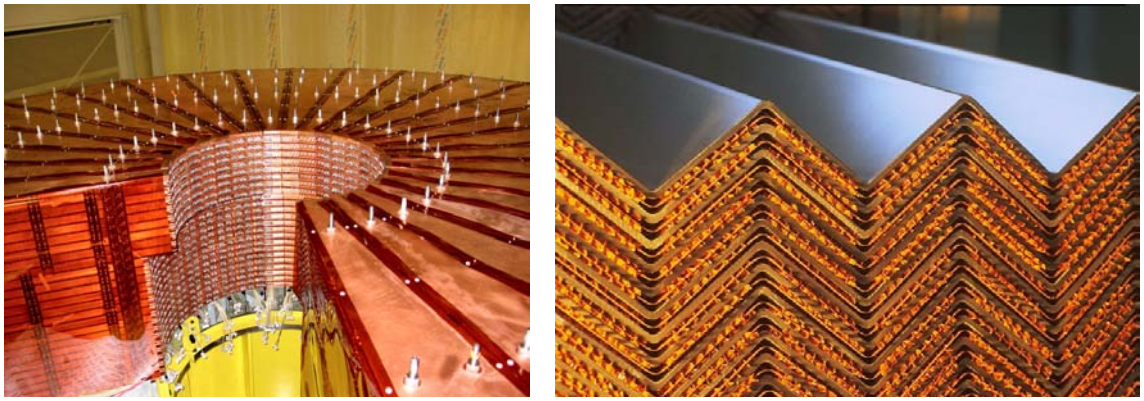

Figure 2-8 End-cap of the Hadronic Calorimeter (left). Accordion structure of the Electromagnetic calorimeter end-cap (right).

2.2.3 The Muon Spectrometer

High-energy muons can traverse the whole detector. Being more than 200 times heavier than electrons they barely interact with the atomic nuclei in the heavy calorimeter material, hence they do not produce the same electromagnetic shower. They are only traced by the electron-ion pairs created along their path, but the energy loss of only 1 GeV per meter of steel lets basically every muon escape the detector. The ATLAS muon spectrometer comprises four different detector technologies (Figure 2-9), two of which provide high-precision tracking (MDT, CSC) and the other two are used for the trigger (RPC, TGC). They are described briefly in the following paragraphs, for more details one should consult Refs. [24] and [25].

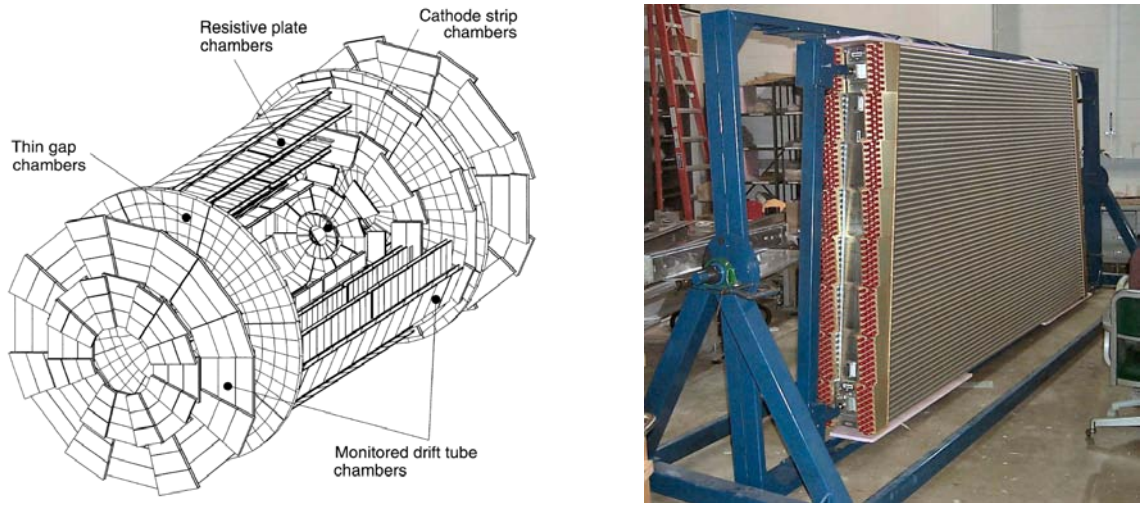

Figure 2-9 The different detector technologies of the ATLAS muon system (left). End-cap muon-chamber with monitored drift tubes (right).

Monitored Drift Tubes (MDT)

The sign and momenta of muon trajectories are recorded by three stations of Monitored Drift Tubes (Figure 2-9). 10 – 1000 GeV muons, bent in the 0.5 T toroidal magnetic field, are measured over a pseudo-rapidity range of $|\eta| \leq 2.7$ with very high precision even at the highest luminosities. The MDT system consists of 1200 chambers with ~400 000 1.2-6.0 m long aluminium tubes of 30 mm diameter with 50 µm gold-plated tungsten wires operating in Ar-CO_2 93/7 at 3 bar pressure and a gas gain of 20 000. They cover an active area of 5500 m^2.

Cathode Strip Chambers (CSC)

For measurements of muons moving at small angles to the beam pipe, drift tubes are unsuitable because of high background conditions. For this purpose 64 4-layer cathode strip chambers are employed in the forward region ($2.1 < |\eta| < 2.7$). They consist of arrays of closely spaced parallel wires in a narrow gas volume enclosed by strip-patterned read-out electrodes (Figure 2-10).

Resistive Plate Chambers (RPC)

Resistive plate chambers (Figure 2-10) are installed as trigger chambers in the barrel region of the Muon Spectrometer. They need to fulfil requirements like 97 % of efficiency and a time resolution of 2 – 3 ns, while operating at rates up to 100 Hz/cm^2. The resolution in the ϕ-coordinate is of the order of 5 – 10 mm. Each layer is made of two 2 mm thick bakelite electrodes ($\rho \sim 10^{10}$ Ω cm), with graphite-coated external faces and internal surfaces treated with linseed oil. An orthogonal two-panel strip read-out allows for independent measurement of η- and ϕ-coordinates. The gas mixture used is $C_2H_2F_4$/iso-C_4H_{10}/SF_6 in the percentages 96.7 %, 3 % and 0.3 %. The over one thousand RPC units cover a total surface of about 3500 m^2.

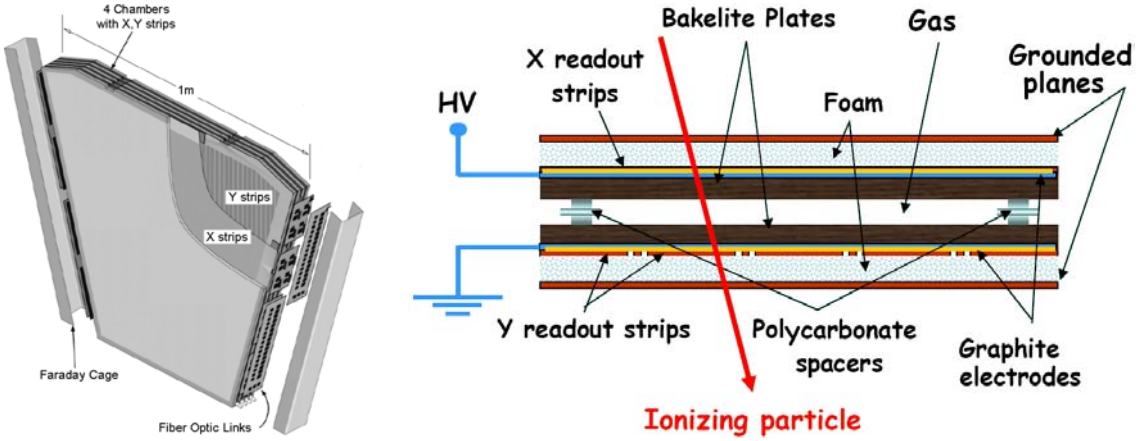

Figure 2-10 Schematic view of an ATLAS cathode strip chamber (left). Schematic cross-sectional view of the ATLAS resistive plate chamber (right).

Thin Gap Chambers (TGC)

The trigger system in the end-cap region is made of thin gap chambers, a robust technology similar to multi-wire proportional chambers with a larger anode wire pitch than the cathode-to-anode gap. They work in saturated mode using a highly quenching gas mixture of 55 % CO_2 and 45% n-pentane (n-C_5H_{12}). Their advantage is the low sensitivity to mechanical deformations, stable pulse height and no streamer formation while providing a short drift time and thus good time resolution (few ns).

2.2.4 The Magnet System

Two magnet systems are installed in ATLAS. A hollow cylindrical **solenoid** coil (Figure 2-11) envelopes the Inner Detector and produces a 2 Tesla solenoidal magnetic field (field lines parallel to the beam axis). Charged particles coming from the collision point are deflected with a radius of curvature proportional to their momentum.

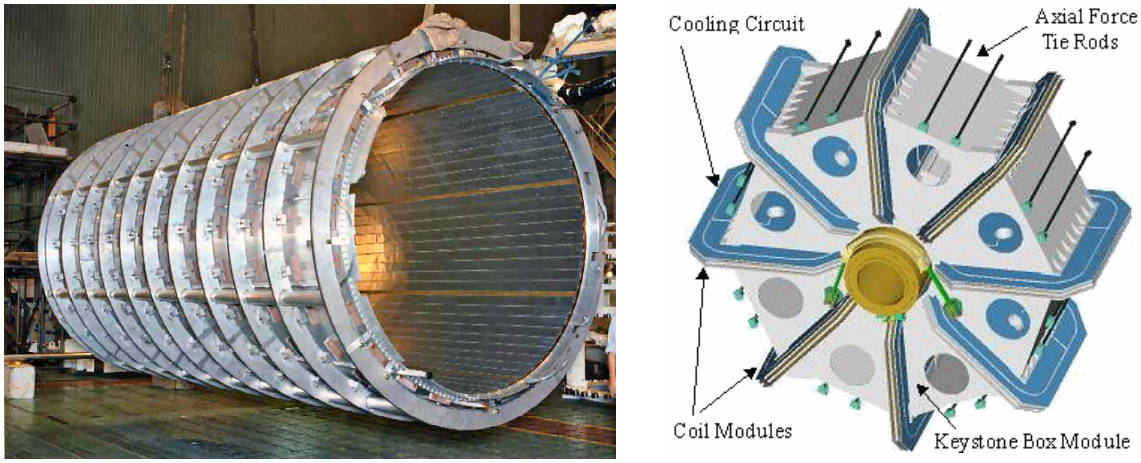

Figure 2-11 The cylindrical solenoid coil of ATLAS (left). Schematic view of the toroid end-cap (right).

To measure with high precision the muons emerging the calorimeter a super-conducting **toroid magnet** has been designed. The toroids are operated at a current of 20 500 amperes and generate a field integral of 2-8 teslametre with quasi-circular field lines (see Figure 2-12) in the plane defined by the beam axis. An important feature is the increase of bending power at higher pseudorapidities. The toroid magnet consists of the 25 m long barrel air core coils and two end-cap toroids of 5 m length (Figure 2-12), each of the three components contained in individual cryostats. The toroid magnet has a total diameter of 20 m and weighs more than 1300 t.

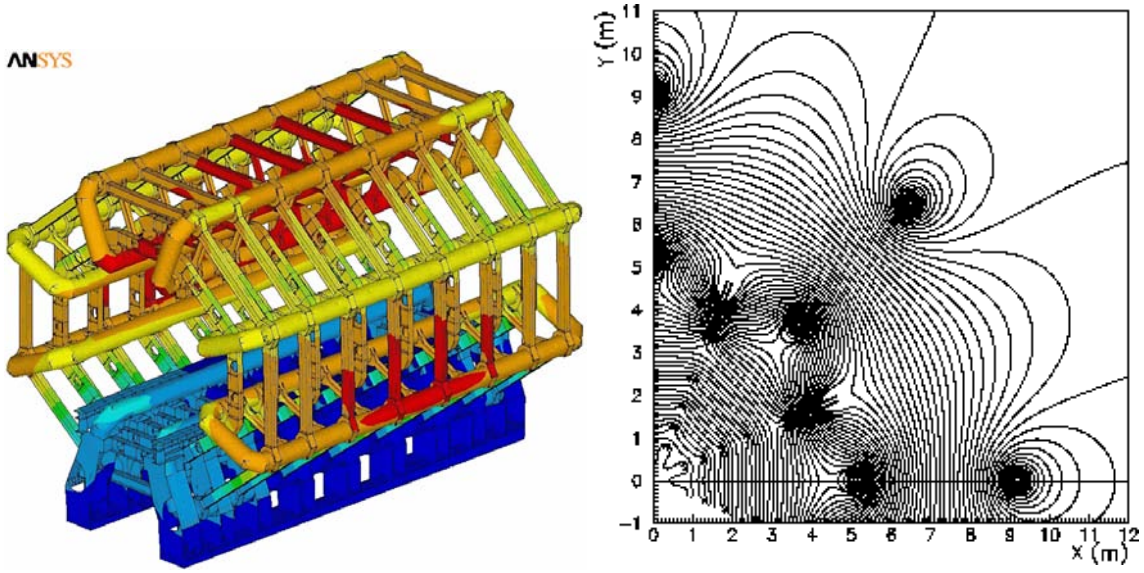

Figure 2-12 The ATLAS superconducting toroid magnet (left) and an illustration of its quasi-circular magnetic field in the XY-plane (right).

2.2.5 Trigger, DAQ and Computing

The bunch crossing rate of 40 MHz will lead to an interaction rate of 10^9 Hz at a luminosity of 10^{34} $cm^{-2}s^{-1}$. In order to select the interesting interactions per bunch crossing a sophisticated three-level trigger scheme (Figure 2-13) reduces the enormous data to a rate of 100 Hz of events that the data acquisition system (DAQ) is able to record. Each trigger level refines the decisions made at the previous level and, where necessary, applies additional selection criteria.

The **first-level (LVL1) trigger** works on a subset of information from the calorimeter and muon detectors. It requires about 2 µs to reach its decision, including the propagation delays on cables between the detector and the underground counting room where the trigger logic is housed.

The **second-level (LVL2) trigger** refines the selection of candidate objects compared to LVL1, using full-granularity information from all detectors, including the inner tracker which is not used at LVL1. In this way, the rate can be reduced to ~1 kHz. Many events are analysed concurrently by the LVL2 trigger system using processor farms, and an average latency of up to ~10 ms is considered reasonable.

For LVL2-selected events, **event building** is performed. Each read-out buffer contains fragments of many events for a small part of one subdetector. The event builder collects all the fragments from one event into a single memory - the memory of an Event Filter processor. Event Filter processing is performed using farms of processors acting on the full-event data.

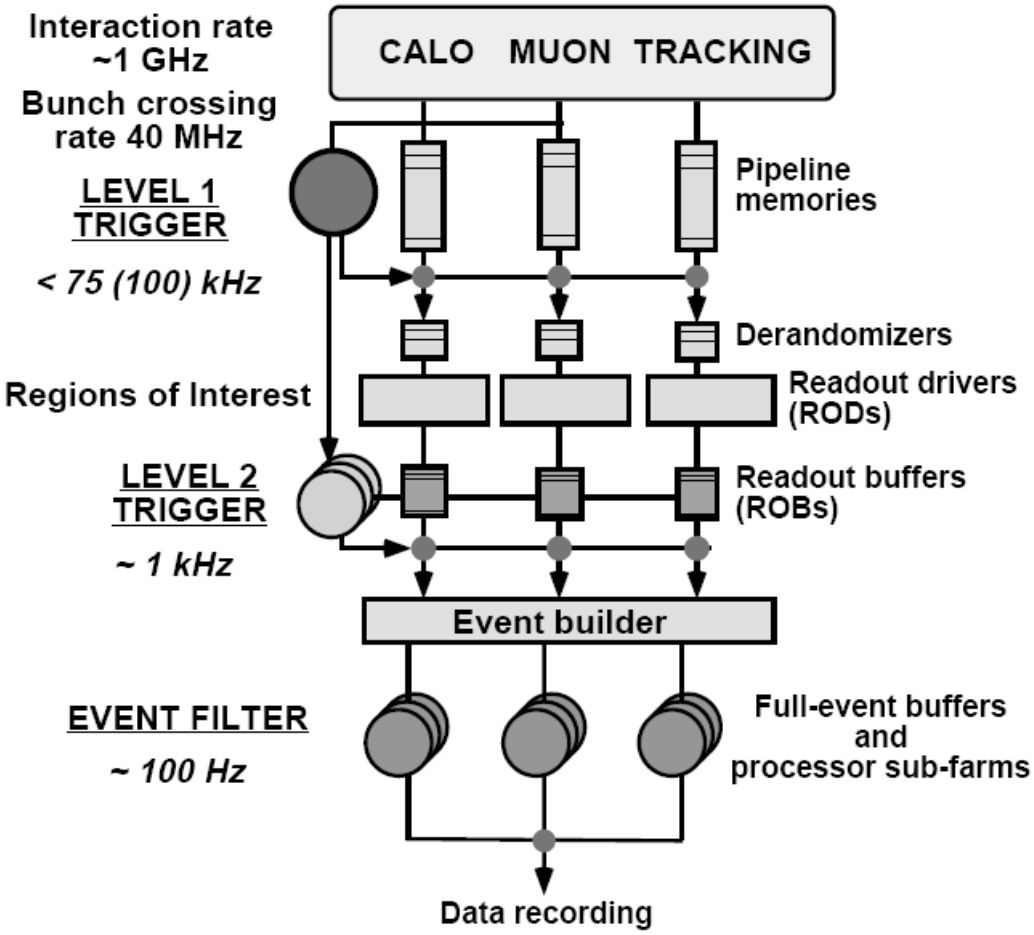

Figure 2-13 The ATLAS Trigger architecture.

The **ATLAS computing system** is designed to analyse the data produced by the ATLAS detectors. The amount of data, expecting 10^9 events per year with an event size of 1 MByte, adds up to 1 Petabyte (10^{15} Byte) of annual data, a volume equivalent to 700 million floppy disks (a ~2500 km high pile!) or the capacity of 5000 - 10000 of today's home-PC hard drives. To analyse these data, a computer power equivalent to 50 000 of today's PCs will be needed.

Figure 2-14 Today's PC farm in the new computing centre (left). The tape unit reel display system (RDS) in 1965 (right).

CHAPTER 3

"Where reason fails, time oft has worked a cure."
Seneca (c. 4 BC - 65 AD)

The Transition Radiation Tracker

Transition radiation (TR) photons are emitted when a relativistic particle traverses an inhomogeneous medium, in particular the boundary between materials of different electrical properties, an effect first predicted and described by Ginzburg and Frank in 1945 [26]. The phenomenon was studied in the following decades until it attracted the attention of the experimentalists, who showed the feasibility of functional Transition Radiation Detectors (TRDs) in the early 70s. An extensive review and discussion of the topic is given in Ref. [27]. Today a variety of TRDs is employed, mainly in high-energy physics experiments (like PHENIX, ATLAS or ALICE), but also in satellite-borne astrophysics experiments (e.g. PAMELA, AMS and ACCESS).
With the Transition Radiation Tracker (TRT) the ATLAS experiment has chosen an intrinsically radiation-hard straw tube tracker combined with transition radiation detection for particle identification, in addition at relatively low cost as compared to other tracking solutions. Thus the TRT constitutes an important part of the ATLAS tracking system and at the same time greatly improves electron identification in the high QCD background at LHC energies (electron/jet ~ 10^{-5}).

3.1 Transition radiation

The energy radiated when a particle with charge *ze* crosses the boundary between vacuum and a medium with plasma frequency ω_p is

$$I = (\alpha z^2 \gamma \hbar \omega_p)/3, \tag{3.1}$$

where

$$\hbar\omega_p = (\sqrt{4\pi N_e r_e^3} m_e c^2)/\alpha = \sqrt{4\pi N_e a_\infty^3}\ 2 \times 13.6 \text{ eV}. \tag{3.2}$$

Here N_e is the electron density in the medium, r_e is the classical electron radius, and a_∞ is the Bohr radius. For polypropylene and similar materials, $\sqrt{4\pi N_e a_\infty^3} \approx 0.8$, so that $\hbar\omega_p \approx 20$ eV.

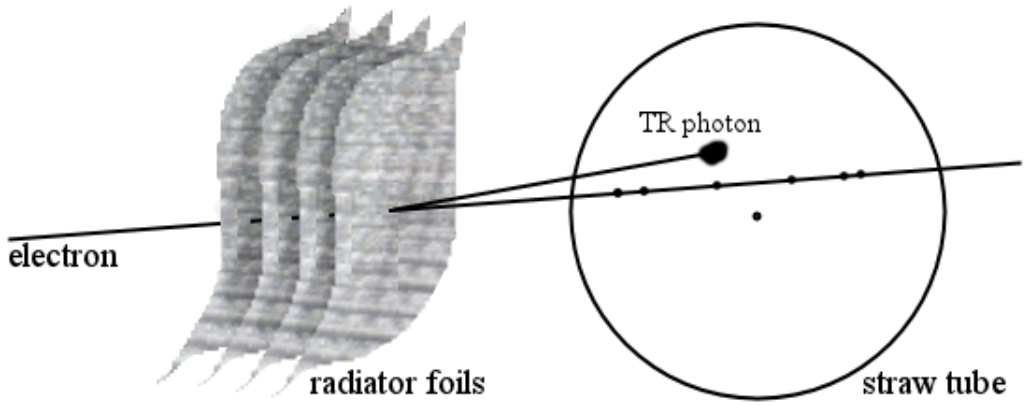

Figure 3-1 A transition radiation photon is emitted at low angle when a high momentum electron crosses the boundary of materials with different dielectric constants (for the TRT: CO_2 and polypropylene).

This radiation hence offers the possibility of *particle identification* at highly relativistic energies, where Cherenkov radiation or ionization measurements no longer provide useful particle discrimination. Electron/hadron discrimination is possible for momenta from about 1 GeV/c to 100 GeV/c or higher, the upper limit being determined not only by particles reaching the Fermi plateau, but also by the radiation of highly relativistic particles. The angular distribution of transition radiation is peaked forward with a sharp maximum at $\theta = 1/\gamma$, hence collimated along the direction of the radiating particle. The total energy radiated by a single foil is found to depend on the squared difference of the plasma frequencies of the two materials; if the difference is large ($\hbar\omega_{air} \approx 0.7$ eV and $\hbar\omega_{polypropylene} \approx 21$ eV), the relation is

$$E \approx \frac{2}{3}\alpha\gamma\hbar\omega_p \qquad \textbf{(3.3)}$$

where $\alpha = 1/137$. The average number of radiated photons is of order $\alpha\gamma$:

$$\langle N \rangle \approx (\alpha\gamma\hbar\omega_p)/(\hbar\langle\omega\rangle) \qquad \textbf{(3.4)}$$

The emission spectrum typically peaks between 10 and 30 keV.

In order to intensify the photon flux, periodic arrangements of a large number of foils are in use, interleaved by X-ray detectors, e.g. multiwire proportional chambers (MWPC) filled with a high-Z gas for efficient X-ray absorption, like pure xenon or a Xe-CO_2 mixture. Thin foils of lithium, polyethylene/polypropylene or carbon are common. Randomly spaced radiators are also in use, like foams, granules, or fibre mats.
In optimizing a detector, the ratio n_{TR}/n_{ioniz} has to be maximised, where n_{TR} is the number of ions caused by transition radiation entering the chamber, and n_{ioniz} the number of ions due to ionization produced by charged particles traversing the chamber; the latter typically results in avalanches with lower energy. Ordinary[1] energy loss can be confused with radiated X-rays due to the Landau tail (Figure 3-2). The optimisation of the radiator/ chamber sandwich has also to include the effects of attenuation of X-rays in the radiator [19].

[1] from charged particles crossing the detection volume

For the end-cap wheels a foil-type radiator is used, which allows to optimise the radiator parameters (foil thickness and spacing) in order to provide the best TR photon yield. However, the modular geometry of the barrel TRT prevents the use of foil radiators, so other solutions had to be investigated. The solution finally adopted for the barrel modules is the use of polyethylene/polypropylene fibres, oriented perpendicular to the charge particle tragectory, which is almost as efficient as regular foil radiators. The TR performance of different radiators has been measured in a test beam using 200 GeV electrons. Figure 3-2 shows the probability to observe an energy deposition in a single straw above a certain threshold, as a function of the threshold and for different radiator types.

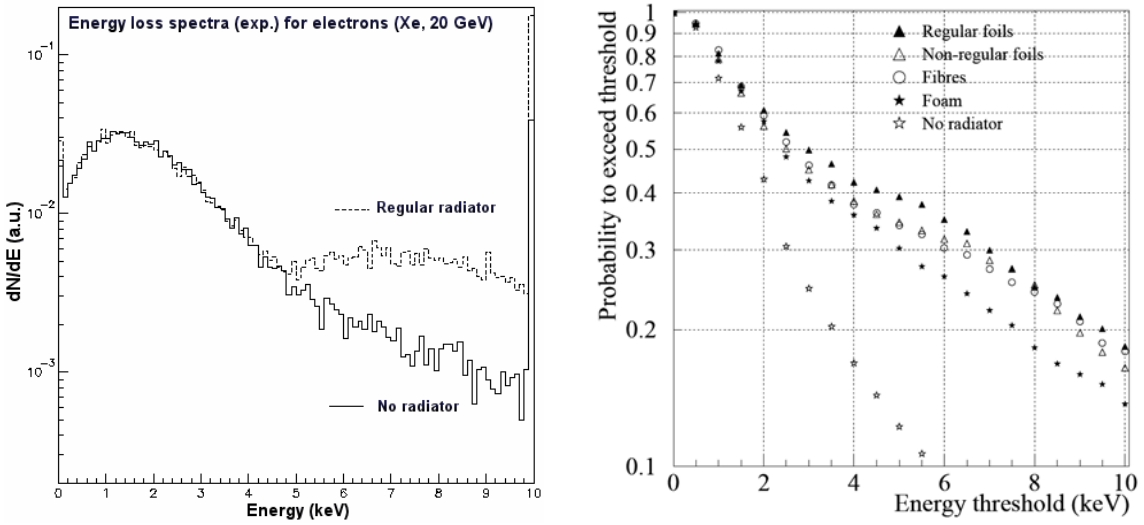

Figure 3-2 Normalised dE/dx and transition radiation spectra for 20 GeV electrons (left). Measured probability of an energy deposition in a single straw above a certain threshold as a function of threshold and for different radiator types (right).

3.2 Requirements and performance

The TRT is the outermost part of the Inner Detector (Figure 2-3), enclosing the Pixel detector system located at the innermost radius and the Semiconductor Tracker with its layers of silicon-strip sensors. It is a large scale gaseous detector that combines particle identification capability with the traditional charged-particle track reconstruction. Its strength lies in its intrinsic radiation hardness and relatively low cost compared to other technologies for tracking over large volumes, however, at the cost of high detector occupancy.

At the LHC design luminosity of 10^{34} $cm^{-2}s^{-1}$, average straw tube counting rates of 12 MHz are expected with a maximum of close to 20 MHz for the innermost barrel straws and the longest end-cap straws. The main rate contribution comes from ionizing tracks, however, also low energy photons and slow neutrons contribute at a significant level.

At such high counting rates, drift-time accuracy and efficiency are appreciably degraded (Figure 3-4), while momentum resolution, pattern recognition and second-level trigger are preserved with adequate performance thanks to an innovative design of the front-end electronics.

After ten years of operation, the most exposed straws will have accumulated a radiation dose of about 10 Mrad, and a neutron fluence of up to $2 \cdot 10^{14}$ n/cm^2. These numbers include a 50 % safety factor for uncertainties in the calculations. The total expected dose translates into unprecedented ionization currents (0.15 µA/cm) and integrated charges (~10 C/cm of wire) for a large-scale gaseous detector. The straws have been shown to sur-

vive these radiation doses and neutron fluences without any significant degradation of their mechanical and electrical properties nor of their performance [28][29]. The induced radioactivity of Xe stored in the detector will be about 8 mCi, a factor that will pose some constrains on the access and maintenance scenarios for the TRT [30].

Tracking capabilities

Quantities of interest in the TRT operation are the maximum drift time and the drift time variations of the electrons in the straw. They determine the most important tracking characteristics, the *drift-time measurement accuracy* (i.e. position resolution) and the *drift-time measurement efficiency*. The *hit-registration efficiency* marks the probability for obtaining a low-level threshold hit when a particle crosses the straw.
The position resolution is defined as the r.m.s. of the Gaussian fit to the peak of the residual distribution, while the drift-time measurement efficiency marks the fraction of selected measurements lying within a range of ± 2.5σ around the peak position. This interval has been chosen as the optimal road width for an accurate track reconstruction in the high-occupancy environment of the TRT [29].
A low-threshold discriminator detects with high efficiency the dE/dx depositions from minimum ionizing particles. The exact drift distance during test beam runs is obtained from beam track extrapolations using position-sensitive silicon-microstrip telescopes (with an accuracy of 5 μm) before and after the straw tubes. A fit of the overall experimental time (*t*) vs. radius (*R*) data with a third-degree polynomial is then used for the position reconstruction in all straws[1]. The typical so-called R-t relationship is shown in Figure 3-3, where drift time is plotted against the radial distance from the wire.

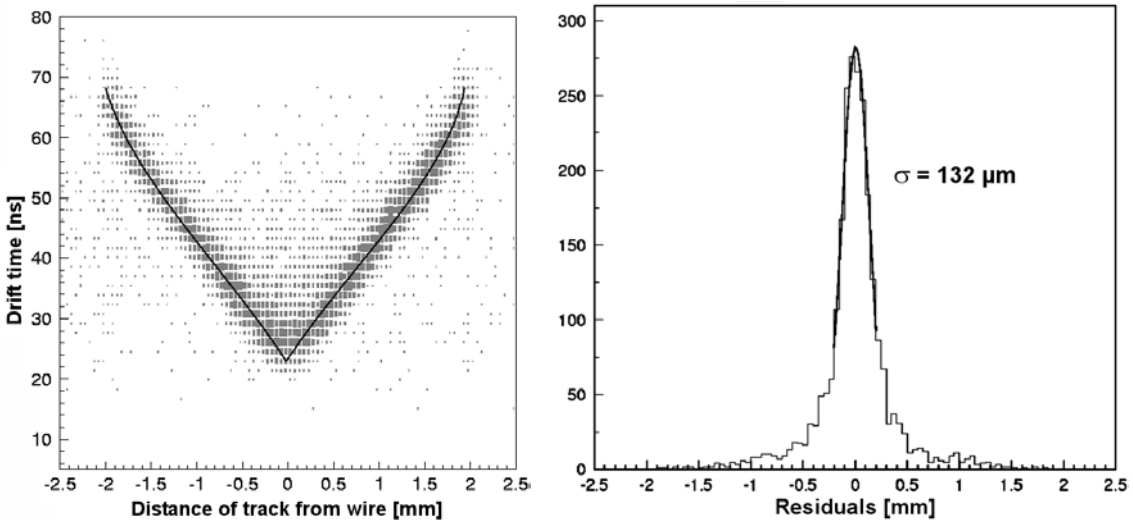

Figure 3-3 Measured relationship between drift time (t) and distance to wire (R) for a straw at virtually no counting rate (left). The corresponding distribution of the resulting residuals (right) reveals a position accuracy of 132 μm at 87 % drift-time efficiency. The plots are from the test beam (2004) with no magnetic field.

Test beam [32] results determined 250 eV as a reasonable low-threshold setting, corresponding to a single-straw noise probability[2] of 4.6 %. At low counting rates a position

[1] *Note:* Using individual R-t dependencies for each straw would give only a small improvement in the position resolution [31].

[2] The single-straw noise probability refers to the fraction of noise counts in the 75 ns event window. The goal of 300 kHz noise rate would then correspond to a noise probability of 2.25 %.

accuracy of 132 µm and a drift-time measurement efficiency of 87 % was achieved, with an overall hit-registration efficiency close to 96 %.

Particle identification

A contribution to particle ID is achieved in the Xenon-based gas mixture by the conversion of TR photons, that are emitted when a charged ultra-relativistic particle crosses the interface between different media - polypropylene fibres/foils and CO_2 gas in case of the TRT. Thus the energy deposition in the TRT is the sum of ionization losses of charged particles (~2.5 keV on average) and of the larger deposition due to TR photon absorption (>5 keV).
A high-threshold discriminator, set around 6-7 keV, is optimised for electron/pion separation. Electron tracks contain more high-threshold hits than pion tracks, and a clean electron/pion separation can be achieved by counting the number of high-threshold hits along a reconstructed track (Figure 3-5).

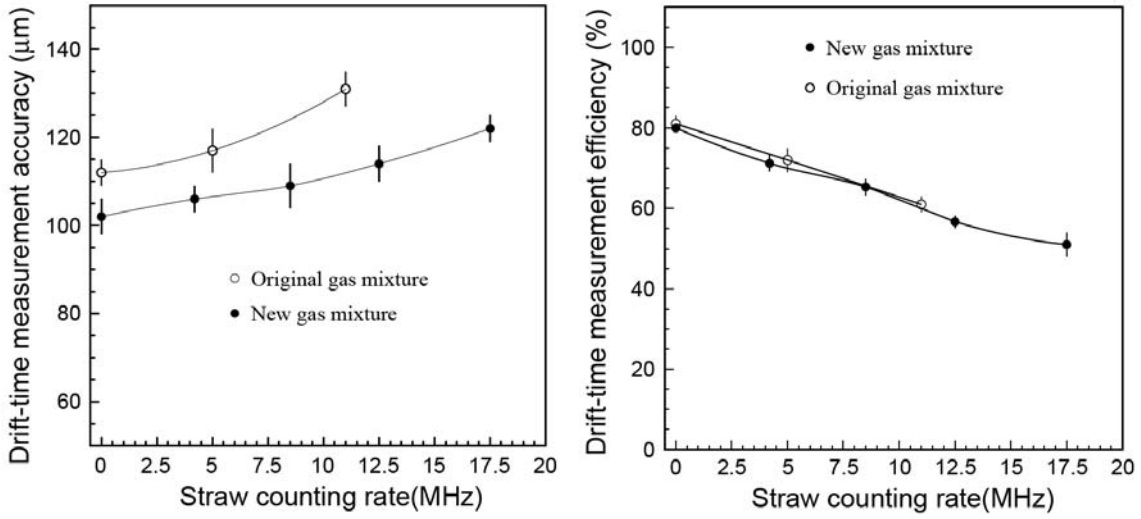

Figure 3-4 Position resolution (left) and efficiency (right) as a function of rate in the TRT (test beam 2002).

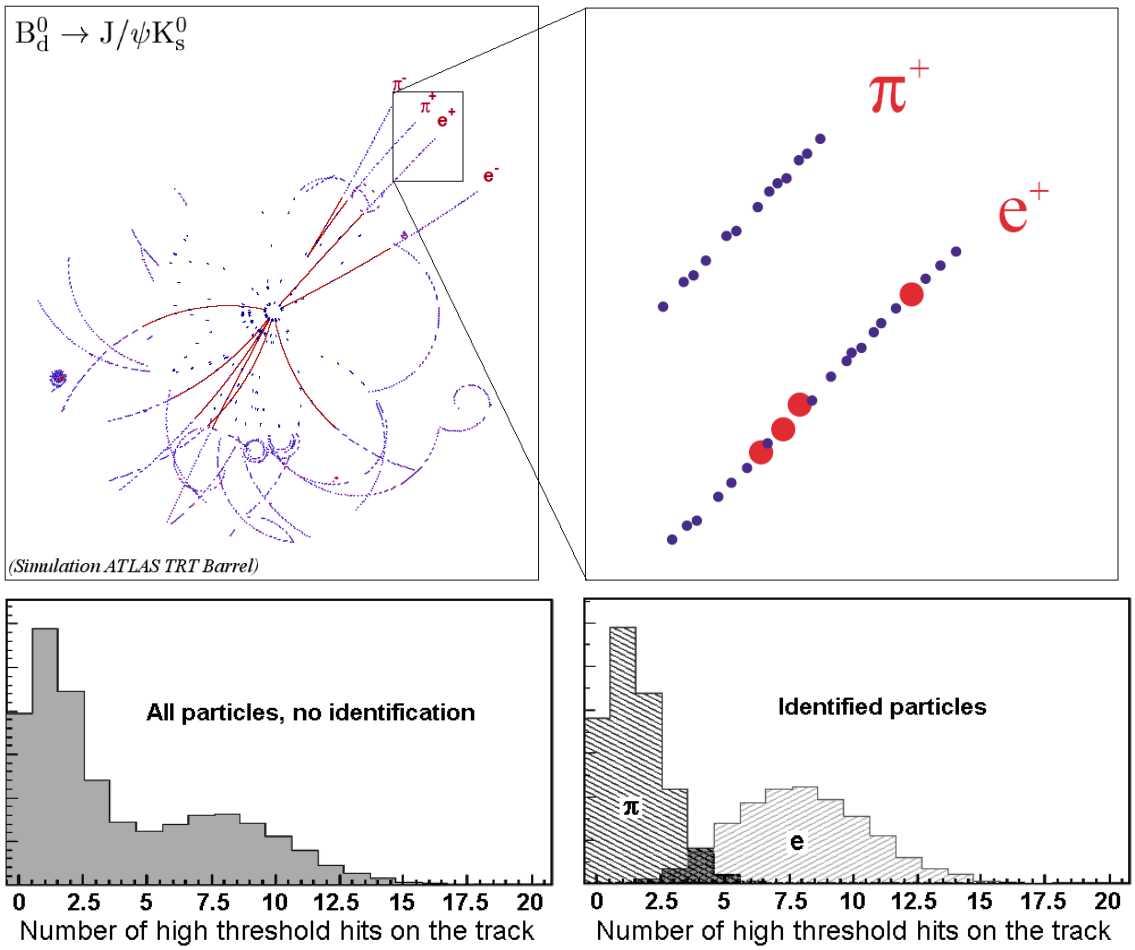

Figure 3-5 Illustration of clusters from electron/positron and pion tracks (simulation). The big dots indicate clusters from TR photon conversion, the small dots are clusters from minimum-ionizing particles (top). The distribution of clusters with large energy deposition (from TR) is shown for electrons and pions (right).

3.3 Detector design

3.3.1 Barrel modules and end-cap wheels

The TRT extends over 6.8 m in length and measures 2.2 m in diameter. It envelopes the Semiconductor Tracker and the Pixel detector, as the outermost part of the Inner Detector, which is enclosed by the solenoid magnet that provides the 2 T magnetic field necessary for charged particle tracking. The TRT provides continuous tracking at large radius with many projective measurements.

As can be seen in Figure 2-3, the ~1500 kg heavy TRT itself comprises a barrel and two end-caps. The barrel covers ±75 cm (with respect to interaction point) along the direction of the beam line with the straw tubes in axial alignment, while the two end-caps with straws in radial orientation accept tracks with pseudo-rapidities $|\eta| < 0.8$. In this way charged particle tracks with $|\eta| < 2.5$ and momenta $p_T > 0.5$ GeV cross about 35 straws, at radii between 56 (64) cm and 107 (103) cm in the barrel (end-cap) TRT.

The barrel consists of three radial sections, each containing 32 identical modules, namely type 1, 2 and 3. The innermost modules hold 329 straws each, the middle ones 520 straws each, and the outer ones 793 straws each. The full barrel TRT thus sums up 52 544 long reinforced straw tubes of 150 cm length. To limit the occupancy (fraction of channels hit per bunch-crossing), each wire is electrically divided in its middle by a glass wire joint and read out at both ends. The space between the straws is filled up with radiator material consisting of randomly distributed low-density polypropylene fibres to produce transition radiation (Figure 3-6). Each module is housed in a carbon-fibre reinforced plastic shell that provides rigidity and dissipates part of the heat generated by the irradiated straws. The particular chevron-shaped arrangement is designed to minimise the probability of losing tracks in the gap between modules.

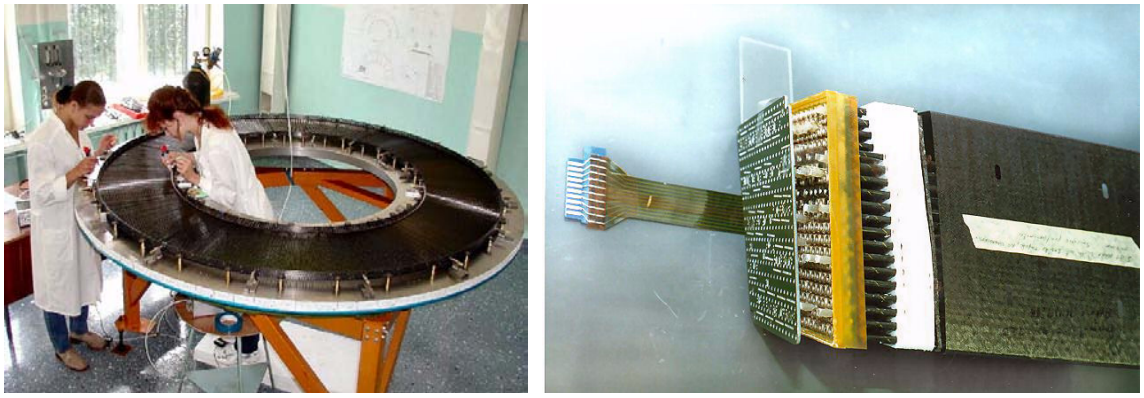

Figure 3-6 Assembly of TRT wheels at a Russian production site (left). Exploded view of a barrel module exposing tension plate, straws and radiator (right).

The end-cap TRT contains three different types of wheels, called type A, B and C. Each full end-cap carries 159 744 straws. While type-A and type-B wheels use 39 cm long straws, type-C wheels, being the most distant from the interaction point, embody straws of 55 cm length. The layers of straws are interleaved with radiator stacks of 13 polypropylene foils, each 15 µm thick, separated by approximately 200 µm by a polypropylene spacer mesh (Figure 3-7). Both wheels of type-A and type-B consist of 3072 straws arranged in four staggered layers of 768 straws (hence called *4-plane wheel*). Type-C wheels contain 576 straws per layer accounting for their 14 cm more length. The spacing between successive layers is 4 mm and 11 mm for wheels of type A respectively B. The straws are inserted and glued to inner and outer carbon fibre (C-fibre) rings with

precisely machined holes, following tolerances of the order of a few hundredth of a millimetre (Figure 3-7). At the time of writing the production of type-C wheels has been staged and will not be discussed further here (February 2005).

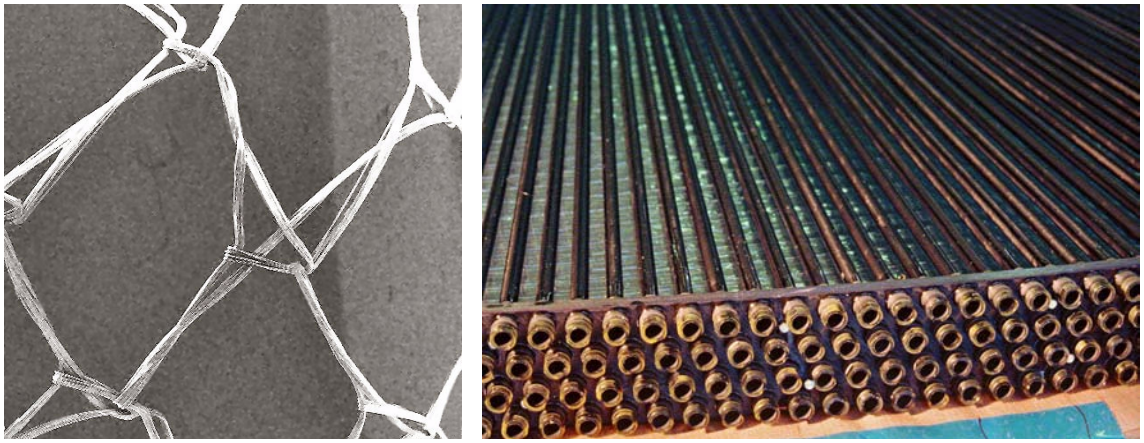

Figure 3-7 *Left:* The spacing of radiator foils is achieved by a woven polypropylene fibre mesh ("haute couture" technology) which comprises 10 % of the radiator material. The thread filaments are of ~20 µm diameter.
Right: Four staggered layers of straws interleaved with radiator foil stacks are glued to carbon fibre rings.

High voltage and signal connections are provided through a flex-rigid printed-circuit board (PCB), referred to as the "active WEB" (**W**heel **E**nd-cap **B**oard). The rigid glass-fibre board holds the flexible parts, electronic components and serves as a part of the gas volume enclosure. The flexible Kapton® flaps lead the signal and high-voltage lines to holes with inward-pointing petals establishing contact with the anode wire resp. the straw inside (for illustration see Figure 3-8 and section 5.3.6). 32 straws (arranged as eight rows of four layers) are combined to a cell, while a WEB holds three cells.

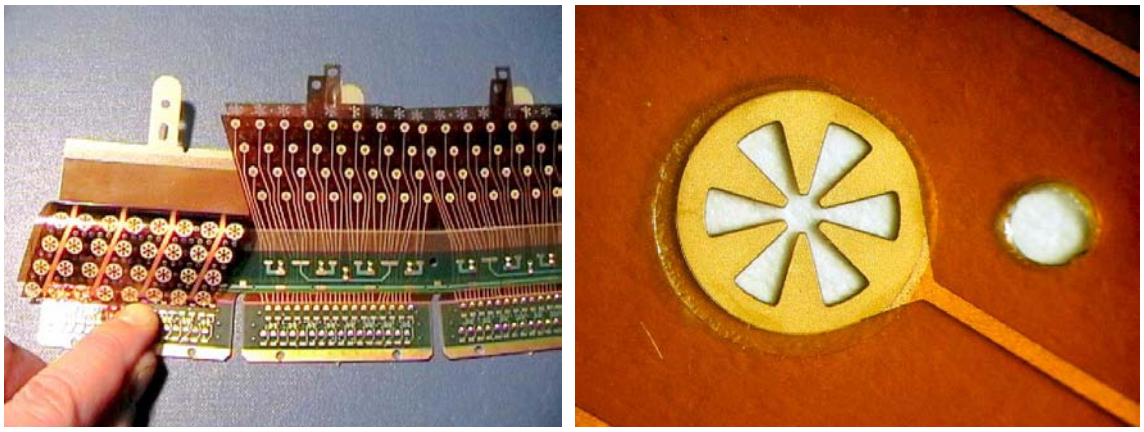

Figure 3-8 The "active WEB" connects the end-cap straws to high-voltage and read-out electronics. The contact with the cathode tube (for HV) and the wire crimping pin (for signal) is made with the help of "daisies" (right), which are bend and pushed by end-plugs against the electrode.

A third carbon fibre ring at the outer radius together with a simpler fibre-glass board (*"passive WEB"*) is glued to the active WEB, and as such it forms the outer gas manifold while providing sturdiness. The inner gas manifold is enclosed by eight reinforced polyimide covers ("*carters*") glued to the inner carbon fibre ring.

At production sites (Figure 3-6) in Russia (JINR Dubna and PNPI Gatchina) wheels carrying four layers of straws are assembled and mounted to units of 8-plane wheels (two back-to-back 4-plane wheels) before they arrive at the acceptance test site at CERN.
Because of their different geometries, barrel and end-cap modules are structurally different, but nevertheless follow the same tight requirements in terms of rigidity, dimensional stability, minimum amount of material and other features, characteristic of any inner tracker in a collider experiment. Specific details about the construction of end-cap and barrel modules can be found elsewhere [19][33]. The assembly procedures have been optimised for reliable mass production. The production strategy and quality assurance methods have been established to efficiently share the construction between different production sites. The quality control procedures and specifications to be met during the course of production are an integral part of the assembly process. A production database and user-friendly HTML interface facilitates the storage of parts, the input-quality control data for all components, as well as the identification and storage of all test results obtained during the assembly itself [34].

3.4 The straw tube

The single straw tube is a proportional counter - i. e. working in the proportional gas amplification mode (Figure 4-2) - of cylindrical geometry. The anode consists of a fine wire on the axis of a hollow tube, which functions as a cathode. The polarisation is chosen in this way for two reasons. Firstly because gas amplification, initiated by the electrons, is achieved only in the high field region around the anode wire. Secondly a uniform multiplication factor is achieved with a small amplification region, an inherent feature of cylindrical counters. In case of the TRT negative high-voltage is applied to the tube, while the anode wire is kept at ground potential.
The TRT's performance is mainly determined by the TR radiator properties, the detecting element (straw tube) and the signal processing. Having dealt briefly with transition radiation this section focuses in more detail on the straw performance. Straw geometry, operating gas and operating parameters are therefore the main issues in the following paragraphs. Earlier and more extensive studies and discussions can be found in Refs. [19], [29], [35], [36], [37], [38], [39], [40] and [41].
Many of the requirements for best performance at LHC are mutually exclusive, hence some compromises have to be found. A large tube diameter would assure a high hit efficiency, but it would not be able to cope with the short bunch crossing rate (40 MHz resp. 25 ns) because of the long drift time (Figure 4-12). The 4 mm diameter of the TRT tubes represents a good compromise between speed of response, number of ionization clusters, mechanical and operational stability.
The straw tube is made of a 60 µm thick multilayer film of carbon-polyimide-aluminium-Kapton®-polyurethane (Figure 3-9). It is manufactured by winding two tapes on a precisely tooled mandrel at a temperature of ~200°C (Figure 3-9). Four reinforcing carbon fibres glued along the straw give it the necessary mechanical stability vital for safe operation. In systems with anode read-out, the cathode resistance must be kept as low as possible (specification <300 Ω/m). A thin aluminium coating serves as a second conductive layer that guards against possible conductivity loss. It has been shown earlier that severe signal degradation can be caused by the removal of the inner carbon-loaded Kapton layer after several breakdowns [35].

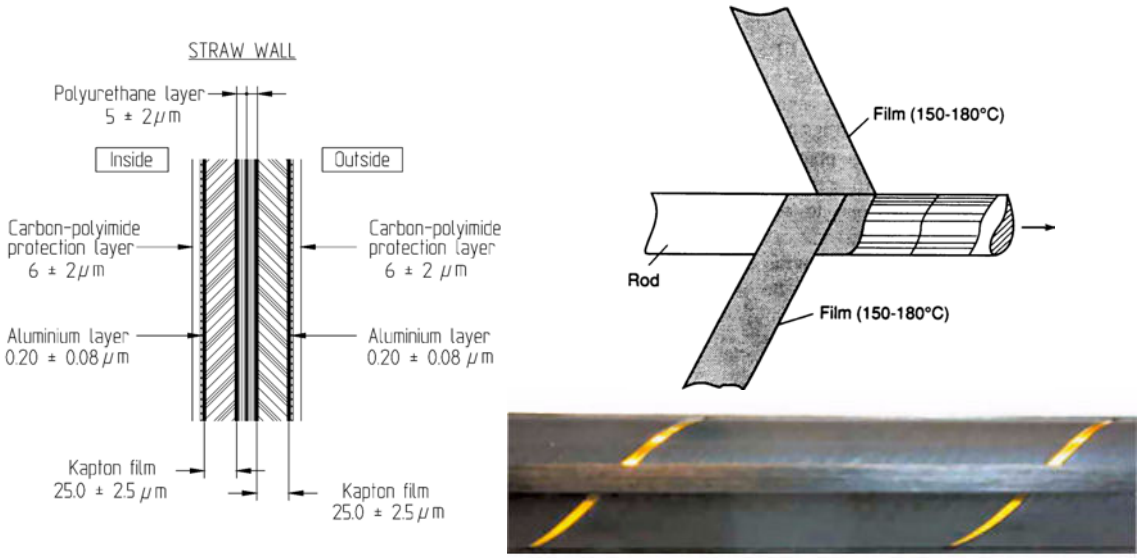

Figure 3-9 A multilayer film (left) is used to produce the straw tubes by winding two tapes of film on a precision mandrel (top right). Four carbon fibres strips on the outside reinforce the straw (bottom right).

Wires of both 30 µm and 50 µm diameter have been tested for performance [19]. The maximum acceptable gas gain in the straw is $2 \cdot 10^4$ for the 50 µm wire, before streamer rate and space-charge effects start impairing operation. The choice was eventually made in favour of the smaller diameter.
The 31 µm thick anode wire[1] [42] is made of gold-plated tungsten, produced by Toshiba. Wire diameter and ellipticity are specified to be better than 1 % and 2 % respectively. The electrical resistivity measures 60 Ω/m. Overall the TRT requires ~450 km of wire for its construction, a fact that imposes strict QC/QA measures. Wire samples from each spool are inspected for electrical resistivity and tensile strength. Surface quality and diameter variations (Figure 3-10) are examined using a scanning electron microscope (SEM).

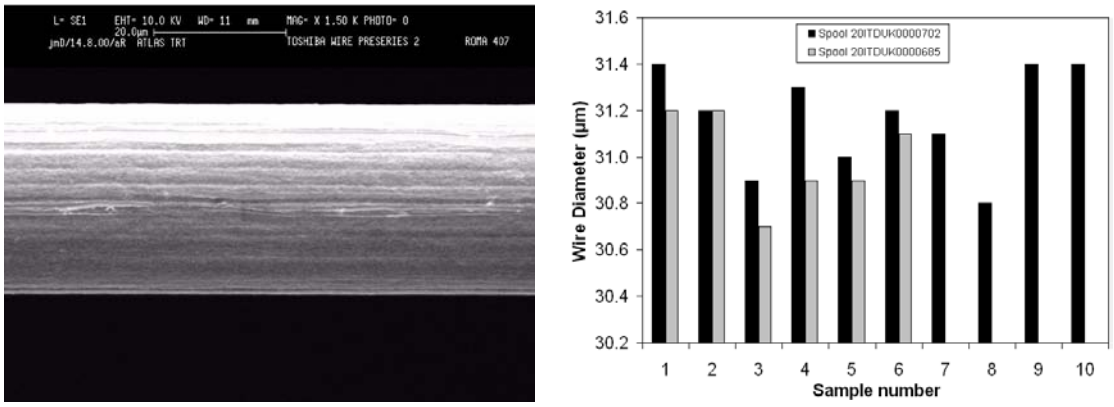

Figure 3-10 SEM picture from the wire surface quality control (left). Wire diameter variations[a] (right).

a. Source: M. Capeans, J.M. Dalin, CERN, 25 November 2002 and Ref. [43].

As mentioned before, the anode wire is kept at ground potential (through protection diodes) and is read out through a 24 Ω resistor by the front-end electronics (see section 3.6).

1 The tungsten wire has a diameter of 30 µm, the Au-coating a thickness of ~0.5 µm.

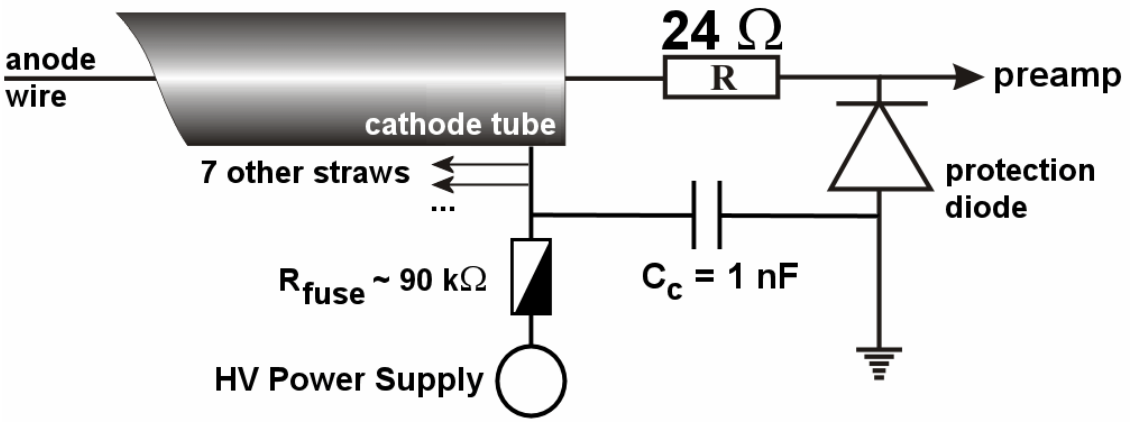

Figure 3-11 Straw high-voltage and signal connection scheme. Straws are connected in groups of eight.

3.5 Operating gases and gas systems

The choice of gas composition for operation is determined by various restrictions ranging from physics requirements to safety and environmental concerns as well as financial considerations. In terms of ageing, when classical hydrocarbon operating gases should be strongly avoided in the operating environment of the new-era high-energy, high-rate collider experiments. They are often flammable and as such require immense effort to insure proper safety precautions.

After an initial choice of Xe-CF_4-CO_2 70/20/10, the baseline mixture was changed to Xe-CO_2-O_2 70/27/3 following insurmountable problems using CF_4.

Among different options, a closed-loop gas system with gas purification has been adopted to prepare, monitor and recuperate the gas. The high costs of xenon demand a recirculation of the 2.5 m^3 of operating gas.

3.5.1 Operating gas components

As a base component, **xenon** (Xe) is chosen for its excellent X-ray absorption (Figure 3-12). The fraction of 70 % marks the balance between transition radiation performance and operational stability.

The quencher **carbon dioxide** (CO_2), known as a “cool gas”, provides excellent drift properties, namely a plateau of constant drift velocity over a large drift range in the straw tubes (Figure 4-9), low longitudinal diffusion and small deflection in magnetic fields. Furthermore it also represents the stabilizing factor in the gas mixture by efficiently absorbing UV photons produced in the ionization processes and, therefore, spatially confining the avalanches. Rather than spreading along the wire, the avalanche only develops radially as a streamer in case of very large charge creation from low momentum heavily ionizing particles or unforeseen electric field enhancement. The suppression of lateral spread thus limits the streamer into a so-called self-quenched streamer (SQS) mode. As an operation mode it is less hostile than a total discharge between cathode and anode. A minimum of 6 % of carbon dioxide is needed for the TRT to confine discharges to SQS mode. For a concise review of the self-quenched streamer mode in gas-discharge detectors one can consult Ref. [44] and references therein.

To improve the ageing and spark proofness characteristics of carbon dioxide, an admixture is required. To regain drift velocity and to minimise pile-up, a fast molecular gas would be desirable. However, the use of flammable gases at the LHC experiments is discouraged, the safety requirements very strict and and not easily met for large detectors.

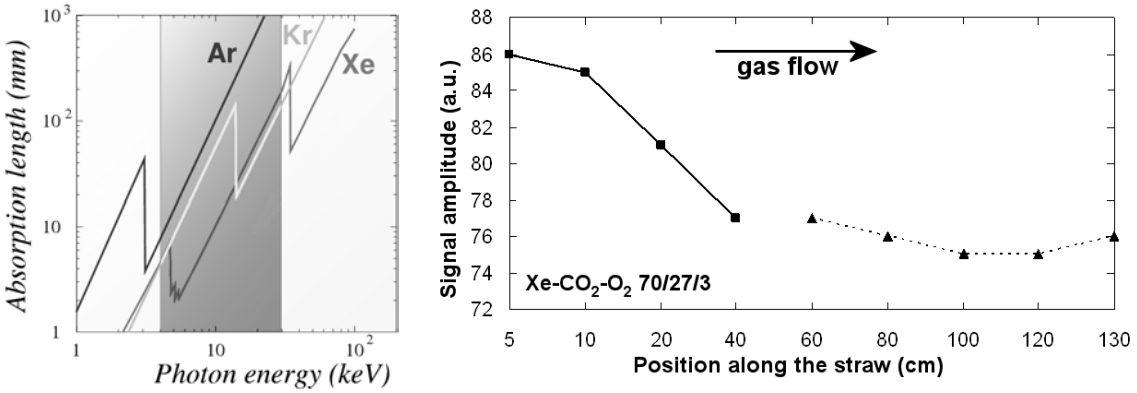

Figure 3-12 Photon absorption length for different noble gases (left). Right: Gas gain along a barrel straw, observed after switching off irradiation (uniformly irradiated for 1.5 hours at the maximum expected LHC current density of 0.125 µA/cm, at nominal gas flow). The accumulation of ozone downstream of the 140 cm long straw induces a 13% reduction of gas gain. The sense wire is electrically separated into two halves by a glass wire-joint and read out at both ends.

Carbon tetrafluoride (CF_4) was the initial choice for the TRT gas mixture. Despite its effectiveness in suppressing hydrocarbon or silicone-containing wire deposits by etching, its use later became a strong matter of concern. It was found that fluoro-based active species (CF_x, F, F_2...) caused a severe degradation of the glass wire joints in the barrel TRT straws and might damage other detector components in the long term [45]. Furthermore a large fraction of CF_4 in conjunction with radiation and water levels above 1000 ppm leads to the production of hydrofluoric acid (HF), which can seriously damage the wire gold [28] and shorten the lifetime of the glass joints, eventually leading to wire slippage or rupture.

Because both binary gas mixtures like Xe-CF_4 or Xe-CO_2 cannot provide stable operation over a sufficient high-voltage range in the straw tubes, the use of a ternary mixture remained the only feasible solution. Hydrocarbon gases stabilise the amplification process, but they are prone to polymerization on the anode wire.

Finally an alternative was found using **oxygen** (O_2), in a composition with ratios 70% Xe + 27% CO_2 + 3% O_2. Concentrations below 3.5-4 % do not affect TRT performance, however, more than 2 % is needed to provide good operational stability (see Figure 6-16). In fact oxygen itself is transparent to UV photons, so the stabilization is provided by the ozone (O_3) molecules created in the avalanches. The consequential loss in amplitude, due to the high electro-negativity of ozone was measured to be at most 13 % at current densities of 0.125 µA/cm (Figure 3-12), corresponding to O_3 concentrations of not more than 150 ppm - an effect that does not significantly affect TRT performance [30].

The new gas mixture has very strong cleaning properties in the case of hydrocarbon deposits. A drawback, however, remains: oxygen does not suppress or remove silicone wire deposits as well as the old CF_4 mixture. Although all possible measures are being taken to minimise the risk of introducing Si-containing impurities into the system, this impairment keeps an argon-based CF_4-containing mixture an option for occasional short “cleaning runs” in future operation.

The change of the baseline gas mixture in 2002 required a remeasurement of the gas properties with strong focus on operational safety aspects. To some extent the new gas Xe-CO_2-O_2 70/27/3 resembles the initial mixture of Xe-CF_4-CO_2 70/20/10 (see e.g. Figure 3-4 or gas parameters in Chapter 4).

3.5.2 Active gas system

The complex closed-loop active[1] gas system for the TRT [46] consists of the following main functional components (Figure 3-13):

- the primary gas supply stations (gas cylinders, dewars)
- a gas mixer module
- a 500 litre buffer volume
- the pre-distribution and Pump module (in the underground service cavern USA15)
- the distribution module (in the detector cavern UX15)
- a purification system with buffer volume
- a CO_2 removal module
- a gas recovery module
- a gas analysis system

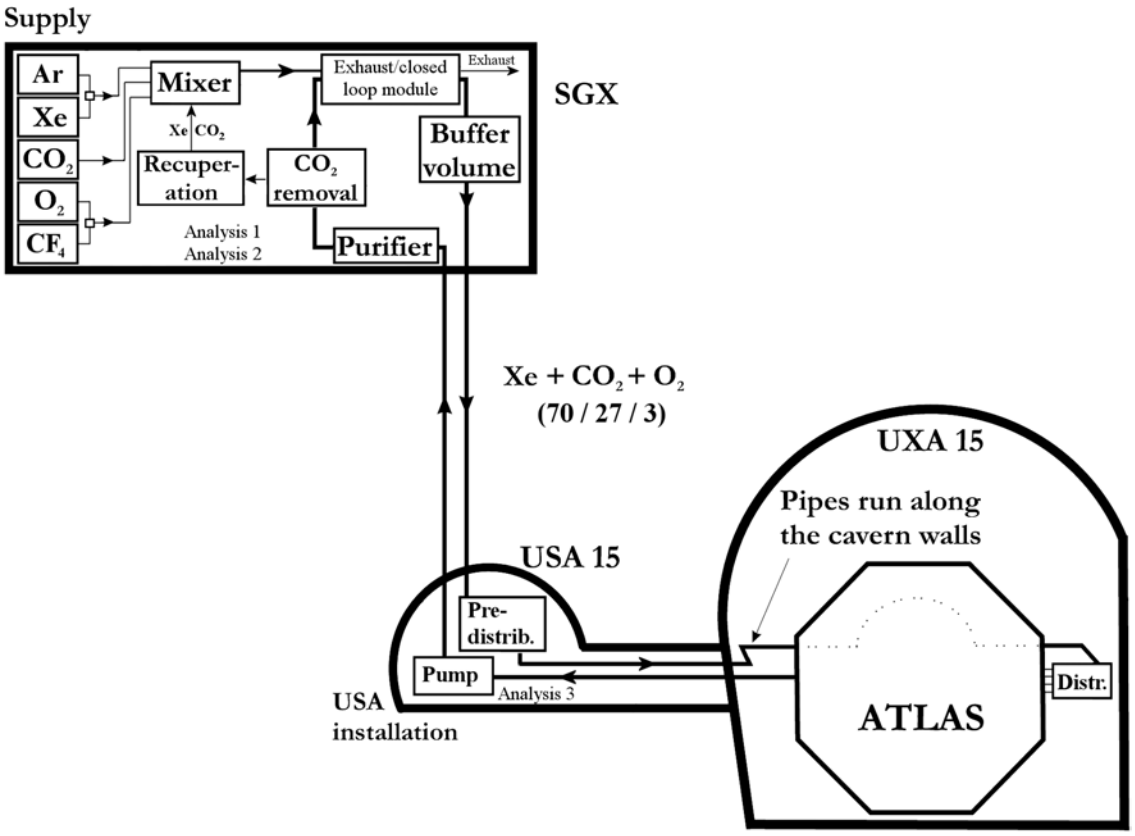

Figure 3-13 Overview of the ATLAS TRT active gas circuit showing its functional units.

The gas system has to supply 84 detector modules with the correct gas mixture (Xe-CO_2-O_2 70/27/3) at an exchange rate of about one volume per hour. For economical reasons the gas is recirculated in a closed loop with an in-line purification. Due to LHC radiation and the normal chamber gas-amplification, a small fraction of Ozone (O_3) is produced, which has to be re-converted via a catalyst to O_2 in the purifier module.

[1] "*Active gas*" is an established term for the TRT and refers to the operating gas of the straw tube. "*Envelope gas*" refers to the gas that surrounds the straw tubes in order to remove unwanted gaseous contamination and to dissipate heat produced in the detector

Mixture stability is very important in any gaseous detector. In contrast to other detectors, the TRT has several processes that can alter the content of the gas composition considerably, e.g. diffusion of envelope CO_2 through the straw walls. CO_2 content is permanently measured and corrected by a CO_2 removal system. In a similar matter the amount of xenon lost into the envelope volume has to be kept at lowest possible level to avoid TR photon losses outside the detection volume and thereby impairing particle identification functionality.
The mixing proportions must be maintained stable to a precision such that detector performance is not affected. For example a reduction of xenon negatively affects the pion rejection power, while an increase of oxygen quickly leads to signal loss. To be more precise, a rise in xenon of 5 % from nominal, improves pion rejection by a factor of 1.5, but causes a three times increase of the streamer rate. While a higher oxygen level would increase the operation safety margin, it significantly deteriorates energy resolution due to primary attachment losses. Changes in gas composition can significantly alter the drift velocity curve and thus immediately affect the R-t dependence that is used for reconstruction of the particle coordinates in the straw (see also section 4.6.3).

3.5.3 Gas cooling and ventilation

An important aspect of straw operation at high counting rates is the necessity of cooling [47][48][49] not only the straw front-end electronics, but also the straws themselves. The average energy deposited in the straw is 2.5 keV per particle for minimum-bias events. The ionization current leads to an overall heat dissipation of 10-20 mW per channel at peak luminosity. In order to maintain detector performance and preserve experimentally established temperature gradients in the detector, this power has to be removed efficiently.

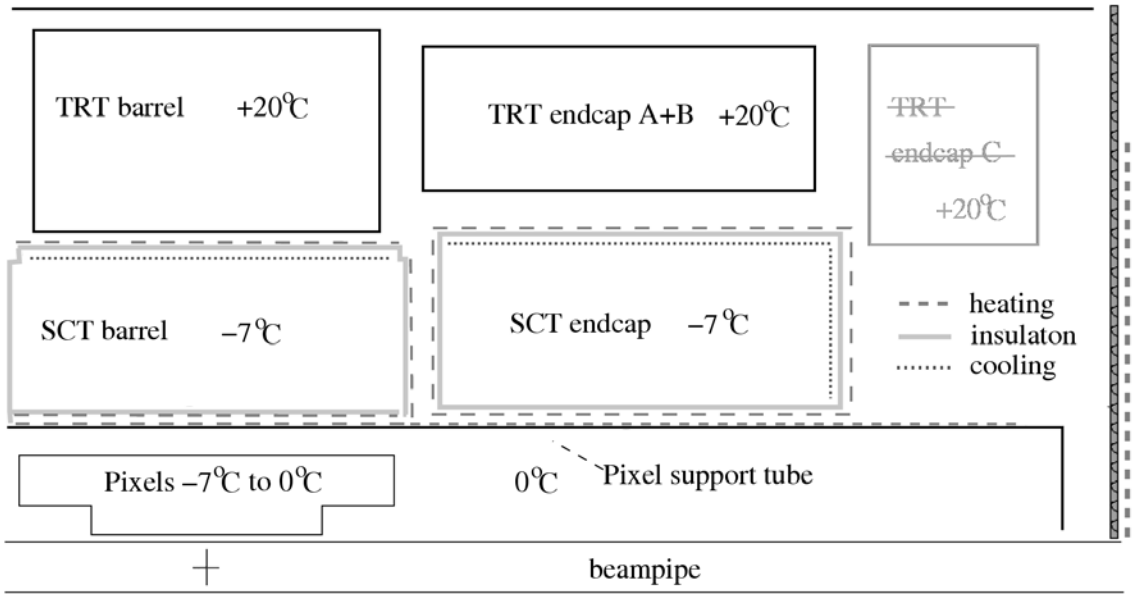

Figure 3-14 Inner Detector cooling scheme [47].

The Inner Detector has to be thermally neutral overall, and the three subsystems must not interfere with each other. While the SCT and the Pixel Detector run cold (-7°C to 0°C) in nitrogen environment, the TRT runs warm (+20°C) in CO_2 (Figure 3-14). Thermal screens or enclosures are indispensable around cold parts.
The total heat load from the straws (electronics) are 3360 (32040) Watts for the end-cap and 800 (10200) Watts for the barrel. The electronics is cooled using a warm C_6F_{14}

monophase system at 16°C through cooling pipes in thermal contact with the front-end electronics boards. End-cap straws are cooled by a flow of dry CO_2 envelope gas through the TRT modules at the enormous rate of 300 m^3/h[1] corresponding to ~35 volume exchanges per hour (6 m^3 detector volume + 2.5 m^3 piping).
Pressure variations must be kept as low as ±5 mbar. At such a large flow rate pressure changes happen at a speed of faster than 1 millibar/second, which makes the detector safety system a major concern[2].
The heat is transferred via heat exchangers to warm C_6F_{14} (Figure 3-15). In the barrel modules, heat is simply conducted to the module shell and removed there by C_6F_{14} cooling pipes.

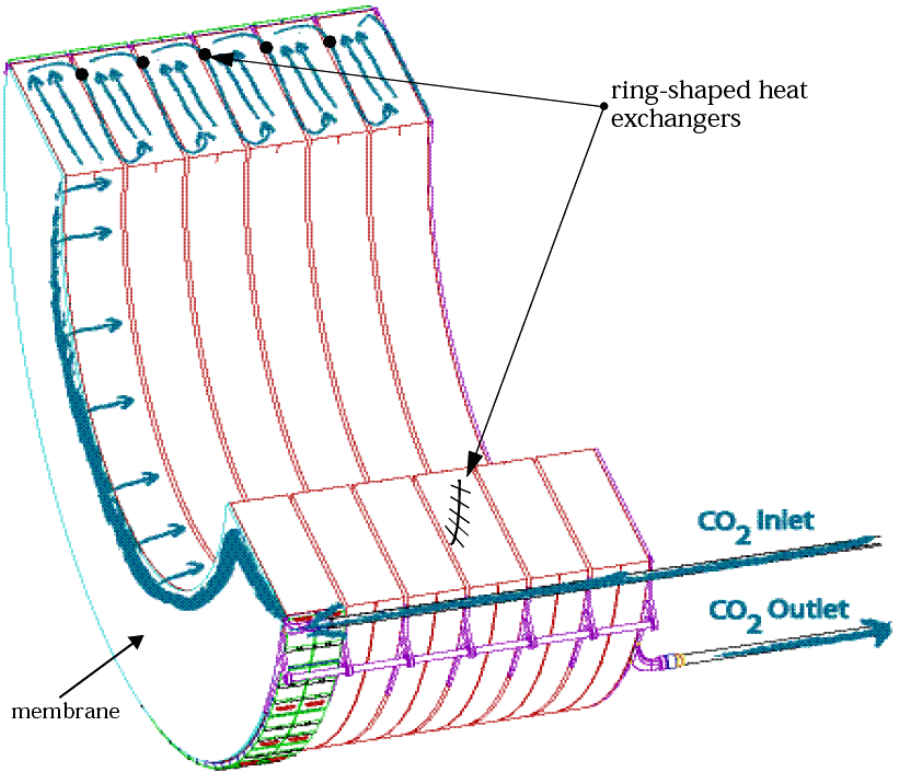

Figure 3-15 Scheme of CO_2 flow through a group of wheels (cross-section).

The second purpose of the CO_2 envelope in the TRT is ventilation. As mentioned before the nitrogen concentration in the CO_2 envelope has to be kept below 1 % (see also section 4.6.3) and water vapour below 500 ppm. To avoid unfavourable absorption of transition radiation photons in the envelope gas xenon level must be kept below 0.1 %.
The TRT barrel will be supplied with 3 m^3/h CO_2, while the end-cap straws are sufficiently ventilated by the cooling flow rate.
Having different choices of envelope gas for the TRT (CO_2) and the SCT/Pixel Detector (N_2) requires to maintain two independent gas volumes. This is due to the fact that nitrogen is incompatible with TRT operation (see also section 4.6.3), while carbon dioxide interferes with the alignment system (FSI[3]) of the SCT/Pixel system and it also adds the risk of acid formation.

---

1 The large flow rate in the small detector volume causes “wind” speeds of up to 300 km/h [50].

2 In fact the worst case of a total gas flow blockage would cause a pressure rise of 5 mbar in 300 ms [50].

3 Frequency-Scanned Interferometry

3.6 Front-end electronics

The custom-made ATLAS TRT front-end read-out architecture (Figure 3-16) is based on a bipolar amplifier/shaper/base line restorer (ASDBLR) [36][37] and a CMOS digital chip (DTMROC) [38][39]. It is custom-made and tailored to the requirements of the TRT. Only a brief overview is given here, followed by the most important results.
To achieve the desired tracking and TR performances, the read-out electronics has to perform the following functions:

1. Amplify the incoming signal from the anode wire.
2. Shape the amplified signal (peaking time 7.5 ns, shaper output width 20 ns) and remove its tail originating from the drift of ions in order to keep retrigger time short and achieve the required efficiency at full luminosity (60 % at 20 MHz).
3. Apply a low-level threshold to detect minimum ionizing particles for tracking functionality. Apply a high-level threshold to detect transition radiation photons for particle identification.
4. Obtain timing information in 3 ns bins (corresp. to a 3-bit subdivision of the 25 ns BX clock) for the low-threshold signal in order to yield the proper position (<160 μm) resp. momentum resolution.
5. Store the timing information in a pipeline and the information whether or not the input signal exceeded the low- and high-threshold values, this must be done every bunch crossing during the full level-1 trigger latency.
6. For each Level-1 trigger signal Accept (L1A), extract from the pipeline the information corresponding to the bunch crossing which gave rise to the L1A and to the two following bunch crossings.
7. Gather in a Read-out Driver (ROD) the data from many channels, compress them, format them and send them to the Read-out Buffer.
8. Timing and control of the DTMROC is governed by a timing and control board, the TRT-TTC, which implements the ATLAS standard TTC protocols for the TRT chip set.

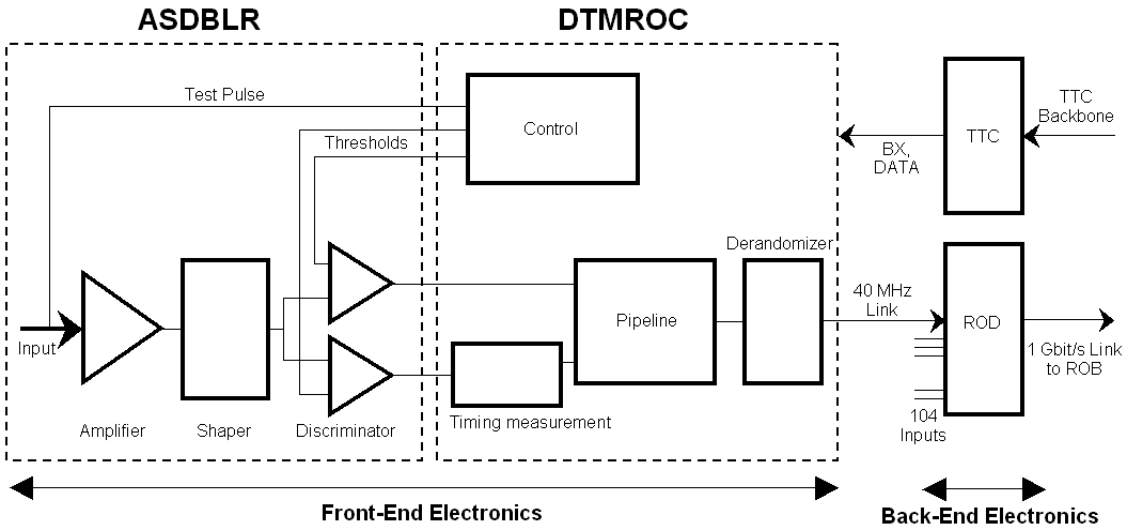

Figure 3-16 ATLAS Front-End and Back-End electronics scheme.

Tasks 1 to 6 are performed by the on-detector front-end electronics (Figure 3-17), comprising of two integrated circuits, the analog ASDBLR (**A**mplifier-**S**haper-**D**iscriminator with **B**ase**L**ine **R**estoration) and the digital DTMROC (**D**rift **T**ime **M**easurement **R**ead-**O**ut **C**hip). The threshold settings on the ASDBLR, *inter alia*, are controlled by the DTMROC.
Task 7 is realised through the back-end electronics, which is located off the detector in the underground service area USA15.
The analog signal processing and the functional blocks of the DTMROC are illustrated in Figure 3-18 and Figure 3-19. An extensive discussion on the impact of the parameters of the front-end electronics on straw performance can be found in Ref. [29]. A detailed description of the front-end electronics is given in Refs. [36], [37], [38], [39].

Figure 3-17 The TRT end-cap (left) and barrel (right) front-end electronics boards.

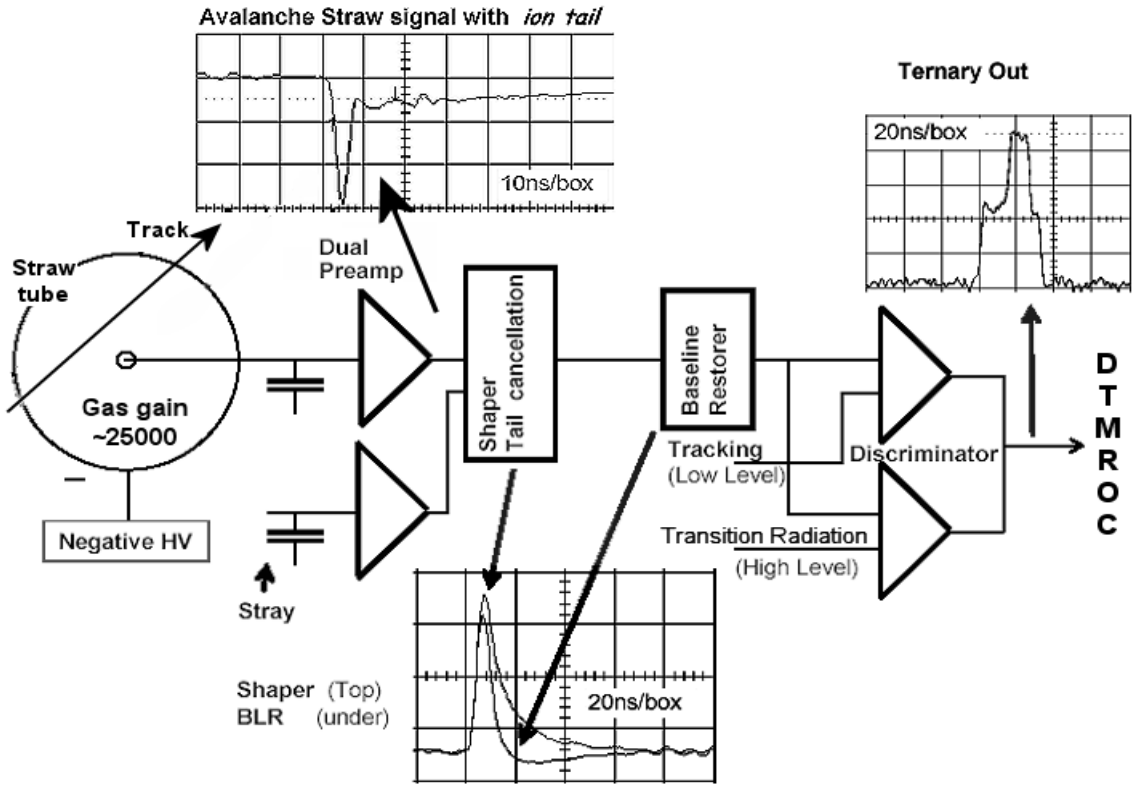

Figure 3-18 Analog part of the TRT front-end electronics (ASDBLR).

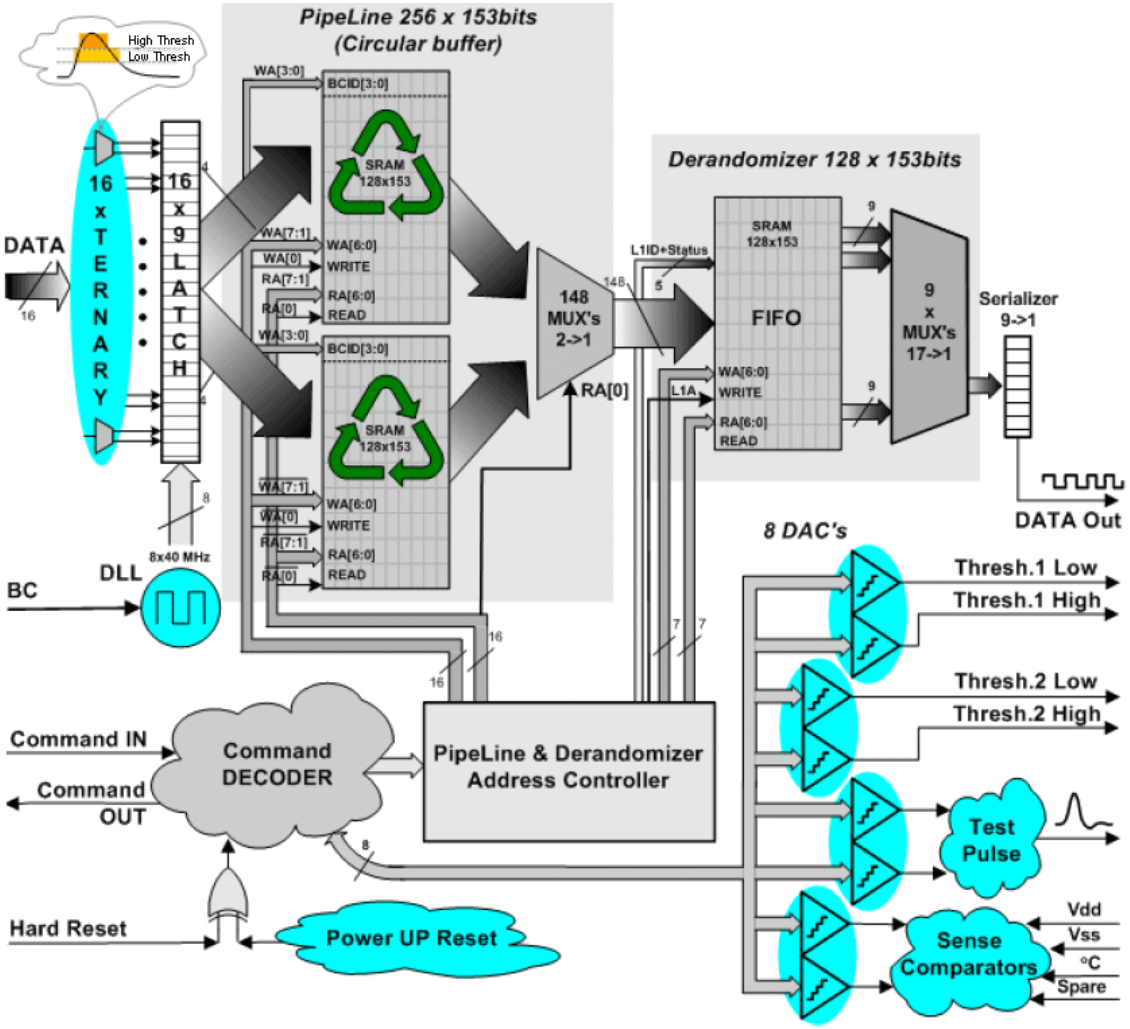

Figure 3-19 Digital part of the TRT front-end electronics (DTMROC).

CHAPTER 4

"The noblest pleasure is the joy of understanding."
Leonardo da Vinci (1452-1519)

Straw Performance Studies

4.1 Introduction

Experimental research and development can quickly become laborious and costly when there is need to optimise a gaseous detector for its application. This can range from tweaking its operating point to modifications of detector geometries and operating gas mixtures. In order to understand the numerous dependencies of the detector's performance on operation variables (geometry, gas, working point), simulations can greatly support, assist or frame the eventually indispensable laboratory studies.
This chapter focuses on both achieving a general understanding of the straw operation in the relevant gases, as well as on problems or difficulties that come with the construction of a complex detector such as the TRT. In the first case the quantities of interest are primarily gas gain and drift behaviour in the straw. Studies motivated by more practical concerns are geometrical straw deformations (wire offset, tube ellipticity), the effects of gas impurities or changes in the operation environment (e.g. temperature).
Atmospheric conditions, however, are not always recorded or documented with the experimental results that are available for comparison with the computed data. This means, if not otherwise mentioned, that simulations are carried out at standardised conditions, namely T = 295 K (22°C) and p = 101.3 kPa (1 atm).
A brief overview of processes in gas detectors is followed by a short description of the used software. The function of the relevant gases is explained before the presentation and discussion of the results.

4.2 General processes in gaseous radiation detectors

Crucial in ionization chambers is the understanding of charge creation (also disappearance) and charge movement in both electric and magnetic fields. The electrons play the main role in ionization chambers. Once released in the gas volume through ionizing collisions of the incoming radiation with the gas molecules, they are transferred in the electric field towards the anode and often undergo multiplication before forming a detectable charge quantity. At the sensing electrode they can then produce a current signal either directly or indirectly (through their mirror charges). These processes distinguish the various types of gas avalanche detectors. A short summary of a few important processes in gaseous detector is given here, however, omitting dispensable details, which are discussed *in extenso* in Refs. [51] and [52].

4.2.1 Motion of electrons and ions in gases

In an external electric field E the electrostatic force will tend to move charges away from their point of creation. The random thermal velocity of electrons v_e is superposed with a net *drift velocity* w_e in the given direction:

$$w_e = \frac{eE}{m_e} \cdot \tau = \frac{eE}{m_e} \cdot \frac{\lambda}{v_e} \tag{4.1}$$

$$v_e = \sqrt{\frac{8kT}{\pi m_e}} \tag{4.2}$$

λ is called the *mean free path* of the electron and τ its *average collision time.*
The drift velocity for ions w_{ion} in the reduced electric field E/p is simply described through the following relation:

$$w_{ion} = \mu_{ion} \frac{E}{p} \tag{4.3}$$

The *ion mobility* μ_{ion} tends to remain fairly constant, similar for positive and negative ions and over wide ranges of the electric field E and gas pressure p, having typical values of 0.5 - 1.5 $cm^2 \cdot atm/V \cdot s$ (Figure 4-1).
As an example, the mobility of Xe^+ ions in Xe is plotted in Figure 4-1 separately for both spin states $2P_{1/2}$ and $2P_{3/2}$ [53]. As mentioned before the ion mobility remains in good approximation constant outside the avalanche region (E < 10-20 kV/cm). For reasons of convenience ion mobility is here plotted against the electric field at 101.3 kPa instead the common practice of plotting ion mobility against the reduced electric field E/p or E/N, where N is the gas density.

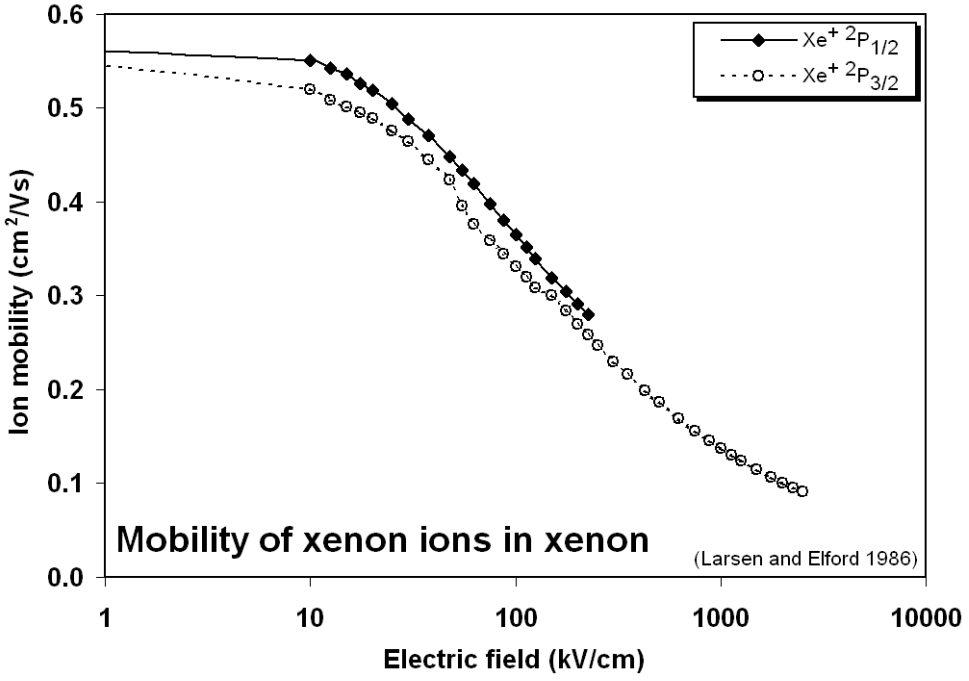

Figure 4-1 Ion mobility of Xe^+ ions in Xe. The zero-field extrapolations are based on guesses [53].

Free electrons have about three orders of magnitude higher mobility and are able to gain much more energy between collisions with neutral molecules. Their drift velocity significantly increases with *E/p*, reaching local maxima and minima in some mixtures before a further increase at higher electric fields.

Due to collisions with the gas molecules, electrons deviate from the direction of the electric field. Their diffusion along any given direction *x* is described by a Gaussian distribution with a standard deviation

$$\sigma_x = \sqrt{\frac{2D_x}{w_e}} \qquad \textbf{(4.4)}$$

where *D* is a field-dependent diffusion coefficient.

In position-sensitive detectors, diffusion perpendicular to the electric field *E*, called *transverse diffusion* ($D_T \perp E$), plays a main role in the achieved resolution in this direction ($\rightarrow$ cluster width). *Longitudinal diffusion* ($D_L \parallel E$) has an impact on spatial/time resolution (like in TPC's) or on signal duration. In contrast to the case of electrons diffusive processes are almost negligible for the much heavier ions, and they follow the flux lines of the electric field.
In most of the gas avalanche detectors, the drift of the positive ions is responsible for the signal creation. These signals usually show a fast rise and a slow decrease sometimes with a long tail, which limits fast amplifiers to integrate only over a small fraction of the total charge.
Often a dedicated tail-cancellation mechanism has to be implemented into the electronics to avoid signal pile-up and thus a shortened dead time (see also section 3.6). As an example, for the ATLAS TRT straw tubes, the full ion collection time is around 60 µs (compared to a bunch-crossing time of 25 ns!), while the electron signal has only 3-4 ns length and therefore contributes to less than 5 % of the collected charge [19].

4.2.2 Ionization processes in the gas

Fast charged particles passing through the gas volume create both excited and ionised gas molecules along their paths. Secondary processes like further ionization through energetic primary electrons (*"delta rays"*) or energy transfer of metastable states (*"Penning effect"*) [54] contribute to the final total number of released *ion pairs* in the gas, which is the practical quantity of interest.
The average energy needed to create an ion pair creation is called the *W-value*, which for gases is typically 25-35 eV/ion pair. Although the average ionization energy of the least tightly bound shell electron accounts for 10-20 eV in most gases, part of the energy of the incident particle is released in non-ionizing processes (e.g. excitation of gas molecules). The W-values of the relevant TRT gases can be found in Table 4-I [55][56].

TABLE 4-I Average W-values for electrons and photons in different gases.

Gas	W [eV / ion pair]
Xe	22.1 ± 0.1
Ar	26.4 ± 0.5
CO_2	33.0 ± 0.7
CF_4	29.2 ± 1.0
O_2	30.8 ± 0.4

It is not correct to assume the fluctuation σ_0 in the mean number of ion pairs N_0 released by each incident particle follows a Poisson distribution and hence has a standard deviation equal to the square root of N_0. In reality many detectors show an inherent fluctuation less than predicted. Thus an empirical constant is introduced, the so-called *Fano factor F*, which multiplied with the predicted variance gives the experimentally observed variance.

$$\sigma_0^2 = F \cdot N_0 \tag{4.5}$$

Estimates of the size of the Fano factor in proportional gases range from 0.05 to 0.30.
Closely connected to the Fano factor is the so-called *Penning effect*, which plays a crucial role in the simulations. It describes the ionisation by charge transfer during a collision of a metastable with a neutral atom or molecule (see section 4.7.2).

4.2.3 Gas multiplication

In electric fields above ~10^4 V/cm electrons start to gain more and more energy between two collisions and produce inelastic phenomena like excitation or ionization. When the energy of an electron exceeds the first ionization potential of a gas molecule, the result of the impact can be an electron-ion pair. The primary electron continues its motion in the field. Its mean free path for ionization is defined as the average distance the electron has to travel between two ionizing collisions. The inverse is called the *first Townsend coefficient*, α, and represents the number of electron-ion pairs produced per unit length of drift. The fractional increase in the number of electrons can therefore be described as:

$$\frac{dn}{n} = \alpha \cdot dx \tag{4.6}$$

In a uniform multiplication field (between parallel plates) the density of electrons grows exponentially with distance as the avalanche progresses:

$$n(x) = n_0 e^{\alpha dx} \tag{4.7}$$

For cylindrical geometries, like the straw tubes, the field increases in direction of the avalanche and the growth is even steeper. So-called proportional chambers operate in a region where the collected charge is proportional to the number of primary electron-ion pairs created from incident radiation. A further increase of the field will lead, over a phase of limited proportionality, to the Geiger-Müller region where the output pulse height is basically constant regardless of the number of primaries. This mode can be used for sim-

ple counting processes. Figure 4-2 illustrates in more detail the different regions of operation in gas-filled detectors.

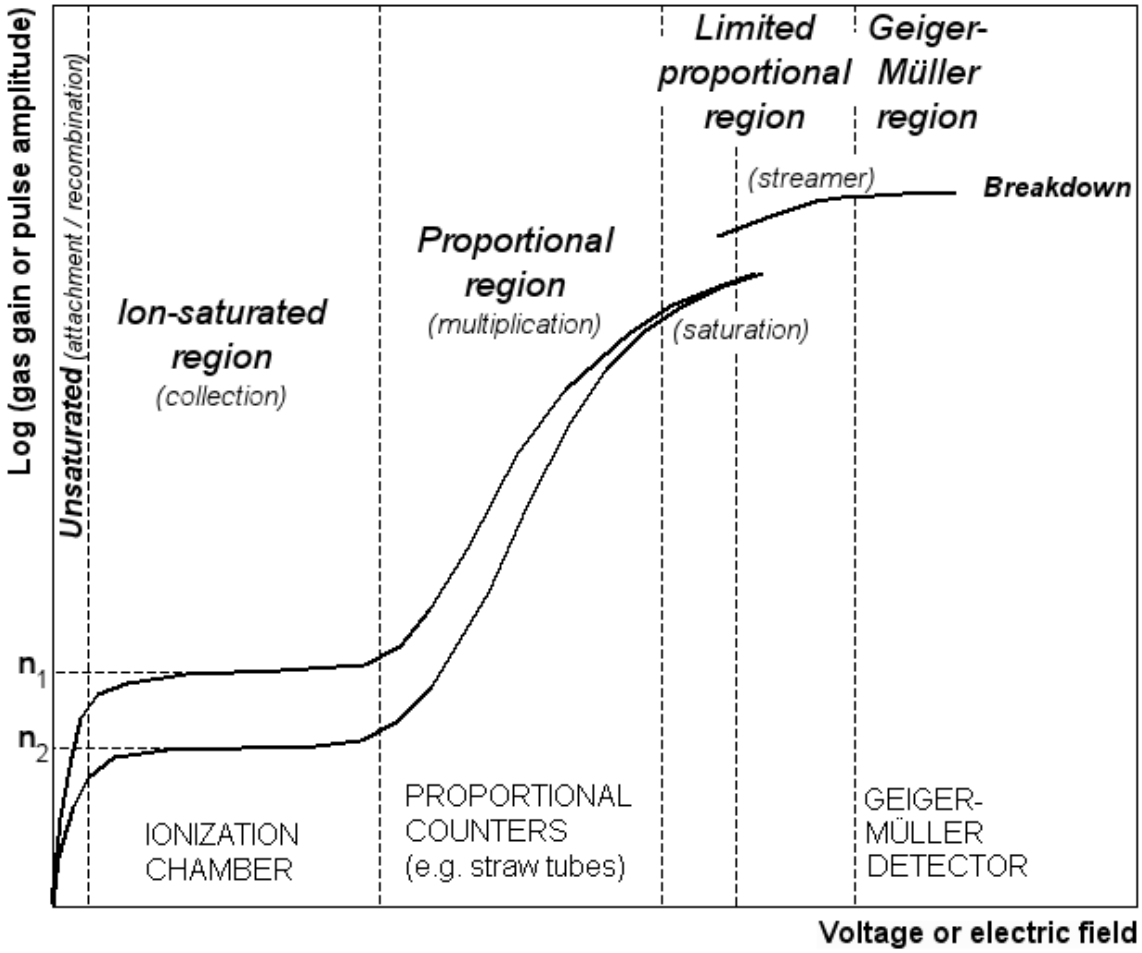

Figure 4-2 Regions of operation in gas-filled detectors are illustrated here [51][57]. The two curves show the total number of charges (directly related to gas gain or pulse amplitude) vs. the applied voltage (or electric field) for different initial numbers of ion pairs ($n_1 > n_2$). At very low values of the electric field recombination processes reduce the collected charge below the original number of ion pairs. As the voltage is raised ion saturation is reached. With further increase of voltage the threshold field of gas multiplication is reached. Over some region the value of collected charge is proportional to the number of ion pairs (*proportional region*), before at higher voltages non-linear processes like space charge effects decrease the slope of multiplication vs. electric field (*limited proportional region*). In the Geiger-Müller region the pulse amplitude is constant regardless of the number of ion pairs from incident radiation. A special region of operation is the self-quenched streamer mode, where the still voltage-dependent large size avalanches are locally confined (see 3.5.1).

4.2.4 Attachment processes in oxygen

In direct competition to the creation of charges are charge losses, in particular electron attachment. Additives to the operating gas, which are of electro-negative nature (high electron affinity) are frequently used in experiments to limit early breakdown through electron attachment. For example, carbon tetrafluoride (CF_4) increases the drift velocity and is also known to inhibit or cure wire deposits to some level (section 3.5.1 and Figure 5-10). Additives like oxygen, SF_6, CF_3Br or other halogen-containing compounds shift the point of break-down and as such improve operational safety. Even controlled levels of H_2O vapour in the operating gas (sometimes introduced from ambient humidity) can have favourable qualities, e.g. partly restoring an ageing-induced conductivity loss of the electrode surface. The loss of primary ionization electrons in attachment processes worsens the energy resolution owing to the strong cluster size fluctuations. The removal of secondary electrons from the avalanches reduces the multiplication factor, but also retards high-voltage breakdown.
In the following, a more detailed description of the attachment mechanisms in oxygen [58], the additive to the xenon-based TRT operating gas, is given.

Two-body or dissociative attachment
The attachment of electrons to free molecular oxygen is in general described by two processes: two-body and three-body attachment.
The first one, also called "*dissociative attachment*", describes the following process:

(1) The attachment of an electron moves the oxygen molecule into an excited state. The energy released in the de-excitation process breaks up the molecule into a neutral oxygen atom and an oxygen anion.

$$e^- + O_2 \rightarrow O_2^{-*} \rightarrow O + O^- \qquad \textbf{(4.8)}$$

Taking the dissociation energy for molecular oxygen, $\mathcal{D} = 5.08$ eV, and the electron affinity of the oxygen anion O^-, $A = 1.46$ eV, the threshold for the described process lies at an electron energy of $\mathcal{D} - A = 3.6$ eV.

Three-body attachment
At lower electron energies other mechanisms are available:

(2) Again the attachment of an electron moves the oxygen molecule into an excited state.

$$e^- + O_2 \rightarrow O_2^{-*} \qquad \textbf{(4.9)}$$

(2a) The excited oxygen molecule can de-excite by exciting a third body M (another gas molecule or atom) or transfer the released energy kinetically (if excitation is energetically not allowed). The electron remains attached to the oxygen molecule.

$$O_2^{-*} + M = O_2^- + M^* \qquad \textbf{(4.10)}$$

(2b) The de-excitation of the oxygen molecule can also cause electron detachment.

$$O_2^{-*} = O_2 + e^- \qquad \textbf{(4.11)}$$

(2c) The de-excitation of the oxygen molecule through third body excitation (or kinetic transfer) can be accompanied by electron detachment.

$$O_2^{-*} + M = O_2 + M^* + e^- \quad \textbf{(4.12)}$$

While two-body attachment processes do not depend on the gas composition, the three-body mechanism involves other molecules or atoms (denoted in *2a-c* as "M") which can receive the released energy in a de-excitation collision. Of course if no lower energy excitation levels are available, which is often the case with atomic gases like argon (see also Table 4-III), the excess energy will be translated into kinetic energy of the molecule/atom "M". The observable of the three-body process is the sum of *2a* and *2c*. It is obvious that these two processes are pressure dependent.

4.3 Software

The programs used, *Garfield* [59], *Magboltz* [60][61] and *Heed* [62], are non-commercial software, available at CERN or directly from the respective author of the program.

4.3.1 Computation of electron impact parameters with MAGBOLTZ

Magboltz calculates electron transport properties like drift velocity, transverse and longitudinal diffusion, multiplication and attachment in gases with applied electric and magnetic fields at arbitrary angles. It allows for both anisotropic elastic and inelastic scattering. Information on the level of excited atomic or molecular states is later used to simulate Penning contributions. The computation is based on cross-sectional data, mostly extracted from earlier electron scattering experiments, and updated on a regular basis by the author of *Magboltz*[1].

An early, analytic version of the program solved the Boltzmann transport equation using a solution for the energy distribution function expanded up to third order of the Legendre polynomials. While this is still the preferred approach for pure noble gases or mixtures exclusively containing noble gases, a Monte-Carlo version was developed by the same author to satisfy accuracy for all other gas mixtures with quenchers or other additives.

The **statistical accuracy** of the calculation improves with the square root of the number of collisions (specified in multiples of 10^7) performed in the Monte-Carlo routine and depends on the gas mixture and the electric field. It usually achieves an error below 1 % on the drift velocity, a few percent on the diffusion parameters and as well better than 1 % on Townsend and attachment coefficients. *Magboltz* is able to determine automatically the appropriate electron energy integration range.

The **electron impact cross-sections** for the different gases used in the simulations are shown in section 4.4. All cross-sectional data has been compiled mainly by S. Biagi (the CO_2 data was worked out with the help of C. Garabatos, GSI, Darmstadt). The data are derived from electron scattering experiments, references can be found in the source code of *Magboltz*.

Ion mobility is not calculated by *Magboltz*, but relevant experimental data can be found in [53] and [63].

[1] An assessment of the "quality" of the cross-sectional data is made by the author of *Magboltz* in the header of the program's source code.

4.3.2 Electric fields, drift and multiplication processes with GARFIELD

Garfield, a software originally written for the simulation of two-dimensional drift chambers, has been developed over years into a powerful tool to perform now also three-dimensional calculations of drift and multiplication processes. Capable of importing computed field maps from finite element programs like *Maxwell*® (from Ansoft Corp.) or *Tosca,* expanded its potential exquisitely. Drifting of charges, diffusion, avalanches and current induction can be treated more accurately now for various complex micropattern detector geometries.

Occasionally used is *Heed,* a program that computes in detail the energy loss of fast charged particles in gases, taking delta electrons and optionally multiple scattering of the incoming particle into account. The program can also simulate the absorption of photons through photo-ionisation in gaseous detectors. The computation is conveniently launched from within *Garfield.*

4.4 Choice of TRT gases

With its large gaseous conversion and detection volume, the ATLAS TRT is unique among former or present gas ionization tracking detectors. The gas medium is the core component of the detector, determining tracking and particle identification qualities, and, last but not least, operation reliability and ageing resistance through its inherent properties. The relevant single gases of the TRT are described in the following paragraphs. Their electron-impact cross-sections, used in the straw simulations, are shown.

4.4.1 The base gases - xenon (Xe) and carbon dioxide (CO_2)

The base components of the TRT gas mixture are **xenon** with its excellent X-ray absorption in combination with the commonly used quencher **carbon dioxide**. A pronounced dip in the elastic collision cross-section (*Ramsauer minimum*) of xenon allows for higher electron energies and hence higher drift velocities in the low field range. Carbon dioxide with its various excited states, rotational and vibrational degrees of freedom efficiently absorbs UV photons created in the avalanche process, disallowing uncontrolled spread of secondary avalanches that cause early breakdown. The corresponding electron impact cross-sections of both gases are displayed in Figure 4-3 and Figure 4-4.

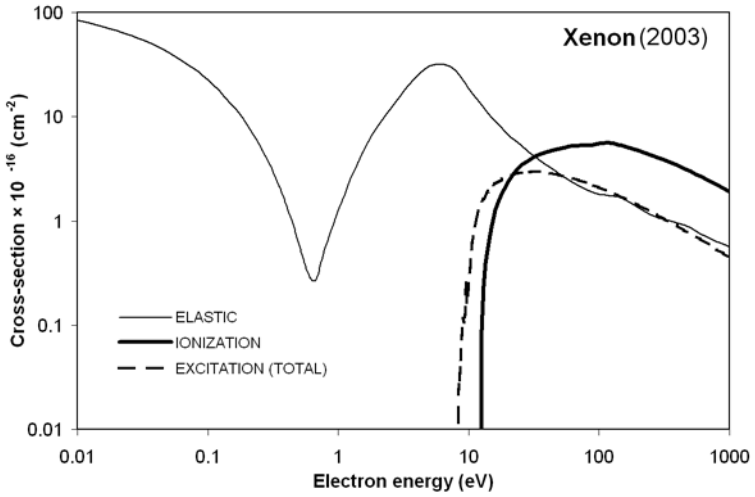

Figure 4-3 Electron impact cross-sections of xenon. The various excitation levels are summed up.

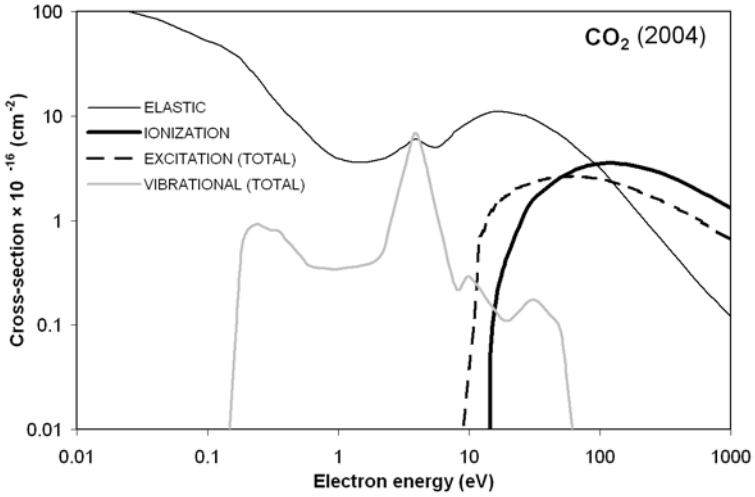

Figure 4-4 Electron impact cross-sections of carbon dioxide (CO_2). The excitation levels and the numerous vibrational modes (e.g. for bending and symmetric/asymmetric stretching) are summed up in order to improve readability. (*Source: S. Biagi and C. Garabatos)*

4.4.2 The "initial" additive - carbon tetrafluoride (CF_4)

For the sake of completeness the computed gas parameters of the initially foreseen CF_4-containing mixture are collected in this section and compared with experimental results. The large fraction of CF_4 (20 %) satisfied both the need for a small maximum drift time (→ *Ramsauer minimum* → *high drift velocity*) and safety (→ *attachment cross-section*) with respect to breakdown and ageing [41]. Thus the CF_4-containing mixture was extensively studied over years. Eventually the aggressive nature of fluoric compounds created in the avalanches let to the abandonment of the additive in 2002.

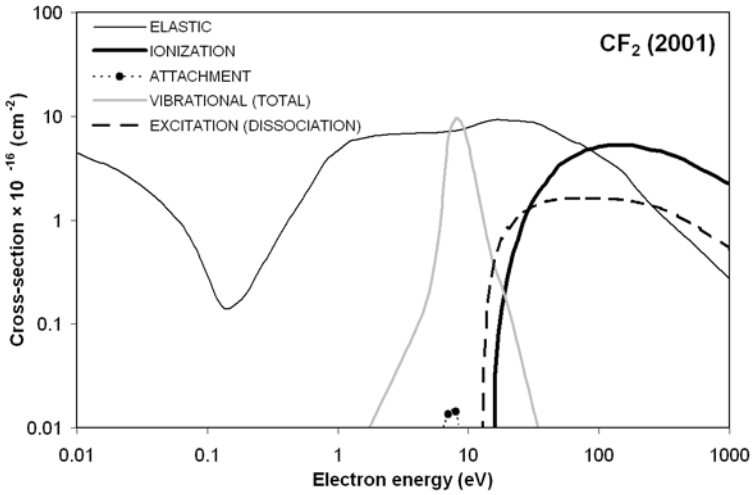

Figure 4-5 Electron impact cross-sections of carbon tetrafluoride.

4.4.3 The "new" additive - oxygen (O_2)

The main function of the admixed oxygen in the gas mixture is to increase the operational safety margin. In comparison with a binary composition, in this case Xe-CO_2 65/35, the distance of breakdown from the operating point is substantially increased by adding 3 % of O_2, as can be seen in Figure 6-16. Its high electron affinity suppresses early avalanche-to-streamer transition and final breakdown. The various electron impact cross-sections for oxygen used in the simulations are plotted in Figure 4-6.

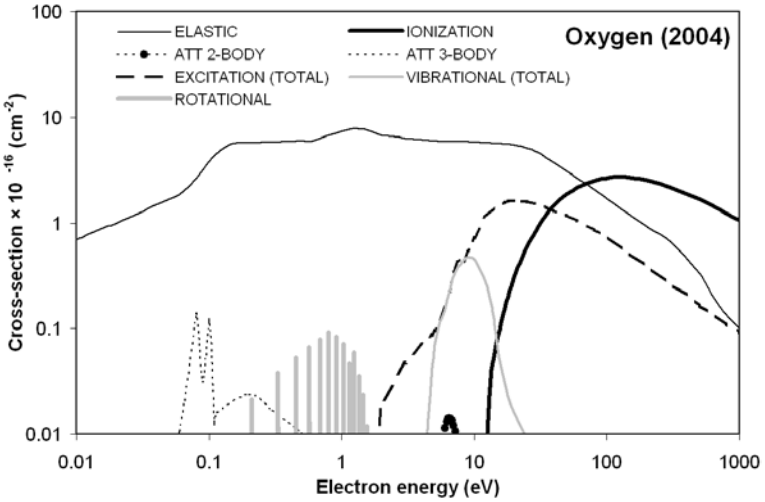

Figure 4-6 Electron impact cross-sections of oxygen.

4.4.4 The ageing and acceptance test gas - argon (Ar)

As a replacement for the costly xenon, the commonly used argon constitutes the base gas for the acceptance tests, where X-ray absorption is not as crucial. No oxygen additives are needed when tests are made at moderate gains ($<10^4$). It was shown [1] that Ar-CO_2 70/30 is well suited to perform straw straightness measurements and high-voltage stability tests. Its missing ageing suppression is irrelevant under the irradiation conditions during those tests.

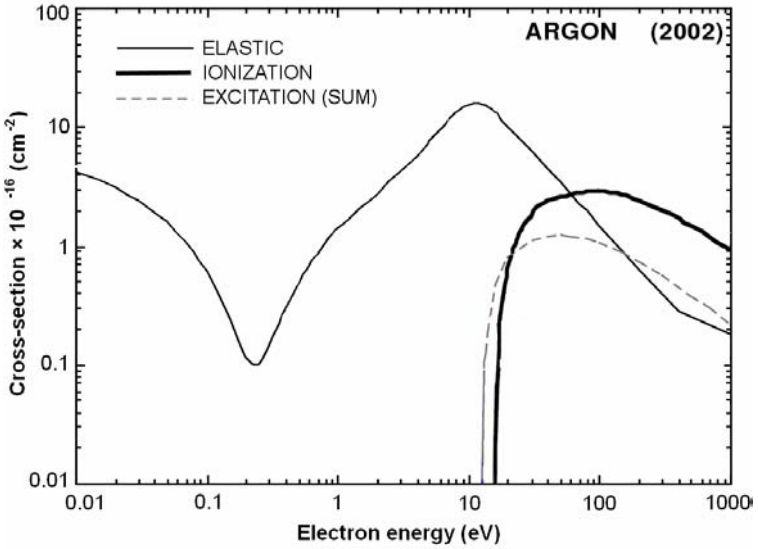

Figure 4-7 Electron impact cross-sections of argon.

4.5 Electric field geometry

The electric field at a certain radius r, in the perfect case of a concentric wire in a circular tube, is described by

$$E(r) = \frac{V}{r \cdot \ln\left(\frac{b}{a}\right)} \qquad \textbf{(4.13)}$$

where
V = voltage applied between anode and cathode,
a = anode wire radius,
b = cathode inner radius.

Field lines concentrate near the wire, which is at positive potential with respect to the tube wall, so that electrons are attracted towards the wire. The radial geometry allows strong field values confined in a rather small region (one tenth of the tube radius) at a large conversion volume (~99 %). Single electron avalanche sizes are hence independent of the position of the primary charges, which are created mostly outside the multiplying region. To reach an average gas amplification of 25 000 with the TRT gas in a parallel-plate avalanche counter (PPAC) of 4 mm thickness it would take a potential difference of more than 8 kV[1], not even considering the poor efficiency (measurable avalanches need around

[1] *Garfield* simulation (P. Cwetanski, 2005)

2 mm avalanche path) and energy resolution (avalanching path length variations of ~2 mm) of such a detector.
The geometry of a “perfect” straw tube has the advantage of symmetry along the straw axis in the simulations. Even the case of a bent tube (within reasonable limits) allows us to investigate the effects assuming parallel displacement of the wire with respect to the tube axis.

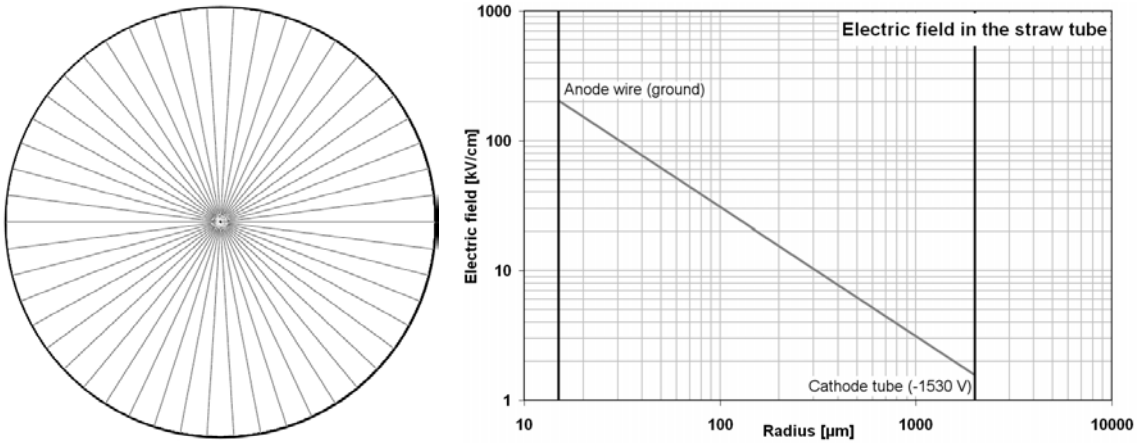

Figure 4-8 Flux lines of the electric field in a perfect straw tube (left) and its magnitude vs. radius (right).

The relevant field in a perfect TRT straw tube at -1530 V ranges from 1.5 kV/cm at the cathoded to 200 kV/cm at the anode (Figure 4-8).

4.6 Electron drift in the straw

4.6.1 Electron drift velocity

Computed electron drift velocities for both gases Xe-CF_4-CO_2 70/20/10 and Xe-CO_2-O_2 70/27/3 are displayed in Figure 4-9 and Figure 4-10. The Ramsauer dip in the elastic electron impact cross-section of CF_4 allows electrons to gain larger energies between two collisions and hence have higher drift velocities for electric field values up to 8 kV/cm compared to the oxygen mixture.

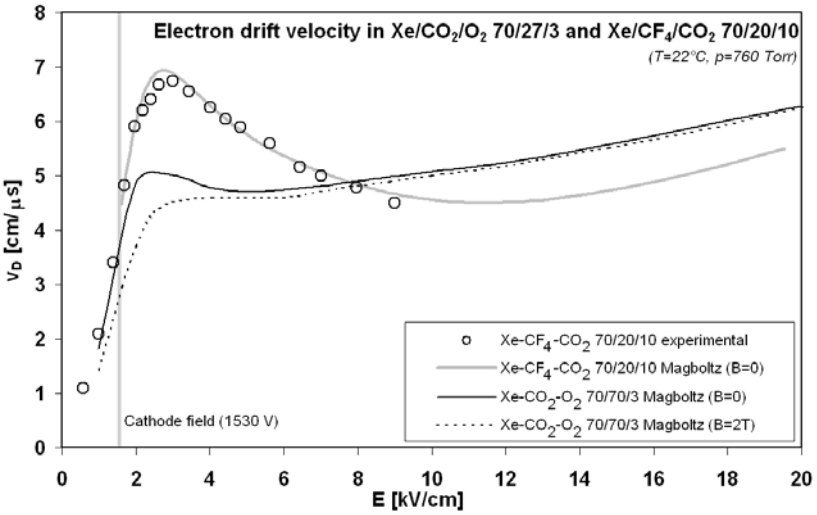

Figure 4-9 Computed and measured drift velocities in Xe-CO_2-O_2 70/27/3 (only simulation) and Xe-CF_4-CO_2 70/20/10 as a function of the electric field E, including values in a magnetic field of 2 Tesla (B⊥E).

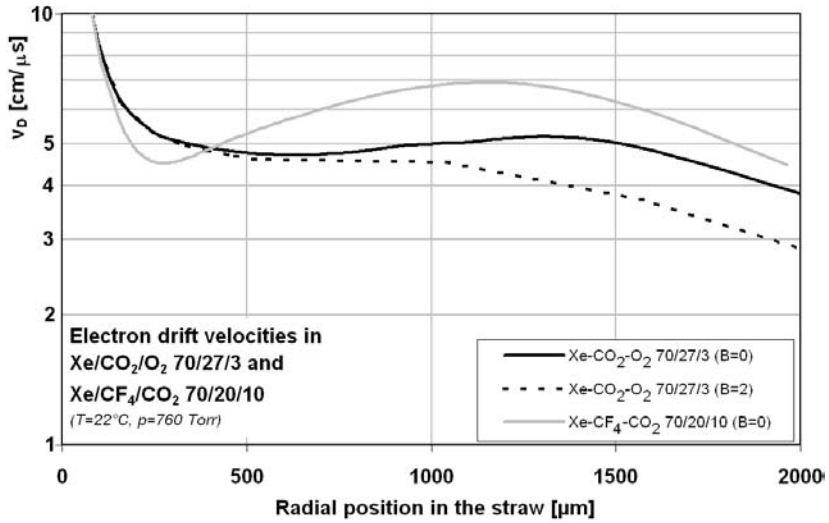

Figure 4-10 Computed drift velocities in Xe-CO_2-O_2 70/27/3 and Xe-CF_4-CO_2 70/20/10 at different straw radii and for a magnetic field of 2 Tesla (B⊥E).

4.6.2 The influence of the magnetic flux density on drift time

In the simulation the quantities of interest were mainly the maximum drift time and the variations due to diffusion, gas contamination or influence of a magnetic field. The presence of a magnetic field alters the trajectory of the electron due to the Lorentz force, so that they no longer follow the electric field lines (illustrated in Figure 4-11).

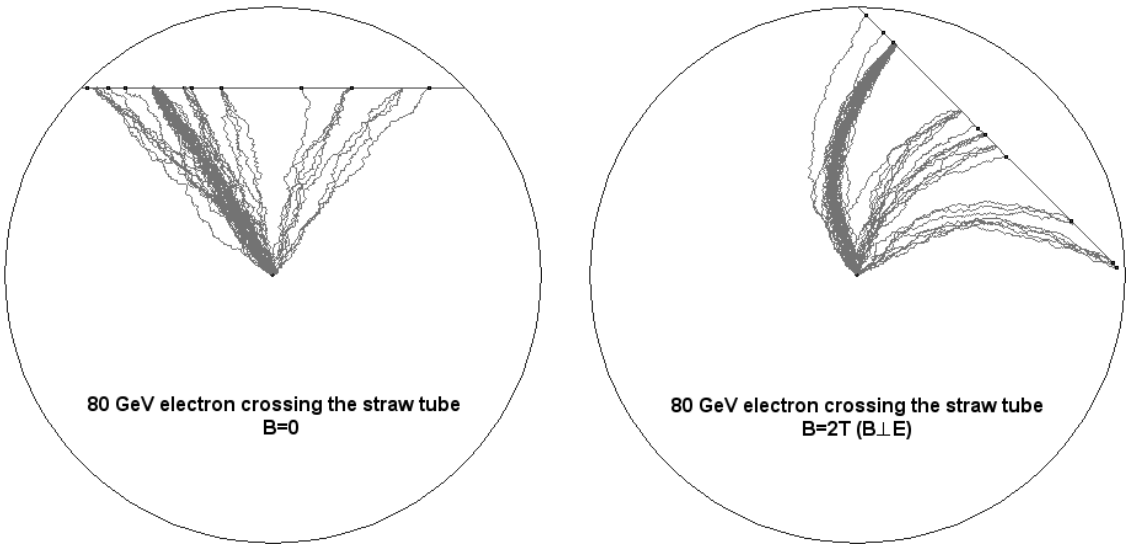

Figure 4-11 Drift of electrons from clusters created by an electron track in the straw.

The effect on the drift velocity of the 2 T magnetic field (B⊥E) in ATLAS is shown in Figure 4-9. The impact is most significant in the low field region, where the drift velocity component perpendicular to E is non-negligible. The affected electric field range corresponds to the outer 1.2 mm of the 2 mm radius of the straw tube.
In the simulation, electrons were randomly distributed in the straw and their recorded drift time plotted against their radial starting point. This yields a “pure” relationship of the drift-time *t* vs. the radial distance *R* (see also R-t relation in section 3.2), where variations are due only to diffusion processes. A 2 T magnetic field increases the maximum drift time by 6 ns (15 %) (see Figure 4-12).

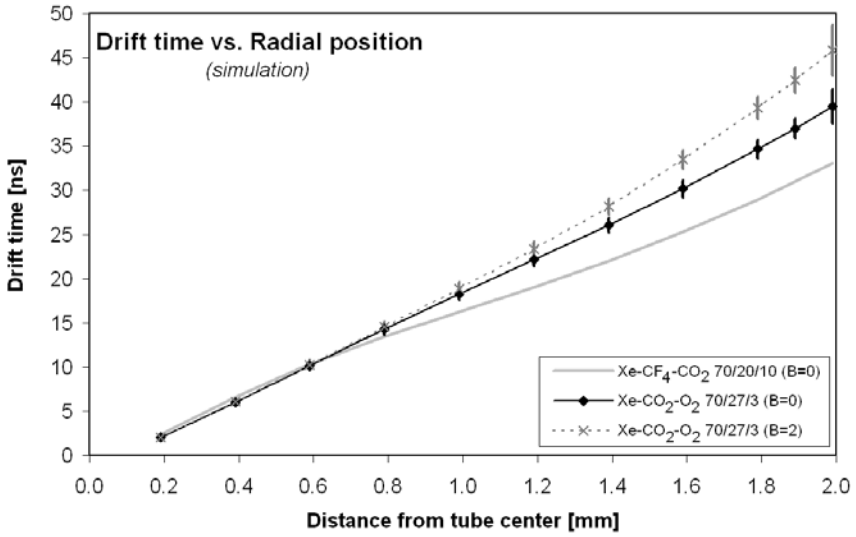

Figure 4-12 Simulated electron drift time vs. radial position in the straw

4.6.3 The impact of nitrogen contamination on the maximum drift time

It was mentioned earlier that the level of nitrogen (envelope gas of SCT/Pixel) in the active gas volume has to be kept as low as possible. Nitrogen contamination has a significant effect on the electron drift velocity. The time for 2 mm drift in the straw was simulated with 2 % and 4 % of N_2 added to the gas mixture (Figure 4-13). As a result, the maximum drift time is reduced by 3-5 ns and such would invalidate the assumed R-t relation and hence the position measurement accuracy.

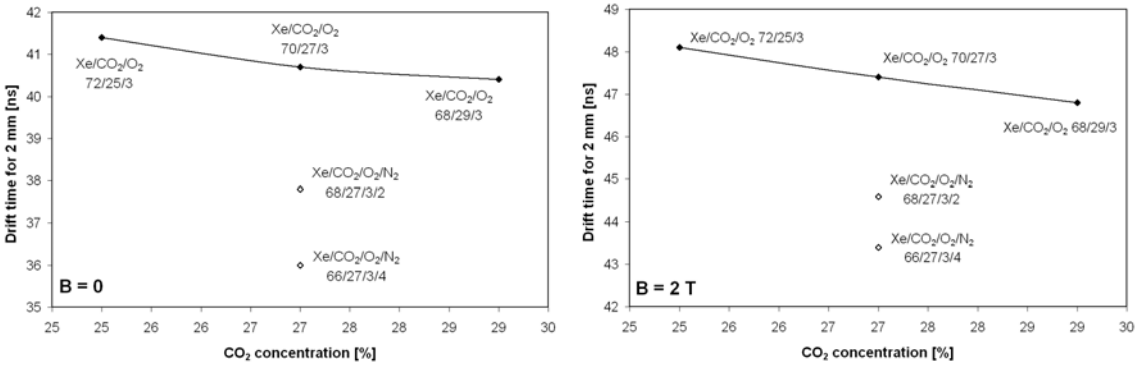

Figure 4-13 Simulated maximum drift time for various concentrations of CO_2 and N_2.

4.6.4 The impact of wire offset on the maximum drift time

It is straightforward to increase the maximum drift time by having an eccentric wire in the straw tube, where the azimuthal field symmetry is lost. Moreover, the electric field near the cathode (tube) corresponds to a region of very steep rise of the drift velocity curve (see e.g. Figure 4-9). This as a direct consequence affects the mean value and variation of the arrival time of electrons from larger radii and thus again position measurement accuracy. Simulated maximum drift time for different wire offsets are shown in Figure 4-14.

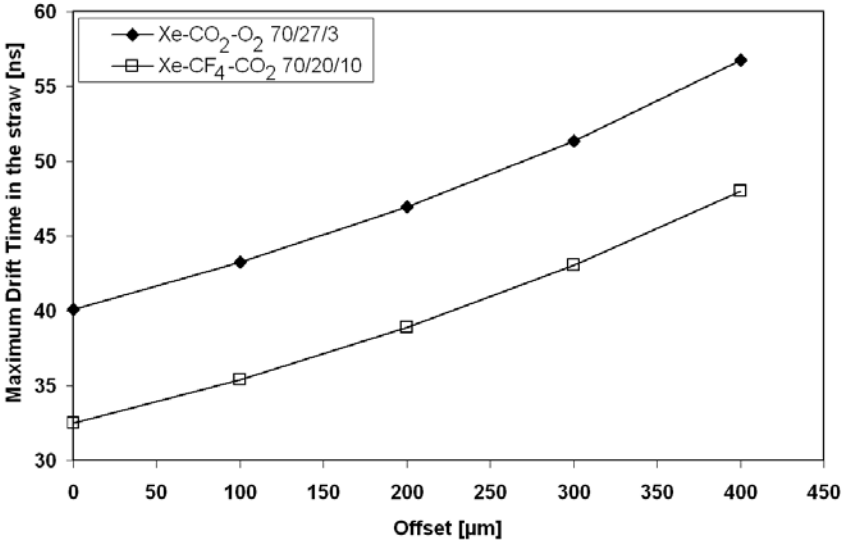

Figure 4-14 Simulation Maximum arrival time in the straw tube vs. wire offset.

4.7 .Multiplication and attachment simulations

4.7.1 Townsend and attachment coefficients

The main input parameters for the gas gain simulations are the Townsend and attachment coefficients (Figure 4-15 - Figure 4-17). They are computed with *Magboltz* based on experimentally derived electron impact cross-sections for single values of the electric field. The points are later interpolated within *Garfield*. Corrections of the ionization rate that account for secondary effects like Penning transfers are applied manually (see section 4.7.2).

TABLE 4-II Number of ion-pairs created by an ^{55}Fe X-ray[a] [64]

Gas	Primaries	Fano factor
Xe-CO_2-O_2 70/27/3	258 ± 6	0.190
Xe-CF_4-CO_2 70/20/10	255 ± 6	0.188
Ar-CO_2 70/30	218 ± 6	0.185

a. based on ^{55}Fe X-ray energy of 5.966 keV (average between K-α and K-β)

For the simulations of charge multiplication and attachment processes it was necessary to consider the earlier measurements with ^{55}Fe X-rays. Contrary to ion-pair creation by minimum ionizing particle tracks, X-ray ionization is in good approximation point-like, which means the total X-ray energy is absorbed in a single spot. In reality some electrons which obtain a large kinetic energy in the ionizing collision trigger further ionization along their path. These so-called “knock-on electrons” or “delta rays” extend few hundred micrometer away from the initial X-ray conversion point, a marginal effect not considered in the simulations.

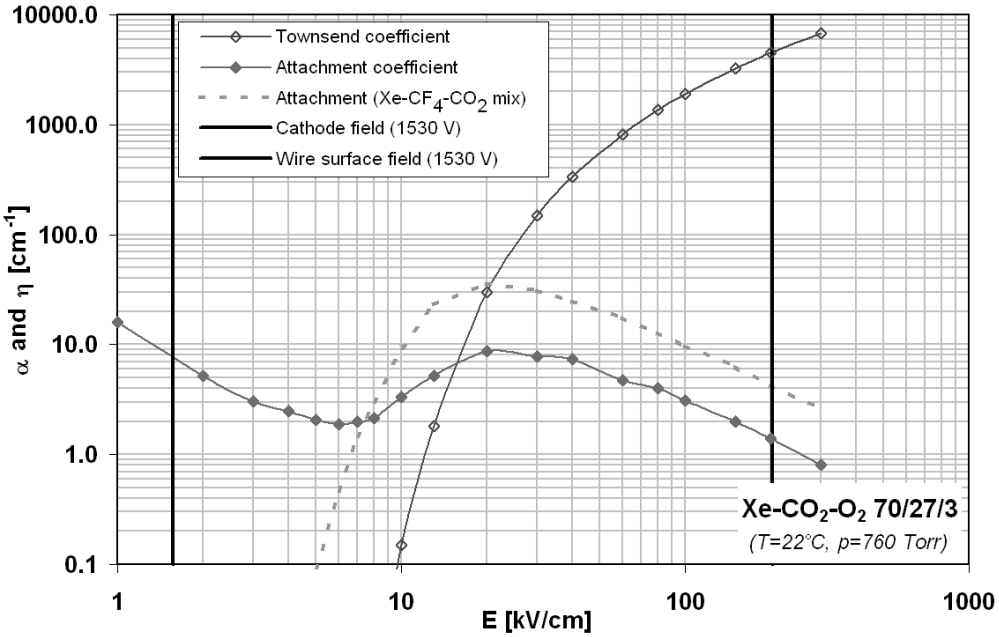

Figure 4-15 Computed Townsend and attachment coefficients in Xe-CO_2-O_2 70/27/3. The attachment coefficient of the Xe-CF_4-CO_2 mixture is shown in contrast. Cathode and anode surface fields in the straw tube for the operating voltage are indicated.

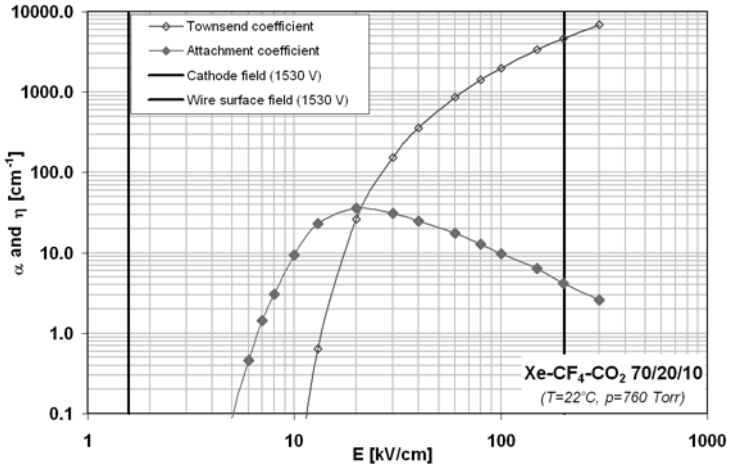

Figure 4-16 Computed Townsend and attachment coefficients in Xe-CF_4-CO_2 70/20/10.

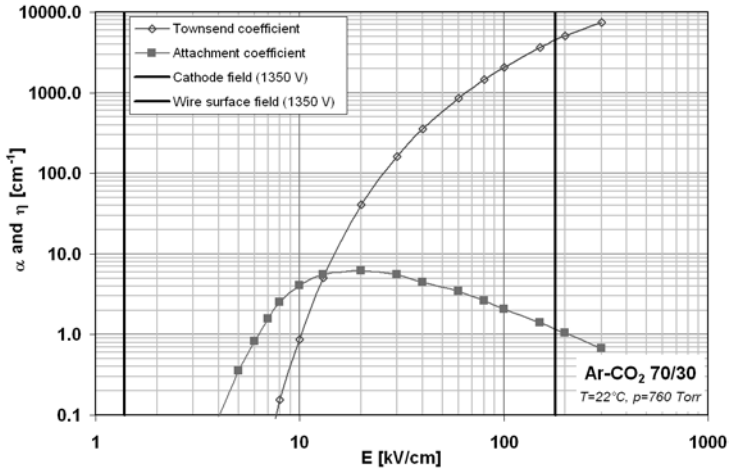

Figure 4-17 Computed Townsend and attachment coefficients in Ar-CO_2 70/30.

4.7.2 Estimation of the Penning effect

The simulations have to account for the Penning effect [54]. It tends to convert a greater fraction of the energy, initially lost in excitation, into ion pairs if the admixed gas component has a lower ionization potential than the available energy of the meta state:

$$Xe + CO_2^{meta} \rightarrow Xe^+ + e^- + CO_2 \qquad \textbf{(4.14)}$$

The excited atoms of the principal gas are then able to transfer this energy in ionizing collision with molecules of the admixed component. The transfer is called “local”, when ionisation of the background gas through an excited atom or molecule happens in a direct collision, within a few nanometers of the original excitation. The non-local energy transfers are caused by photon emission at wavelengths of less than 150 nm and have typical absorption lengths less than 1 µm at atmospheric pressure. In the simulations no difference was made between these two processes.

Fill gases that consist of Penning mixtures (e.g. argon + DME, ethylene or isobutane) are commonly used, especially if improved energy resolution is required (since a greater fraction of the deposited energy is converted into measurable charge). Estimates of the Penning effect at high field can be obtained in *Magboltz* by inspection of the detailed collision frequencies for excited states in the gas mixtures. Previous results in Argon hydrocarbon mixtures indicate a transfer efficiency of around 30 % from excited states in argon to ionization of hydrocarbons [65][66][67].

Table 4-III lists the single gases used in TRT operation or acceptance tests with their ionization potentials and excitation levels. One can identify the allowed Penning contributions in the conversion of the deposited energy into ion pairs.

While xenon mixtures - due the low ionization potential of their base component - are more likely to exhibit Penning contributions from quenchers like CO_2 or CF_4, the Penning effect is less pronounced in the commonly used Ar-CO_2 gas composition.

TABLE 4-III Ionization potentials and excitation levels in eV of various gases used in the TRT.

Gas	E_{ion}	E_{exc1}	E_{exc2}	E_{exc3}	E_{exc4}	E_{exc5}	E_{exc6}
xenon	*12.13*	8.3	9.4	9.9	11.7		
argon	*15.70*	11.5^S	**13.0^P**	**14.0^D**			
carbon dioxide	*13.77*	7.9	8.9	10.5	**12.2**	**13.2**	**15.0**
oxygen	*12.07*	0.9	1.6	4.5	6.1	8.4	9.3
carbon tetrafluoride	*15.90*	**12.5**					

In practical simulations, the Penning transfers are realised as follows: For a given value of the electric field, *Magboltz* yields, *inter alia*, the first Townsend coefficient α_{tot} and the collision frequencies for ionizing and excitation collisions. In a first step, the excitation collision frequency of the relevant CO_2 levels is translated into number of excited states per cm with help of the known Townsend coefficient α_{tot} and the ionization collision fre-

quency ν_{tot}^{ion}. A Penning transfer efficiency of 30 % then leads to the number of CO_2 excited levels per cm that ionise xenon atoms by energy transfer, α_{penn}.

$$\alpha_{penn} = 0.30 \cdot \frac{(\nu_{CO_2}^{exc3} + \nu_{CO_2}^{exc4} + \nu_{CO_2}^{exc5})}{\nu_{tot}^{ion}} \cdot \alpha_{tot} \qquad \textbf{(4.15)}$$

The total Penning-corrected Townsend coefficient is then calculated as:

$$\alpha_{tot}^{corr} = \alpha_{tot} + \alpha_{penn} \qquad \textbf{(4.16)}$$

Only the three highest excitation levels of CO_2 are taken into account, because their energies lie above the ionization potential of xenon (Table 4-III). In the case of Ar-CO_2, the transfer functions in the opposite direction with the highest argon levels are able to ionise CO_2 molecules. The resulting data is plotted in Figure 4-18, showing the uncorrected Townsend coefficients and the total number per cm of the relevant CO_2 excitation levels.

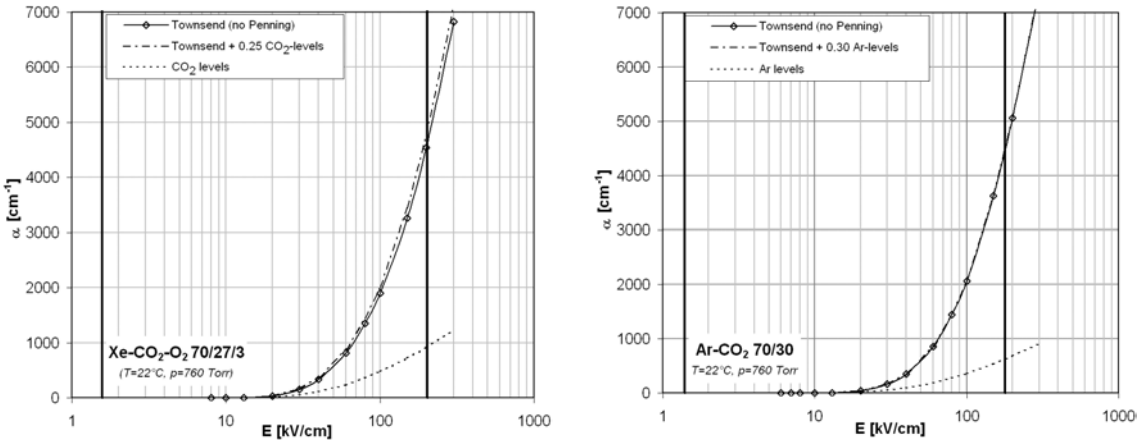

Figure 4-18 Penning corrections in Xe/CO_2/O_2 70/27/3 and Ar-CO_2 70/30. The total number of excited states of the relevant gas component is indicated.

4.7.3 Gas gain simulations

The simulated gas gains are compared with the available experimental data. Pressure and temperature values were known and the Townsend coefficient for the simulation was scaled properly.

An exponential fit of the low gain experimental data indicates that the onset of space charge effects, viz. a deviation from exponential behaviour, is seen roughly at a gas gain

of 40 000 (Figure 4-19). The observed increase in gas gain after 1650 Volts is attributed to the large avalanches from self-quenched streamers.

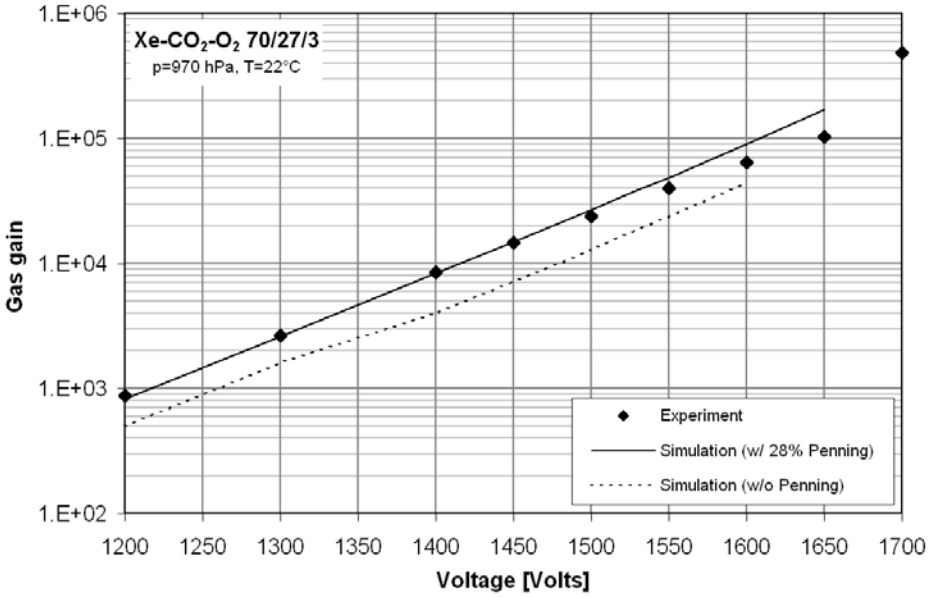

Figure 4-19 Gas gain in $Xe/CO_2/O_2$ 70/27/3 (experimental data [68] and simulation).

Gas gain computations and experimental data for the former CF_4-containing operating gas and for the argon-based acceptance test mixture are shown in Figure 4-20 and Figure 4-21 respectively. The importance of the Penning transfer in the gas gain simulations is obvious, the graphs show a disagreement of almost a factor of two if this phenomenon is not included. The error of the computations accounts for approximately 10 %, not including uncertainties in the atmospheric conditions, which are often not available with the experimental data and hence assumed as "*standard*" (101.3 kPa, 22°C).

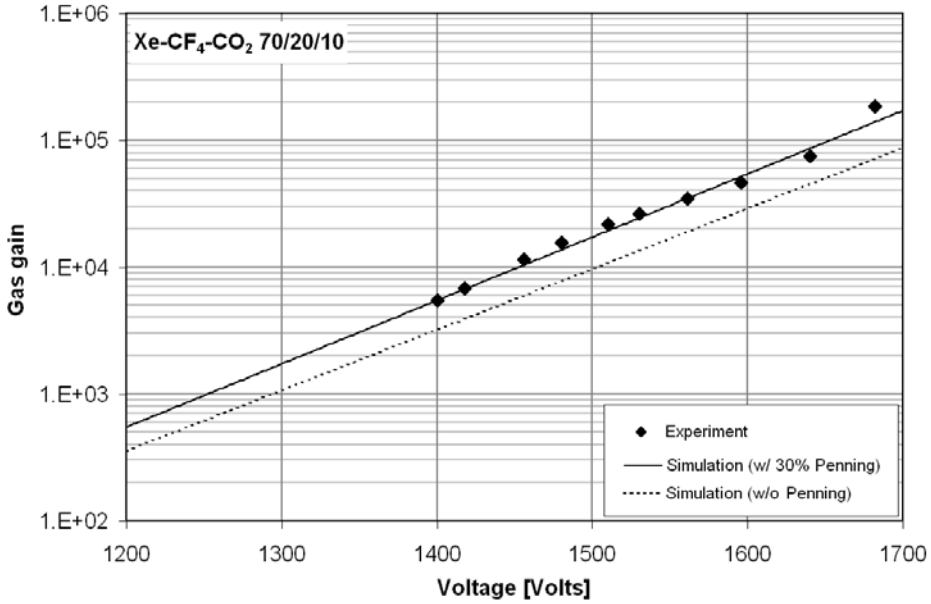

Figure 4-20 Gas gain in $Xe/CF_4/CO_2$ 70/20/10 (experimental data and simulation).

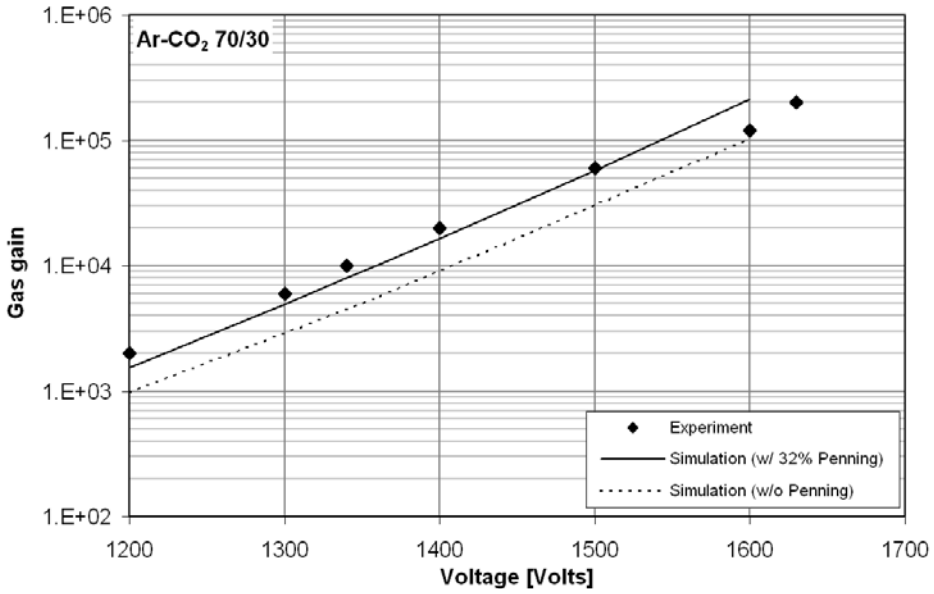

Figure 4-21 Gas gain in Ar/CO_2 70/30 (experimental data and simulation).

The results of the gas gain simulations show best agreement with the experimental data when assuming about 30 % contribution of the excited states in ionizing collisions, thus confirming earlier observations [65][66].

4.7.4 Position-dependent gas gain

In simulations great attention should be paid to gas mixtures containing highly electro-negative components, like carbon tetrafluoride or oxygen in the case of the TRT. In the oxygen mixture, the attachment coefficient dominates beyond radii of 200 µm, i.e. basically outside the avalanche region, that covers almost 99 % of the straw's cross-sectional area. Ionization clusters from minimum ionizing particles (MIP) contain few electrons, of which a significant fraction can be lost in attachment processes. In laboratory measurements, ^{55}Fe sources are commonly used, where clusters from X-ray conversion contain well above 200 electrons (Table 4-II), that always result in measurable avalanche sizes. The obtained avalanche size of electrons from ^{55}Fe X-ray conversion depends on their radial cluster position in the straw, where electro-negative gas components deplete the clusters of primary electrons. This phenomenon is simulated and shown in Figure 4-22.

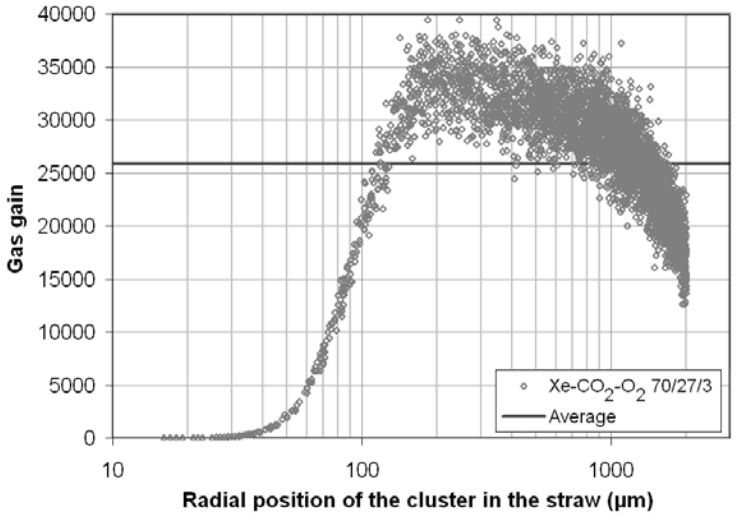

Figure 4-22 Radial dependence of the avalanche size of electron clusters from ^{55}Fe X-rays. Clusters from X-ray conversions closer to the tube are more likely to be depleted by attachment processes, while electrons created in the wire vicinity cannot take advantage of the full avalanche path length.

4.7.5 The effect of temperature on gas gain

A dedicated gas gain stabilization system is employed to compensate changes in gas gain due to atmospheric pressure and temperature changes, as well as for effects from ambient gas impurities. Gas gains from ^{55}Fe clusters have been computed for temperatures of 12-32°C in steps of 5°C. The Townsend coefficient α scales with temperature T, thus an increase in T leads also to a increase in α ($\rightarrow$ mean free path), hence the higher gas gain.

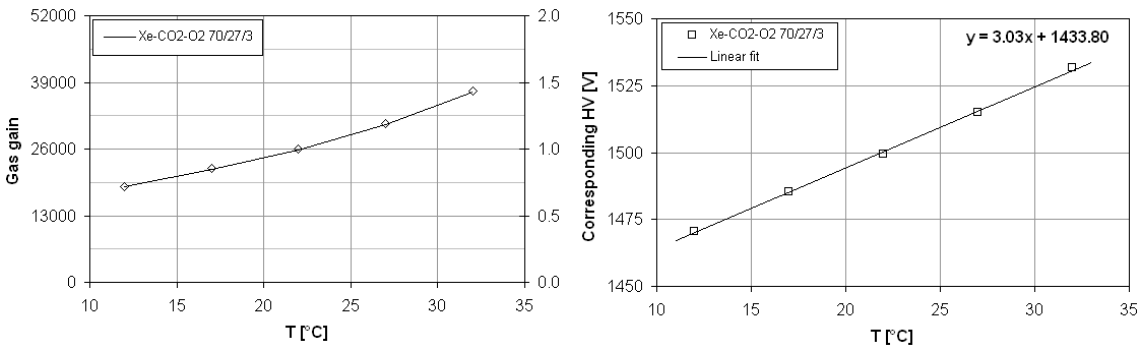

Figure 4-23 The effect of temperature on gas gain in the TRT straw tube.

The simulation shows a temperature effect on gas gain of 3-4 %/°C or 3 V/°C if related to a fluctuation around the operating point. The corresponding high-voltage values were computed using the relation in Figure 4-23. These values are in very good agreement with experimental observations [68].

4.8 The Effect of geometrical distortions on the straw

4.8.1 Wire displacement

Ex ante, when studying wire offset, a parallel dislocation of the wire with respect to the cathode tube axis is assumed. It allows to exploit symmetry and perform 2-dimensional computations. The approach is feasible when the wire offset in the irradiated spot (width normally less than 1 cm) remains fairly constant for non-parallel dislocations. Fractions of the *Garfield* run file are presented in the Appendix B, allowing the interested reader to reproduce the simulations. However, less relevant details, yet necessary parts of the script for the comprehensive simulation work, are left out at this point for the sake of clarity.
The straw geometry is conveniently described in *Garfield* by making use of the `tube` and `rows` commands in the `&CELL` section. During the computation, the program calculates the field map for configurations with a displaced wire through a conformal mapping of the solution for the centred wire; a method valid and exact in the thin wire limit [69].
The script example in Appendix B shows the description of a 4 mm tube with a 31 µm wire displaced by 500 µm in positive y-direction. The cathode tube is kept at -1530 Volts, the anode wire remains on ground. As an example, a magnetic field of 2 T in y-direction (i.e. B⊥E) is added (not used in the wire offset simulations). The distortion of the electric field (for B = 0) can be seen when looking at the field line plot in Figure 4-24 (technically these are the flux lines of the electric fields, along which the electrons and ions move).
In order to display flux lines, i.e. a “no-diffusion” drift, the gas properties are required. *Magboltz* is called from within *Garfield*, the correction of gas data for higher fields can be added in form of tables (not shown here for clarity reasons). Electron drift in a magnetic field (no wire offset) in the straw tube is shown in Figure 4-11.
At the end of the script example, the gas gain of single electrons is computed using the Monte-Carlo drift and avalanching routine. The expected relative gas gain for single primary electrons, depending on their point of creation, is illustrated in the gas gain map in Figure 4-24. The field enhancement on the side of reduced distance between the tube and wire is visualised in yellow, orange and red. The gain area plot in Figure 4-24 was computed earlier for the CF_4-containing mixture, and is shown only to illustrate generic gas gain non-uniformities in straws with eccentric wires.

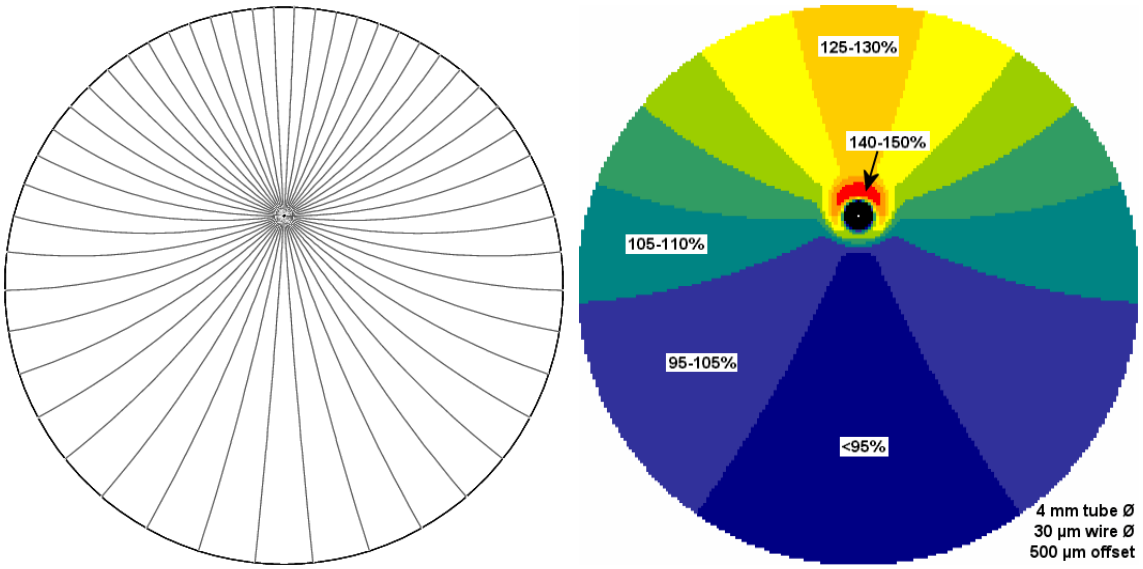

Figure 4-24 Distortion of electric field (left) and distorted gas gain symmetry (right) in a TRT straw tube with 500 µm wire offset. The gain area plot was computed for the Xe-CF_4-CO_2 mixture.

It should be noted that, although the field far from the wire decreases with offset (on the side with increased wire-tube distance), the field near the wire surface is enhanced at any azimuthal position (see Figure 4-25). With the avalanches taking place in the close wire region one measures a total increase in gas gain with wire offset also evident in Figure 4-26.

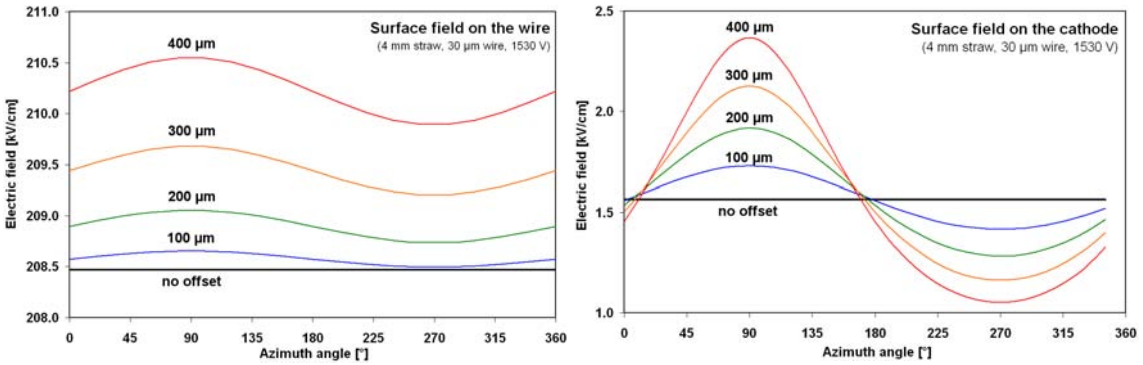

Figure 4-25 Computed electric field on the wire (left) and tube (right) surface as a function of the azimuth angle for different wire offsets.

The use of highly electro-negative gas components (CF_4 resp. oxygen) in both the old and new TRT operating gas, leads to a significant attachment probability in the low field region ($E << 15$ kV/cm) corresponding to radii > 200 µm. At fields above 30 or 40 kV/cm, i.e. close to the wire, the ionization probability is already by an order of magnitude higher in both gas mixtures and electron losses have little impact on the avalanche size. An off-centred wire distorts both the radial symmetry of ionization and attachment dominated regions, which becomes evident through the geometric change of the main peak in the ^{55}Fe spectrum (Figure 4-26). The increased probability of large avalanche sizes manifests in a high energy tail, which serves as another excellent indicator to expose straws with significant wire eccentricity. The relative change in gas gain and in the width of the peak are well correlated. This behaviour was studied in detail and is described in section 6.5.3.

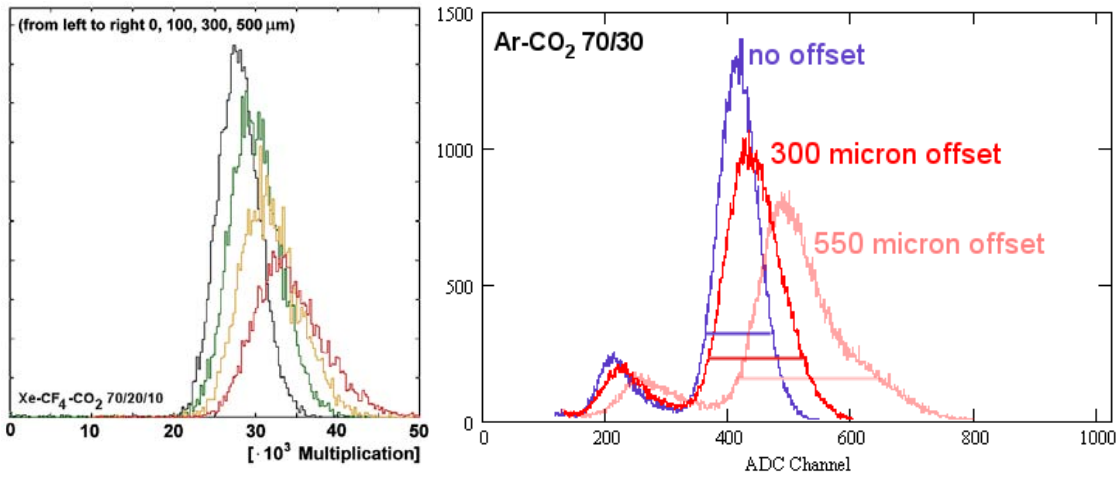

Figure 4-26 Simulated (left) and measured (right) ^{55}Fe spectra for different wire offsets. The simulation was done earlier in Xe-CF_4-CO_2 70/20/10 [40], the measurement in Ar-CO_2 70/30. *Note:* the escape peak seen in the measurement (at ADC channel 200) is insignificant for the simulation and thus not reproduced.

Now, simulating the exact method, which was used in the experimental setup, appears to be very time consuming, since it involves computing a large number of electron avalanches (approximately 10^6-10^7) to obtain an adequately resolved ^{55}Fe argon peak at each wire offset point. The simulated change of gas gain in the straw corresponds to the mean gas gain of only 1000 single ^{55}Fe clusters (each containing ~200-250 electrons), keeping the statistical error reasonably low. The clusters were randomly distributed in the straw, following certain rules explained later. In the end the simplified approach is found to be in good accordance with measurements, validating the approximations made.

It was shown earlier that the efficient absorption of the 6 keV X-rays in the xenon mixtures causes a dependence of gas gain on the azimuthal position of the radiation source [40]. Irradiating the straw from the side where the wire is closer to the tube wall gives a higher probability for large size avalanches, thus a higher average gas gain and vice versa. In the TRT straw straightness measurements, the direction of a wire offset is not known, and could impose an error on the measured offset. In the argon-based acceptance test gas the absorption attenuation is negligible over 4 mm.

Previously the X-ray attenuation was simulated with *Garfield* and *Heed* by simply recording the cluster position of 5.966 keV photon conversions in the TRT xenon mixture. Figure 4-28 shows the number of X-rays absorbed at a certain penetration depth. One can see that after 4 mm depth the absorption rate is reduced by a factor of two. This was taken into account in the wire offset simulations and was shown to be closer to reality than a uniform cluster distribution, the latter being adequate for argon mixture. Illustrations and results are shown in Figure 4-27 and Figure 4-28.

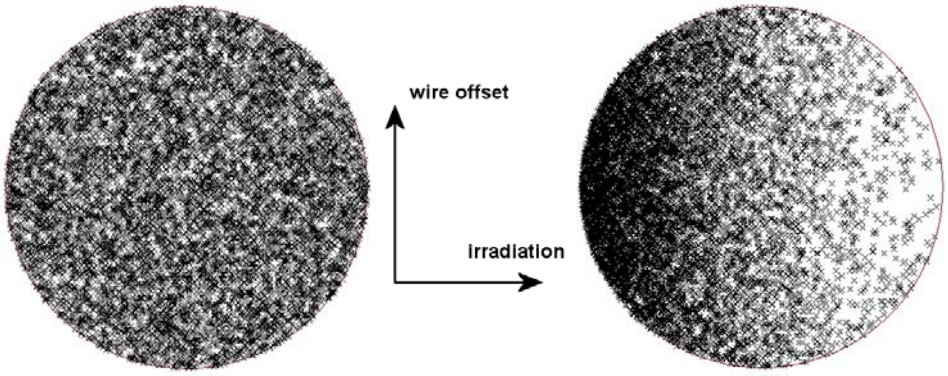

Figure 4-27 Different X-ray absorption models in the gas gain simulations. The small crosses mark the origin of ^{55}Fe clusters in the straw. *Left*: uniform cluster distribution (adequate for Ar). *Right:* lateral exposure with (exaggerated) exponential attenuation (adequate for Xe). Wire offset in the positive y-axis.

For the gas gain simulation in eccentric straws the following assumptions were made:

- lateral X-ray irradiation (i.e. from 90° with respect to wire offset direction),
- exponential attenuation towards the straw centre (in accordance with the simulated attenuation shown in Figure 4-28)
- gas gain at point of no wire offset around 10^4
- all avalanche sizes (whether technically measurable or not) are counted

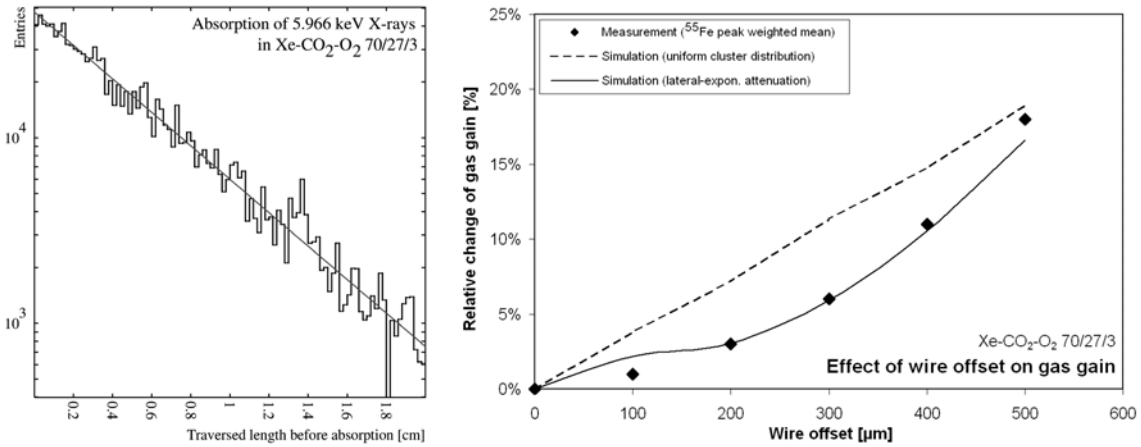

Figure 4-28 ^{55}Fe X-ray absorption in the xenon mixture (left). Measured and simulated relative change in gas gain for different wire offsets, comparing the different absorption models of Figure 4-27 (right).

The agreement within errors with the experimental data in the xenon mixture, as shown in Figure 4-28, is excellent. It confirms the quality of the gas cross-sections and the underlying avalanche model.

4.8.2 Straw tube ellipticity - a few considerations

Less likely to happen under given conditions, however conceivable, is a local deformation of the tube which distorts its circular shape. The effect has previously been found, when a Kapton straw (with its four reinforcing carbon fibres) was inserted incorrectly into the outer socket that contains four corresponding grooves to ensure a precise fit. This could result in a rounded-square tube cross-section (see Figure 6-7), or other anomalous shapes, keeping in mind the complex mechanical co-action of wound tube film, fibres and glue under stress. A simpler case to study is a quasi-elliptic deformation of the straw

("squeezed" tube), which has been examined in both simulation and experiment. The presented results are not exhaustive. These simulations were triggered to achieve a better understanding of gas gain non-uniformities in the straw straightness measurements, which could not be classified as "eccentric" or "ageing" (see 6.5.2).
The difficulty with this simulation is caused by the fact that the description of a continuous tube wall in *Garfield* assumes circularity. A "work-around" was found by defining the tube through a dense set of field wires (Figure 4-29), which is shown to be sufficient for the simulation. In this approximation, the avalanche field close to the anode wire remains undisturbed from field distortions close to the cathode field wires. Proof is simply brought forward by comparing the radial fields in a circular configuration between the closed tube and field wire geometry. The electric field in the field wire simulation deviates from the ideal round tube geometry by not more than 0.3 % for radii smaller than 1.7 mm in the 2 mm tube (Figure 4-29). This allows us to study the relative change of multiplication of single electrons, however, with the caveat that attachment processes in the cathode vicinity cannot be simulated correctly due to the inadequately described electric field.

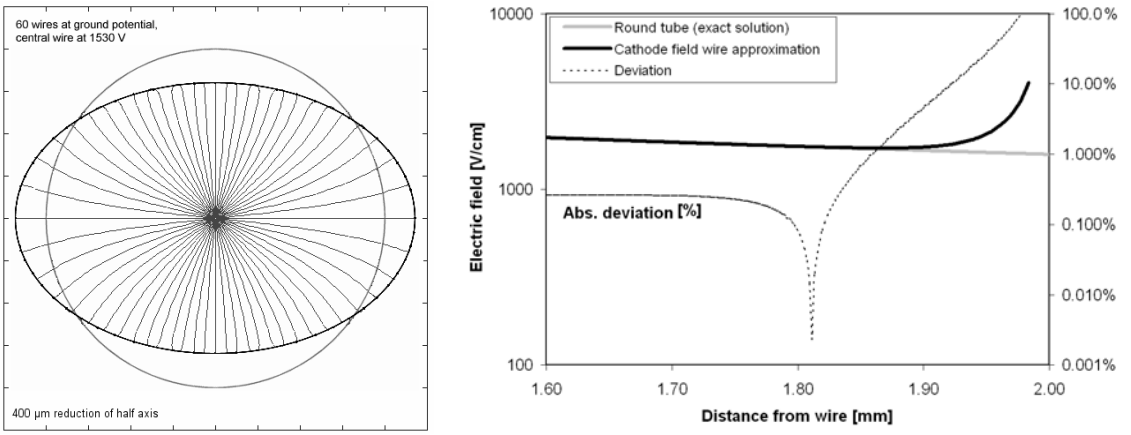

Figure 4-29 Flux lines of the electric field in an elliptic straw (left) and comparison of the electric field in the field wire approximation and in a perfect tube.

Figure 4-30 shows how the electric field changes with progressing tube ellipticity or wire eccentricity. The deviations are relative changes of the electric field along certain radii with respect to the field in a round and concentric straw. Those radii lie on the long half axes of the ellipse.
Looking at the electric field in the multiplication region near the wire, it is noticeable that for both the elliptic tube and eccentric wires the wire surface field increases. Azimuthal symmetry on the other hand is only disturbed in the latter case.
From Figure 4-22 it is evident that the multiplication region extends up to 120-150 µm from the anode wire. While an elliptic deformation of 400 µm (half axis reduction), as shown in Figure 4-30, enhances the entire multiplication zone, in the tube with a 400 µm eccentric wire only part of the avalanche region experiences field growth. The part where the wire is farther away from the cathode, sees a net reduction of the electric field with respect to the "perfect" straw field.

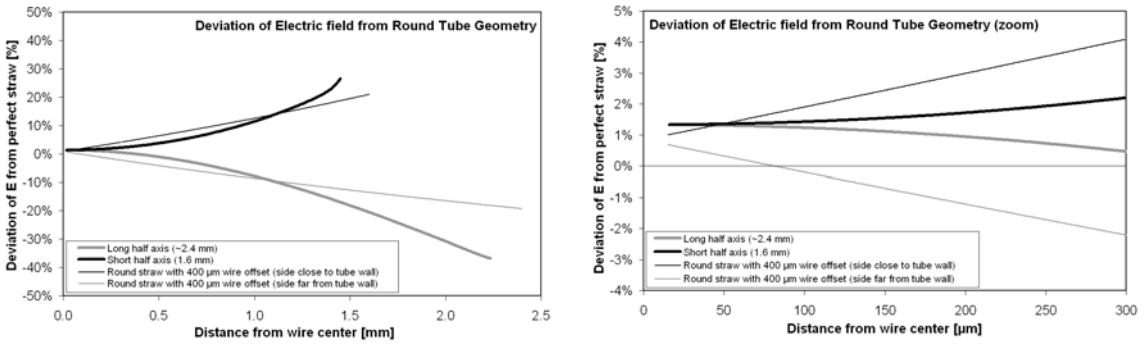

Figure 4-30 Relative change of the electric field in an elliptic straw with respect to a circular straw. Also shown is a comparison with the case of a circular tube with an eccentric wire.

The overall increase of the electric field in the multiplying region in the elliptic straw suggests a steeper rise in gas gain for progressing ellipticity than expected for comparable wire offsets. Fluctuations of total gas gain strongly depend on variations in the number of primaries, whereas in the avalanche region they are fairly small. While field asymmetry is more pronounced in the avalanche region in the eccentric straw, its overall deviation in the conversion/drift region is more moderate compared to the elliptic case. This fact suggests a much stronger degradation of energy resolution in elliptic straws.
Both trends on gain and peak width are observed in the laboratory, giving confidence that the before-mentioned considerations point into the right direction. First dedicated measurements of the ellipticity effect have been performed at CERN [70], their preliminary results are shown in Figure 4-31.

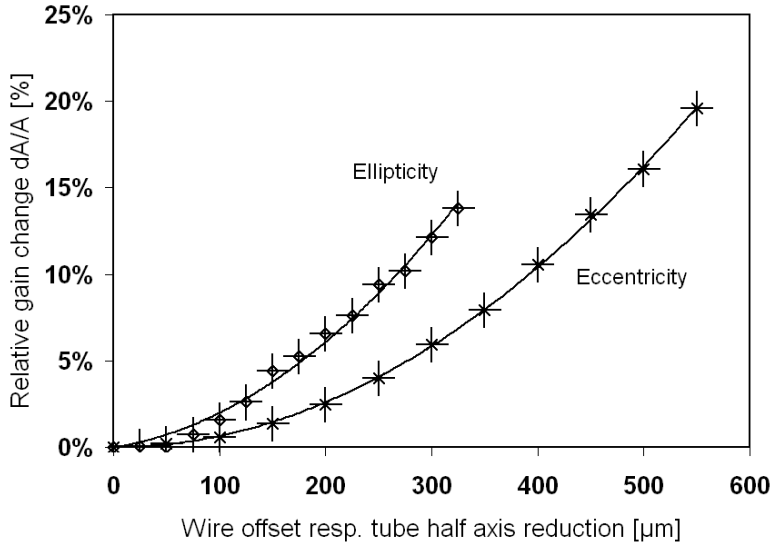

Figure 4-31 The effect of wire eccentricity and tube ellipticity on gas gain (preliminary measurements).

4.9 Conclusions and critical discussion

Simulations have been proven to be helpful in giving insights into phenomena and observations in gaseous detectors. They have been useful to evaluate and optimise numerous types of detector geometries and many different operating gas mixtures. Realizing that they by no means substitute experimental studies, they have been a valuable support in the quest for new gas compositions or in the optimization of detector geometries and operating modes. Increasingly accurate electron impact cross-sections implemented into *Magboltz* and the refinement of the avalanche routine, *inter alia,* in *Garfield* have greatly improved the outcome of simulation studies. The simulations are often in remarkable agreement with experimental observations.

The number of free parameters should be kept small in order to minimise the freedom of the researcher to manipulate simulations to the point of perfect agreement without physical meaning. In this work, **drift velocity, diffusion parameters and multiplication/attachment coefficients** have been obtained from *Magboltz* which uses electron impact cross-sections derived from experimental results. The errors of the obtained gas parameters relate to the uncertainties in those cross-sections, since the computational accuracy is high.

The radial nature of the electric field in the straw is easily described in the symmetric case. **Field distortions** due to a magnetic field or a wire dislocation were simulated, especially their effect on the maximum drift time of electrons in the straw.

The effect of a **nitrogen contamination** of the gas (e.g. from the SCT envelope) on the maximum drift time was examined. It alters the drift velocity and such invalidates the assumed drift-time to radius relation, used for the position measurement in the straw (2-4 % of N_2 decrease the maximum drift time by ~10 %).

Gas gain as a function of voltage was simulated for ^{55}Fe clusters in Xe-CF_4-CO_2, Xe-CO_2-O_2 and Ar-CO_2. The effect of temperature on the straw gas gain was examined for the operating gas. The work involved the computation of the respective Townsend and attachment coefficients with *Magboltz*, and accounting for the point-like charge creation of the ^{55}Fe X-rays. The necessary inclusion of **Penning transfers** in the performed gas gain computations offered a quasi-free parameter, namely the fraction of excited states contributing to ionization by energy transfer. However, in various independent simulation studies this parameter was found to be fairly constant with little dependence on gas composition and electric field geometry. This fact gives further strength to the validity of the results. For the argon and xenon mixtures, Penning transfer efficiencies around 30 % were found to achieve best agreement of the simulated gas gain with experimental results.

Secondary effects, like influence of space charges on the local electric field and hence gas gain, are difficult to include in the simulations. They would significantly increase computation time and thus were not considered. Relevant space charge effects are absent in the foreseen gas gain operation range, their onset can be seen experimentally beyond those amplification values.

Given the TRT design, straws with perfectly centred wires are hardly achievable. The most probable **wire offset** is found to be 100-150 µm (see 6.6.1), which corresponds to an increase in gas gain of about 2 %, close to the measurement accuracy.

The loss of radial gas gain symmetry in an eccentric straw was simulated and illustrated in a gain map, demonstrating the interplay of the field-dependent Townsend and attachment coefficients.

Studies have shown that wire eccentricities up to 400 µm are acceptable for the TRT, maintaining a sufficiently safe margin before streamer onset and breakdown. In dedicated measurements it was found that this offset corresponds to a 11 % change in gas gain (see

6.5.3), a value well reproduced in the simulations. The strong X-ray absorption of xenon had to be taken into account in the simulation (like in the experiment), causing an azimuthal dependence of the average gain in a straw with an eccentric wire. The evolution of mean amplitude and energy resolution of the ^{55}Fe spectrum with increasing wire offset was well reproduced.
Small-scale geometrical deformations of the straw are not necessarily limited to simple dislocations of the tube, causing wire eccentricity. The TRT straw tube cylinder is made of wound flexible film, then reinforced by carbon fibres and fixed at both ends to rings, and, as such, forming a complex mechanical structure, difficult to realise in the simulations. However, the spot of radiation exposure during straw straightness measurements (see 6.2.5) is short compared to the expected variation of wire position along a straw with a non-parallel wire displacement (from parabolic or helical straw shapes)
A simpler case was studied - the “squeezed” tube - which was assumed, in a first approximation, to have an elliptic cross-section. It was shown with a few simplified considerations, that under **elliptic deformations** of the tube cross-section the amplification increases more rapidly than for comparable wire dislocations. Spectra from single straws found during the acceptance tests, which are not consistent with a wire offset signature, support the simulation results. Moreover, first dedicated measurements, performed in collaboration with summer students at CERN, point into the same direction.

CHAPTER 5

"Aging seems to be the only available way to live a long life."
Daniel François Esprit Auber (1782-1871)

Cleanliness Validation and Ageing Studies

5.1 Introduction

As a large scale gaseous tracking detector, the ATLAS TRT faces the challenge to not only withstand, but work reliably for 10 years under the irradiation conditions of the high luminosity LHC. Materials, in particular those inside the detection volume, have to tolerate significant rates of heavily ionizing particles. With the foreseen operating conditions (gain of $2 \cdot 10^4$, 12-20 MHz rate, 0.15 µA ionization current), at the design luminosity of 10^{34} $cm^{-2}s^{-1}$, the anode wires will accumulate the enormous charge of 1 C/cm per year. Thus radiation hardness and ageing resistance has been a major concern in the design and construction of the TRT.
Firstly, operating gas purity is absolutely crucial for the ATLAS TRT:

- Concentrations of more than half a percent of water or nitrogen (SCT/Pixel envelope gas) in the active gas volume have a significant impact on the drift time and thus on the TRT's position resolution.
- Changes in the gas composition might alter gas gain and thus produce signal loss or high-voltage breakdown. Carbon dioxide, for example, penetrates through the straw tube walls and thus its fraction in the TRT gas mixture must be controlled actively in the gas system.
- Impurities like hydrocarbons or silicone compounds can polymerise and deposit on the straw tube or wire surface, causing gradual signal loss and eventually high-voltage breakdown (this process is henceforth referred to as "*ageing*").

Non-polymerizing impurities of a purely gaseous nature (nitrogen, oxygen, carbon dioxide, water etc.) will generally cause no permanent damage to the detector and can be controlled through relatively simple measures. This, however, is not true for heavier and complex compounds that are transformed in the radiation environment into the solid phase. They are mostly found to be hydrocarbons, but also silicone compounds, that rearrange in larger molecular chains and are seen to deposit in the detector volume. As insulating wire coatings, whiskers or crystalline structures, they distort the given geometry and electric field conditions, and finally render the detector inoperative, often in an irreversible manner.
On one hand, it is important to control detector purity as much as technically feasible. On the other hand, extensive knowledge on the detectors inclination towards ageing under the

required operating conditions is indispensable. This is where ageing tests enter the game. Despite more than five decades of experience on ageing in numerous gaseous detector technologies, and gas compositions, the reproducibility of tests have been found to be poor. Still, while there are many “Do not’s”, there are few “Do’s”. Moreover, an aggravating fact is the goal to operate the detector at least for ten years, while only a fraction of this time is allocated to ageing R&D. The acceleration of ageing by “boosting” one or more parameters (e.g. irradiation rate, ionization current or gas flow) in the ageing tests remains a hot topic among experts in the field.

A few general words about cleanliness validation of gas system components is followed by the description of the construction and the use of a gas and ageing monitor counter (henceforth referred to as “*gas-monitor*”). The gas-monitor was originally developed for monitoring purposes during acceptance tests, but it has been also employed to validate gas system parts or perform pure ageing runs. A selection of validation and ageing runs are presented and discussed at the end of this chapter.

5.2 Cleanliness and ageing

Without exaggeration, it can be emphasised that particular care has to be taken to avoid any contamination caused by frequently used lubricants in valves, flow-meters and other gas system components. While hydrocarbon-based deposits are less tenacious and tend to be suppressed in the actual oxygen-containing baseline mixture, this is not the case for silicone. Ageing tests demonstrated the effects of silicone deposits on anode wires in the straw tube, quickly leading to severe degradation of performance, and eventually to total signal loss. The initially considered CF_4-containing gas mixture was known to inhibit or effectively slow down ageing, under foreseen operating conditions, due to its etching capability. The underlying mechanism is attributable to various fluoro-based radicals, created under irradiation. They break up chemical bonds of polymers and thus reduce them to volatile products, eventually removed by the gas flow. The undesirable consequence is that silicone compounds can be distributed ubiquitously in the passive part of the detector and the gas system. The aggressiveness of fluorine radicals towards many materials remains a drawback, as experienced with the glass wire joint in the barrel straws (see also section 3.5).

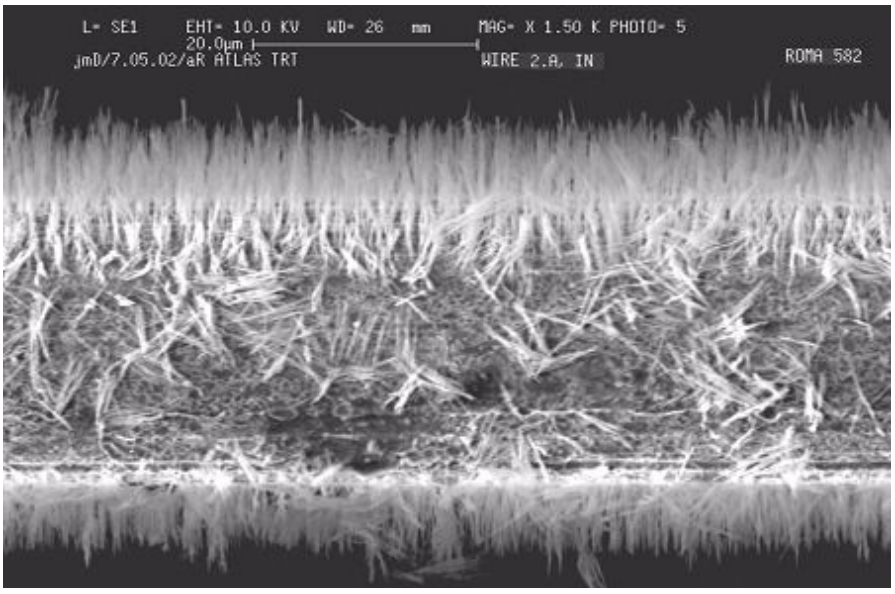

Figure 5-1 Scanning electron microscope (SEM) picture of a straw exhibiting silicon-type deposits.

5.2.1 Component validation

All gas system components are selected with care to avoid any pollution of the initially clean gas mixture[1]. There still remains a risk that cleanliness standards are not met in single cases when ordering large supplies of a component, and there are no means to test every single element. Once an adequate product (see Table 5-I and Table 5-II) has been chosen, a few sample pieces undergo a strict validation process in dedicated ageing runs. Test samples are placed in a vessel or, if applicable, mounted upstream of a straw tube counter, within an ultra-clean gas system. The operating gas is generally Ar-CO_2 70/30, running at ten times nominal gas flow. An X-ray tube irradiates the straws over 1-2 cm creating an ionization current density of ~100 nA/cm.
Eventually a component is considered *validated*, if the straws shows no signs of ageing[2] during 200 hours [71]. This is, after many years of tests under laboratory conditions, believed to be an adequate approach, keeping in mind the difficulty of ageing test acceleration and the completion of the full detector in the existing time frame.
The laborious validation procedure frequently raises the question of how to accelerate the process without distorting the results. While the speed of ageing can be altered by tuning parameters such as operating gas, gas gain, gas flow rate, ionization current density or irradiation area (see also section 5.4), it is important to understand how to extrapolate the test results to “real” operating conditions. Through stringent criteria on components’ purity, the inclusion of safety factors and the possibility to perform “cleaning runs” (only in the unforeseen event of detector ageing), the TRT is expected to perform reliably over at least 10 years of operation.

TABLE 5-I An excerpt of the list of numerous gas system components which have been successfully validated in ageing tests in Ar-CO_2 70/30 and Xe-CO_2-O_2 70/27/3 [72].

Element	Details	Preparation	Ageing in Ar-mix	Ageing in Xe-mix
Pipe	Stainless steel 316L	ultrasonic bath in isopropyl alcohol	NO	NO
Fitting	Gyrolok	ultrasonic bath in isopropyl alcohol	NO	NO
Fitting	Swagelok	-	NO	NO
Flow-meter	Gilmont ACCUCAL	-	NO	NO
Electronic mass flow controllers	Bronkhorst	-	-	NO
Pressure regulator	Scott C21-8	-	-	NO
Pressure regulator	Scott 218	-	NO	-
Valve	Swagelok SS-43S6MM-SC11	-	NO	NO
Valve	SS Needle valve Gyrolok	-	NO	NO

[1] The level of purity of the gases (Ar, CO_2) is an issue not treated here. Long-term tests have led to believe that no significant ageing-relevant trace constituents are introduced with the single gas mixture components.

[2] No signs of ageing practically means an amplitude degradation of less than 2 %, which is in the range of the measurement accuracy.

TABLE 5-II Cleanliness specifications for the TRT gas system [73].

Materials		
Elastomers (gas seals)	preferred	EPDM, Viton, Teflon
	forbidden	Rubber (NBR, Buna N)
Metals	preferred	Stainless steel, copper, brass
	forbidden	Aluminium
Plastics	preferred	ULTEM, PEEK+
Thread tightening	preferred	Teflon band
	forbidden	Si-joint, Loctite
Glues	preferred	Araldite® AY103/HY991 TRA-BOND 2115
Bubbler oils	preferred	None (water, if needed)
	forbidden	All Si-containing and low pressure organic oils
Lubricants	preferred	To be avoided; if needed use Kryotox or Apiezon
	forbidden	Any other

5.2.2 Gas flow meters

A crucial point in the design of the WTS gas panel was the choice of flow-meters in order to control the gas mixture. By balancing applicability, accuracy, cleanliness and costs the choices left were electronic mass flow controllers - previously used in a different setup - or brand-new manual rotameters.

Figure 5-2 Electronic mass flow controller (left) and rotameter flow-meter (right)

ACCUCAL® Rotameter Flow-meters[1]

The rotameters consist of a spherical float (stainless steel ball) moving vertically in a glass flow tube with a tapered inside diameter. As the flow through the flow tube increases, the float rises in the flow tube.

[1] Gilmont® Instruments, Barrington, IL 60010-2392, United States - http://www.barnant.com

The flow-meters are calibrated for air, therefore gravity correction factors (f_g) for each gas have to be applied to compute the real flow of the used gas:

$$Flow_{gas} = Flow_{air} \times f_g \quad \textbf{(5.1)}$$

by using the gravity correction factors in Table 5-III.

TABLE 5-III Gravity correction factors for various gases.

Gas	f_g
argon	0.85
CF_4	0.556
CO_2	0.81
oxygen	0.95
xenon	0.47

An inconvenience is caused by the non-linear scales of the rotameters, requiring the use of flow conversion tables or diagrams (Scale units 0-100 vs. $Flow_{air}$ in ml/min).
The most serious drawback appeared to be the rotameters' high sensitivity to mechanical disturbances and ambient temperature, preventing the required stability of flow and thus mixing ratio. Eventually this led to the abandonment of the rotameters for gas mixing, in favour of the electronic mass flow controllers. Nevertheless rotameters are used in many of the other test stations or setups to set the flow of single or premixed gas, where an accuracy of not better than 5 % is needed.

EL-FLOW® Mass Flow Controllers[1]
The electronic mass flow controllers have been proven to maintain the desired mixing ratio stable and with an accuracy better than 1 %, but at a higher costs. The use of second-hand devices was investigated, keeping in mind that requirements on cleanliness are high, which meant that the mass flow controllers had to be tested carefully. This proved to be a feasible solution for the WTS gas system. The validation test results are presented in section 5.5.2.
The electronic mass flow controllers are operated through the common WTS slow control unit. With the help of an HTML form, flow rates are set and monitored conveniently.

5.3 Development and assembly of a gas-monitor

5.3.1 Purpose

The gas-monitor, as shown in Figure 5-3, is a small straw tube detector connected in parallel to the gas feed line of the WTS. Its purpose is to monitor any change in the gas system, e.g. caused by modifications or maintenance of the gas system. Likewise, any introduction or emission of pollutants within the system leads to a sudden amplitude loss or even severe ageing processes, which have to be detected in due time. The primary goal is to detect potential dangers for the TRT wheels during the acceptance runs and avoid irreparable damage. The gas-monitor has also been used extensively to validate the as-

[1] Bronkhorst Hi-Tec, 7261 AK Ruurlo, Netherlands - http://www.bronkhorst.com

sembled gas system in the acceptance test laboratory during long-term ageing runs. In the same way various single gas system components were tested before use in the wheel acceptance test setups.

5.3.2 Design

A prototype version of the gas-monitor was designed and built to investigate its functionality for the foreseen purpose. It consists of a row of eight straws of 15 cm length at 8 mm pitch. Straws are glued on both ends to two straw carrier plates made of stainless steel. Two gas inlet and outlet manifold lids are manufactured of stainless steel to maximise the amount of inert surface in the active gas system. The only non-stainless steel components of the gas-monitor, which are exposed to the active gas are the straw tubes themselves and the printed-circuit board material of the active WEB, both components used in the actual TRT. It is self-evident that the gas monitoring system should not suffer ageing from intrinsic pollution or outgassing. This is not entirely avoidable under certain conditions which will be discussed later, however, it has no implications on operation safety at the Wheel Test Station or the TRT detector at large. The detection unit with the straws is placed inside a stainless-steel box with a Mylar window to allow for a closed gas volume and irradiation from outside.

The gas-monitor prototype was first tested in a long-term ageing run and its functionality confirmed. Because of the absence of ageing, the detailed test results are omitted in this work in favour of more relevant tests.

The box option was the first design feature to be abandoned and the envelope for the detection elements was reduced to a small Mylar-windowed lid covering the straws only. Furthermore, a reduction from eight to six straws facilitated the redesign without significant limitations in its functionality. The initially chosen, but meticulous process of metal sheet folding and gas-tight welding was avoided by moving to the more simple technique of milling the gas manifold lids.

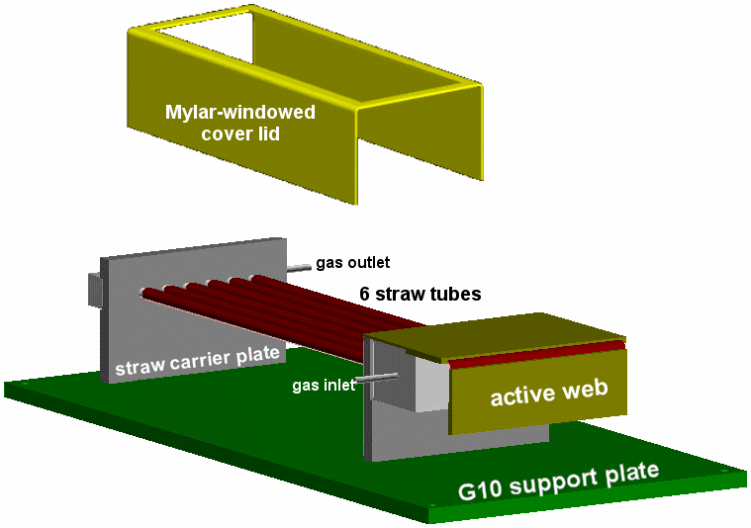

Figure 5-3 Schematic model of the gas-monitor (final design).

5.3.3 Manufacturing of components

The first prototype was entirely manufactured at CERN's mechanical workshop. However, the workshop's high degree of utilization by the LHC experiments made it necessary to investigate external capacity for a small series production. Besides, the welding of the thin-sheet gas volume lids and the rather heavy gas-tight box appeared to take up unnecessary time and costs. These shortcomings were finally overcome through the redesign

and the cooperation of the Helsinki Group at the University of Helsinki in Finland. All stainless steel parts and the G10 plates were machined with high-precision in the mechanical workshop at Kumpula campus[1] at reasonable costs.

5.3.4 Drawings

Depictions and drawings of the single gas-monitor components can be found in Appendix B.

5.3.5 Electronics and DAQ

For the straw signal read-out an 8-channel electronics preamplifier board[2] (see Figure 5-4) was designed at PNPI, St. Petersburg, Russia. It connects onto the active WEB's Fujitsu connector. The preamplified signal is then transferred for further processing (shaping, gate generation) to a CAMAC module[2]. Both signal and gate are finally fed into the standard WTS 8-channel ADC (design PNPI), which is read out through a PC DAQ card using LabVIEW® [3].

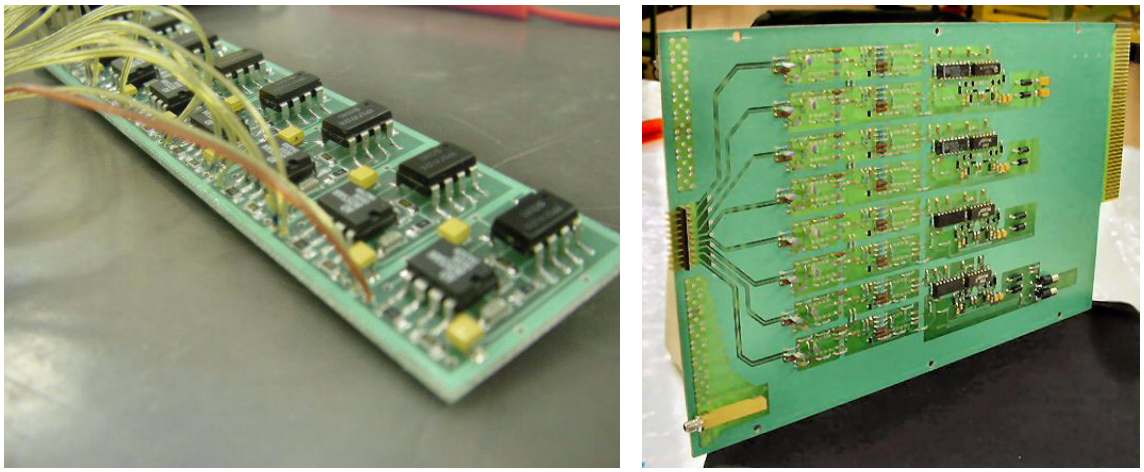

Figure 5-4 Gas-monitor preamplifier card (left) and CAMAC shaper/discriminator module (right)

5.3.6 Assembly and preparation

Assembly consists of two operations: glueing of parts and wire stringing followed by a curing and cleaning process. The assembly can be done in two days taking into account the extra time needed for the hardening of the glue. It should be re-emphasised that clean working conditions during assembly are indispensable in order to ensure efficient operation and exclude intrinsic ageing. For that reason, rubber gloves should be worn. Contact of components with any type of grease or lubricants must be avoided, especially for parts which are exposed to the active gas (wire, gas volume lids and WEB). The consecutive steps of assembly are illustrated in Figures 5-5 to 5-10.

Preparatory steps

Six straws are visually inspected for mechanical accuracy and intactness (straightness, excessive glue, reinforcing carbon fibres, dust or dirt inside). This can be done by eye, while at the production sites a CCD camera is able to detect non-straightness efficiently for the large number of straws needed (Figure 5-5)[74]. It exploits the phenomenon of multiple reflections of the incident light by the inner walls of the tube [75].

---

1 Department of Physical Sciences, University of Helsinki, Finland

2 A. Nadtochy, Petersburg Nuclear Physics Institute, Gatchina, St. Petersburg 118300, Russia.

3 National Instruments™ Corp., Austin, TX 78759-3504, United States - http://www.ni.com

Figure 5-5 Straw straightness is inspected with the help of concentricity of the light pattern. At production site it is done with a CCD camera. The window on the left shows the correlation of the change of light pattern with increasing lack of straw tube concentricity. For the gas-monitor assembly, a visual check against a light source is sufficient (right).

Straw gluing

Both ends of the straws are glued to the straw support plates which are fixed on the detection unit carrier plate (Figure 5-6). The glue used is a high strength and low viscosity epoxy adhesive, viz. TRA-BOND 2115[1]. In this step, an automatic glue dispenser helps to control the exact dose to the desired amount. After applying the glue onto the inner and outer socket of the partly inserted straw, it is fully inserted with a rotating movement. This ensures a uniform distribution of glue and at the same time avoids it from running into the tube. Curing time is 24 hours at 25°C or 2-3 hours at 65°C.

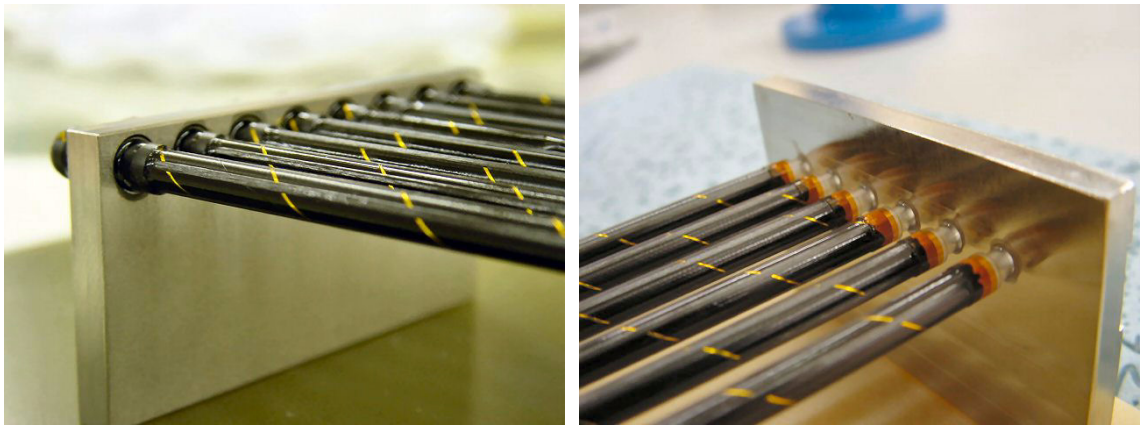

Figure 5-6 Glue fixation of the straws to the support plates. The left photograph shows the gas inlet side (gas-monitor prototype with eight straws), the right photograph the gas outlet side (standard gas-monitor with six straws).

Connecting and wiring

The detection unit carrier plate with the plates is fixed in the vertical position is prepared for WEB connection and straw wiring (Figure 5-7). The unused part of the Kapton signal and high-voltage flaps of the WEB is cropped to necessary size in order to fit into the gas inlet manifold and to avoid electric short-circuiting by folding up inside.

[1] Tra-Con Inc., Bedford, MA 01730, United States - http://www.tra-con.com

The “daisies” of the Kapton flap with the high-voltage lines are carefully connected with the high-voltage plugs to the straw (Figure 5-7). In this manner the “petals” are bent and pressed onto the inside straw wall establishing electrical contact.

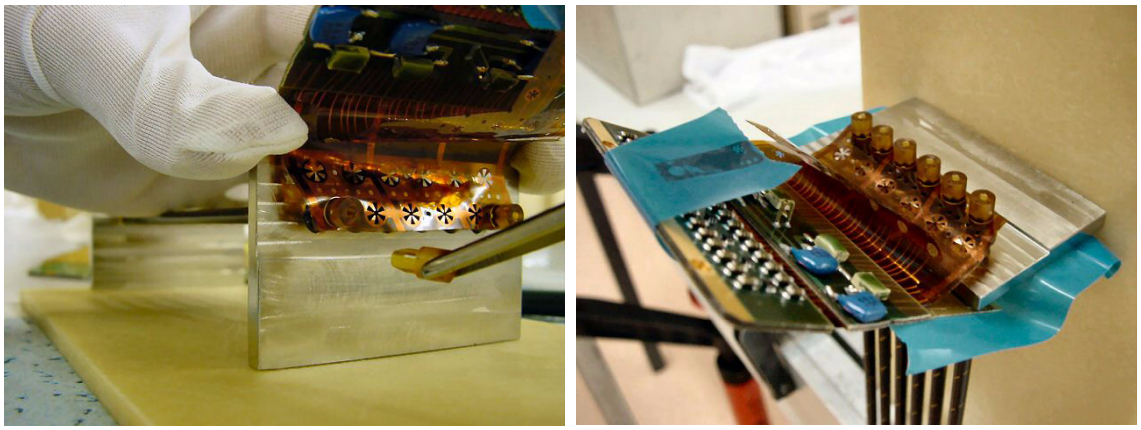

Figure 5-7 Insertion of high-voltage plugs (left) and preparation for wiring (right).

A delicate work step is the insertion of the 30 µm wire through the signal connection flap daisies and the tube, followed by threading it into the 100 µm hole of the outer crimping pin. After that, the crimping pin is inserted into the high-voltage plug thus establishing signal line contact with the petals of the signal flap. These operations bear the risk of kinking the wire or injuring the gold surface layer and thus should be repeated in case of doubt. The crimping of the outer crimp tube is done with a custom-made pneumatic crimp tool, assuring correct crimp force and dimension (Figure 5-8).

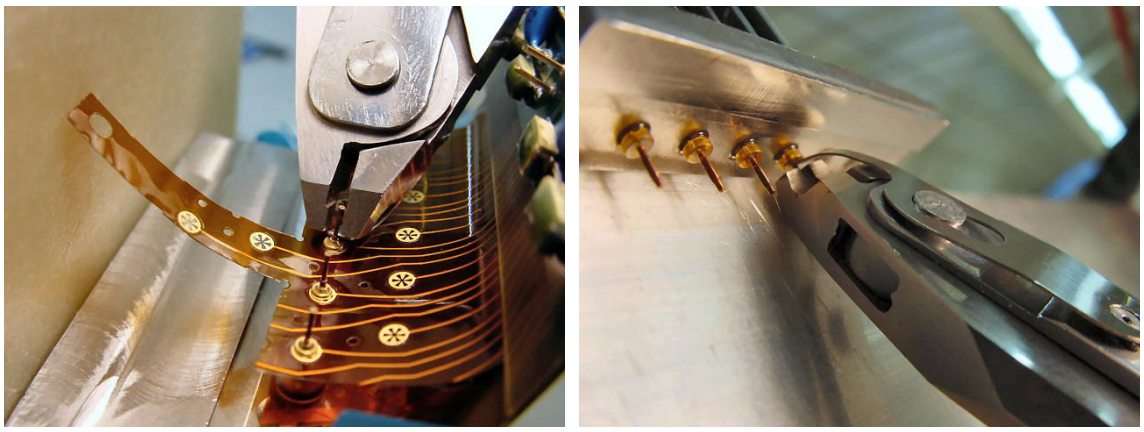

Figure 5-8 Crimping of the outer (left) and inner (right) crimp tube.

The wire is now threaded through the inner crimp tube, the tube then inserted into straw. A 60 g weight, clipped to wire and kept hanging freely, applies the proper tension, then the inner tube is crimped (Figure 5-8). The protruding wire ends are cut off.

Gas volume enclosure

While the straws are fixed and sealed with TRA-BOND glue, the gas manifold components including the active WEB are glued with the more viscous two-component epoxy adhesive Araldite® AY103/HY991. All pieces are kept in position with the help of clamps and weights before applying the mixed epoxy glue onto the gaps and edges (Figure 5-9). This is normally done in two steps, since the glue on all edges facing sideways or downwards naturally runs down, which can lead to insufficient mechanical strength and gas-

tightness. After a few hours of glue polymerization, the gas-monitor can be turned upside down to perform the second gluing step.

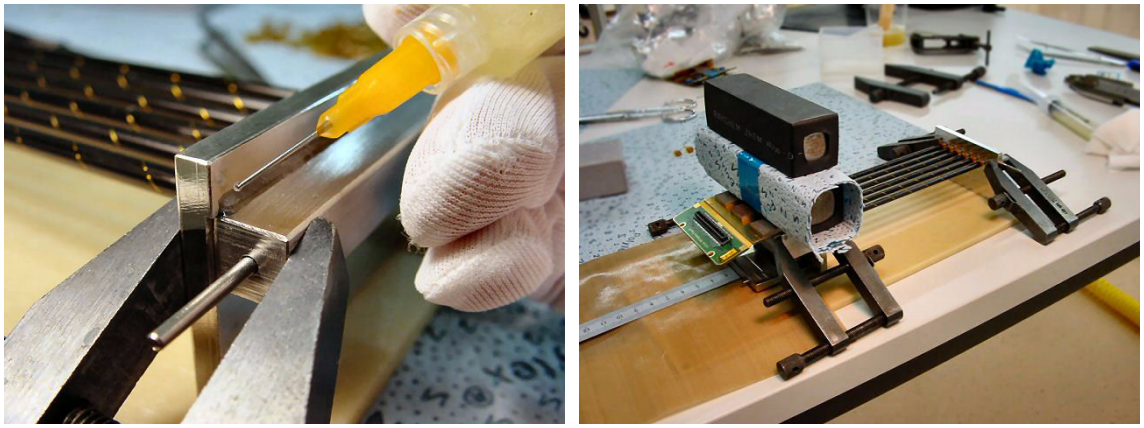

Figure 5-9 Application of epoxy with a pneumatic glue dispenser (left). Fixation of glued parts during polymerization (right).

Post-preparation: glue curing and X-ray cleaning

Large leakage currents (~20–1000 nA between 1900–2000 V) were observed in few cases when applying high-voltage to the straw tubes, in one case not even allowing to reach the operating point. Enclosed humidity during polymerization is believed to be the culprit, since the problem disappears after *baking* the gas-monitor at 40–50°C, usually done over a night.

Because the risk of a trace contamination of detector parts, primarily of the straws, cannot be dismissed, a precautionary cleaning process was carried out for all gas-monitors. During the cleaning run, straws are exposed in the first few centimetres on the gas inlet side to X-rays of energy 6-10 keV. Fluorine radicals, created in the CF_4-containing gas mixture, are able to attack possible wire deposits along the gas flow direction. It has become an established procedure to recover straws with degraded amplitudes from silicone-based or hydrocarbon-based wire deposits within hours (Figure 5-10). A prophylactic *X-ray cleaning run* for about 20 hours therefore seemed a reasonable precaution before operating the gas-monitor.

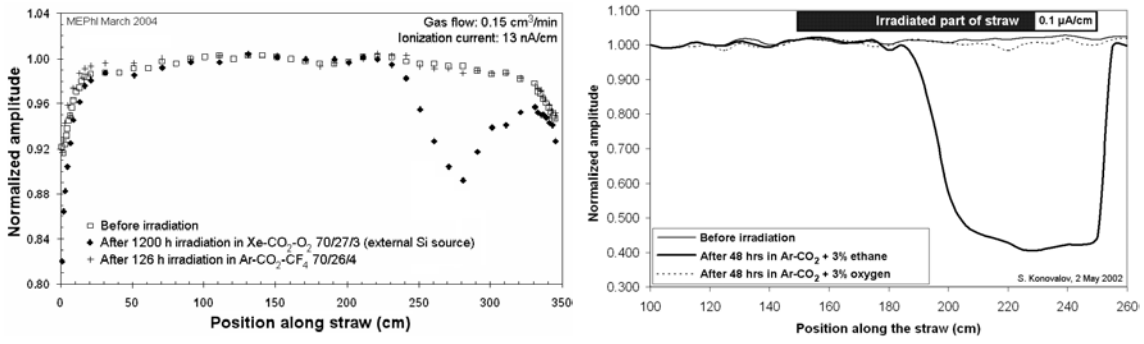

Figure 5-10 *Left*: Cleaning with a CF_4-containing mixture. Silicone introduced from an external source leads to ageing in the standard oxygen mixture. The amplitude is recovered within 125 h running under irradiation in a mixture with 4 % of CF_4.

Right: Example of the cleaning effect of the Ar-CO_2 + 3 % O_2 mixture. The straw was previously operated with 3 % of ethane instead, which led to deposits of hydrocarbon nature. Exposing the straw afterwards for 17 h to irradiation with the O_2-mixture recovered the amplitude. However, the oxygen mixture is not effective in removing silicon-based wire deposits.

5.4 Ageing tests parameters and methods

J. Kadyk has already discussed in Ref. [76] the variety of physical parameters, which have more or less significant impact on ageing in wire chambers. The fact that some parameters are interdependent and that their consequential effects operate in different directions with respect to ageing rate manifests in the generally poor reproducibility of ageing experiments. In the following paragraphs, observations that were made during the ageing runs are presented and discussed together with present knowledge [77][78][76][79][80][81], which may well be speculative in some cases. The method of determining the amplitude degradation during the ageing runs is described at the end of this section.

5.4.1 Operating gas

The property of many hydrocarbon-based gases to break up under irradiation and to polymerise to longer chains of non-volatile compounds rendered them unfavourable as quenchers in the high irradiation environment, that most present gas detectors in high-energy physics are exposed to. The remaining options are few, among the most popular ones are CO_2 or CF_4. Still, the ageing-etching competition process of fluorine-containing gases is not always under sufficient control to remain a fool-proof solution for gaseous detectors. The ability of the very reactive fluoro-based species to remove various types of wire deposits is beneficial. However, at the same time, they remain hostile to many materials used in the detector construction (e.g. epoxy, compounds, fibre-glass, plastics) and the long-term risk for the detector and gas system remains unassessable and uncertain[1].

5.4.2 Gas gain

A decrease of the ageing rate at higher gains is usually observed and explained with the increased charge densities and avalanche temperature. Space charges weakening the local electric field would disfavour the creation of ions and radicals, while at higher temperatures polymerization and condensation of non-volatile polymers on the wire is suppressed. However, the gas gain in the presented validation and ageing runs was held constant at 10^4 (with an uncertainty in the region of 10-20 %), and requires no further attention at this point.

5.4.3 Gas flow

An increased gas flow is generally found beneficial. It depletes the system of ambient oxygen and water and tends to flush out harmful long-lived radicals or ions. At the same time it is also obvious that it boosts the possible influx of contaminants from polluted or outgassing system components and materials. In the case of the TRT, nominal operating conditions are one volume exchange per hour (henceforth abbreviated “vol/h”). Acceleration of ageing in the TRT straw tubes at large gas flows (Figure 5-19) has been demonstrated in various occasions [73].

5.4.4 Detector geometry

Important for break-up and polymerization processes besides gas composition and flow rate is the configuration of the electric field and the active volume. In some ageing tests an ultra-clean stainless-steel single wire proportional chamber (SWPC)[2] was used beside the gas-monitor for reference measurements. For both straw tubes and the SWPC, the close field around the anode wire is equal, so that plasma processes are assumed to be comparable. The latter detector, however, offers a large drift region where pollutants can

---

[1] Most of the gaseous detectors of the LHC experiments have eventually banned CF_4.

[2] Provided by F. Sauli and L. Ropelewski (CERN Gas Detectors Development group).

effectively “act” through electron attachment, dissociative processes or catalytic behaviour. For example, a strong deterioration of energy resolution in the SWPC with only a few tens of centimetres of polypropylene tubing, which is transparent to ambient humidity, was observed. Stainless-steel tubing and a sufficiently large gas flow rate (3 litres resp. 40 vol/h) was indispensable to remove omnipresent oxygen from the system.

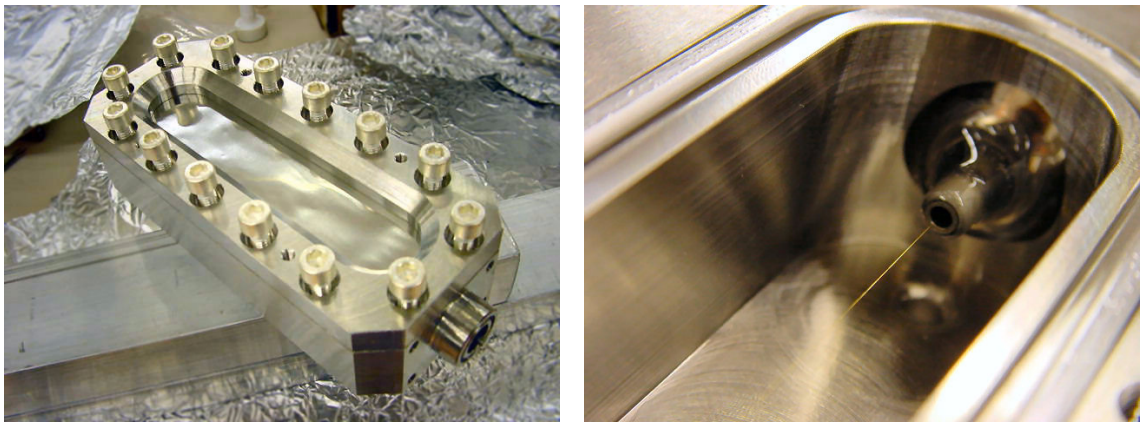

Figure 5-11 The stainless-steel single proportional wire chamber[a] used in some ageing setups.

a. courtesy of Gaseous Detector Development (GDD) group at CERN (F. Sauli, et al.)

5.4.5 Irradiation conditions

The idea that radiation intensity (dose rate) influences the ageing rate is true, if one contests the assumption that at both high and low dose rates plasma and gas come into equilibrium between ionizing events [76]. The legitimation in ageing tests to accelerate the accumulation of the total charge, that a detector would collect normally in its many years of operation, has often been contested [79]. However, this practice remains inevitable for obvious reasons. In the investigated regime of dose rates (0.1-10 nA/cm), fast ageing at both low and high rates has been seen. These are observations from the various tests and not results of a systematic study on dose dependence. Parameters that have not been changed in the presented test, were the energy and nature of the radiation exposing the straws. All ageing runs reported henceforth have been set up with ^{55}Fe sources, which yield X-rays of 6 keV energy.

5.4.6 Amplitude measurement in the ageing runs

As an alternative to monitoring ageing processes by measuring currents during X-ray irradiation, it was decided to record ^{55}Fe pulse height spectra, last but not least because the relatively small total current of a few nA obtained with these sources are poorly resolved at the accuracy of the used high-voltage module (1 nA).
The mean amplitude of the argon peak in the ^{55}Fe spectrum is determined automatically by a Gaussian fit in the on-line program. Each single spectrum can be stored if desired.
There have been two approaches to correct for non-ageing related amplitude variations which are due to changes of atmospheric conditions. Initially the amplitude from a heavily irradiated straw was normalised to the amplitude of a *reference straw*, a straw exposed to a weak source. The irradiation rate of the reference straw was believed to cause no degradation in the time frame of the test. However, at a later stage it was observed, that, under certain conditions, ageing occurred already at rates as low as 10 Hz/mm. The “reference straw approach” proved inapplicable in this case. Thereafter the *measured* amplitude was *normalised* to an “*expected*” amplitude, calculated by accounting for changes only due to the measured pressure and temperature fluctuations.

Two parameterisations of gas gain were tested:

1. The *exponential* parameterisation takes into account, that the Townsend coefficient scales with T/p:

$$G_i = A \cdot e^{B\frac{T_i}{p_i}} \tag{5.2}$$

The parameters *A* and *B* are retrieved from an exponential fit of the amplitude vs. *T/p* data in an unbiased period of the run, i.e. where no ageing is expected (see Figure 5-12)

2. If pressure and temperature fluctuations are small, one can also perform a *linear* fit of the amplitude vs. T/p data following the approximation:

$$G_i = A\frac{T_i}{p_i} + B \tag{5.3}$$

The feasibility of the parameterisation methods can easily be seen in Figure 5-12. Eventually ageing is verified by wire scans and possibly by analysis of the anode wire (see e.g. section 5.5.3)

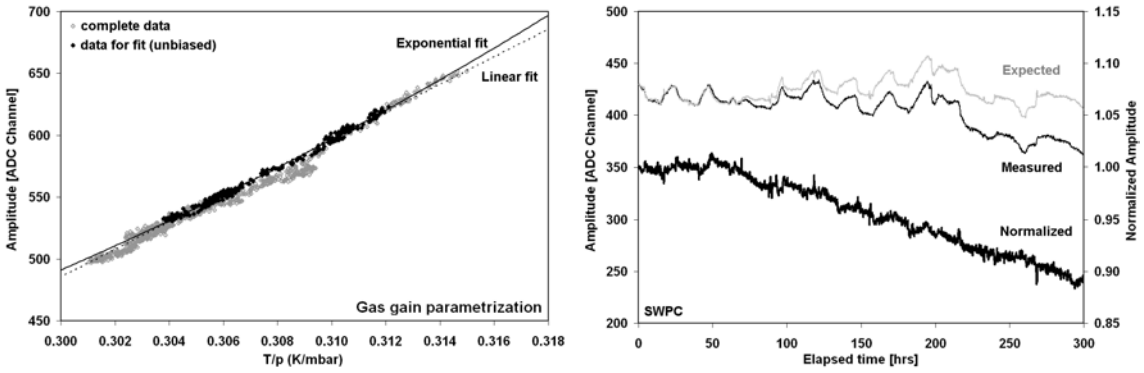

Figure 5-12 Gas gain parameterisation through linear or exponential fit of unbiased amplitude vs. T/p data (left). The amplitude can thus be predicted with the help of the gain parameterisation and the knowledge of temperature and pressure at a certain point in time. A normalization of the measured to predicted gain reveals ageing-induced amplitude degradation (right).

5.5 Ageing and validation runs - results

The choice of gas for the Wheel Test Station (WTS) runs was initially Ar-CO_2-CF_4 63/27/10. It shows similar properties to the former Xe-based, CF_4-containing operating gas in terms of discharge stability, wire offset sensitivity and ageing suppression. In the course of research and development activities the ternary mixture was replaced by the common binary gas composition Ar-CO_2 70/30, exhibiting the same wire offset sensitivity at the cost of ageing robustness (compare Figure 4-28 and Figure 6-25). With the absence of the etching capabilities of fluorine compounds created in the avalanches, a higher susceptibility to polymerizing pollutants was expected, and eventually experienced. From this point on, the validation of gas system components has become more sensitive, knowing that polymerization processes are not suppressed in the binary gas mixture. During the WTS runs irradiation exposure time is short (1-2 minutes) and gas gain reduced (10^4), minimizing the risk of discharges or ageing.
A schematic illustration of the setup that was used in many ageing and validation runs is shown in Figure 5-13.

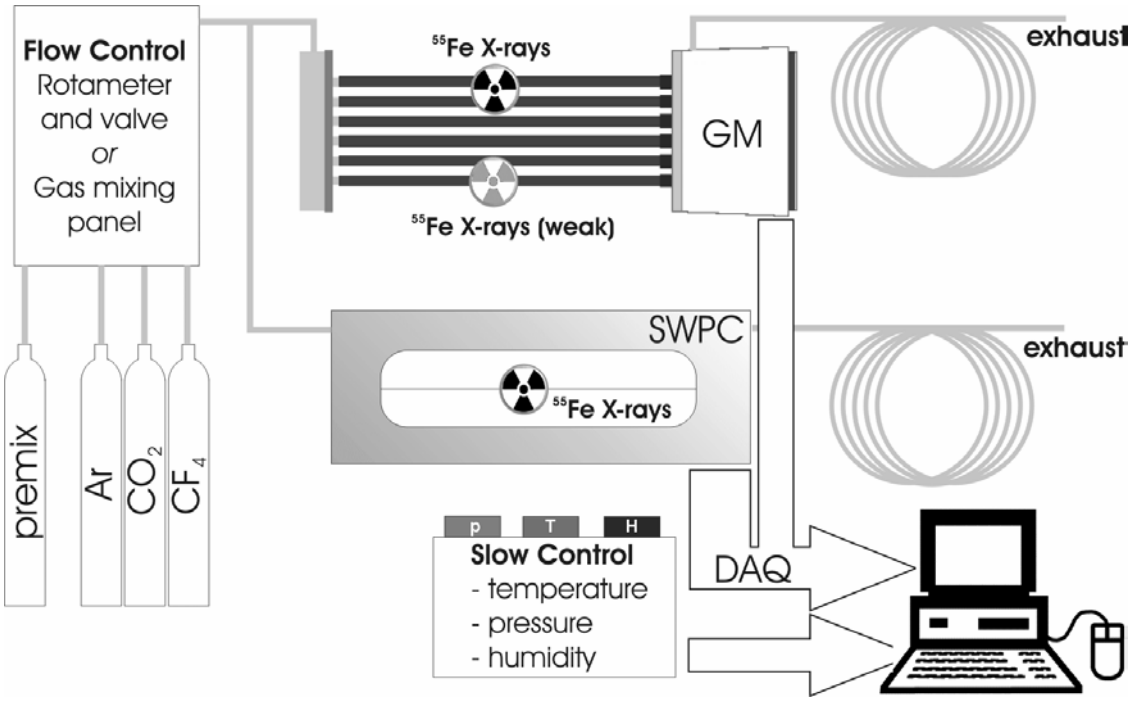

Figure 5-13 Schematic view of a common ageing setup.

For ageing tests with the binary mixture Ar-CO_2 70/30, it is convenient to use premixed gas eliminating mixing as another possible source of error or uncertainty. There still exists the possibility to mix custom gases at the 3-component mixing station. Flows are regulated in various stages. In-line pressure regulators avoid instabilities introduced by load on other gas outlets. The electronic mass flow controllers allow exact mixing and a microvalve at the mixer outlet permits fine adjustment of flow. To minimise back-diffusion of ambient air into the straws at low gas flows, 2 m long exhaust pipes are connected at the gas outlet.
The irradiation conditions were varied during tests to study the dependence on rate and exposure spot size, within the limits given by the aperture of the available ^{55}Fe sources. The irradiation of a single straw at very low rate was initially used for reference measurements. After observing ageing even under those rate conditions, the method was abandoned (discussion in section 5.4.6).

The preamplifier/shaper and the ADC to process the straw signals are described in 5.3.5. Ambient parameters like temperature and pressure are needed for the gas gain parameterisation and they are constantly monitored. Similarly the ambient humidity level is recorded. A standard PC acquires, saves and displays all parameters through a LabVIEW® module, allowing fast on-line checks. More precise ageing monitoring is done in frequent off-line analyses.
A few runs were performed in combination with a single wire proportional counter (SWPC), both as principal and as a reference detector. A great advantage is the inertness of this particular SWPC, a counter entirely built of stainless steel and glass, unlike the gas-monitor, which has printed-circuit board material (epoxy-glass-fibre composite), glue and the inner layer of the straw tubes exposed to the active gas. The standard 31 µm diameter Au-plated tungsten anode wire for both counters was taken from a TRT production batch. The SWPC has been operated both in parallel flow configuration and downstream of the gas-monitor.
In the following paragraphs, a number of selected validation runs are described, illustrated and briefly discussed. They were used to verify gas system cleanliness and to help understanding the ageing behaviour of the acceptance test gas in the detector modules.

5.5.1 Validation of a gas mixing panel using Ar-CO_2-CF_4 63/27/10

In the first validation runs, the gas-monitor operated with the ternary mixture that was used at that time for the straw straightness measurements, Ar-CO_2-CF_4 63/27/10. The run was set up to validate the cleanliness of a gas mixing panel, which had been assembled of various gas system components like in-line pressure regulators, valves and mechanical rotameter flow-meters (see section 5.2.2). All components were cleaned beforehand to remove any grease or lubricants, frequently used in valves and flow-meters.

Setup

The gas flow rate for the test was 200 ml/h, corresponding to 18 vol/h. By placing the gas-monitor inside a Styrofoam-padded box, temperature fluctuations around the detector, caused by the regulation cycle of the laboratory's air-conditioning system (± 2-3°C), are reduced to $\Delta T \sim 0.03$°C on a small time scale (minutes) resp. $\Delta T \sim 0.75$°C at long term, as shown in Figure 5-14. Five straws were irradiated with X-rays of 6 keV energy from ^{55}Fe sources, over different lengths and at various rates (Table 5-IV). The amplitude from the straw with the lowest irradiation rate was used as a reference to compensate temperature and pressure fluctuations.
The gas gain in the straw tubes was adjusted to 10^4. A calibration pulse (Figure 5-14), injected into the electronics chain and recorded together with the spectrum was used to monitor single channel pedestals.

TABLE 5-IV Validation run with CF_4-containing triple mixture (gas panel)

Ageing counter	**Gas-monitor #1**
Operating gas	Ar-CO_2-CF_4 63/27/10 premixed
Gas flow	20 vol/h
Operating voltage	-1430 V (gain ~10^4)
^{55}Fe irradiation rate (irrad. spot size)	Straws #1, #3 4 kHz (8 mm) Straws #5, #6 1 kHz (3 mm) Straw #4_{ref} 800 Hz (8 mm)
Run time	516 h

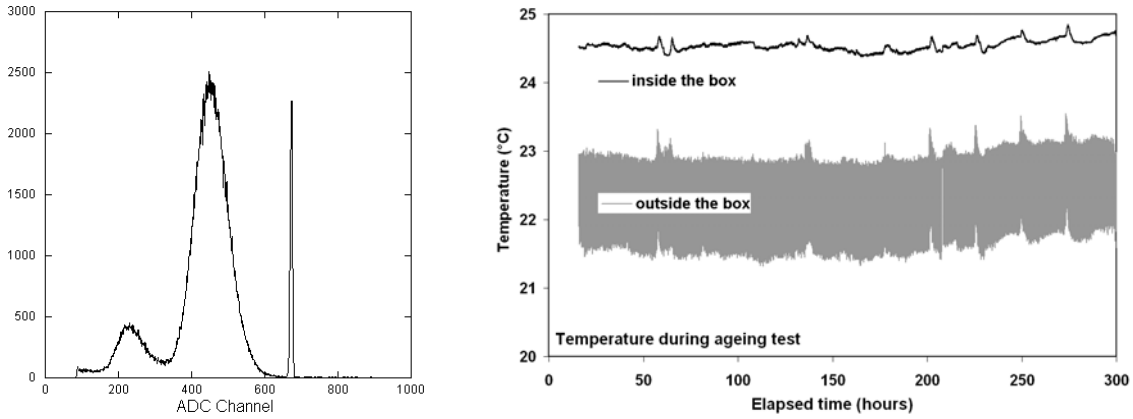

Figure 5-14 Typical ^{55}Fe spectrum in the straw, showing the small escape peak, the main argon peak and a narrow calibration pulse peak (left). Temperature fluctuations around the gas-monitor are greatly reduced with the help of a styrofoam box (right).

Results and discussion

After more than 500 hours, no degradation of the normalised amplitudes of any straw was found. Moreover the absence of ageing is confirmed by following wire scans (Figure 5-15). Single channel pedestal variations are significantly smaller than 1 % compared to an amplitude measurement accuracy of 1-2 % (depending on statistics).

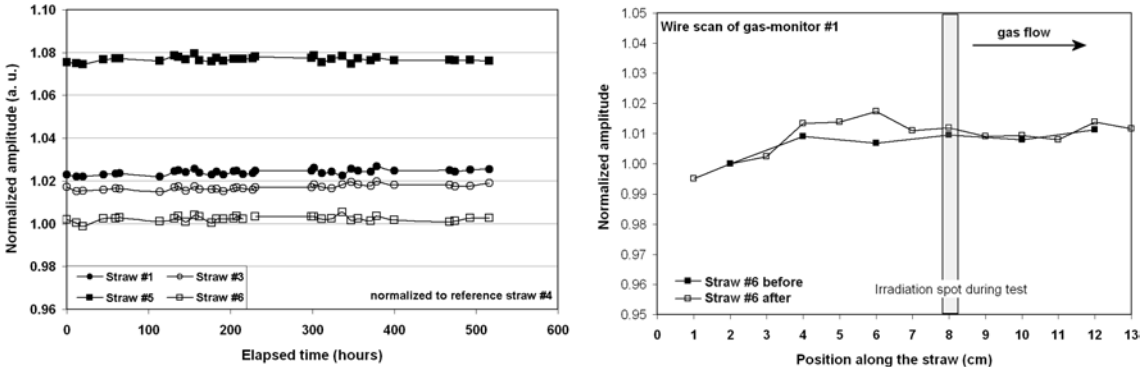

Figure 5-15 Normalised amplitudes (left) and wire scans (right) do not indicate any ageing processes to take place.

Similar to the validation of the gas mixing panel, the stainless steel piping of the acceptance test laboratory was tested for pollution in a nearly 500 h ageing run. In the last 140 h

the gas was changed to the more ageing-sensitive mixture Ar-CO_2 70/30, but, no amplitude degradation was observed.

5.5.2 Validation of electronic mass flow controllers using Ar-CO_2 70/30

Three electronic mass flow controllers have been acquired and used as before; however, under insufficiently known conditions. In this case, validation of cleanliness was indispensable, in order to avoid an irreversible pollution of the end-cap wheels.
The gas-monitor setup was extended by mounting the single wire proportional counter (SWPC) in the parallel flow configuration. The larger conversion volume in the SWPC, with a cathode-to-wire drift distance of 25 mm (unlike the 2 mm radius of the straw), offers an increased sensitivity to any "pollutant". Its sensitivity was immediately noted with the plastic gas inlet tubes which are transparent to water vapour from ambient humidity. They were replaced by stainless steel pipes. The flow rate had to be at least 100 vol/h, in order to deplete the gas volume in the SWPC of air and humidity, and to achieve reasonably resolved ^{55}Fe spectra. In the SWPC high-voltage is applied to the anode wire with the case remaining at ground potential. An equal signal amplitude corresponding to a gas gain of 10^4 is reached at +2000 V. Two straws of the gas-monitor and the single wire in the SWPC were exposed to 6 keV X-rays over a few mm at rates of 1-2 kHz/mm.

TABLE 5-V Second validation run with Ar-CO_2 70/30 (el. mass flow controllers) using SWPC

Ageing counter	**Gas-monitor GM#3 + SWPC (in parallel)**		
Operating gas	Ar-CO_2 70/30 premixed		
Gas flow	2-4 vol/h in the GM and 100 vol/h in the SWPC (7 l/h total)		
Operating voltage	-1340 V (GM) and +1990 V (SWPC)		
^{55}Fe irradiation rate (irrad. spot size)	Straw #3 Straw #5 SWPC	11 kHz 6 kHz 10.5 kHz	(~5 mm) (~5 mm) (~5 mm)
Run time	477 h		

At a first glance, the plots in Figure 5-16 show no obvious deviation from the expected amplitude during almost 500 hours under irradiation. Still, the more accurate wire scans reveal an amplitude loss region, slightly downstream the irradiation spot in the SWPC, at a level of 1.5 %. For the straw tube wires, signs of gain loss in the irradiation area are not conclusive, amplitude changes range too close to the measurement accuracy of 1 %.

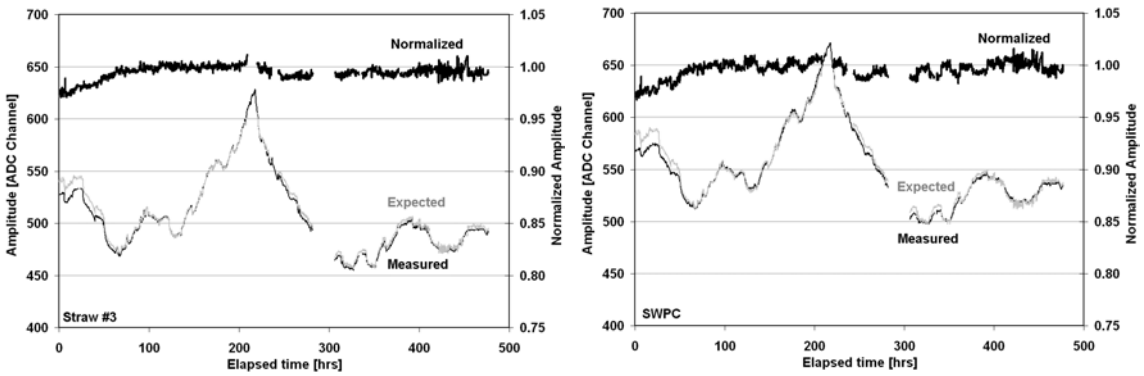

Figure 5-16 Amplitude behaviour in the gas-monitor (left) and the SWPC (right) during the run.

The results comply with the desired degree of cleanliness for the WTS gas system. The reader is reminded that a straw during straightness measurement runs is exposed at six wire positions for only 1 minute at comparable irradiation conditions and at the nominal gas flow of only 1 vol/h.

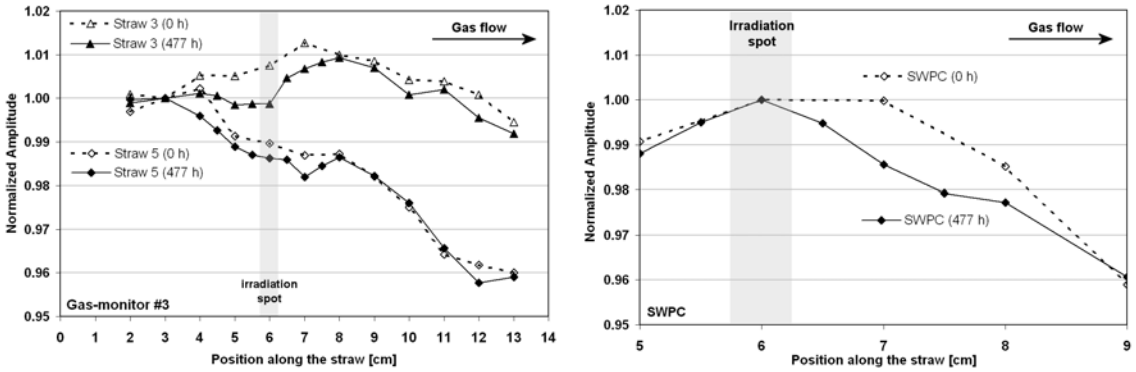

Figure 5-17 Wire scans in the gas-monitor (left) and of the SWPC wire (right) reveal onset of ageing.

In retrospect, the larger volume and higher gas flow in the SWPC favour polymerization processes and, as such, a faster loss of amplitude. Furthermore one can see that the large gas flow moves the point of wire deposition downstream of the irradiation zone.
In general, remnant traces of ageing-relevant contaminants can be found, if the ageing run parameters (flow, detector geometry) are adjusted accordingly. In this particular case, the level of contamination is not significant at the operating conditions used for straw straightness measurements at the WTS.

5.5.3 Ageing run in Ar-CO_2 70/30 with the gas-monitor

To achieve a better understanding of the ageing behaviour of Ar-CO_2 70/30 in the TRT straw tubes and to identify possible sources of pollutants, the ageing test gas system for the following run was minimised. Using premixed gas it was reduced to a pressure regulator, a rotameter and a micro valve, all gas components that were previously validated (as described in 5.2.1). The gas-monitor used was running already for 153 hours in “monitoring” mode during WTS runs, at gas flow rates of 5 vol/h up to 10 vol/h. In monitoring mode, the gas-monitor flow changes according to the gas flow of the WTS, being connected to its gas system.
After connection to the ageing setup, the gas-monitor flow rate was increased by more than an order of magnitude, to ~150 vol/h, while adding two additional X-ray sources irradiating straws at a lower rates. Again after 100 hours the gas flow rate was changed to 400 vol/h. Exact details of the setup are given in Table 5-VI.

TABLE 5-VI Double mixture (Ar-CO_2 70/30) ageing run with gas-monitor only

Ageing counter	**Gas-monitor #3**		
Operating gas	Ar-CO_2 70/30 premixed		
Gas flow	1.5 - 4 l/h (~150-400 vol. ex./hour)		
Operating voltage	-1340 V (gain ~10^4)		
^{55}Fe irradiation rate (irrad. spot size)	Straw #1	2.5 kHz	(10 mm)
	Straw #2	**500 Hz**	**(10 mm)**
	Straw #3	**3.4 kHz**	**(3 mm)**
	Straw #4	4.6 kHz	(3 mm)
	Straw #5	1.4 kHz	(3 mm)
Run time	Straws #1, #2:	167 h at 150-400 vol/h	
	Straws #3 - #5[a]:	153 h at 5-10 vol/h, 167 h at 150-400 vol/h	

a. Straws #3 - #5 were operated already 153 h in WTS monitoring mode before the start of the dedicated ageing test.

Within less than 50 hours after the start of the test, an amplitude degradation due to ageing is observed in all straws (Figure 5-18), most notably in the ones under low irradiation rate, but with the larger irradiation spot size. This confirmed the earlier observation that even at the lowest irradiation rates fast amplitude loss can occur. Secondly, it leads us to the observation, that one of the conditions favouring ageing are large flows (Figure 5-19). While often sufficiently high flow rates are chosen to eliminate remnant nitrogen, oxygen or humidity from the detector, they can introduce simultaneously outgassing contaminants, e.g. from glues, lubricants or greases, at a higher rate into the active volume. Still, as mentioned before, the detector was connected to a minimal gas system, which exceeds the usual standards of cleanliness.

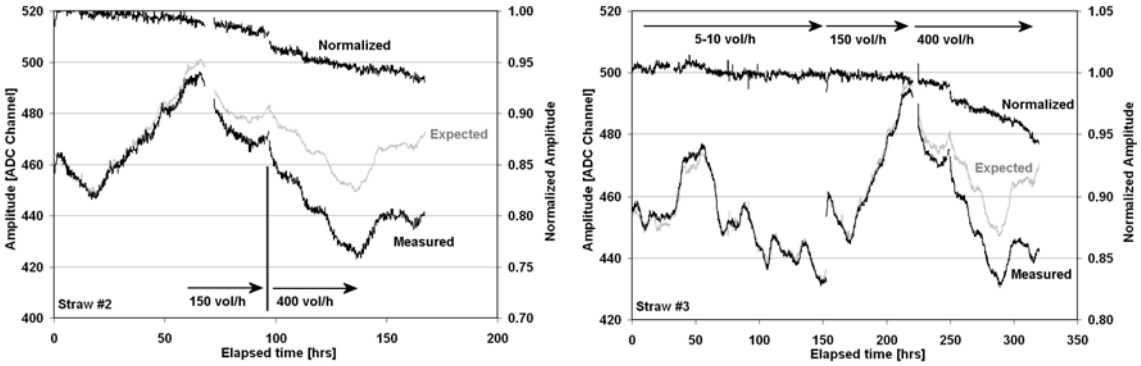

Figure 5-18 Amplitudes of straw #2 (left) and straw #3 (right).

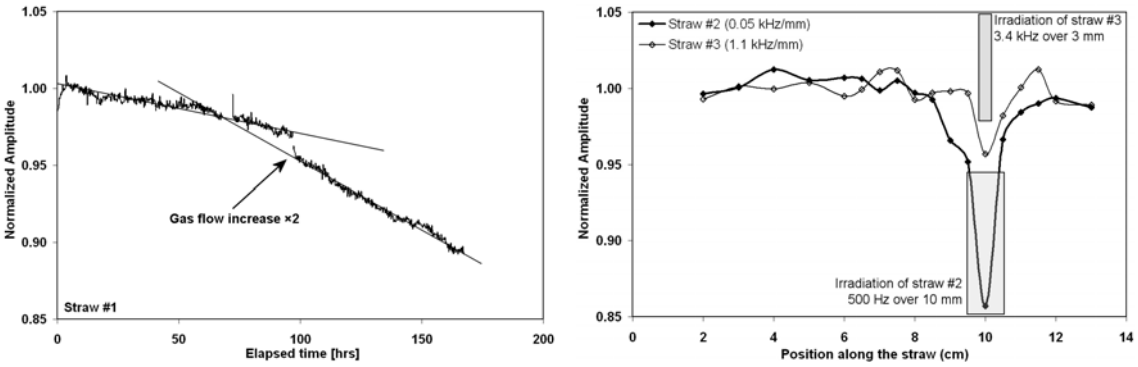

Figure 5-19 The ageing rate clearly depends on gas flow (left). The local amplitude drop can be seen in the wire scans (right).

To identify the deposit, the wire of straw #1 was removed and submitted for an Energy Dispersive X-ray (EDX) analysis in conjunction with a Scanning Electron Microscope (SEM). A non-conductive film was found on the wire surface, only visible through the charging-up during electron beam exposure in the microscope (Figure 5-20). It is presumably of hydrocarbon nature, undetectable with the EDX (thickness < 100 nm) [82]. A positive outcome remains, that no traces of silicon, much more worrying for the TRT, were found on either wire or inner straw tube surface.

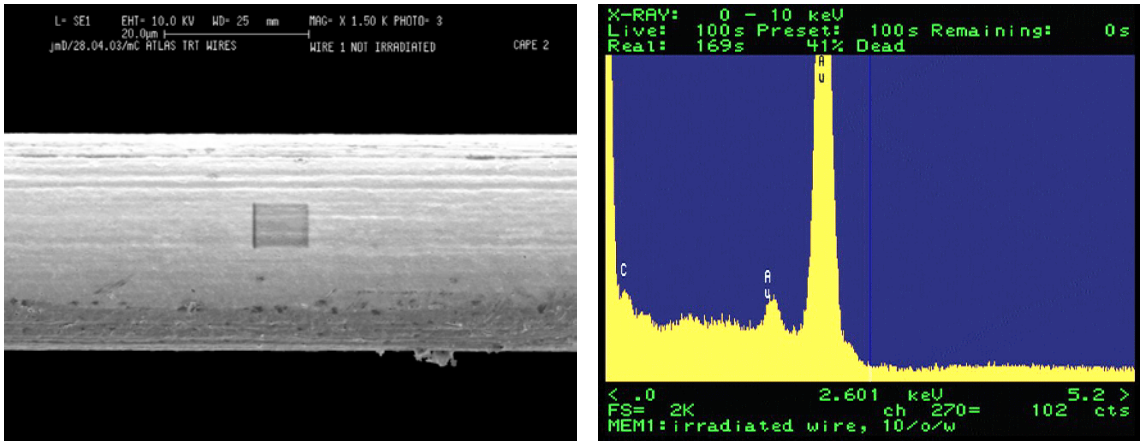

Figure 5-20 The SEM picture (left) shows a charging-up of the wire surface by the electron beam, which is due to a non-conductive layer, of thickness less than 0.1 µm. No silicon traces are found in the EDX analysis, the deposit is possibly of hydrocarbon nature, undetectable with this method (right).

5.5.4 Ageing runs in Ar-CO_2 70/30 with the gas-monitor and the SWPC

In the course of validating the acceptance laboratory gas system, and in the face of abandoning CF_4 as an additive, the motivation of the tests changed towards a more fundamental understanding of ageing processes in the gas-system-detector regime. Moreover the source(s) of the hydrocarbon pollution, found in the previous run (5.5.3), had not been identified at this point. In any case this level is not considered dangerous for TRT operation.

There is little reason to exclude contaminants outgassing from within the gas-monitor. A two-stage setup was prepared, with the SWPC playing a decisive role. The setup was planned according to the following reasoning. If in parallel flow configuration both gas-monitor and SWPC would exhibit amplitude degradations, the origin of the contamination must be found in the gas system. However, if the more sensitive stainless steel counter would suffer no ageing, the gas-monitor remains the culprit, which could then be verified in the second stage, in which the SWPC is mounted downstream of the gas-monitor, to examine its exhaust gas (Figure 5-21). An SEM and EDX analysis would eventually round off the picture.

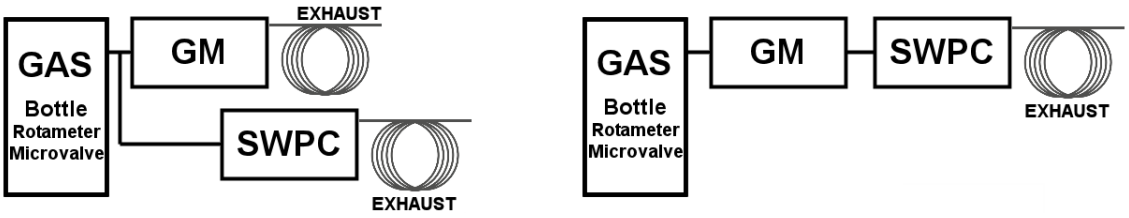

Figure 5-21 Running in parallel configuration probes for pollution in the gas system (left). If only the gas-monitor exhibits ageing it could be outgassing from within, which is verifiable by placing the SWPC downstream and operate it with the exhaust gas of the gas-monitor (right).

Parallel setup

The flow of premixed Ar-CO_2 70/30 was adjusted to 10 l/h total, shared in equal parts by both devices, which results in different volume exchange rates in the two detectors (the gas volumes of the gas-monitor and the SWPC are approximately 10 cm^3 and 60 cm^3 respectively). After the occurrence of ageing the flow rate was doubled for about a 100 h, to reconfirm the flow rate dependant ageing rate. Details of the setup are given in Table 5-VII.

TABLE 5-VII Ar-CO_2 70/30 ageing run with SWPC and gas-monitor in parallel

Ageing counter	**Gas-monitor #3 + SWPC (parallel)**
Operating gas	Ar-CO_2 70/30 premixed
Gas flow	5-10 l/h (500-1000 vol/h for GM) (80-160 vol/h for SWPC)
Operating voltage	-1340 V (GM) and -1990 V (SWPC)
^{55}Fe irradiation rate (irrad. spot size)	Straw #3 6.8 kHz total (2-3 mm) Straw #6 1.4 kHz total (2-3 mm) SWPC 11 kHz total (~15 mm)
Run time	482 h[a] (620 h)

a. Loss of slow control data after 482 h.

The amplitude jitter in the gas-monitor during the initial 176 h (Figure 5-22) was caused by a faulty power supply, which did not render the run data unusable, since amplitude fluctuation during this time remained at a level of 5-10 %. Recording of slow control data failed after 480 h, but irradiation continued for another 140 h. The stable performance of the SWPC in the first 480 h, in contrast to 3-5 % amplitude loss in the straws, suggested the absence of pollutants in the gas system. Because no significant amplitude degradation was expected until the end of the run, the straw amplitudes were normalised to the SWPC amplitude, as shown in Figure 5-23. The faster ageing rate at higher gas flows in the straws is evident as observed already in the earlier run (Figure 5-19).
Now that the absence of ageing confirms the high degree of gas system purity, it had to be verified that the gas-monitor itself lost its ageing-resistance, however, under considerably boosted operating conditions (more than 10^2 times nominal flow and 10^4 times usual exposure time!).

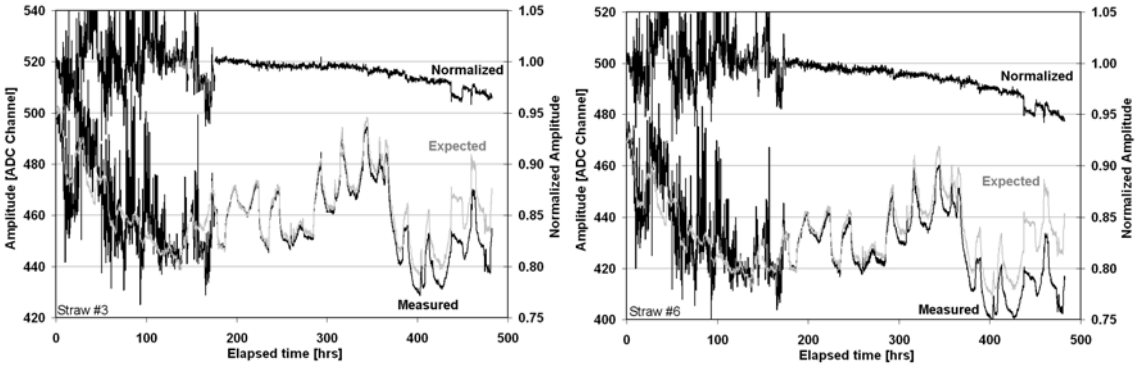

Figure 5-22 Amplitude behaviour in two straws of the gas-monitor. During the first 175 h the run was suffering high-voltage instabilities from a broken power supply, causing 5-10 % of gain fluctuations. However, it had no significant impact on the outcome. The expected amplitudes determined with the gain parameterisation are shown in light-grey.

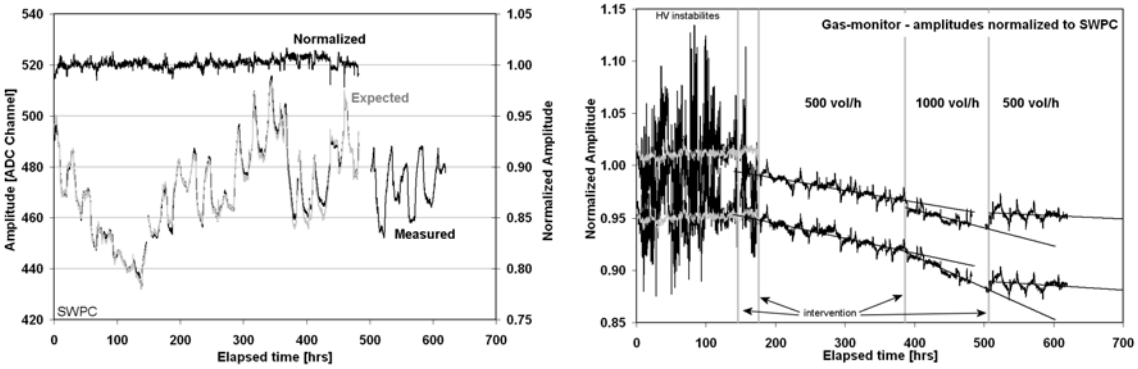

Figure 5-23 The normalised amplitude behaviour of the SWPC remains stable over 500 h (left). An acceleration of amplitude degradation at higher gas flows is seen in the gas-monitor straws (right) In this plot the straw amplitude are normalised to the amplitude of the SWPC.

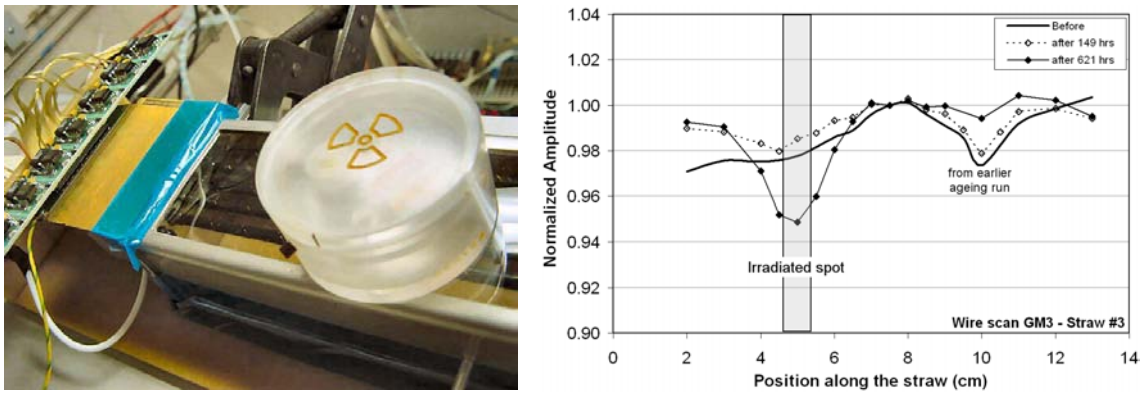

Figure 5-24 Gas-monitor under ^{55}Fe X-ray irradiation during the ageing run (left). The wire scan of straw #3 shows a 5 % amplitude drop in the irradiated region (right).

Serial setup

The suspicion that the contaminant, deposited in the straws, outgassed from gas-monitor material itself, could be verified by relocating the SWPC downstream of the gas-monitor, to "examine" its exhaust gas. The detailed settings of the second stage of the ageing run are listed in Table 5-VIII.

TABLE 5-VIII Ar-CO_2 70/30 ageing run with SWPC and gas-monitor in series

Ageing counter	**Gas-monitor #3 + SWPC (downstream)**
Operating gas	Ar-CO_2 70/30 premixed
Gas flow	10 l/h (~1000 vol/h for GM, 160 vol/h for SWPC)
Operating voltage	-1340 V (GM) and -1990 V (SWPC)
^{55}Fe irradiation rate (irrad. spot size)	Straw #3 7 kHz total (30 mm) Straw #6 7 kHz total (30 mm) SWPC 11 kHz total (3 mm)
Run time	497 h (GM) resp. 811 h (SWPC)

The total flow rate of 10 l/h was left unchanged and thus the gas flow for both detectors doubled in the serial mode. This would favour an accelerated amplitude degradation, as seen in the first stage during 100 hours under this flow rate. The ^{55}Fe sources were used without collimation exposing the last 30 mm of wire and tube at the gas outlet side of the straws, so that composites created in the irradiated volume would more likely escape into the SWPC volume.

As a result, a quick degradation of the amplitude in the stainless steel counter, beginning already after 75 hours, was measured, at a steady rate of about 5 % per 100 h. After 500 h the high-voltage of the gas-monitor was switched off and the X-ray sources irradiating the straws were removed, stopping possible radiation-induced build-up of compounds in the active gas. The amplitude degradation in the SWPC progressed at an unchanged rate for another 140 h. As a last step, the gas-monitor was removed out of the line, disallowing any delivery of compounds from the straw detector to the SWPC. After a further amplitude loss in the SWPC at a faster rate a partial recovery was observed (see Figure 5-25).

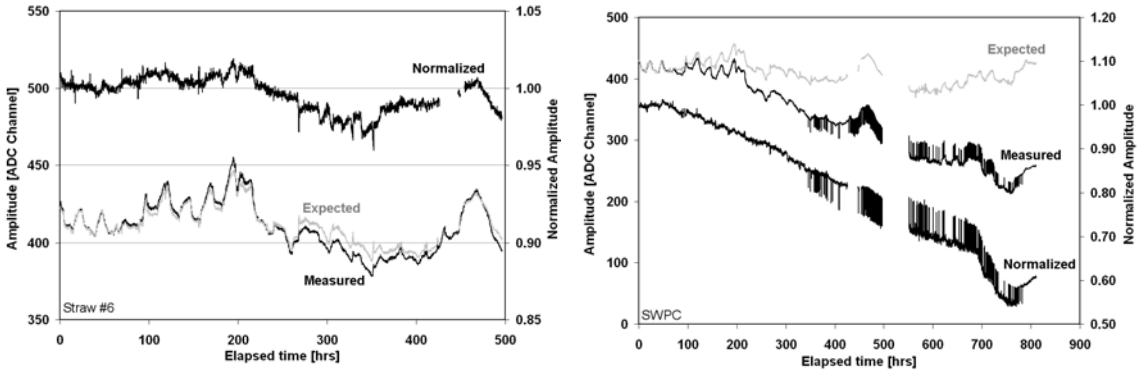

Figure 5-25 Ageing is seen in both the gas-monitor (left) and the stainless steel SWPC (right). After an interruption the SWPC continued ageing. The origin of the amplitude jitter starting after 350 hours has not been examined since it shows no significant influence on the principal result.

We conclude that the gas system does not introduce significant amounts of ageing sensitive pollutants and the actual source of contamination must be the gas-monitor's material, which exposed to the active gas, namely the active WEB (Kapton, glass fibre epoxy laminate FR4) or the inner straw walls (carbon-loaded polyimide).
Following amplitude scans along the straws and the SWPC, the wire from the SWPC was removed and submitted for inspection with the scanning electron microscope (SEM) and an energy dispersive X-ray analysis (EDX).

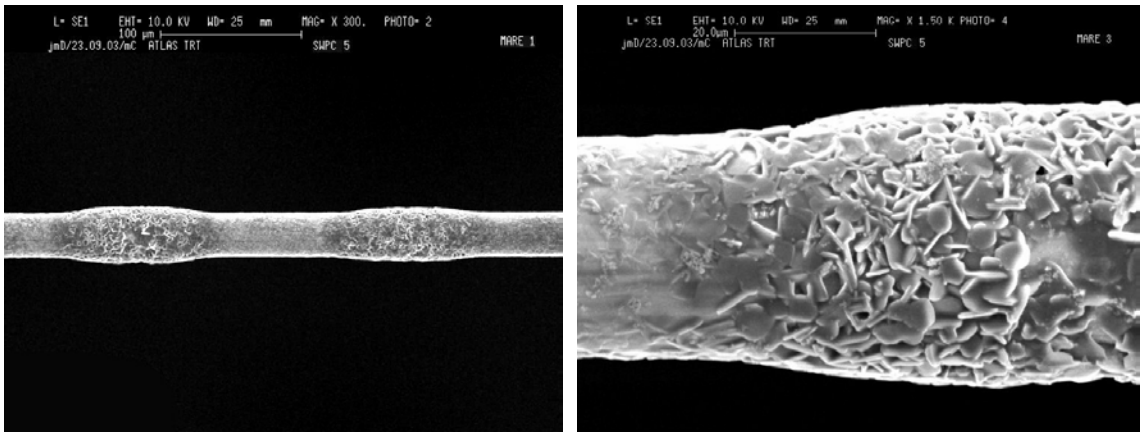

Figure 5-26 Wire deposits of crystalline nature.

Over the irradiated area of 3 mm, the SEM pictures show several equidistant spots of approximately 100 µm width, where a crystalline deposit has formed around the wire, increasing its diameter by 10 µm (Figure 5-26). The EDX analysis reveals a sulphuric component on top of the presence of hydrogen, carbon and oxygen (Figure 5-27). The gold coating remains unaffected, but is found to be covered with a thin layer of hydrocarbon based compounds and the sulphuric crystals.

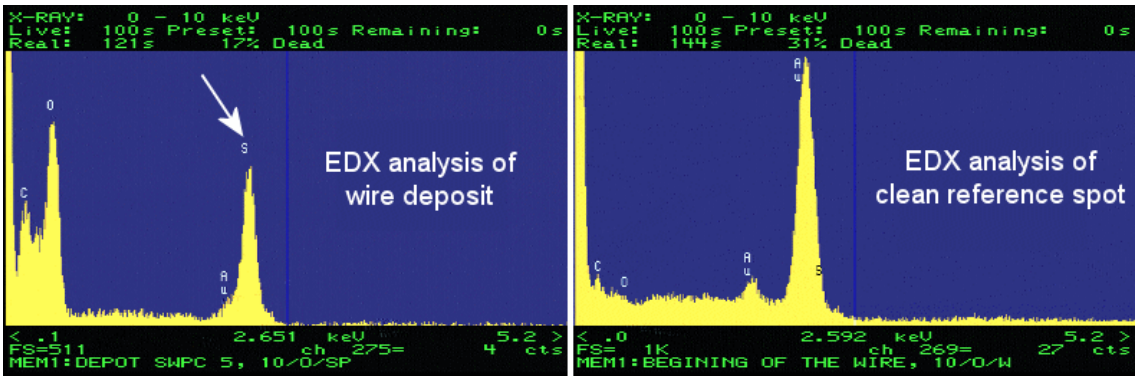

Figure 5-27 EDX analysis of the wire deposit in the SWPC. The crystalline wire deposit contains significant amounts of sulphur (left), absent in the reference spectrum from a clean wire spot (right).

The straw tube film - as a rather intuitive choice - was the first suspect for the source of sulphur. Although neither the Kapton film nor the polyurethane glue *per se* contain sulphur, residue of sulphur-containing lubricants (e.g. MoS_2) on the cylinders in the straw film production cannot be excluded. Therefore a fresh piece of the multilayer straw film was taken from a production roll and sent for EDX analysis as a reference. While at higher electron beam energies no sulphur was found, at very low energies a noticeable sulphur peak could be identified on the unprocessed film (Figure 5-28). Because at lower electron beam energy the penetration depth is small, it means the sulphur is deposited on the surface of the carbon layer.

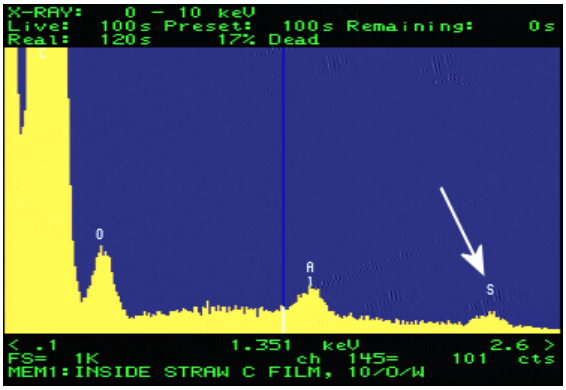

Figure 5-28 Traces of sulphur are identified on the carbon surface of unprocessed straw tube film (left).

Eventually, further effort to determine the source of the contaminant would go beyond the scope of this work. Again it shall be reminded that ageing phenomena of this kind are strongly suppressed at the operating conditions of the acceptance tests, as discussed with the results of the first stage of the ageing run. With the two-stage run the high purity of the acceptance test gas system is verified and the sensitivity of the setup is proven to be adequate to detect ageing reliably.

5.6 Conclusions

The TRT end-cap wheels (like the barrel modules) are subject to numerous, repetitive tests that involve flushing with gas (leak tightness) and applying high-voltage (long-term high-voltage test), and in the case of the Wheel Test Station (WTS) these are made even under irradiation (straw straightness measurement). The extensive quality checks during and after wheel production aim at delivering a highly reliable detector for installation in the ATLAS experiment, where access in the future will be complicated, tedious and very restricted, due to the compactness of the Inner Detector and the expected high radiation levels.

While the final recirculating active gas system is designed to remove effectively any pollutants from the operating gas, the open gas system arrangement in the production and acceptance sites is much simpler, but has to follow the same strict cleanliness criteria. It would be fatal to pollute the end-cap wheels already during production and testing. In order to first validate and then monitor the purity of the gas system, the *gas-monitor*, a small straw tube counter, has been developed, assembled and tested successfully. It was provided for the production sites in Russia and for the acceptance test laboratory at CERN. Apart from validation test runs, the gas-monitor was also used to study the ageing properties of the binary mixture Ar-CO_2 70/30, after it was chosen as the acceptance test gas.

A selection of validation runs and ageing tests is presented, that prove the adequacy of choice of gas system components and acceptance run conditions. In particular the selection of piping, fittings and valves could not be identified as sources of pollution, as the electronic mass flow controllers were shown to be sufficiently clean for use at the WTS.

It is shown that under the operating conditions at which the TRT straws are tested for straightness at the WTS, i.e. gas gain of 10^4, moderate gas flow (order of 1 vol/h) and irradiation (order of 10 kHz with 6 keV X-rays), the straws exhibit no ageing for many few hundred hours. This is a comfortable safety margin for the usual straw exposure time during tests which is of order few hundred seconds. The successful implementation of the stringent cleanliness criteria is borne out by the extremely low number of straws found to be locally affected by a gas gain drop, which can be attributed to wire pollution ($<10^{-4}$).

On the other hand, it is shown that wire ageing can be provoked and accelerated, especially by significantly increasing gas flow (by at least 1-2 orders of magnitude) and by using a more sensitive detector geometry (SWPC). While this proves the omnipresence of trace contaminants in a gas system, mainly of hydrocarbon nature, it has no implications on the detector safety for the TRT, but provided us with a better understanding of the various operating domains. In the high gas-flow ageing runs it proved inadequate to use a reference straw under low irradiation, in order to monitor the amplitude behaviour of strongly irradiated straws. Even in the reference straw tubes ageing was seen at X-ray irradiation rates as low as 10 Hz/mm.

CHAPTER 6

"Striving to better, oft we mar what‘s well."
William Shakespeare (1564-1616)

Acceptance Tests of the End-Cap Wheels

6.1 Introduction

The TRT consists of 96 barrel modules and 112 end-cap wheels, containing a total of 372 032 straw tubes. All modules and wheels have to pass a series of stringent acceptance tests before being equipped with front-end electronics and being integrated with the SCT barrel and end-caps. These tests have been designed to guarantee reliable operation over 10 years at the LHC. The TRT's functional units have to adhere to strict QA specifications based on which these tests are defined and conducted. While strict envelopes are required for smooth assembly and integration, local acceptance criteria such as wire eccentricity have considerable influence on the operational behaviour of each single straw. This behaviour has to be monitored closely since it might affect the functionality of the neighbouring straws, connected e.g. to the same high-voltage component or front-end ASIC.
The majority of the acceptance tests are conducted using the commonly used and easily available Ar-CO_2 70/30 gas mixture. It has been demonstrated that it represents a valid alternative to the costly Xe-based operating gas. Sufficient safety margins are guaranteed through strict acceptance criteria in order to compensate for the differences between the test and future operating mixture.
Tests are carried out at the assembly sites, followed by a full set of tests at CERN before wheels and modules enter the stage of final assembly with the front-end electronics. Test results are recorded in data bases and permanently fed back to the institutes engaged in the production.
In this chapter the acceptance test setups, methods and criteria are described in adequate brevity. Special attention is given to wire tension and straw straightness measurements as they presented a particular focus of acceptance work.
Detailed acceptance test procedures and specifications for the TRT end-cap wheels are described in Ref. [83].

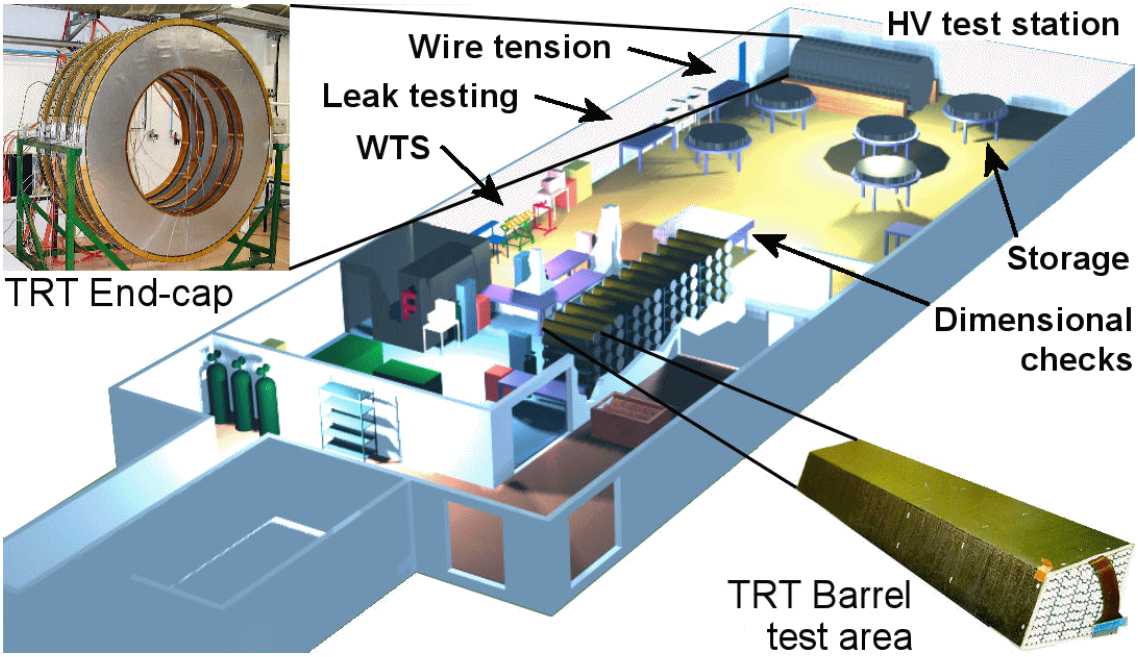

Figure 6-1 Artist view of the CERN TRT acceptance site (Building 154)

6.1 The gas system for the acceptance tests

The gas system associated to the *Wheel Test Station* (WTS) has been built with high purity components, which were carefully selected during extensive cleanliness validation runs. The process of "*validation*" is explained in more detail in section 5.2.1 and in Refs. [84] and [85]. Specially cleaned (electro-polishing, ultrasonic-bath) supply lines of stainless steel piping (stainless steel grade 316) feed the different gases from large batteries or bottles stored outside the test building to various outlets of the test stations inside. The operating gas for the WTS runs, Ar-CO_2 70/30, is prepared in a gas mixing station (Figure 6-2) where mixing ratios and flow rates are adjusted. The gas mixer is equipped with a panel, that holds in-line pressure regulators reducing the supply pressure of 5 bar to 2 bar. They connect to three electronic mass flow controllers (section 5.2.2), that regulate the required gas flow of the single gases, which are then fed to a mixing buffer volume and finally to various outlets. All components are connected through stainless steel pipes.

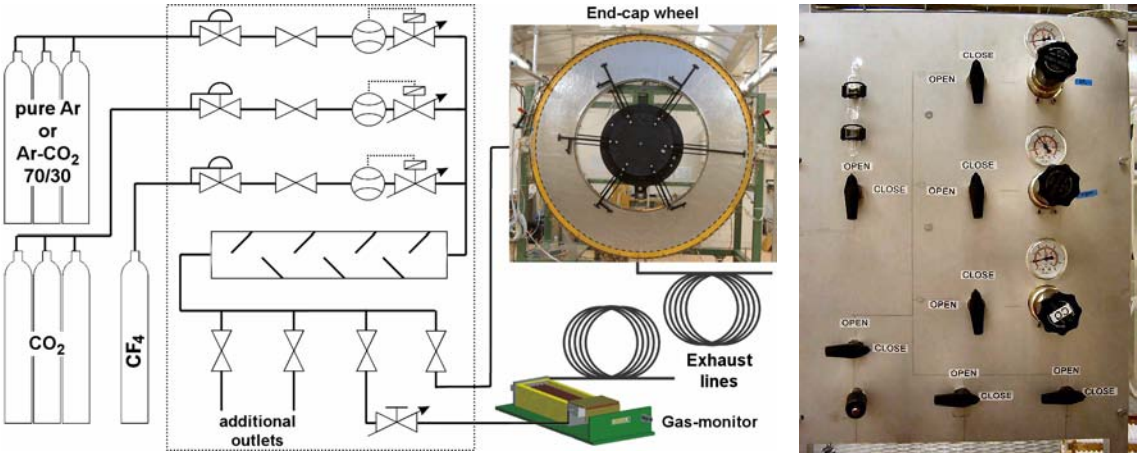

Figure 6-2 WTS gas system (left) and gas mixing panel (right)

The nominal flow for the TRT wheels is one volume exchange per hour. This corresponds to 20 or 40 l/h for a 4-plane resp. 8-plane wheel. On the gas mixing panel a line is branched off to feed a fraction of gas to the gas-monitor using a micro valve allowing fine adjustment of flow. The corresponding flow of 1 vol/h for the monitor counter accounts for approximately 10 ml/h, which can be tuned by counting bubbles at its exhaust. Sensitivity to extraneous pollution can be increased by boosting gas flow to multiple volumes per hour, desirable in particular cases.

6.2 Acceptance test stations

The acceptance test stations for both TRT barrel modules and end-cap wheels are accommodated in Building 154 at CERN. The two areas are separated and kept in clean and reasonably dust-free conditions. A schematic drawing of the building can be seen in Figure 6-1. The following paragraphs describe the various acceptance test setups and procedures, mostly for the end-cap wheels, although setups are similar for the barrel modules.

6.2.1 Dimensional test table

Considering the tight geometrical tolerances for the TRT, which is placed in between the SCT and Liquid Argon calorimeter, it is extremely important to comply with the given dimensional envelopes. The required precision for production and assembly of the TRT (Ø 2.2 m, 6.8 m length) is of the order of 0.1 mm. All critical dimensions of the end-cap wheels and barrel modules are checked and compared to the drawings' specifications. They include, for the end-cap wheels, inner and outer radii and thickness, and, for the barrel modules, length, flatness and torsion.

The apparatus to measure a 4-plane or 8-plane wheel consists of a rotary arm, which holds digital measuring probes and a reference plate that enables the wheel to be correctly registered and the apparatus calibrated. The seven *Sylvac*[1] capacitive probes are sensors with a range of ±10 mm and a least count of 1 µm. The measurement is carried out on a precision granite table of dimensions 2 m × 2 m and a quoted flatness within 7 µm.

[1] Sylvac SA, CH-1023 Crissier, Switzerland

A beam of length 1170 mm rotates around a vertical axis that, in turn, is attached via a rotary point to a pivot fixed with respect to the precision table (Figure 6-3).

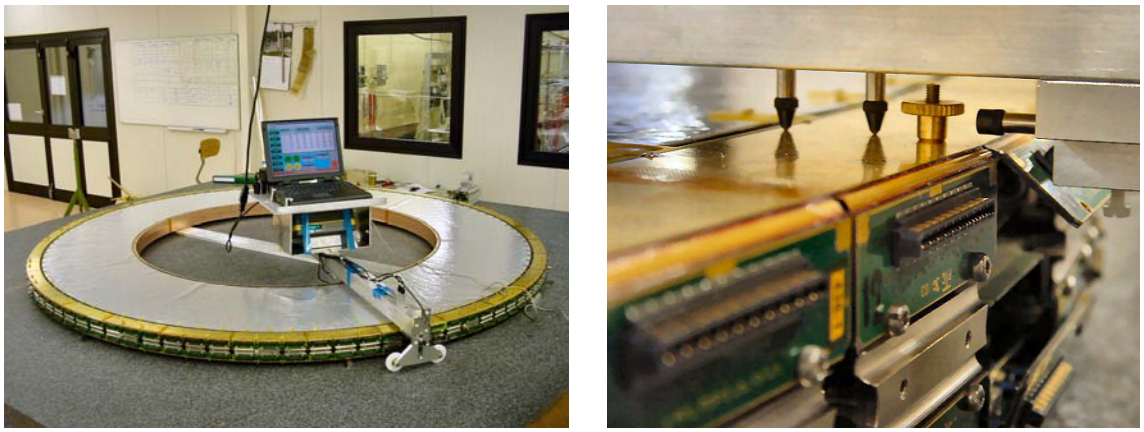

Figure 6-3 Test setup for dimensional measurements

In particular, the following measurements are made and recorded in a database:

- Radial position of the upper and lower part of the inner gas seal (“carter”), respecting the inner envelopes allocated to the SCT.
- Height above the table surface of the upper wall of the inner gas seal and
- height above the table surface at the inner, middle and outer radius of the WEB, which serves as a control of the final end-cap height after stacking and prevents an accumulation of “bumps” at any azimuthal position.
- Radial position of the centre of the reference holes at the outside of the WEB, through which long rods have to pass, holding the end-cap stack together.

A LabVIEW® data acquisition program is used to read out the sensors and to store the data on a portable PC for further processing. An example diagram below is shown in Figure 6-4.

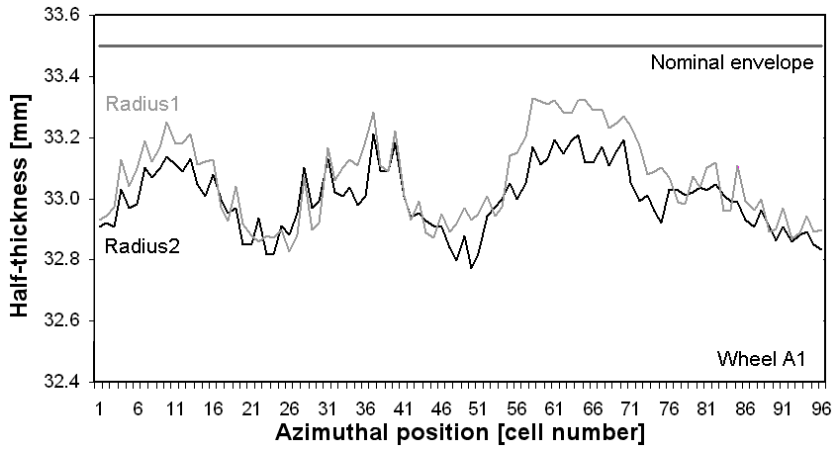

Figure 6-4 Measured half-thickness of a 4-plane wheel type A (azimuthal dependence), which is well within specifications.

The dimensional envelopes for the two 8-plane end-cap wheel types are:

- Inner radius (R_{min}) : 623.75 mm **before** mounting the inner signal-return carter
- Inner radius (R_{min}) : 623.35 mm **after** mounting the inner signal-return carter
- Thickness type A : 67 ± 0.4 mm (68.7 mm)
- Thickness type B : 114 ± 0.4 mm (115.2 mm)

Note: For the thickness envelopes the values in parentheses indicate the limits for which a wheel is labelled non-conforming, but acceptable for stacking.

The detailed acceptance test description and criteria can be found in Ref. [86].

6.2.2 Active gas leak-tightness

The first leak test is already done at the production site, after all straws are glued to the inner and outer carbon fibre rings. The goal of that test is to find possible leaks due to imperfect glue joints between the plastic parts of the straw tubes and the holes in the carbon fibre rings.
For the gas-tightness test at CERN [87][88] an assembled 4-plane or 8-plane end-cap wheel is connected to a clean ("validated") gas system and filled with 20 mbar over-pressured argon. The leak rate R_L in mbar/min/bar is then evaluated by measuring the pressure drop as a function of time (over 12-16 hours) and calculated according to the expression

$$R_L = \frac{p(t_1) - p(t_2)}{t_1 - t_2} \cdot \frac{1000}{p(t_1) - p_{atm}} \qquad \textbf{(6.1)}$$

where
t_1 and t_2 are start and end points of the measurement (min),
$p(t_1)$ and $p(t_2)$ are the pressure (mbar) in the gas volume at the corresponding time and
p_{atm} is the atmospheric pressure (mbar).

Before fitting a linear function to the pressure-time curve the data are corrected to account for temperature fluctuations according to the ideal gas law $pV/T = constant$ (Figure 6-5). For the expected small leak rates, a linear fit is an adequate approximation of an otherwise exponential pressure drop behaviour.
The maximum acceptable leak rate of 1 mbar/min/bar is motivated by the high price of xenon gas. However, a leak rate of order 0.1 mbar/min/bar remains the goal and is in the majority of cases achieved (Figure 6-5).
The measurement setup comprises pressure gauges, a PT-1000 temperature sensor and a PC-DAQ system as illustrated in Figure 6-5.

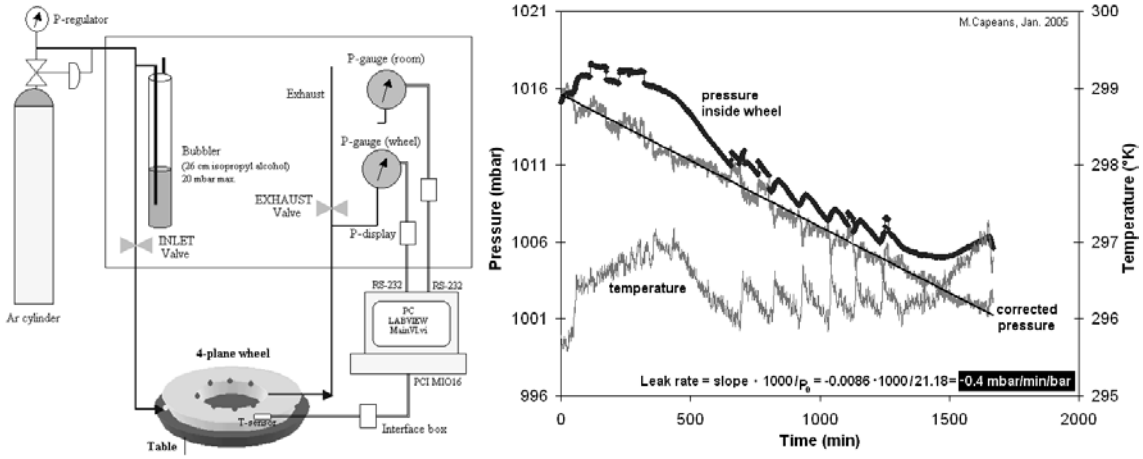

Figure 6-5 Gas leak test setup and typical pressure vs. time curve

6.2.3 Long-term high-voltage stability

Short-term high-voltage stability tests are carried out already at the production sites to detect leakage currents or shorts, mainly through the outer barrel and wheel structures, since high-voltage is applied to the straw tubes. They are performed in air and CO_2, before and after the closure of the gas manifolds.

A crucial long-term high-voltage test is conducted at CERN [89] to identify faulty channels (Figure 6-6). In this setup 16 independent high-voltage lines are connected to supply each 192 straws (six cells). The test is carried out for 15 days in Ar-CO_2 70/30 at an elevated voltage of -1550 V, which corresponds to a gas gain of 10^5, meaning 2-4 times the nominal value. Currents and numbers of trips are recorded over two and four weeks for end-cap wheels and barrel modules respectively. All channels with trips over the last ten days (barrel: three weeks) are subject to review and possible disconnection. The requirements for the barrel wires are more stringent, because they have been handled before stringing for assembly of a glass wire joint at the middle of the wire, and hence the stringing process has induced more problems for the barrel modules than for the end-cap wheels.

The problematic straw(s) causing the discharges are localised with the help of a custom-made test box. The corresponding channel is then disconnected by removing the 24 Ω resistor (Figure 3-11), if more than two discharges have occurred. Recurrent wire-to-tube discharges are a rather rare phenomenon. Experience has shown that high-voltage trips most often disappear after an initial test period, indicating a "cleaning process" in the straw tubes after first application of high-voltage.

An acceptable leakage current should not exceed 150 nA/192 straws, i.e. remain below 1 nA/wire. Excessive leakage currents are normally due to insufficient high-voltage insulation and dark currents inside the straw (*"hot wire"*). During production the end-cap wheels undergo a CO_2 test under elevated voltage to eliminate exactly the former case. Elevated levels of humidity are usually the culprit of shell-to-ground leakage currents, which will be absent in the controlled dry environment of the running experiment.

Humidity-related problems can easily be verified by examining the current while flushing with dry and warm air or nitrogen. On the other hand *"hot wires"* are revealed with the help of the test box measuring a voltage drop (~500 mV) at the protection diode. Experi-

ence shows that dark currents from the anode wire can sometimes be treated through conditioning, e.g. applying reverse voltage to the particular cell.

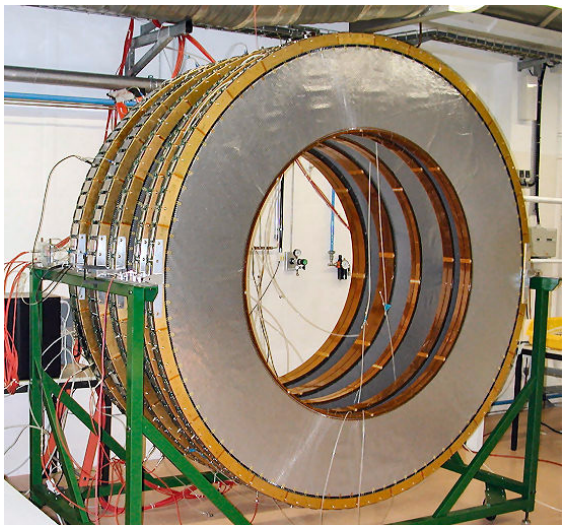

Figure 6-6 High-voltage test stand with several end-cap wheels under high-voltage.

6.2.4 Wire tension test station

The detailed description of the wire tension setup, measurements and analysis of the obtained data will follow in sections 6.3 and 6.4.

6.2.5 Straw straightness measurements at the Wheel Test Station (WTS)

A subject touched before in a more theoretical manner is the effect of eccentric wires in the straw tube (section 4.8). As mentioned before, for the end-cap straws the main cause is a displacement or deformation of the 40 cm long straw tube (cathode) rather than a dislocated wire, thanks to the small tolerances of the wire-locating crimp tubes. In one case improperly stretched radiator foils had been found, accidentally putting weight on a sector of a straw layer. Also, a mismatched insertion of the straw tube into the high-voltage insulating outer socket during straw production could create a non-circular deformation of the straw end (“squeezed” straw) as illustrated in Figure 6-7. This also favours non-straightness, since the tube forms a complex mechanical element, composed of wound film strips, reinforcement fibres and fixed at both ends to the inner and outer rings. A dedicated discussion of acceptance criteria concerning non-straightness will follow in section 6.5.

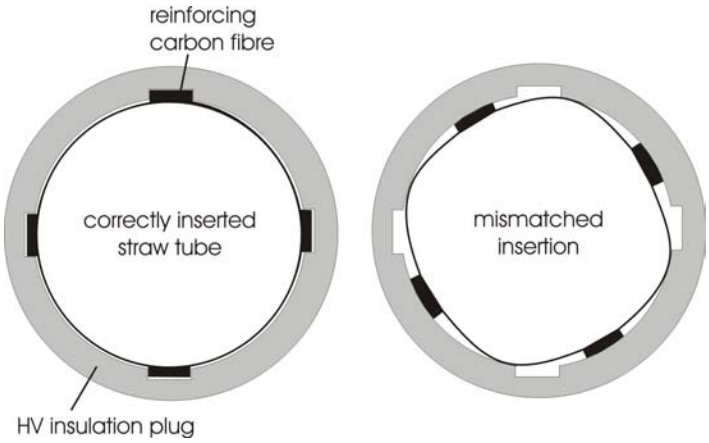

Figure 6-7 Geometric distortion of straw end, due to improper insertion of the tube into HV outer socket during production.

The technical difficulty to directly determine the wire offset in 370 000 straws tubes demands an indirect way to assess eccentricity or other geometric deformations, that compromise detector operation. For that purpose an automatised gain mapping setup - the Wheel Test Station (WTS) [90][91] - is employed, that automatically scans each of the 3072 straws of a 4-plane wheel in one run (Figure 6-8).
For the test run an 8-plane wheel is mounted in vertical position on the WTS. After connection to the WTS gas system, it is flushed with at least ten volumes of Ar-CO_2 70/30 at a rate of 1 vol/h (corresponding to ~40 l/h for an 8-plane wheel). This is indispensable to rid the gas volume of humidity and ambient air. In order to avoid artefacts from gas flow non-uniformities, two gas inlet and two outlet lines are provided.
During the process of gas flushing the 96 electronic read-out boards are connected to the active WEBs on the wheel. The designated read-out chip for TRT testing purposes is the Gassiplex chip, a 16-channel, sample-and-hold, sequential read-out, amplifier custom chip. Each of the 96 boards is identified through an individual bar-code. Its position in one of the six branches is set with on-board jumpers from 0 to 15. A calibration pulse of stable amplitude is injected into the electronic read-out chain in order to correct for pedestals and to monitor eventual baseline instabilities. Before the actual straightness measurements, a channel-by-channel calibration at reduced high-voltage is performed. The complete configuration (bar-codes, positions, connections) and the calibration data is stored in a database [92].
During the 40-50 hours run time[1] a step motor automatically rotates a plate with six bars at different radii, each holding radioactive ^{55}Fe sources. At each step the six ^{55}Fe sources expose a group of straws at different radial positions. After a full turn of the plate six spectra along each of the 3072 straws are recorded, every time together with a reference spectrum in a nearby straw to compensate for atmospheric fluctuations. This is especially important since the acquisition time between two points along the straw is around 7 hours, allowing for significant changes of pressure and temperature[2].
At the end of the run the 3072 straw profiles are determined by normalizing the measured amplitude at each point to the measured amplitude of the corresponding reference straw.

[1] The acquisition time naturally depends on the source activity.

In an "*express analysis*" the upper part of the argon peak is fitted to a Gaussian, its mean and standard deviation are stored together with the spectrum in the database. The gas gain variation along a single straw is then calculated as the difference between the largest and the smallest normalised amplitude, divided by the smallest normalised amplitude, $(A_{max} - A_{min})/A_{min}$, examples are shown in Figure 6-9 and section 6.5.2. All straws with a gas gain variation of 9 % or more are flagged for a detailed off-line analysis afterwards.

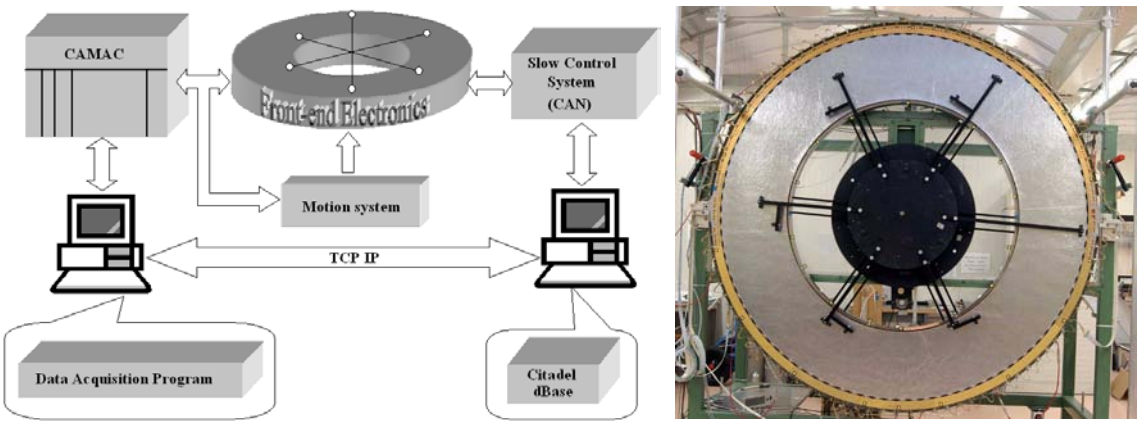

Figure 6-8 Schematic setup (left) and picture (right) of the Wheel Test Station

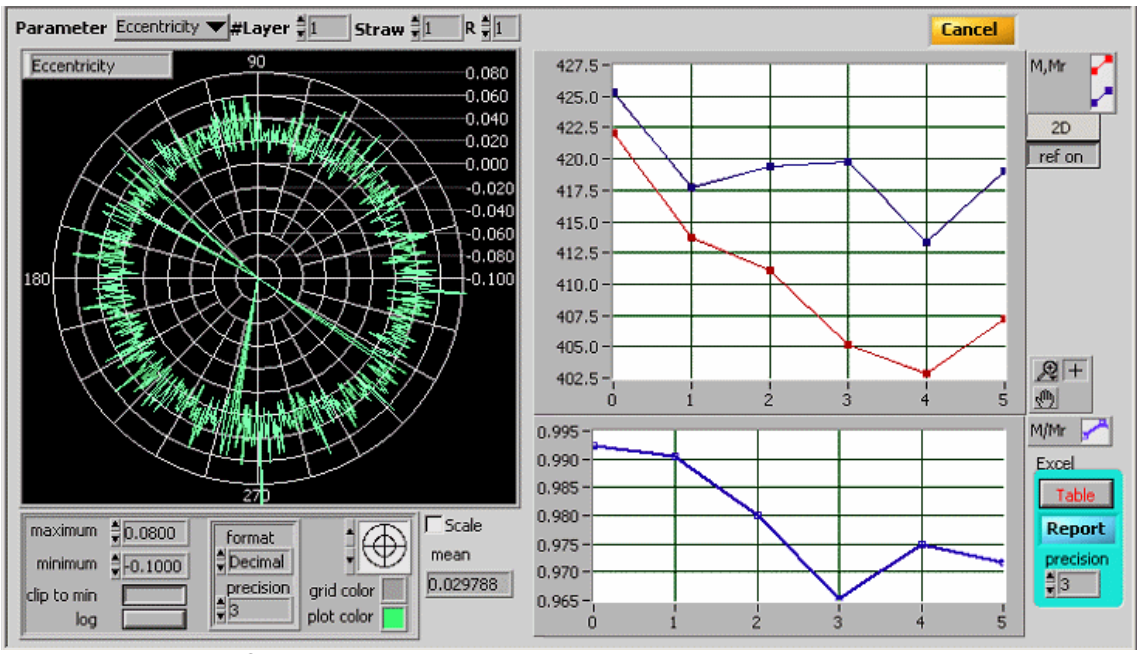

Figure 6-9 LabVIEW® module displaying eccentricity data from a Wheel Test Station run. On the left azimuthal plot the measured amplitude variation in one layer of 768 straws is shown. On the top right the graph displays the measured amplitudes [ADC counts] at the six radii along a selected straw (A) and its reference straw (A_{ref}). On the bottom right the normalised amplitudes (A/A_{ref}) at the six radii are plotted.

[2] Through the vertical mounting of the wheel the temperature difference between top and bottom part measures around 1-2 K corresponding to 3-6 % of changes in amplitude. However, within a 40 cm long straw, oriented in vertical position, the room temperature effect is negligible.

6.3 Wire tension measurements

While wire tension is less crucial for position resolution in the short end-cap straws, it has to be controlled - like straw straightness - for reasons of operating stability. Wire sag due to very low tension will reduce the distance between the anode wire and the cathode tube and such decrease the margin to streamer on-set or eventually high-voltage breakdown. Wire tension is also monitored since all TRT wires are crimped (end-cap) or pinned (barrel), proven to be a clean and technically feasible method.
The compact design of the end-cap wheels (and barrel modules) does not permit the use of the classic magnetic resonance method where a current in the wire brings it into oscillation when located in a strong magnetic field. The method requires electric contact with the anode wires and access to the individual straw tubes to place the magnetic coils. For this reason the TRT had to adopt an alternative method explained in the following paragraph.
The existing wire tension measurement setup, which had rather prototype character, was reviewed and improved in many points trying to eliminate poor or faulty measurements and to shorten acquisition time.

6.3.1 Measurement principle and setup

Wire tension is derived from the change of capacitance that an oscillating wire causes in a straw tube under voltage, when excited (mechanically or acoustically) with its eigenfrequency. The capacitive coupling of tube and wire induces a current in the wire with a time dependence given by the oscillation. A spectrum analyser module written[1] in LabVIEW® extracts then the resonance frequency from the rather complex response signal through a Fourier analysis (Figure 6-10). The eigenfrequency ν [Hz] is then translated into tension T [g] using the formula

$$T = \frac{4\mu L^2 \nu^2}{g} \qquad \textbf{(6.2)}$$

where
μ is the mass per unit length (14.6 mg/m for Au-W wire of 31 µm diameter),
L the free wire length (38.6 cm in the ideal case[2]) and
g the gravitional acceleration at the surface of the earth (9.81 m/s^2 for Geneva).

The nominal tension of 60 g thus gives a resonance frequency of 260 Hz.

[1] S. Katunin (PNPI, Gatchina, Russia)

[2] The free length can vary due to the nature of crimping.

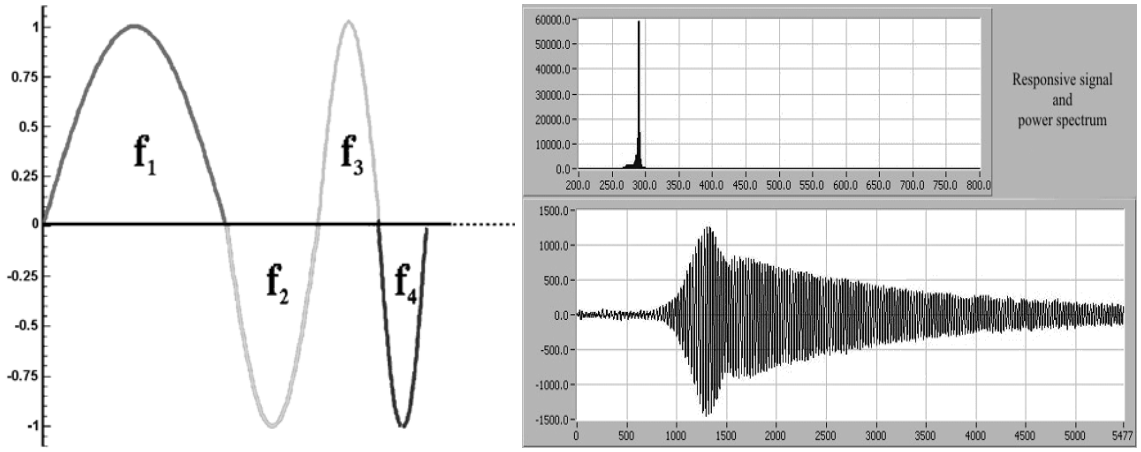

Figure 6-10 The excitation signal is a waveform composed of increasing frequencies (left). The rather complex response (bottom right) is transformed through a Fourier analysis into a resonance peak (top right).

In practice, after applying –200 V to the cathode tube, a waveform (Figure 6-10) with a continuous frequency sweep from 200-800 Hz is sent to a loudspeaker. The range from 400-800 Hz accounts for the second harmonic, increasing measurement accuracy and efficiency, and enables resonance extraction from wires with low first harmonic response signal. An excitation through *white* or *pink noise*[1] was tested, but turned out to be unsuitable in the rather narrow frequency band.

Dedicated studies have been performed to understand the transmission of vibration from the speaker to the wire through the complex wheel structure. As a result, the vibration of the speaker magnet is transmitted through a glassfibre-epoxy plate onto the wheel structure. Firm contact is assured by adding an effective load of 1 kg on top of the speaker (Figure 6-11).

A great improvement was made by using the WTS electronics (based on the Gassiplex chip), which makes possible the measurement of the induced signal of 32 wires in about 1 minute. This reduced the time to measure an entire 8-plane wheel from many days to few hours. The program checks for a signal-to-noise ratio of 10:1, otherwise it automatically remeasures the channel with increased speaker volume. In the end the trained operator is able to correct or determine manually the resonance peak position in case of faulty identification. Also a visual inspection of the 32 resonance spectra aims to detect mismeasurements and such prevents erroneous results from entering the database. Although the DAQ program checks for proper signal-to-noise conditions and double-checks the result with the frequency of the second harmonic, the human inspection guarantees the quality of the obtained data.

---

1 *"White noise"* is a sound that contains every frequency within the range of human hearing (generally from 20 Hz to 20 kHz) in equal amounts. *"Pink noise"* is white noise that has been filtered to reduce the volume at each octave. This is done to compensate for the increase in the number of frequencies per octave. Each octave is reduced by 6 decibels, resulting in a noise sound wave that has equal energy at every octave.

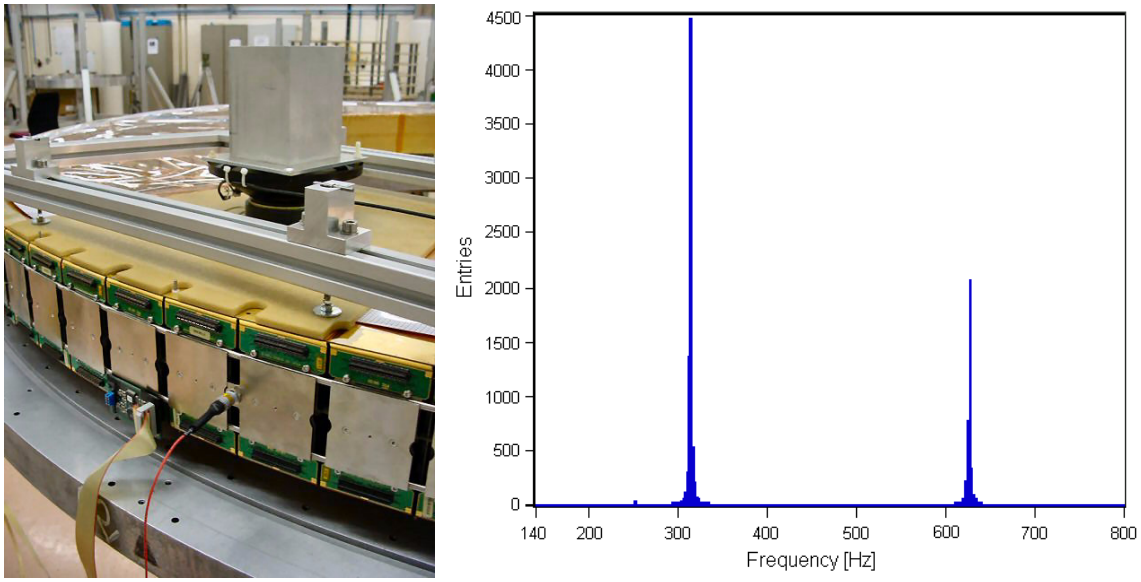

Figure 6-11 Wire tension setup, showing the loudspeaker with its load sitting on a glassfibre-epoxy plate to transmit the speaker magnet's vibration to the wheel structure. Read-out electronics is connected to a cell of 32 straws (left). Resonance spectrum showing the first and second harmonic (right).

6.3.2 Production and acceptance specifications

In practice, wire tension is applied through a mechanical leverage on the wire stringing tool, designed to effectuate a 60 g strain. The limit of elastic deformation was measured at 150 g while rupture occurs around 220 g (Figure 6-12) [93]. Whereas the design of the barrel modules allows wire restringing, the end-cap wheels lack this option, a fact that demands more stringent limits during production (55-80 g). Large changes in tension are of concern, posing a threat to a full high-voltage group, if a single wire slips into the instability regime. Barrel straws are accepted, if their wire tension is measured to be within 47-100 g, and furthermore exhibit no subsequent loss of tension bigger than 8 g. For the end-cap wheels, all straws with less than 40 g of tension or a tension loss (see 6.3.3) greater than 15 g (barrel: 5 g) must be disconnected. For the barrel straws with the electrically split wires held together by a glass wire joint, an additional acceptance criterion is set, requiring a back-to-front tension difference of 8 g at most.
The possibility of tension loss through "slippage", creeping or other relaxation effects will touched briefly in the following paragraph. Wires with tension close to the elastic limit should technically not exist and have indeed not been observed at this point, hence the absence of an "official" upper tension limit.

6.3.3 Wire sag, tension loss

Gravitational and electrostatic forces cause a pull on the wire moving it out of centre resp. tube axis. The electrostatic component is more significant, it feeds back positively growing stronger with wire eccentricity. The wire can thus be moved out of the allowed range and towards an unstable electrical regime.
The gaseous detector simulation software *Garfield* can be used also to compute wire sag. The maximum wire sag depends on the applied tension and is shown in Figure 6-12. Curves for various initial wire offsets have been computed.

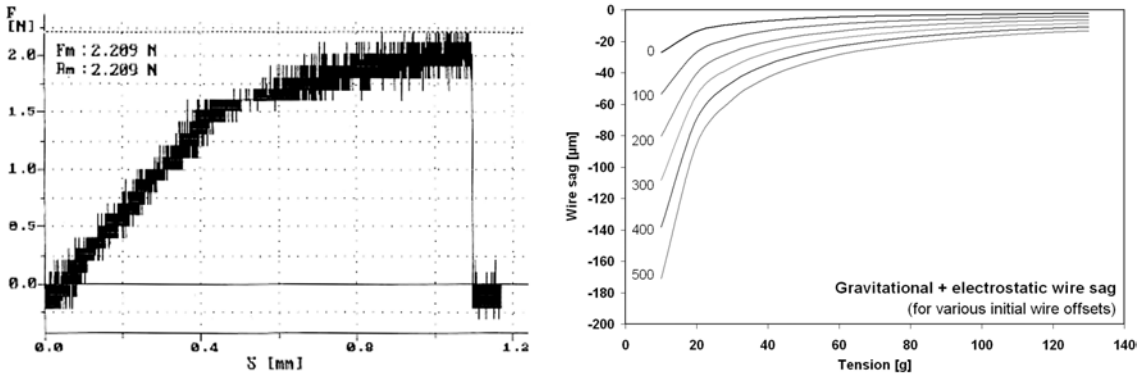

Figure 6-12 Measured traction test curve showing the applied force vs. elongation. The point of the elastic deformation limit at 150 g and the point of rupture above 200 g is clearly visible (left). Total wire sag vs. tension was computed for wires with various initial offsets of 0-500 µm (right).

It is evident that gravitational sag is independent of the initial wire eccentricity, however, as mentioned before, the electrostatic pull becomes stronger when the wire is located outside the centre of equilibrium. Nevertheless above 20 g of tension the total sag constitutes a negligible contribution to wire eccentricity. There are still other factors acting upon wire tension, like temperature, slippage or mechanical deformation. A few estimates are now made to asses the risk of moving a wire out of the 300 µm acceptance window.

A first order temperature effect, i.e. expansion or contraction of the tungsten wire, can be calculated according to the relation

$$\frac{\Delta\tau}{\Delta T} = \frac{\alpha(W)}{g} \cdot \pi r^2 \cdot E \qquad \textbf{(6.3)}$$

using the thermal coefficient for expansion of tungsten $\alpha(W)$ ($4.5 \cdot 10^{-6}$ 1/K),
the gravitional acceleration at the surface of the earth g (9.81 m/s^2 for Geneva),
the wire radius of r ($15.5 \cdot 10^{-6}$ m)
and the Young's modul for tungsten of E ($3.6 \cdot 10^{11}$ N/m^2).

As a result, the tension variation $\Delta\tau$ due to a temperature change ΔT is of order 0.1 g/K (Figure 6-13), hence of no concern in the temperature-controlled environment. It contributes to the statistical spread in the tension measurement.
We know that the incomplete insertion of a crimping pin before crimping can result in a relaxation process in time, when the pin moves inwards under the pull of the wire, initiated e.g. by mechanical vibrations applied to the wheel.

We can calculate that the measured average tension $\tau = 60$ g elongates the wire by $\Delta L \sim 0.8$ mm with the formula

$$\Delta L = \frac{\tau \cdot g \cdot L}{\pi \cdot r^2 \cdot E} \qquad \textbf{(6.4)}$$

using a wire length $L = 0.38$ m,
the gravitional acceleration at the surface of the earth g (9.81 m/s^2 for Geneva),
a wire radius of $r = 15.5 \cdot 10^{-6}$ m
and the Young's modul for tungsten of $E = 3.6 \cdot 10^{11}$ N/m^2.

Figure 6-13 shows the relation between applied tension weight and elongation of the tungsten wire assuming 60 g of tension weight, which represents the average. From there one can read, that 15 g of tension loss correspond to a relaxation of less than 250 µm, which would move the wire below the specified tension of 40 g.

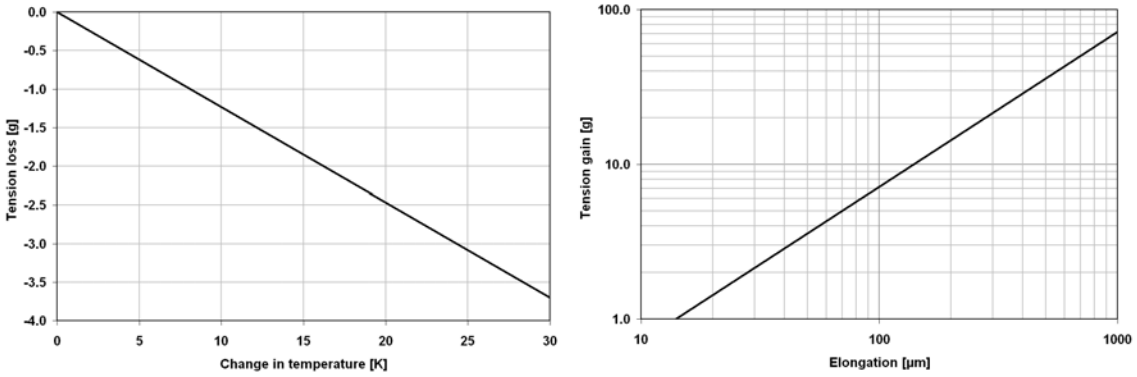

Figure 6-13 Calculated tension change vs. temperature (left) and elongation/contraction (right).

Occasionally recorded tension losses of the order of 5-20 g raised the question of their origin. The relaxation due to wire material fatigue (creep[1]) can be ruled out. While long-term tension loss in aluminium wires is a known problem (few percent per year), tungsten wires do not show this characteristic, but remain with stable tension after a small initial loss [95].
However, it cannot be excluded that strained wires relax due to slippage after improper crimping or imperfect insertion of the crimping pin (0.2 mm relaxation correspond to the loss limit of 15 g). At the point of acceptance testing there is no technical possibility to determine the cause for large tension losses of single wires, because there is no access to the crimping pins. Specific long-term studies of the evolution of wire tension with time have shown no tendency towards global loss of tension in any module or wheel. Cases of large change of tension are extremely rare ($<10^{-4}$) for ~120 000 wires measured to-date, confirming the reliability of the wire stringing method.

[1] The phenomenon is best described as the "time-dependent part of deformation which accompanies the application of stress to a solid" - prevalently called creep [94]. The issue of metallic creep has been examined already in 1831 by Louis Vicat. The beginning of scientific studies of those phenomena dates back to the beginning of the twentieth century.

6.4 Distribution and variation of wire tension

It is interesting in terms of production quality and to assess large-scale effects on wire tension to investigate the distribution of tension and tension variation. The latter helps especially in monitoring possible tension loss with time.
Distributions of absolute wire tension and tension changes in a type-A 4-plane wheel (3072 straws) are displayed in Figure 6-14 and Figure 6-15 respectively.

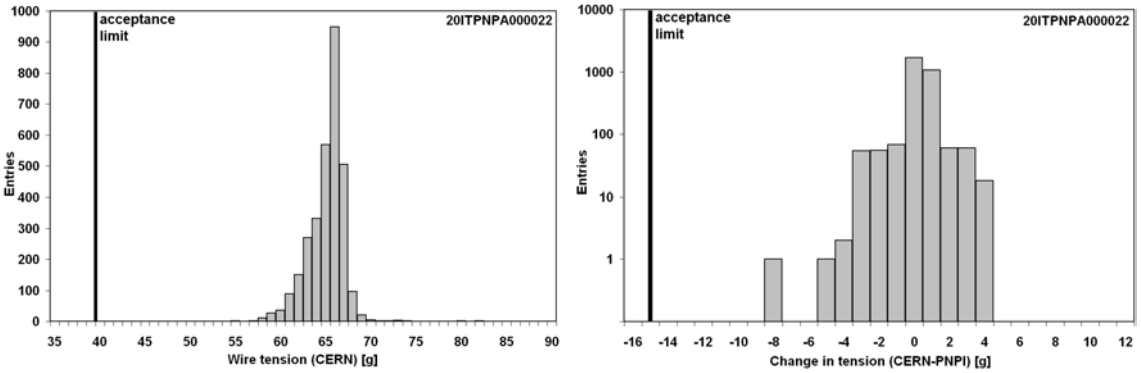

Figure 6-14 Typical wire tension distribution in a 4-plane wheel (3072 straws) as measured at the acceptance test site (left). The distribution of tension variation (difference between acceptance and production site) shows no indication of significant tension losses (right).

We can see in Figure 6-14 that the most probable measured tension value in this particular case is 66 g. The difference to the design value of 60 g can have its origin both in the design *per se* or in the calibration of the measurement (see Eq. 6.2), however, the eventual cause is of little relevance and will not be examined further. Systematic and statistical errors are expressed in the measurement variations of ±2 g r.m.s. The tendency to measure a lower tension than the most probable value can be due to relaxation processes (crimping pin slippage, inherent stringing process feature) after crimping. Still, in such a case they must happen on a small scale (few ten µm).
Figure 6-14 also shows the typical distribution of the difference in wire tension, that is measured between the production site (after assembly of an 8-plane wheel) and the acceptance site (after transport from Russia to CERN). While the distribution reveals the statistical and systematic error of the measurement (±0.9 g r.m.s.), no significant tendency for tension loss was observed.
Some large tension loss values (< -15 g) have been measured, but at a level much smaller than 10^{-4} (few out of more than 120 000 examined straws).

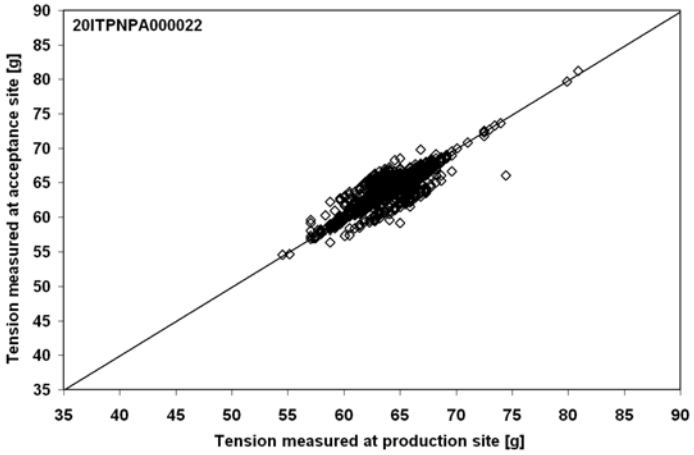

Figure 6-15 Correlation scatter plot between wire tension measurements made at the production site and at the acceptance site (left). The spread along the line of perfect correlation contains variations in the stringing process, the systematic as well as statistical error of the measurements. The width of the distribution perpendicular to the line shows only the latter variations in the measurement.

6.5 Straw straightness measurements - the Wheel Test Station (WTS)

6.5.1 Determination of the acceptance criteria

After the change of gas mixture from Xe-CF_4-CO_2 70/20/10 to Xe-CO_2-O_2 70/27/3 it was necessary to investigate the implications on the present acceptance criteria. They had to be critically reviewed with strong focus on the operational safety features of the gas. Among those are the rate of self-quenched streamers as well as the onset of corona discharges and eventually the point of total breakdown. The relation of the relative change in gas gain (*dA/A*) with wire eccentricity was remeasured, having in mind the different interplay of multiplication and attachment in the oxygen-containing mixture (section 3.5 and 4.7).

The foreseen nominal gas gain in the TRT straws is 25 000, leaving some margin to the upper limit of 40 000, which is mainly determined by operational safety. The lower limit marks the point of reasonable noise counting rates in conjunction with a front-end electronics low threshold discriminator level of 250 eV (2.5 fC) on the energy scale. With these settings the required drift-time measurement efficiency and drift-time accuracy are achieved (see also section 3.2).

The upper gas gain limit is usually conditioned by various factors. For the CF_4-containing mixture the lowest acceptable rate of self-quenched streamers (SQS) and large amplitudes from heavy ionizing particles was the limiting point, knowing that the electronics dead-time from a single SQS is about 600 ns. Therefore in order to keep idle periods at a 1–2 % level the SQS rate should remain below 10^{-3}. The probability of SQS rises quickly with gas gain. In Xe-CO_2-O_2 70/27/3 the SQS rate is much lower reaching 10^{-3} only at gas gains closet to 10^5. The onset of space-charge effects that degrade TR performance, remains also in the new gas at a gas gain of 40 000. The useful operating range in the end corresponds to a voltage difference of about 50 Volts. Measured gas gain and SQS rate are shown in Figure 6-16.

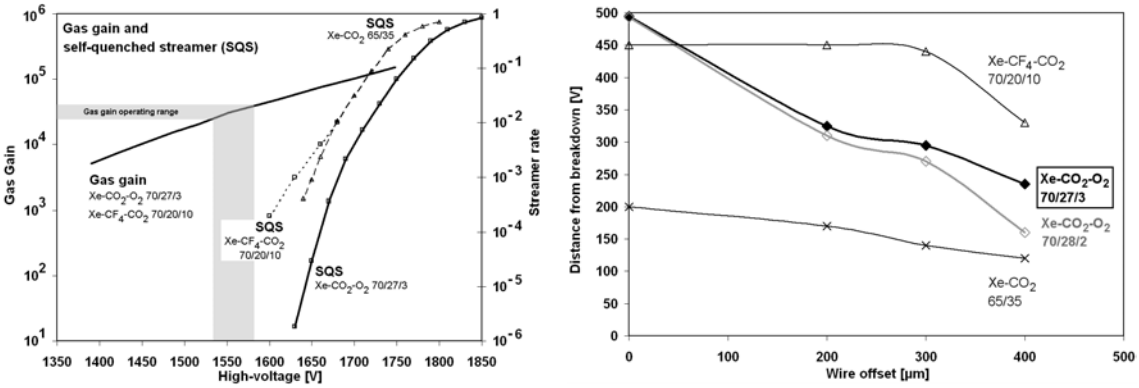

Figure 6-16 Gas gain and self-quenched streamer rate in various xenon mixtures (left). Distance from operating voltage to point of high-voltage breakdown in the straw for different wire offsets and gases (right).

The major concern remains the distance to the point of high-voltage breakdown for straws with wires offsets close to 400 µm. At the operating point there is a margin of 450 and 500 V before breakdown for a geometrically perfect straw in Xe-CO_2-O_2 70/27/3 resp. Xe-CF_4-CO_2 70/20/10. For straws with 400 µm offset this gap decreases to 220 V for the oxygen-containing mixture, while it was still 270 V for the former CF_4-mixture (Figure 6-16). Applying safety factors that account for variations of temperature in the detector volume, and the effect of highly-ionizing particles, the realistic margin remains a mere 170 V compared to 50 V for the binary mixture.

Temperature affects gas gain at the level of 3 %/°C. 10°C variations along the straw or across a group of adjacent straws are acceptable from a physics performance point of view. A dedicated gas gain stabilisation system compensates for pressure and temperature fluctuations with a feedback loop, keeping gas gain stable to better than 2 %.
Crucial for a uniform gain response and resistance towards chemical and radiation damage is the **quality of the wire** and the cathode tube surface. It is assured before and during mass production in QA/QC measures and is of minor concern in the finally assembled detector. Wire and tube inner diameters are accurate to 1–2 % or better (Figure 3-10), namely, 31.1 ± 0.3 µm and $4.00 \pm \frac{0.02}{0.00}$ mm respectively [19][43].

In the end the biggest threat to safe operation are shortcomings in the mechanical quality of the straw tubes. Geometric deformations like non-straightness or non-circularity cause distortions of the electric field. Wire offset generally has its cause in bent tubes and not in dislocated crimping pin or inserts, since they meet very strict mechanical tolerances.
As an outcome of a tube deformation the region where the wire stays closest to the tube wall experiences an enhancement in the electric field and vice versa (see section 4.8). The radial symmetry of the field is lost, affecting gas gain response. This is easily seen in the pulse height distribution of the ^{55}Fe source used in the straw straightness assessment. The total energy of the electric field grows with wire offset, resulting in an increased mean amplitude, while the field asymmetry leads to large differences in the avalanche sizes that affect energy resolution. Since the change of mean amplitude and resolution are correlated they serve as an excellent indicator of bent straws. The spectrum's shape can offer valuable information on the origin of anomalies in the straw.

6.5.2 Signatures of anomalous straws

In the following, gain non-uniformities in the TRT straw tubes are discussed on the basis of different examples, looking at amplitude and resolution profiles as well as the shape of ^{55}Fe spectra. In the majority of cases signatures are clearly attributed to one of the identified causes. There are rare cases of less pronounced profiles or unusual shapes, where the anomalous straw will be disconnected. They only insignificantly contribute to channel losses. Often unrevealed remains the actual cause of deformation. Although straws are visually inspected for straightness before assembly, it cannot be ruled out that a flawed one is missed in the quality control process of 320 000 straws. Furthermore the difficulty to precisely align 3072 straw tubes in the two concentric carbon fibre rings, at minimum tolerances, could lead to local stress phenomena on single straw tubes. The end-cap wheel remains a complex structure that has to resist the traction from 3072 wires and the mechanical stress from the numerous glued components.

The classical signature of a **bent straw** is seen in Figure 6-17, where the wire is consequently out of centre. The increase of amplitude and of avalanche size variations with growing eccentricity (see section 4.8) leads to the characteristic profile.

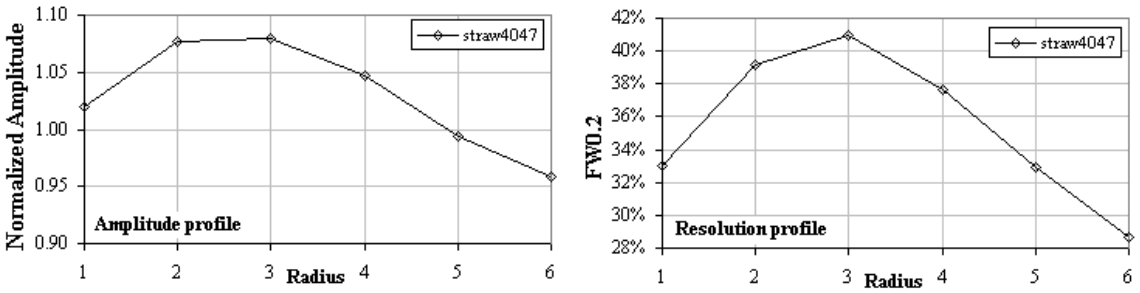

Figure 6-17 Gas gain and resolution profile of a bent straw tube.

In few cases straws with large rise in amplitude at one straw end have been found. Peak resolution is severely deteriorated there, signaling a significant distortion of the electric field. More likely than being bent at the outer point, where the straw is very rigid, is the effect of a local **non-circular deformation** that affects the straw over its full length. An identified cause has been the faulty insertion of a tube into the high-voltage insulation sleeve as illustrated in Figure 6-7. A **non-circular** deformation of the straw tube ("squeezed straw") results in an amplitude and resolution profile as seen in Figure 6-18 and was also subject of study (see section 4.8.2).

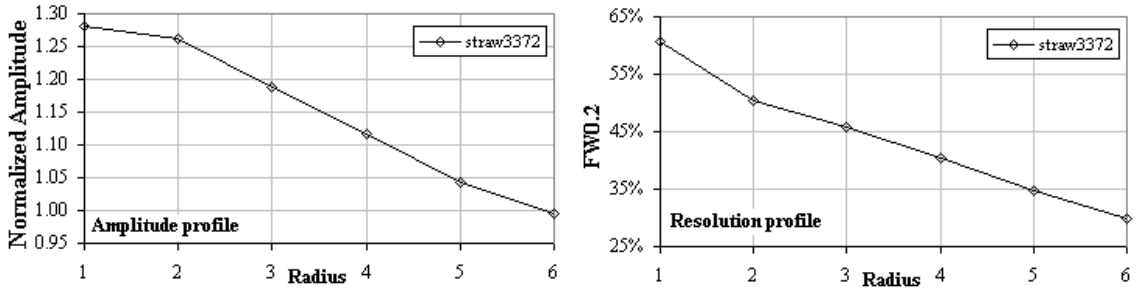

Figure 6-18 Gas gain and resolution profile of a straw with local non-circular deformation. Unlike for bent straws the maximum amplitude is located at the outer radius. Changes in amplitude and resolution are higher than seen for bent straws.

In some cases the longest arm of the WTS holding the radioactive ^{55}Fe source irradiates a point where excess glue at the outer straw socket impedes X-rays penetrating into the tube (**"edge effect"**). (Figure 6-19). In this case the obtained spectrum is of poor quality due to low statistics (Figure 6-22). This effect is rare and is of no threat to operation, consequently such straws do not have to be disconnected.

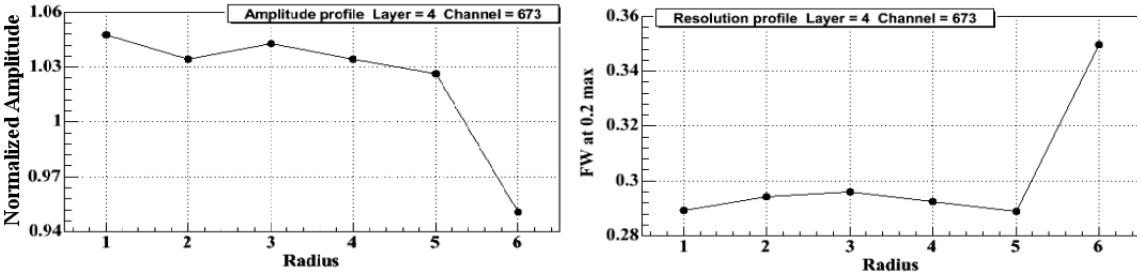

Figure 6-19 Gas gain and resolution profile of a straw exhibiting an "edge effect". There the spectrum is of poor resolution caused by insufficient counting statistics (X-ray attenuation from excess glue on the straw).

Dust particles, lint or "finger prints" on the wire caused by incautious handling leave a **spot on the wire surface** at which the electric field is disturbed. While a loosely attached particle has the chance to blow, fall or "burn" off, a surface coating of greasy nature is likely to remain, altering the conductivity of the region, and the electric field near the wire surface. Generally in both of the above-mentioned cases the wire field is locally reduced, leading to a decrease in amplification and a deterioration of resolution owing to the larger avalanche size variations. Figure 6-20 shows an example where the wire exhibits a local gain drop of 5 % in conjunction with a slightly worsened resolution at the same point (sufficiently far from the wire end). Nevertheless these straws can normally remain operative if the affected area is small.

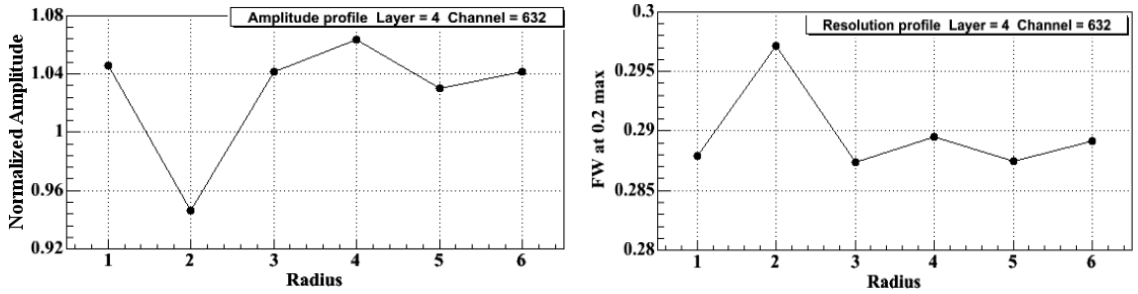

Figure 6-20 Gas gain and resolution profile of a straw with a locally aged or polluted wire.

A number of ^{55}Fe spectra are shown in Figure 6-21 and Figure 6-22, found in anomalous end-cap straw tubes.

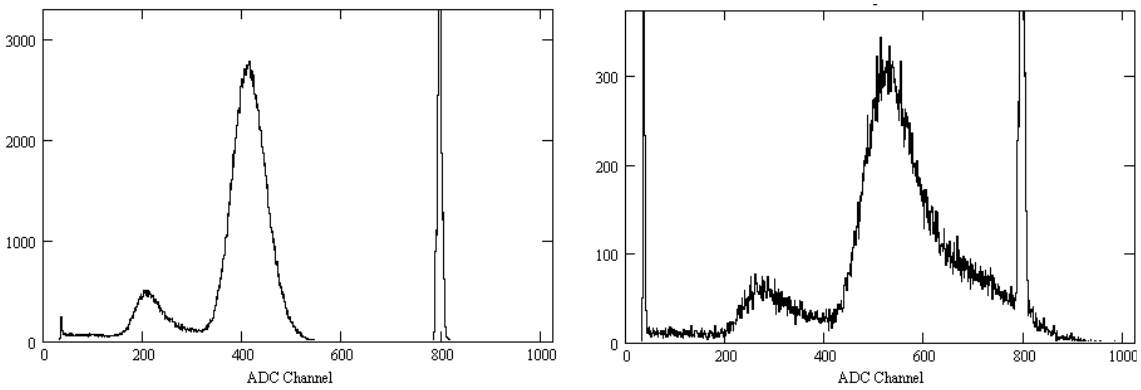

Figure 6-21 ^{55}Fe spectrum of a faultless straw showing the argon escape peak, the main peak and the narrow peak from an electronic calibration pulse (left). A straw likely to suffer from a non-circular deformation exhibits a large high energy tail (right). This spectrum corresponds to radius 1 in Figure 6-18).

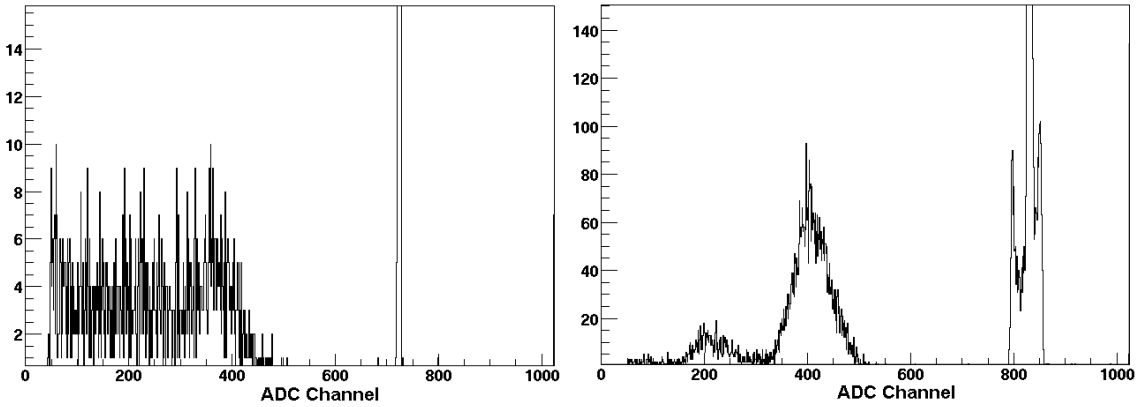

Figure 6-22 Poor quality spectrum from straw edge where excess glue attenuates irradiation (left). A spectrum widens when affected by baseline instabilities evident in the electronics calibration peak (right).

6.5.3 Measured change of gas gain and resolution with wire offset

An important measure to guarantee stable operation is to identify straws in which the electric field has entered a regime where an increased rate of streamers and a reduced distance to breakdown jeopardises efficient operation. The unwanted enhancement of the electric field in the straw has been discussed already in section 4.8.

For the former CF_4-containing gas mixture measurements have demonstrated a significant rise in the rate of self-quenched streamers and large amplitudes with gas gains above $5 \cdot 10^4$. A maximum acceptable streamer rate was reached at a wire eccentricity of 300 µm which corresponded to a 5-6 % of change in gas gain [19]. The new oxygen-containing mixture shows a significantly lower streamer probability in the relevant gas gain range, however, the distance to breakdown is much closer (see section 6.5.1). For this reason the acceptance limit could only be slightly relaxed to an eccentricity of 400 µm, which leads to a local increase of gas gain of 11 %.

Methods to scan the wire position in single straw tubes with an X-ray tube have been developed previously [96]. Still, a laboratory setup to determine the position of each wire is not feasible for the systematic measurements of the more than 320 000 end-cap straws. As discussed before, an indirect method is used, which exploits the gradual distortion of an ^{55}Fe spectrum with increasing wire eccentricity. Enhanced reliability of this method was achieved by looking at two parameters of the spectrum's argon peak, namely its mean value and the peak width at the bottom part. Peak resolution changes even more drastically than its position; however, the error on the peak width is larger especially for spectra with low statistics, evident e.g. in Figure 6-22.

The relation between eccentricity and spectrum "distortion" was studied in a dedicated set of measurements, in cooperation with two summer students[1] at CERN. A series of ^{55}Fe spectra has been recorded while causing a controlled dislocation of the straw tube with respect to the wire. The setup shown in Figure 6-23 comprises a pair of precision arms with micrometer gauges. For this purpose a gas-monitor was modified to hold the original

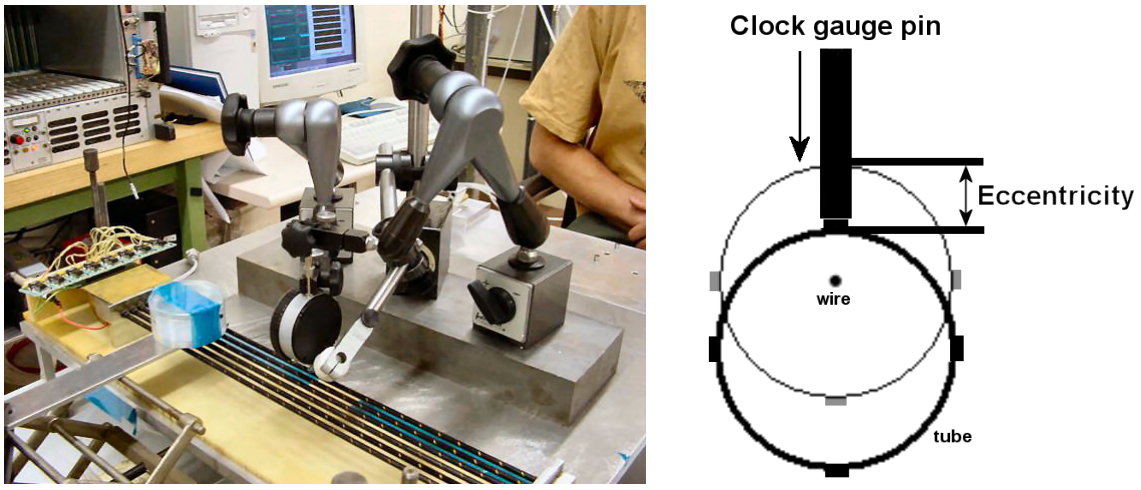

Figure 6-23 Picture and illustration of the straw deformation experiment.

[1] A. Ekström, Department of Physics, Lund University, P.O. Box 118, SE-221 00 Lund, Sweden. M. Kagan, Department of Physics, University of Michigan, Ann Arbor, MI 48109 USA.

40 cm long end-cap straws. Six production straws, carefully glued to the support plates, were wired with the standard Au-plated tungsten wire of 31 µm diameter using a tension weight of 60 g. High-voltage connection and read-out electronics are identical to the gas-monitor (see section 5.3). The operating gas used was Ar-CO_2 70/30 at flows of 5-10 vol/h.

After selecting the straw with the best achievable energy resolution (i.e. smallest initial eccentricity), a controlled dislocation of the tube with respect to the wire was performed recording ^{55}Fe along the straw. This was realised by pushing the straw at half length with the clock gauge pin of the micrometer allowing for an accuracy of 10 µm. The gauge pin pushed the straw, as illustrated in Figure 6-23, on top of the reinforcing carbon fibre to avoid causing a local dent rather than the desired dislocation over its full length. Spectra were recorded for clock gauge settings 0-600 µm in steps of 50 µm. Four sets of consecutive measurements were made; namely, two times starting from gauge setting zero to a tube deflection of up to 600 µm and back to zero.

In order to extract amplitude mean and resolution, the spectrum is analysed in a *MathCAD*®[1] script performing a double-Gaussian fit of the argon main peak. A more reliable and sensitive method was to calculate the weighted mean considering only the upper 60 % of the peak height, instead of determining the most probable amplitude (Figure 6-24). The characteristic change of peak shape with increasing eccentricity suggests the use of the width at the bottom of the peak. Alternatively to the common FWHM (full width at half maximum) the full width at 20 % of the maximum is measured, which divided by the peak's mean is defined as the resolution $FW_{0.2}$.

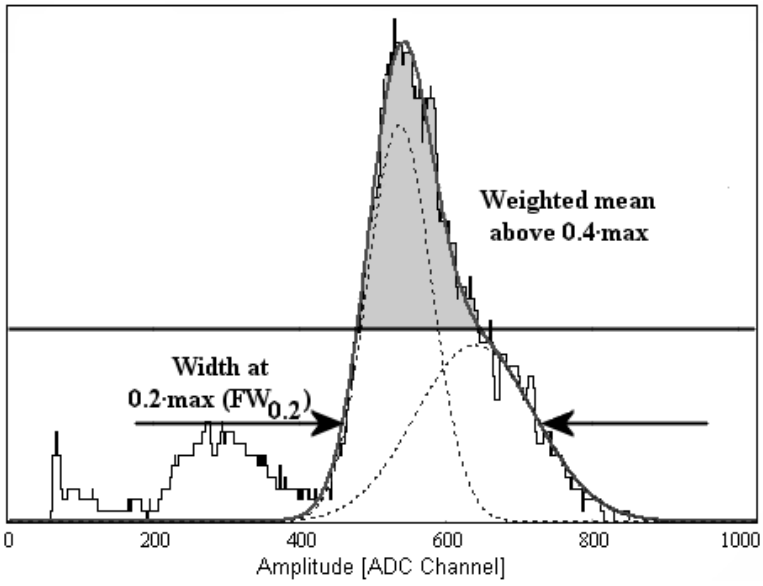

Figure 6-24 Description of ^{55}Fe spectra in terms of gain and resolution (end-cap). The histogram shows the distorted spectrum of a bent straw at a position were the wire is off-centred. The main peak can be fitted with a double-Gaussian function to determine the specific mean and width.

[1] Mathsoft™ Engineering & Education Inc., Cambridge, MA 02142-1521, United States

The resulting curves relating wire eccentricity to change in gas gain (*dA/A*) and resolution ($FW_{0.2}$) are shown in Figure 6-25. A good correlation between relative change in gas gain and resolution ($FW_{0.2}$) exists in the measured range and thus allows an unambiguous identification of bent straws.

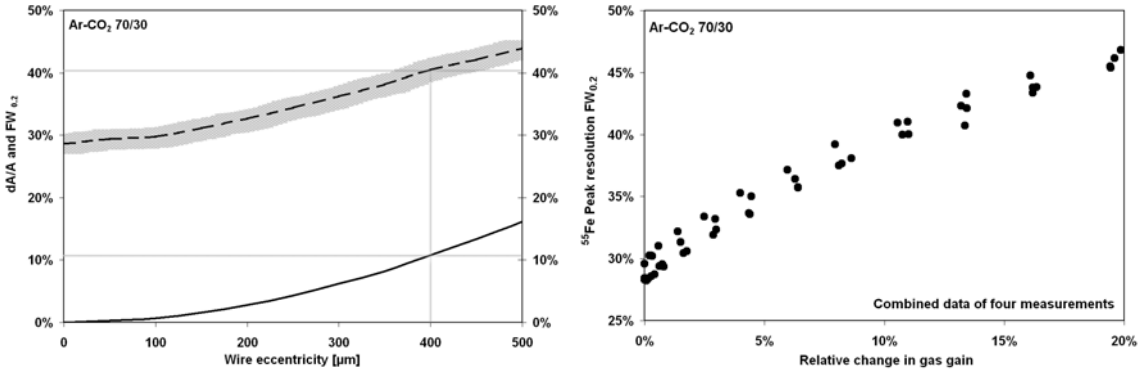

Figure 6-25 Measured relative change in gas gain and peak resolution against wire eccentricity (left). The systematic error on dA/A is of order 1 %, however, somewhat larger on the width ($FW_{0.2}$). This is well taken into account in the acceptance cuts. A good correlation between the change in gas gain and peak width with increasing wire eccentricity is found, so that bent straws are clearly identified (right).

In the end **acceptance cut is set at 9 % dA/A** variation of amplitude along the straw. This complies with the stability limit at 400 µm eccentricity and leaves some safety margin. As a further conclusion, the width at 20 % of the peak height, $FW_{0.2}$, has to be more than 35 % for those straws, to ensure that the change of amplitude is due to a geometric deformation of the straw rather than a local variation of ambient parameters (p, T, humidity) or electronic artefacts. Contrary to geometric distortions, straw ageing results in a decrease of gas gain while the peak width increases.

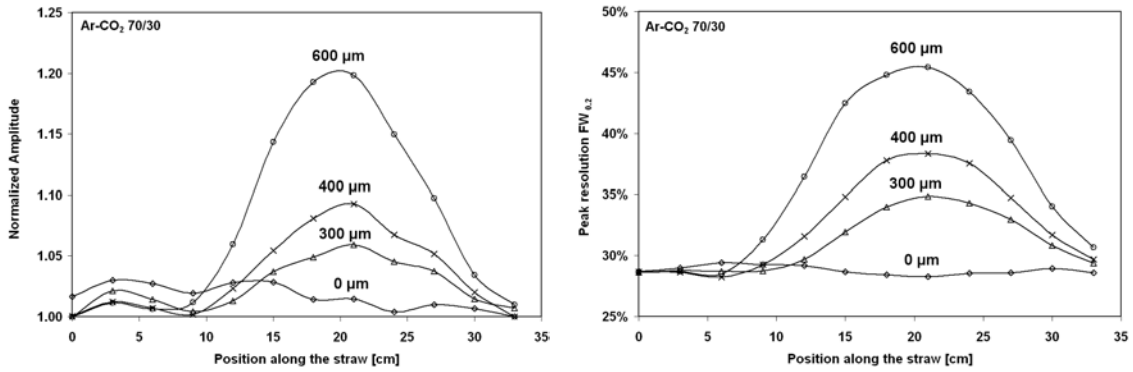

Figure 6-26 Gas gain and resolution behaviour along the straw for different eccentricities.

The characteristic relative gain and resolution profiles along the straw for various provoked eccentricities can be seen in Figure 6-26. The rigidity of the straw close to the active WEB renders this region fairly insensitive. At this side the straw is reinforced by the high-voltage insulating outer socket and excessive glue. The nature of deterioration of the ^{55}Fe spectrum was illustrated earlier in both simulation and measurement (Figure 4-26).

6.6 Statistics from the first end-cap

6.6.1 Overall wire eccentricity

The quality of straw production and selection for the type-A and type-B wheels of the first end-cap reflects the distributions of wire eccentricity. As described before wire offset is expressed as a gas gain variation along the straw, since the eccentricity values are not directly measurable in the TRT wheels and modules. Figure 6-27 shows, for both type-A and type-B wheels, the distributions of gas gain variations measured in the straws. Also indicated in the plot is the acceptance limit, below which all straws have wire offsets smaller than 400 µm. To-date less than 0.04 % of straws have been disconnected because of unacceptably large gas gain variations, an overall satisfactory result, confirming the high quality of the production standards.

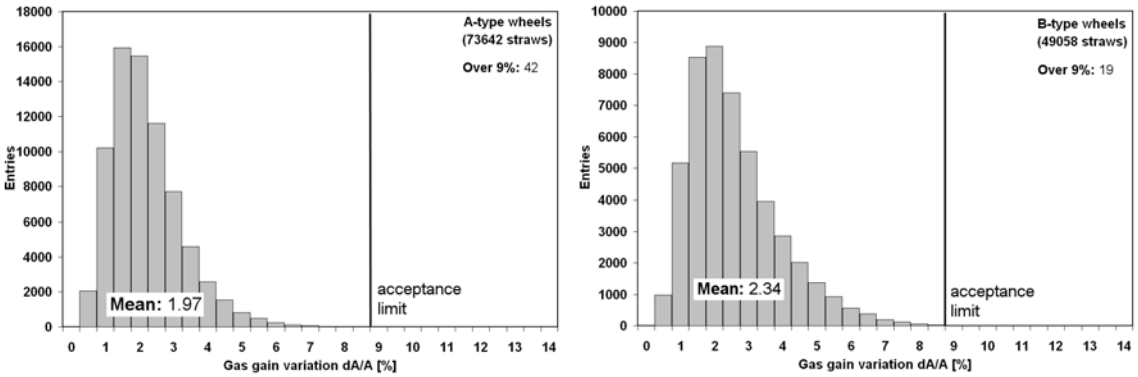

Figure 6-27 Measured distribution of gas gain variations in single straws, which are related to wire eccentricity. The plots contain the information of the first end-cap (total of 122 880 straws): 12 type-A 8-plane wheels (left) and 8 type-B 8-plane wheels (right). The number of straws with dA/A > 9 % is the result of an automated analysis, which especially in the case of B-wheels is too conservative. The exact numbers are listed in Table 6-I an Table 6-II.

6.6.2 Lost straws from the first end-cap

A number of straws appear dead after production or are lost during acceptance testing. Without going into depth and detail, the causes identified were broken traces in the flexible part of the printed-circuit board (e.g. due to incautious handling), large or infinite resistance of microvias or blindholes in the active WEB (from printed-circuit board production). With a reinforcement of the PCB's flexible part as well as through intensive cooperation with the WEB production site it was possible to prevent larger losses.
Table 6-I (type-A wheels) and Table 6-II (type-B wheels) give details on end-cap straws which are lost out of the more than 120 000 straws analysed to-date[1]. All straws which are listed under "Total lost" have been disconnected by removing the protection resistor. They include straws which are bent or otherwise deformed, unstable under high-voltage, with low wire tension or showing no signal due to a disruption in the signal path.
Not listed are channels which are lost due to front-end electronics problems.

[1] Status: March 2005 (one full end-cap)

The headers in Table 6-I and Table 6-II refer to the following cases:

Lost	Channel with no signal response or purposely disconnected because of an operating problem (bent straw, high-voltage, wire tension)
Deformation	Bent or non-circular straw causing unacceptable gain non-uniformity
HV	Disconnected because of high-voltage instabilities (excessive dark currents, reoccurring high-voltage trips)
Tension	Disconnected because of low tension (< 40 g) or large tension loss
Connectivity	No response or small amplitude from broken trace/connection or high blind-hole/microvia resistance

6.7 The end-cap wheel passport

Each 8-plane end-cap wheel is issued a so-called “End-cap Wheel Passport”, which is filled with the relevant acceptance test results [83]. The review of acceptance test data leading to approval or disapproval is done in a “Quality Circle” meeting, shortly after completion of the tests. A second supplementary document to each 8-plane wheel (“Quality Report”) contains a channel-by-channel analysis of straws with nonconforming and anomalous behaviour (“candidates for disconnection”). Straw amplitude and resolution profiles are examined together with the recorded ^{55}Fe spectra in order to identify the cause of the anomality and make a decision whether to disconnect a straw or not.
In addition to the acceptance test results the passport holds information on the position of the 8-plane wheel in the end-cap stack and a summary table of all disconnected channels (i.e. all dead or purposely disconnected straws). Repair information that has been done at production or acceptance site is listed at the end. A sample end-cap wheel passport is shown in Appendix C.

TABLE 6-I Lost channels out of a total of 73 728 straws measured (type-A wheels).

Type A 8-plane ID	Total lost	Deformation	HV	Tension	Connectivity
20ITPNPA800002	21	8	0	0	13
20ITPNPA800003	28	1	1	1	25
20ITPNPA800004	33	18	2	0	13
20ITPNPA800005	9	2	2	0	5
20ITPNPA800006	4	1	0	1	2
20ITPNPA800007	9	1	1	0	7
20ITPNPA800008	1	1	0	0	0
20ITPNPA800009	5	1	1	0	3
20ITPNPA800010	3	1	0	1	1
20ITPNPA800011	3	0	0	0	3
20ITPNPA800012	6	5	0	0	1
20ITPNPA800013	2	1	1	0	0
Total	**124 (0.17 %)**	**40**	**8**	**3**	**73**

TABLE 6-II Lost channels out of a total of 49 152 straws measured (type-B wheels).

Type A 8-plane ID	Total lost	Deformation	HV	Tension	Connectivity
20ITJNRB800002	15	1	0	0	14
20ITJNRB800003	26	0	0	0	26
20ITJNRB800004	2	1	0	0	1
20ITJNRB800005	16	1	0	0	15
20ITJNRB800006	15	3	0	0	12
20ITJNRB800007	8	1	0	0	7
20ITJNRB800008	10	1	0	0	9
20ITJNRB800009	7	1	0	0	6
Total	**99 (0.20 %)**	**9**	**0**	**0**	**90**

6.8 Conclusions

The TRT's successful operation depends not only on its intrinsic design features but also on the careful realization of the concept into the real detector. Many exclusive requirements on functionality, stability, safety, cost-effectiveness and producibility pose a challenge in the detector construction. Its survival for 10 years in the LHC's harsh radiation conditions, with little possibility to debug, repair or patch failures in the detector, is mainly predetermined by permanent and resolute quality assurance and quality control measures.

Therefore the 40 (8-plane) end-cap wheels (as well as 96 barrel modules), containing a total of ~300 000 straws, have to pass a series of stringent acceptance tests before the integration with the front-end electronics. A number of tests will be repeated until the completed Inner Detector, including SCT and Pixel, will be installed in the ATLAS experiment. The TRT's functional units have to adhere to strict quality assurance specifications, based on which acceptance tests have been defined.

The majority of the acceptance tests are conducted using the commonly used and easily available Ar-CO_2 70/30 gas mixture. It has been demonstrated that it represents a valid alternative to the costly Xe based operating gas (Xe-CO_2-O_2 70/27/3), to perform all tests relevant to the TRT performance.

Strict **mechanical envelopes** are required for smooth assembly and integration. Adhering to given tolerances, already at the single wheel level, prevents violating the defined envelopes when stacking twenty 8-plane wheels to a complete end-cap.

With the gas leak tests the proper sealing of the active gas volume is verified, with more than 12 000 glue joints in an 8-plane wheel (from 6144 straws and the enclosure of the gas manifolds). Xenon contamination of the straw envelope volume as well as significant losses of the expensive noble gas must be avoided. As a result in most of the cases a significantly smaller leak rate was achieved than the requirement of 1 mbar/min/bar.

In the **long-term high-voltage test** faulty straws exhibiting large leakage currents or frequent trips are identified and disconnected. However, experience has shown that high-voltage trips most often disappear after an initial test period, indicating some kind of "cleaning process" in the straw tubes. The fraction of straws lost due to high-voltage problems remains well below 10^{-4}.

Special attention was paid to wire tension since all wires in the TRT are pinned (barrel) or crimped (end-cap). These are clean and technically feasible options. Large changes in tension are of concern, posing a threat to a full high-voltage group, if a single wire slips into the instability regime. While material fatigue (creep) of the tungsten wires can be excluded, incompletely inserted crimp pins could lead to significant tension loss after relaxation.

The **wire tension** measurement setup at CERN has been modified to allow fast and reliable measurements of the more than 6000 wires in an 8-plane wheel. Influences on wire tension like temperature or slippage have been evaluated and made consistent with the requirements. The only real threat would come from imperfectly inserted crimping pins, a technical flaw that can easily be avoided during production. Specific studies of the distribution and evolution of wire tension with time have shown no tendency towards global loss of tension in any module or wheel. Cases of large change of tension are extremely rare ($<10^{-4}$) for more than 120 000 wires measured to-date.

Acceptance criteria such as **wire eccentricity** have considerable influence on the operational behaviour of each single straw. This behaviour has to be monitored closely since it might affect the functionality of the neighbour straws, connected e.g. to the same high-voltage component or front-end chip. Wire offset, predominantly caused by non-straightness of the straw tube, manifests itself in the loss of gas gain uniformity along the straw. The distortion of the radial symmetry of the electric field in the straw results in an overall increase in gain and amplitude variations decreasing the safety margin to the point of high-voltage breakdown. The measurement of the large number of straws in the TRT requires a automated and reliable mechanism, implemented through the Wheel Test Station (WTS). Acceptance criteria were defined with the help of experimental studies on the properties of bent straws, taking into account the change to a binary gas mixture. With the definition of two acceptance criteria, namely the change in gas gain in conjunction with the change in energy resolution (peak width), bent straws can easily be identified and distinguished from other observed and classified anomalies. Simulation studies, described in Chapter 4, are in line with the experimental observations. The number of disconnected straws because of too large wire eccentricity is of order 0.05 %, well within the goal of 1 % maximum dead channels, confirming the high standards required and achieved during production and testing.
The results of all acceptance tests are stored in production data bases and summarised in so-called electronic passports, an example of the latter is shown in the Appendix C.
The end-cap wheel testing is well under way with an expected completion by Fall 2005. The integration process of both barrel modules and end-cap wheels is in full swing and expected to be complete towards the end of 2005. Before final installation in the ATLAS cavern in spring 2006, the TRT barrel and end-caps will be integrated and tested with their respective SCT counterparts.

CHAPTER 7

"The great tragedy of Science -
the slaying of a beautiful hypothesis by an ugly fact."
Thomas H. Huxley (1825-1895)

Conclusions

The Transition Radiation Tracker of the ATLAS experiment is large-scale gaseous straw drift tube detector that will operate under unprecedented radiation conditions at the LHC. It is part of the Inner Detector, and combines charged particle track reconstruction with electron identification capability. Constraints on the access and maintenance scenarios therefore demand a high degree of operation stability and reliability.

In a number of repetitive **acceptance tests,** quality attributes such as adherence to given dimensional envelopes, wire tension, leak-tightness, high-voltage stability and straw straightness are surveyed. Particular subjects of study were wire tension and straw straightness, the former mainly from a instrumental point of view, the latter was re-evaluated in the course of change of gas mixture.
The main goal to improve reliability in the wire tension setup was reached and led to a significant decrease in test duration and higher reliability of the obtained wire tension data. Dedicated studies and the statistics from a large number of straws have shown an extremely low rejection rate due to low tension in the end-cap, verifying the stringing method and quality.
Straw deformation studies yielded a clear relation of loss of gain uniformity and energy resolution in the straw with wire offset. In such a way bent straws are reliably identified, and those with wire offsets larger 400 µm disconnected for operational safety reasons. Other phenomena like wire pollution/ageing or straw non-circularity are distinguishable, albeit, extremely rare. The number of disconnected straws in the first end-cap due to large wire eccentricity remains far below the acceptable limit, again a result of the stringent quality control and assurance measures.
The fraction of lost channels of 0.2 % in the first TRT end-cap lies well within the envisaged 1 % limit.

A small straw tube counter (the *gas-monitor*) was developed, constructed and employed to monitor and validate the cleanliness of the TRT's gas systems at production and acceptance sites. The **gas-monitor** was also successfully used to study the ageing properties of Ar-CO_2 70/30 with respect to operating parameters like gas flow and irradiation conditions. As a conclusion, under the operating conditions during end-cap testing there is no evidence of a risk of ageing, mainly due to the strict selection and validation of all gas

system components. This gives great confidence to deliver a clean detector system to ATLAS experiment, where any intrinsic pollution would be fatal in combination with the expected radiation environment at the LHC.

With the help of computing tools **straw performance** was simulated and properties of the TRT gas mixtures studied. In a remarkable way, experimental facts and effects are reproduced in the simulations, increasing both confidence in observations and measurements as well as in the simulation tools itself (i.e. the models represent an adequate description of reality). In particular the influence of temperature, nitrogen contamination and wire offset on electron drift times and gas gain were analysed. The consideration of Penning transfers in the gas gain computations was shown to be crucial. The required transfer efficiencies to reproduce experimental data are in excellent agreement with earlier findings.

The TRT has recently accomplished the assembly of its first end-cap (the barrel section was completed at the end of 2004) with excellent results in terms of channel losses. The production and acceptance testing of the remaining twenty 8-plane wheels for the second end-cap is in full swing with an expected completion by end of 2005.

Bibliography

[1] P. Cwetanski, et al, *Acceptance Tests and Criteria of the ATLAS Transition Radiation Tracker*, IEEE Trans. Nucl. Sci. Vol. 52, Issue 6, Part 2, 2911-2916 (2005).

[2] O. Brüning, et al., *LHC Design Report Vol.1*, CERN-2004-003, CERN, Geneva 2004.

[3] ATLAS Collaboration, *ATLAS Technical Proposal*, CERN/LHCC/94-43, CERN, Geneva, 1994.

[4] CMS Collaboration, *CMS, the Compact Muon Solenoid: Technical Proposal*, CERN-LHCC-94-38, CERN, Geneva, 1994.

[5] ALICE Collaboration, *ALICE: technical proposal for a large ion collider experiment at the CERN*, CERN-LHCC 95-71, CERN, Geneva, 1995.

[6] LHCb Collaboration, *LHCb: Technical Design Report - Reoptimized Detector Design and Performance*, CERN-LHCC-2003-030, CERN, Geneva, 2003.

[7] The TOTEM Collaboration, *TOTEM Technical Design Report*, CERN-LHCC-2004-002, 7 January 2004.

[8] S. F. Novaes, *Standard Model: An Introduction*, Proceedings of the 10th Jorge Andre Swieca Summer School: Particle and Fields, World Scientific, Singapore, 2000, `hep-ph/0001283`, and references therein.

[9] R. Barate, et al., *Search for the standard model Higgs boson at LEP*, Phys. Lett. B 565 (2003) 61.

[10] The LEP Electroweak Working Group, <http://lepewwg.web.cern.ch/LEPEWWG/>

[11] S. Martin, *A Supersymmetry Primer*, contribution to “Perspectives on Supersymmetry”, G. Kane (ed.), World Scientific, Singapore, 1998, `hep-ph/9709356`, and references therein.

[12] P. Jacobs and X. Wang, *Matter in extremis: ultrarelativistic nuclear collisions at RHIC*, Prog. Part. Nucl. Phys. 54 (2005) 443, `hep-ph/0405125`, and references therein.

[13] CMS Collaboration, *CMS, the Tracker System Project: Technical Design Report*, CERN-LHCC-98-006, CERN, Geneva, 1997.

[14] CMS Collaboration, *The CMS Tracker TDR: Addendum 1*, CERN-LHCC-2000-016, CERN, Geneva, 2000.

[15] CMS Collaboration, *The Electromagnetic Calorimeter Project: Technical Design Report*, CERN-LHCC-97-033, CERN, Geneva, 1997.

[16] CMS Collaboration, *CMS, the Muon Project: technical design report*, CERN-LHCC-97-032, CERN, Geneva, 1997.

[17] ALICE Collaboration, *ALICE: Technical Design Report of the Time Projection Chamber*, CERN/LHCC 2000–001, CERN, Geneva, 2001.

[18] ALICE Collaboration, *A Transition Radiation Detector for Electron Identification within the ALICE Central Detector*, CERN/LHCC 99–13, CERN, Geneva, 1999.

[19] ATLAS Collaboration, *ATLAS Inner Detector Technical Design Report,* CERN/ LHCC/97-17, ATLAS TDR 5, 30 April 1997.

[20] F. Hügging, on behalf of the ATLAS Pixel collaboration, *The ATLAS Pixel Detector*, IEEE NSS & MIC Conference Record (2004).

[21] M. Turala, for the ATLAS SCT collaboration, *The ATLAS semiconductor tracker*, Nucl. Instr. and Meth. A 466 (2001) 243-254.

[22] ATLAS Collaboration, *Liquid Argon Calorimeter: Technical Design Report*, LHCC-96-41, CERN, Geneva, 1996.

[23] ATLAS Collaboration, *Tile Calorimeter: Technical Design Report*, LHCC-96-42, CERN, Geneva, 1996.

[24] The ATLAS Muon Collaboration, *ATLAS Muon Spectrometer Technical Design Report,* CERN/LHCC/97-22, Geneva, May 1997.

[25] Adele Rimoldi, on behalf of the ATLAS Muon Group, *The ATLAS muon trigger chamber system*, Nucl. Instr. and Meth. A 409 (1998) 669-674.

[26] V. L. Ginzburg and I. M. Frank, *Radiation of a uniformly moving electron due to its transition from one medium into another*, Zh. Eksperim. i Teor. Fiz., 16 (1946) 15; J. Phys. USSR, 9 (1945) 353.

[27] B. Dolgoshein, *Transition radiation detectors*, Nucl. Instr. and Meth. A 326 (1993) 434-469.

[28] T. Åkesson, et al, *Aging studies for the ATLAS Transition Radiation Tracker (TRT)*, Nucl. Instr. and Meth. A 515 (2003) 166-179.

[29] T. Åkesson, et al, *Straw tube drift-time properties and electronics parameters for the ATLAS TRT detector*, Nucl. Instr. and Meth. A 449 (2000) 446-460.

[30] T. Åkesson, et al, *Operation of the ATLAS Transition Radiation Tracker under very high irradiation at the CERN LHC*, Nucl. Instr. and Meth. A 522 (2004) 25-32.

[31] V. Tikhomirov (private communication), February 2004.

[32] T. Åkesson, et al, *ATLAS Transition Radiation Tracker test-beam results*, Nucl. Instr. and Meth. A 522 (2004) 50-55.

[33] T. Åkesson, et al, *Status of design and construction of the Transition Radiation Tracker (TRT) for the ATLAS experiment at the LHC*, Nucl. Instr. and Meth. A 522 (2004) 131-145.

[34] M. Capeans, on behalf of the ATLAS TRT collaboration, *The Transition Radiation Tracker of the ATLAS Experiment*, IEEE Trans. Nucl. Sci. Vol. 51, 994-1000 (2004).

[35] T. Åkesson, et al, *Study of straw proportional tubes for a transition radiation detector/tracker at LHC*, Nucl. Instr. and Meth. A 361 (1995) 440-456.

[36] B. Bevensee, et al, *An Amplifier-Shaper-Discriminator with Baseline Restoration for the ATLAS Transition Radiation Tracker*, IEEE Trans. Nucl. Sci. Vol. 43, 1725-1731 (1996).

[37] N. Dressnandt, et al, *Implementation of the ASDBLR Straw Tube Readout ASIC in DMILL Technology*, IEEE Trans. Nucl. Sci. Vol. 48, 1239-1243 (2000).

[38] C. Alexander, et al, *Progress in the Development of the DTMROC Time Measurement Chip for the ATLAS Transition Radiation Tracker (TRT)*, IEEE Trans. Nucl. Sci. Vol. 48, 514-519 (2001).

[39] V. Ryjov, et al, *Implementation of the DTMROC-S ASIC for the ATLAS TRT Detector in a 0.25µm CMOS technology*, IEEE NSS & MIC Conference Record (2002).

[40] P. Cwetanski, et al, *Studies of wire offset effects on gas gain in the ATLAS TRT straw chamber*. ATL-INDET-2000-016, CERN, 2000.

[41] B. Dolgoshein, et al, *Gas Mixtures for Transition Radiation Detectors at High-Luminosity Colliders*. Nucl. Instr. and Meth. A 294 (1990) 473.

[42] A. Romaniouk, *Specification for gold-plated tungsten wire*, ATL-IT-ES-0012, CERN, March 2000.

[43] M. Capeans and J. M. Dalin, *Validation of the Wiring of Wheel 20ITJNRB000003 assembled at Dubna* and *Validation of the Wiring of the 4-plane Wheel 20ITPNPA000006 assembled at PNPI*, ATL-IT-QC-0023, CERN, 2002/2003.

[44] V. I. Razin, *Self-Quenched Streamer Operating Mode of Gas-Discharge Detectors (Review)*, Instr. and Exp. Tech. 44 (2001) 425-443.

[45] M. Capeans, *Aging and materials: lessons for detectors and gas systems*, Nucl. Instr. and Meth. A 515 (2003) 73-88.

[46] F. Hahn, et al, *The ATLAS TRT (active) Gas System Modules*, ATLAS Internal Note, CERN, 2004.

[47] R. Hawkings, et al, *Inner Detector Thermal Management and Environmental Gas*, ATL-IC-EN-0009, CERN, 2003.

[48] J. Godlewski and P. Skarby, *The Straw Cooling System in the ATLAS TRT*, ATL-INDET-2002-022, CERN, 2002.

[49] J. Grognuz, H. Danielsson and M. Bosteels, *TRT End-Caps CO_2 Cooling and Ventilation System*, ATL-IT-ES-0033 , CERN, 2005.

[50] J. Grognuz (private communication), April 2005.

[51] G. F. Knoll, *Radiation Detection and Measurement*, 2nd edition, John Wiley & Sons, Inc., 1989.

[52] A. Peisert and F. Sauli, *Drift and diffusion of electrons in gases: a compilation*, CERN-EP/84-08.

[53] P.H. Larsen and M. T. Elford, *The mobilities of xenon ions in xenon and the derived charge transfer chross section for $Xe^+(^2P_{3/2})$ ions in xenon*, J. Phys. B: At. Mol. Phys. 19 (1986) 449-461.

[54] L. B. Loeb, *Basic Processes of Gaseous Electronics*, University of California Press, Berkeley, California, 1961.

[55] International Commission on Radiation Units and Measurements, *Average Energy Required To Produce An Ion Pair*, ICRU Report 31, Washington, United States, 1 May 1976.

[56] S. F. Biagi (private communication), May 2005.

[57] F. Sauli, *Gas-filled detectors*, Short Course at the 2002 IEEE NSS/MIC, Norfolk, United States.

[58] D. Rapp and D. D. Briglia, *Total Cross Sections for Ionization and Attachment in Gases by Electron Impact. II. Negative-Ion Formation*, J. Chem. Phys. 43, 1480 (1965).

[59] R. Veenhof, *Garfield - A drift chamber simulation program*, CERN Program Library W5050, 1984 <http://consult.cern.ch/writeup/garfield/help>

[60] S. F. Biagi, et al, *A multi-term Boltzmann analysis of drift velocity, diffusion, gain and magnetic field effects in argon, methane and water vapour mixtures*, Nucl. Instr. and Meth. A 283 (1989) 716.

[61] S. F. Biagi, *Monte Carlo simulation of electron drift and diffusion in counting gases under the influence of electric and magnetic fields*, Nucl. Instr. and Meth. A 421 (1999) 234-240.

[62] I. Smirnov, Heed - Interactions of particles with gases.
CERN Program Library W5060, 1995.

[63] H. Helm, *The mobilities of atomic krypton and xenon ions in the 2P1/2 and 2P3/2 state in their parent gas*, J. Phys. B: At. Mol. Phys. 9 (1976) 2931-2943.

[64] S. F. Biagi, private communications, 2004/2005.

[65] S. F. Biagi, et al, *Experimental results from a microdot detector overcoated with a semiconducting layer*, Nucl. Instr. and Meth. A 419 (1998) 438-443.

[66] P. Cwetanski, *Studies on detector prototypes for the inner tracking system of LHCb*, Diploma Thesis, Univ. Heidelberg, 2000 (also CERN-THESIS-2004-007).

[67] A. Andronic, et al, *Drift velocity and gain in argon- and xenon-based mixtures*, Nucl. Instr. and Meth. A 523 (2004) 302-308.

[68] T. Kowalski (private communication), September 2004.

[69] R. Veenhof (private communication), November 2000.

[70] A. Ekstroem and M. Kagan, *The ATLAS TRT straws and effects of geometrical straw deformations on signal amplitudes*, CERN Internal Report, 2004. Contact: Andreas.Ekstroem@cern.ch or makagan@umich.edu.

[71] A. Romaniouk, *Validation of the gas system components: concept and plans*, Active Gas Production Readiness Review Meeting, CERN, 3 March 2004.

[72] M. Capeans, et al, *Recent Aging Studies for the ATLAS Transition Radiation Tracker*, IEEE Trans. on Nucl. Sci. Vol. 51, 960-967 (2004).

[73] A. Romaniouk, *Specifications for the gas system components and validation concept and plans*, Active Gas Final Design Review Meeting, CERN, 4 July 2003.

[74] A. O. Golunov, et al, *An automatic system for controlling the quality of straws installed in the ATLAS TRT detector*, Nucl. Instr. and Meth. A 524 (2004) 142-145.

[75] D. K. Cohen and J. E. Potts, *Light transmission through reflecting cylindrical tubes*, Am. J. Phys. 46 (1978) 727.

[76] J. Kadyk, *Wire Chamber Aging*, Nucl. Instr. and Meth. A 300 (1991) 436-479.

[77] J. Kadyk (Ed.), Proceedings *Workshop on Radiation Damage to Wire Chambers*, Berkeley 1986 (LBL-21170).

[78] J. Va'vra, *Review of Wire Chamber Aging*, Nucl. Instr. and Meth. A 252 (1986) 547-563.

[79] K. Kurvinen, et al, *Analysis of organic compounds formed in electron avalanches in a proportional counter filled with Ar/C_2H_4 gas mixture*, Nucl. Instr. and Meth. A 515 (2003) 118-125.

[80] Proceedings *International Workshop on Aging Phenomena in Gaseous Detectors*, DESY, Hamburg, 2001 (Nucl. Instr. and Meth. A 515 (2003) 1-385).

[81] M. Titov, *Radiation Damage and Long-term Aging in Gas Detectors*, Proc. of the 42nd Erice Workshop on Innovative Detectors for Supercolliders, Erice, 2003.

[82] J. M. Dalin (private communication), 28 April 2003.

[83] M. Capeans, et al, *TRT Wheel acceptance tests and specifications*, ATL-IT-QP-0105 v.3, CERN, 2004.

[84] M. Capeans, *Gas System Components Choice*, ATL-IT-MM-0025.

[85] S. Konovalov, *Validation of Gas System Components*, TRT report under preparation.

[86] ATLAS TRT Quality Procedure, *Final dimensional checks after 4 and 8-plane assembly*, ATL-IT-QP-0101 v.2, CERN, 2003.

[87] ATLAS TRT Quality Procedure, *Procedure for the gas leak test of 4-plane wheels*, ATL-IT-QP-0083 v.2, CERN, 2002.

[88] M. Capeans, et al, *Active gas tightness test*, ATL-IT-QP-0083 and addendum ATL-IT-TP-0007, CERN, 2002-2004.

[89] ATLAS TRT Test Procedure, *Long-term HV test* , ATL-IT-TP-0009, CERN, 2002.

[90] ATLAS TRT Test Procedure, *Operation of the Wheel Test Station*, ATL-IT-TP-0008, CERN, 2002.

[91] ATLAS TRT Test Procedure, *Test of TRT End-cap Wheels*, ATL-IT-TP-0008, CERN, 2002.

[92] ATLAS TRT Operation Procedure, *Database software for TRT End-cap wheel acceptance tests at CERN*, ATL-IT-OP-0002 v.2, CERN, 2002.

[93] A. Romaniouk, *Toshiba Wire Validation*, ATLAS Note ATL-IT-TR-0004, 2000.

[94] A. H. Sully, *Metallic Creep and Creep Resistant Alloys*, Butterworths Scientific Publications, London, 1949.

[95] C. Lu and K.T. McDonald, *Drift Chamber Wire Quality Control: Preliminary Test Results*, BaBar Drift Chamber Technical Note TNDC-96-46, 22 August 1996.

[96] T. Akesson, et al, *An X-ray scanner for wire chambers*, Nucl. Instr. and Meth. A 507 (2003) 622-635

APPENDIX A

A. Relevant publications

Acceptance Tests and Criteria of the ATLAS Transition Radiation Tracker
P. Cwetanski, et al. (ATLAS TRT collaboration)
Presented at IEEE Nuclear Science Symposium & Med. Imag. Conf. 2004, Rome, Italy.
IEEE Transactions on Nuclear Science, Vol. 52, No. 6, December 2005, pp. 2911-2916.

Status of design and construction of the Transition Radiation Tracker (TRT) for the ATLAS experiment at the LHC
T. Åkesson, et al. (ATLAS TRT collaboration)
Nuclear Instruments and Methods in Physics Research A 522 (1-2) (2004) 131-145.

Recent Aging Studies for the ATLAS Transition Radiation Tracker
M. Capeans, et al. (ATLAS TRT collaboration)
IEEE Transactions on Nuclear Science, Volume 51, No. 3, June 2004, pp 960-967.

Aging studies for the ATLAS Transition Radiation Tracker (TRT)
T. Åkesson, et al. (ATLAS TRT collaboration)
Nuclear Instruments and Methods in Physics Research A 515 (2003) 166-179 .

An X-ray scanner for wire chambers
T. Åkesson, et al. (ATLAS TRT collaboration)
Nuclear Instruments and Methods in Physics Research A 507 (2003) 622-635.

Gas flow uniformity studies for the end-cap ATLAS TRT
V. Mitsou, P. Cwetanski, S. Mouraviev
ATLAS Internal Note, ATL-INDET-2002-012, CERN.

Systematic studies of gas mixtures for straw-based transition radiation detectors
A. Romaniouk, P. Cwetanski, V. Sosnovtsev
Presented at the "Workshop on advanced Transition Radiation Detectors for accelerator and space applications 2001", Bari, Italy;
published in INFN-LNF, Frascati Physics Series, Volume XXV, pp. 109-113.

Progress in simulations of micropatterned gas avalanche detectors
P. Cwetanski
Presented at IEEE Nuclear Science Symposium & Med. Imag. Conf. 2000, Lyon, France.
Nuclear Science Symposium Conference Record, 2000 IEEE Volume 1, p. 5/39 - 5/43.

Studies of wire offset effects on gas gain in the ATLAS TRT straw chamber
P. Cwetanski, A. Romaniouk, V. Sosnovtsev
ATLAS Internal Note, ATL-INDET-2000-016, CERN.

APPENDIX B

B. Garfield script

```
* SIMPLIFIED EXAMPLE SCRIPT TO ILLUSTRATE DRIFT AND GAS GAIN SIMULATIONS
* WITH GARFIELD (IN CONNECTION WITH MAGBOLTZ).
* THE SCRIPT CAN BE SAVED AND EXECUTED, HOWEVER, THE RESULTS
* MIGHT NOT AGREE WITH THE PRESENTED ONES, SINCE CRUCIAL
* REFINEMENTS ARE LEFT OUT FOR REASONS OF CLARITY.

&CELL
Global xoff=0
Global yoff=0.0500

Tube r 0.2 v -1530
Rows
 s 1 0.0031 {xoff} {yoff} 0

&GAS
Global temp=295
Call inquire_file(xenon-mix.gas,exist)
If exist then
  Get xenon-mix.gas
Else
 Magboltz xe 70 co2 27 oxygen 3 e-field-range 1 300 n-e 15 coll 10
 Write xenon-mix.gas
Endif

* APPLY CORRECTIONS COMPUTED WITH MAGBOLTZ (INCL. PENNING)
Read-vector emag   vd     dl     dt        alpha     att    alpenn
            1000   1.42   137.8  199.56    0.00      16.11  0.00
            2000   3.70   218.7  144.05    0.00      5.23   0.00
            3000   4.51   252.2  106.68    0.00      3.04   0.00
            6000   4.60   257.3  117.09    0.00      1.88   0.00
            7000   4.70   251.3  111.06    0.00      1.99   0.00
            8000   4.81   245.1  112.74    0.01      2.13   0.01
            10000  5.00   233.1  110.55    0.15      3.32   0.15
            13000  5.30   217.3  116.18    1.83      5.22   2.12
            20000  6.26   188.6  126.00    29.96     8.75   32.83
            30000  8.14   160.0  125.16    149.70    7.80   164.20
            40000  10.25  141.0  114.82    338.00    7.40   368.76
            60000  14.72  117.8  103.42    811.00    4.70   877.22
            80000  19.24  104.2  101.91    1355.80   4.00   1457.15
            100000 23.75  95.4   95.71     1897.80   3.10   2030.41
            150000 34.54  82.7   84.41     3260.90   2.00   3462.23
            200000 44.65  75.9   77.16     4536.00   1.40   4792.43
            300000 62.78  69.0   70.57     6823.40   0.80   7169.06


**** keep empty line after table **********
************************************************************
* E[V/cm], v[cm/microsec], dt/dl[microns/cm**0.5], a,n[cm^-1]
* computed at T=295 K and p=760 Torr
************************************************************
```

```
Global temp=295
Global E_p=emag/760
Global alpha_p=alpenn*(temp/295)/760
Global att_p=att*(temp/295)/760

add drift-velocity vd vs E_p
add townsend alpha_p vs E_p
add attachment att_p vs E_p
&DRIFT
Int-par int-acc 1e-12 mc-dist 0.0010 projected-path
Drift wires lines=50

area -0.2 -0.2 -0.2 0.2 0.2 0.2 view 0.6*x+y+0.4*z=0 3D outline
track 0.15 -0.2 0 0.15 0.2 0 lines 15
drift track

* COMPUTE THE GAS GAIN OF 10 SINGLE ELECTRONS STARTING
* AT RADIUS 1.9 MM (0.1 MM AWAY FROM TUBE WALL) ******

For i from 1 to 10 do
 Call drift_mc_electron(0,0.19,0)
 Call rnd_multiplication(g)
 Say “Gain : {g}”
Enddo

* COMPUTE THE AVERAGE GAS GAIN OBTAINED FROM 100 RANDOMLY DISTRIBUTED
* 55FE CLUSTERS ****************************************************
Call book_histogram(gain,100,0,100000)
Global r=0.2
Global nclus=100
Global fe55yield=258
Global fano=0.190
Global fluct=sqrt(fano*fe55yield)
Global nprim=fe55yield+entier(fluct*rnd_gauss)
Global abstot=0

For j from 1 to nclus do
 Global g_avg=0
 Global g_tot=0

** RANDOMIZE CLUSTER POSITION (AVOID TOO CLOSE TO TUBE WALL AND WIRE) ***
Global rpos=0.00255+(0.9897*r*rnd_uniform)

 for i from 1 to nprim do
  call drift_mc_electron(0,rpos,0)
  call rnd_multiplication(g)
  Global g_tot=g_tot+g
 enddo

 Global g_avg=g_tot/(fe55yield)
 Global abstot=abstot+g_avg
 Say "({j}) r_clus={entier(10000*rpos)}   G_clus={g_avg}"
 call fill_histogram(gain,g_avg)
Enddo

Say"========================================"
Say "Fe55 gain average: {abstot/nclus}"
Call plot_histogram(gain)
```

APPENDIX C

C. Technical drawings of the gas-monitor

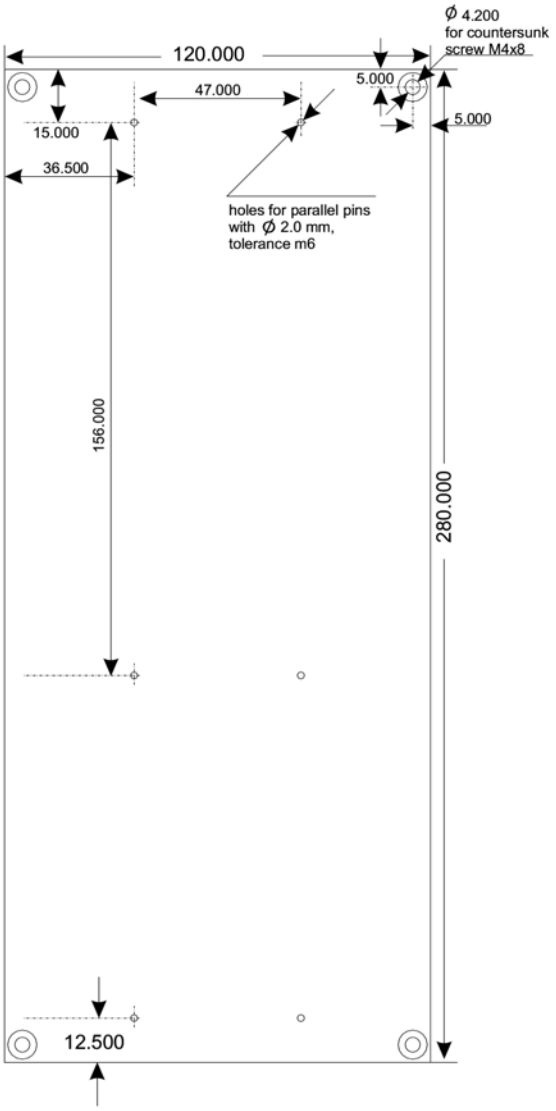

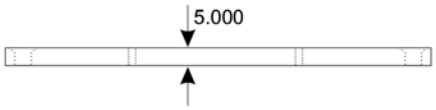

Author: Peter Cwetanski
Date: 21 Nov 2001
Part: detection unit support plate (design v.2)

Units: mm
Scale: 1 : 2

Project: ATLAS TRT gas monitor

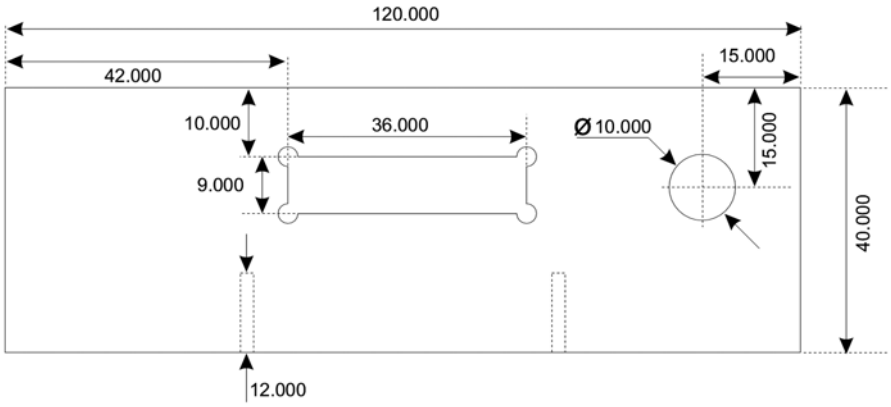

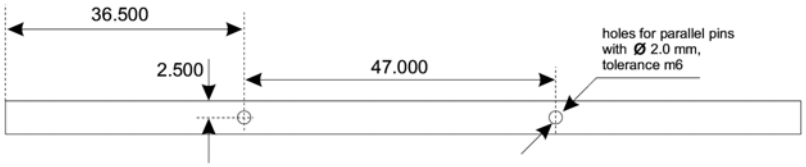

Author: Peter Cwetanski
Date: 9 Jan 2002
Part: panel plate (for flat cable connector)

Units: mm
Scale: 1 : 1

Project: ATLAS TRT gas monitor

front view

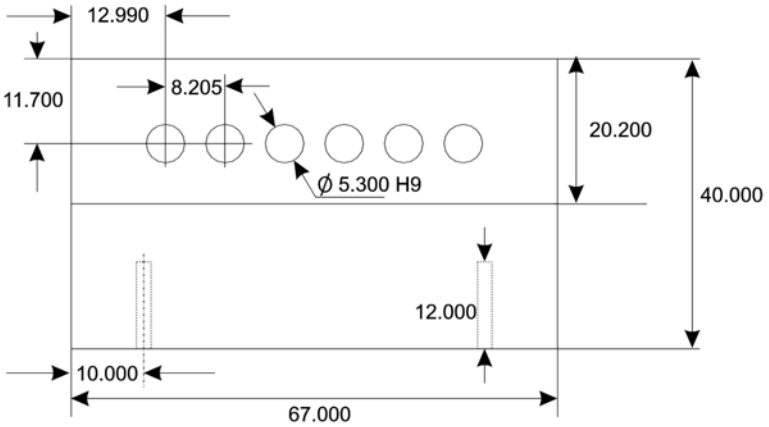

side view

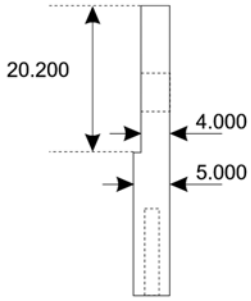

bottom view

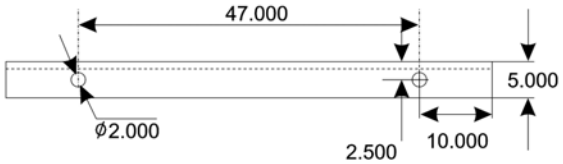

Author: Peter Cwetanski
Date: 7 Nov 2001
Part: straw support plate 1 design v.2

Units: mm
Scale: 1 : 1

Project: ATLAS TRT gas monitor

front view

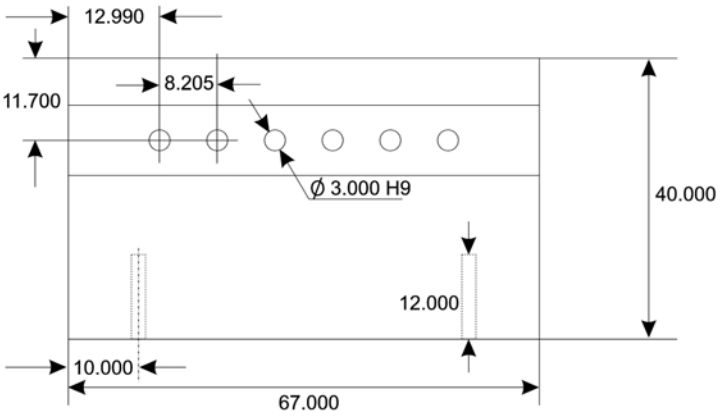

side view

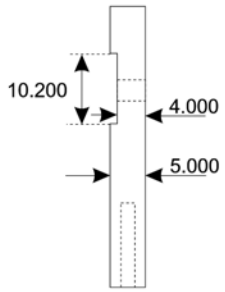

bottom view

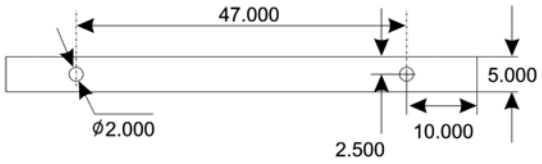

Author: Peter Cwetanski
Date: 7 Nov 2001
Part: straw support plate 2 design v.2

Units: mm
Scale: 1 : 1

Project: ATLAS TRT gas monitor

front view

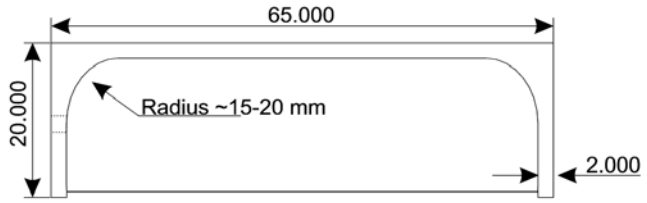

bottom view

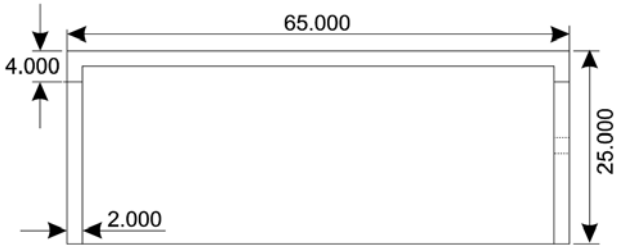

side view

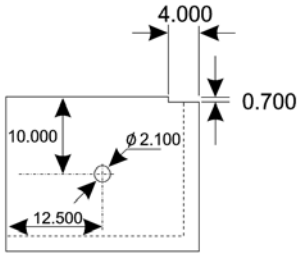

Author: Peter Cwetanski
Date: 9 Nov 2001
Part: gas distribution volume lid (design v.2)

Units: mm
Scale: 1 : 1

Project: ATLAS TRT gas monitor

front view

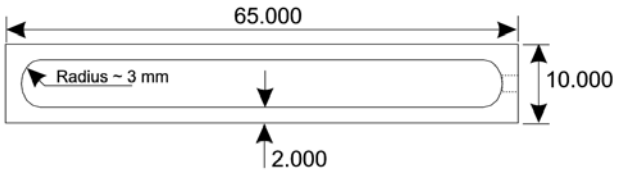

side view

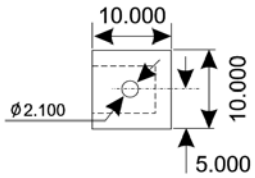

Author: Peter Cwetanski
Date: 9 Nov 2001
Part: gas exhaust volume lid (design v.2)

Units: mm
Scale: 1 : 1

Project: ATLAS TRT gas monitor

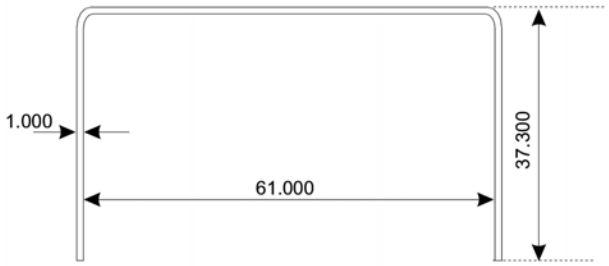

front view

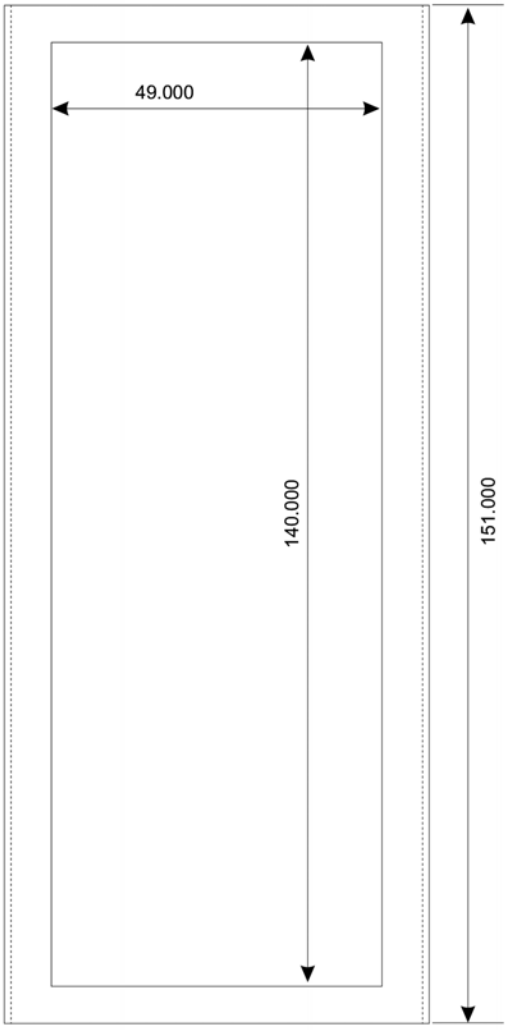

top view

Author: Peter Cwetanski
Date: 11 Feb 2002
Part: straw cover (for design v.2)

Units: mm
Scale: 1 : 1

Project: ATLAS TRT gas monitor

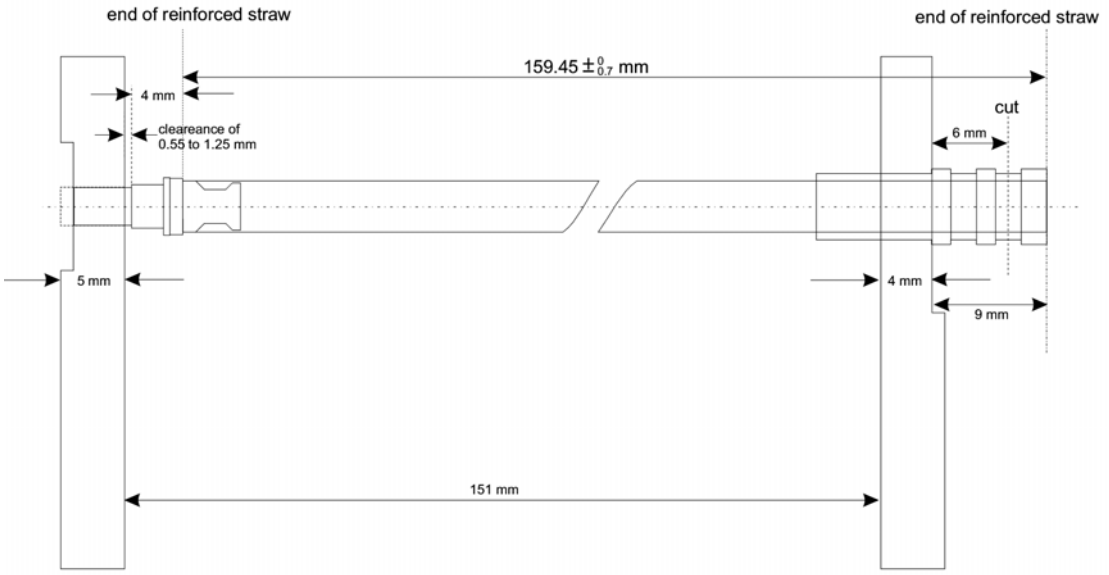

Author: Peter Cwetanski
Date: 21 Nov 2001
Part: reinforced straw cutting length (design v.2)

Units: mm
Scale: 2 : 1

Project: ATLAS TRT gas monitor

APPENDIX D

TRT end-cap wheel acceptance passport

This is a sample passport, which does not correspond to an actual wheel.
It has been altered for the sake of clarity and readability. (*Peter Cwetanski, 19.05.2005*)

General information

Product ID: **20ITPNPA800005**

4-plane wheels ID:	**20ITPNPA000009**	**20ITPNPA000008**
Position (front/back)	front	back
ABS part number:	ATL-0000001267	Wheel A inlet 8-plane, fully completed

Z-position in a stack:

1	2	3	4	5	6	7	8	9	10	11	12
		X									

Wheel position label: **A03C**

Stack side (A or C): **C**

Quality circle meeting date: 30 August 2004

☑ **- Approved by xxx**
☑ **- Approved by xxx**
☑ **- Approved by xxx**

Summary results:

List of dead and disconnected channels:

4-plane ID	Cell	Row	Layer	Chn	Reason & Comments	Status
20ITPNPA000008	3	7	4	23	dead on WTS	disconnected
20ITPNPA000008	23	1	3	177	dead at tension measurement	disconnected
20ITPNPA000008	23	3	1	179	dead at tension measurement	disconnected
20ITPNPA000008	23	4	2	180	dead at tension measurement	disconnected
20ITPNPA000008	28	4	4	220	dead on WTS	disconnected
20ITPNPA000008	67	8	3	536	dA/A=35.7 % FW0.2=54.0 % (bent or non-circular)	disconnected
20ITPNPA000009	30	1	3	233	dA/A=10.5 % FW0.2=47.6 % (bent)	disconnected
20ITPNPA000009	87	5	3	693	dead at tension measurement	disconnected
20ITPNPA000009	94	3	3	747	unstable at WTS	disconnected
Total:					**9**	

List of anomalous channels:

4-plane ID	Cell	Row	Layer	Chn	Reason & Comments	Status
20ITPNPA000009	27	7	1	215	dA/A=10.40 % FW0.2=33.50 % Small amplitude @Radius 6	OK
Total:					**1**	

Other anomalies:

Description	Repair	Comments

Test results

Reception and Dimension information

Reception date: 26/02/2004
Reception comments:

Wheel weight (in grams)		
8-plane wheel	23450	
4-plane wheels	9988	10045

Radiators structure	
4-pl. wheel ID	**Radiator foils**
20ITPNPA000008	7/15/15/14/7
20ITPNPA000009	7/15/15/15/7

Critical dimension measurements			
Max. thickness for Ring2	**Max. thickness for Ring3**	**Min. inner radius 1 (ch. 1)**	**Min. inner radius 2 (ch. 2)**
67.499	67.53	625.519	625.579

Web hole position measurement: DONE

HV connection check: DONE

Diode current test: DONE

Gas leakage test

dP/dT: -.0009 mbar/min **Leak rate:** .045 mbar/(bar·min)

Wire tension test

Tension distribution at CERN										
Wheel ID	**Measured**	**No data**	**<50**	**50-55**	**55-60**	**60-65**	**65-70**	**70-75**	**75-80**	**>80**
20ITPNPA000009	3072	**1**	**0**	0	32	1721	1311	6	0	**1**
20ITPNPA000008	3072	**3**	**1**	2	90	1437	1262	242	34	**1**
Total	6144	**4**	**1**	2	122	3158	2573	248	34	**2**

Tension histograms from assembly site

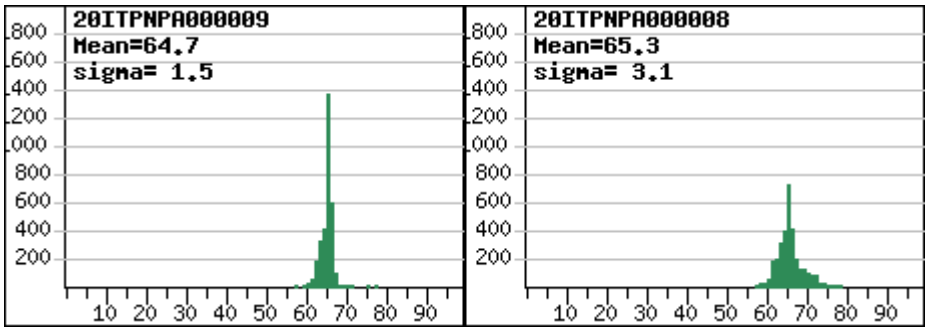

Tension histograms at CERN

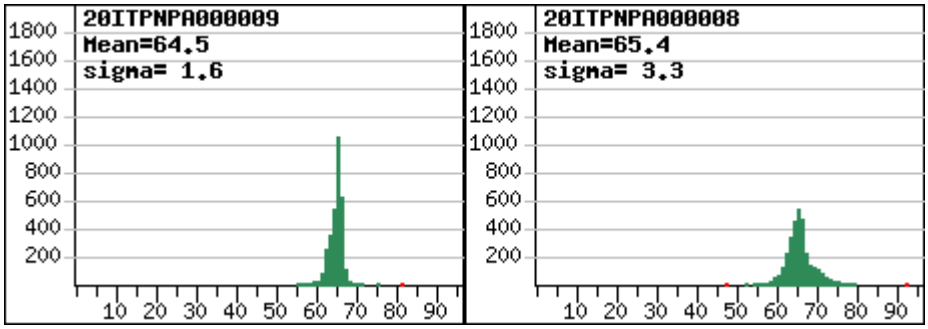

No data

ID	Cell	Row	Layer	Chn	Comments
20ITPNPA000009	87	5	3	693	
20ITPNPA000008	23	1	3	177	
20ITPNPA000008	23	3	1	179	
20ITPNPA000008	23	4	2	180	

Channels out of spec.(<50gr. or >80gr.)

ID	Cell	Row	Layer	Chn	Tension	Comments
20ITPNPA000009	7	2	1	50	81.34	
20ITPNPA000008	54	2	3	426	92.40	
20ITPNPA000008	70	6	4	558	46.75	

Channels with large tension loss

ID	Cell	Row	Layer	Chn	Site	CERN	Δ	Status
20ITPNPA000008	14	4	2	108	65.44	52.05	-13.39	OK
20ITPNPA000008	70	6	4	558	66.82	46.75	-20.07	OK

Comments

Cell#3, Row 6, Layer 3 - slippage= -5.6

Link to acceptance DB

Wheel test station

WTS run description

Wheel ID	Date	Description
20ITPNPA000008	07-03-2004	Repetition of previous run. Gas: premixed Ar/CO2 70/30, flow - 20 l/h. Flow direction: wheel #9 - inlet, wheel #8 - outlet. HV=1325 V. Slow control - ON. Monitor box - OFF.
20ITPNPA000009	04-03-2004	Repetition of previous run. Gas: premixed Ar/CO2 70/30, flow - 20 l/h. Flow direction: wheel #8 - inlet, wheel #9 - outlet. HV=1325 V. Slow control - ON. Monitor box - OFF.

Gas gain distribution table

Wheel ID	Measured	No data	<5%	5-9%	>9%
20ITPNPA000009	3072	**2**	3030	38	**2**
20ITPNPA000008	3072	**5**	2985	79	**3**
Total	6144	**7**	6015	117	**5**

dA/A histograms from assembly site

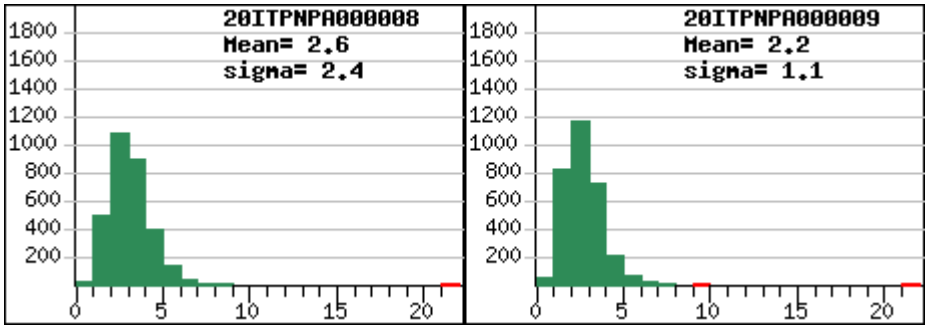

dA/A histograms at CERN

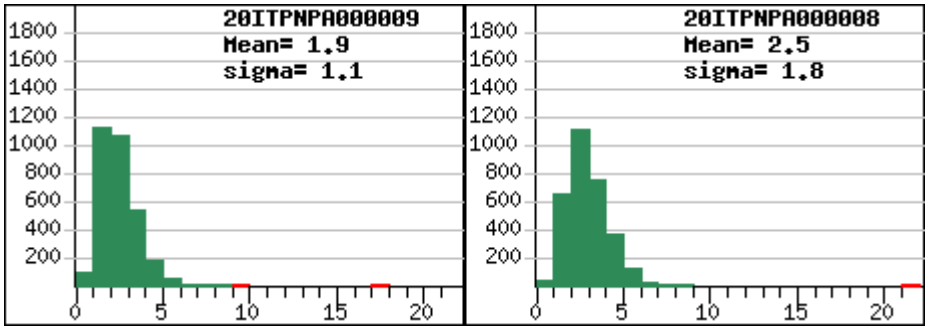

No data

ID	Cell	Row	Layer	Chn	Comments
20ITPNPA000009	87	5	3	693	
20ITPNPA000009	94	3	3	747	
20ITPNPA000008	3	7	4	23	
20ITPNPA000008	23	1	3	177	
20ITPNPA000008	23	3	1	179	
20ITPNPA000008	23	4	2	180	
20ITPNPA000008	28	4	4	220	

Channels out of spec.(dA/A>9%)

ID	Cell	Row	Layer	Chn	dA/A
20ITPNPA000009	27	7	1	215	9.25
20ITPNPA000009	30	1	3	233	17.30
20ITPNPA000008	25	2	2	194	50.48
20ITPNPA000008	25	7	3	199	52.72
20ITPNPA000008	67	8	3	536	29.47

Comments

Large dA/A of straws 25/2/2 and 25/7/3 (Cell/Row/Layer) is due to faulty reference straw behaviour.

Link to acceptance DB

Detailed Analysis of WTS

Dead channels

ID	Cell	Row	Layer	Chn	Spectrum	Generator peak	Problem
20ITPNPA000008	3	7	4	23	NO	YES	dead
20ITPNPA000008	23	1	3	177	NO	YES	dead
20ITPNPA000008	23	4	2	180	NO	YES	dead
20ITPNPA000008	23	3	1	179	NO	YES	dead
20ITPNPA000008	28	4	4	220	NO	YES	dead
20ITPNPA000009	87	5	3	693	NO	YES	dead
20ITPNPA000009	94	3	3	747	@R2,3,4	YES	Non stable

Non-conforming channels

dA/A>9% and FW0.2$_{max}$>35%							
ID	Cell	Row	Layer	Chn	dA/A	FW0.2$_{max}$	Problem
20ITPNPA000008	67	8	3	536	35.70%	54.00%	Bent or elliptic
20ITPNPA000009	30	1	3	233	10.5	47.6	Bent

dA/A>9% and FW0.2$_{max}$<35%							
ID	Cell	Row	Layer	Chn	dA/A	FW0.2$_{max}$	Comment
20ITPNPA000009	27	7	1	215	10.40%	33.50%	Small amplitude @R6. Ok.

Anomalous channels							
ID	Cell	Row	Layer	Chn	Spectrum	Generator peak	Problem

Other channels from online analysis							
ID	Cell	Row	Layer	Chn	dA/A	FW0.2$_{max}$	Comment
20ITPNPA000008	25	2	2	194	50.48	Small	Unstable reference spectra.
20ITPNPA000008	25	7	3	199	52.72	Small	Unstable reference spectra.

Other anomalies							
ID	Cell	Row	Layer	Chn	dA/A	FW0.2$_{max}$	Problem

Link to offline anlysis report in EDMS

HV test

Long-term HV test results:				
Voltage(V)	Date	N trips	Board/channel	Comments
1480	04/05 - 05/05/2004	no	-	ok
1480	06/05/2004	4	01/05	high humidity - 65%
1480	07/05/04	no	-	ok
1550	09/05/2004	1	01/01	trip when HV was increased
1550	10/05 - 19/05/2004	no	-	ok

Repair information

Channels repair during assembly and acceptance						
Wheel ID	Cell	Raw	Layer	Chn.	Object	Status
20ITPNPA000009	67	8	3	536	Microvia was repaired at PNPI.	OK
20ITPNPA000008	1	6	4	6	Broken trace during wiring. Conductive paste used to restore contact.	OK
20ITPNPA000008	3	6	2	22	Microvia was repaired at PNPI	OK
20ITPNPA000008	23	1	3	177	Microvia was repaired at PNPI. Broken trace during wiring. Conductive paste used to restore contact.	dead
20ITPNPA000008	23	4	2	180	Protection resistor unsoldered because of HV problem	disconnected
20ITPNPA000008	23	6	2	182	Blind hole was repaired at PNPI. Broken trace during wiring. Conductive paste used to restore contact.	OK
20ITPNPA000008	28	1	2	217	Broken trace during wiring. Conductive paste used to restore contact.	OK
20ITPNPA000008	28	4	4	220	Protection resistor unsoldered because of HV problem	dead

Repair and replacement information			
What	Where	Why	Action
Web	Wheel 20ITPNPA000008: leak between flaps 90 and 91	Bubbles in Kapton strip joint between webs	Repaired on 10/06/04 with new glue and new Kapton joint.